Shells, Bubbles and Holes: The Porosity of the Interstellar Medium in Galaxies

Ioannis Bagetakos

A report submitted in partial fulfilment of the requirements of the University of Hertfordshire for the degree of Doctor of Philosophy

November, 2011

This programme of research was carried out in the Centre for Astrophysics Research, School of Physics, Astronomy and Mathematics, Faculty of Science, Technology and Creative Arts, University of Hertfordshire

Abstract

We present an analysis of the properties of H I holes detected in 20 galaxies that are part of "The H I Nearby Galaxy Survey" (THINGS). We detected more than 1000 holes in total in the sampled galaxies. Where they can be measured, their sizes range from about 100 pc (our resolution limit) to about 2 kpc, their expansion velocities range from 4 to 36 km s^{-1}, and their ages are estimated to range between 3 and 150 Myr. The holes are found throughout the discs of the galaxies, out to the edge of the H I disc; 23% of the holes fall outside R_{25}. We find that shear limits the age of holes in spirals; shear is less important in dwarf galaxies which explains why H I holes in dwarfs are rounder, on average than in spirals. Shear, which is particularly strong in the inner part of spiral galaxies, also explains why we find that holes outside R_{25} are larger and older. We derive the scale height of the H I disc as a function of galactocentric radius and find that the disc flares at large radii in all galaxies. We proceed to derive the surface and volume porosity (Q_{2D} and Q_{3D}) and find that this correlates with the type of the host galaxy: later Hubble types tend to be more porous.

The size distribution of the holes in our sample follows a power law with a slope of $a_\nu \sim -2.9$. Assuming that the holes are the result of massive star formation, we derive values for the supernova rate (SNR) and star formation rate (SFR) which scales with the SFR derived based on other tracers. If we extrapolate the observed number of holes to include those that fall below our resolution limit, down to holes created by a single supernova, we find that our results are compatible with the hypothesis that H I holes result from star formation.

We use H I data from THINGS, 8μm, 24μm, 70μm and Hα maps from SINGS, CO(2–1) data from HERACLES and FUV data from NGS to present a visual comparison of these maps with respect to the locations of H I holes. We find that the vast majority of H I holes are also prominent in the 8μm map and to some extent in the 24μm map. There is a lack of molecular gas from the interior of nearly all the holes, which is consistent with the idea that the latter are filled with hot gas. About 60% of young holes have FUV emission detected in their interiors highlighting the presence of the parent OB association. In addition, FUV is detected on the rims of some of the older H I holes, presumably due to the dispersion of the OB association with respect to the gas. We describe the development of a 2–D cross-correlation method to compare multi-wavelength maps

in a quantitative way (quantified by C_{coef}) and give some first results from the application of this method to the nearby galaxy NGC 2403. We find that the all the dust tracers are well correlated ($C_{coef} > 0.7$) with the 8μm–24μm correlation being the highest ($C_{coef} > 0.88$). Similarly all the star formation tracers are well linked as expected ($C_{coef} > 0.6$). With respect to the relations between star formation and dust tracers we found that most are well matched ($C_{coef} > 0.7$) as dust grains are heated by radiation in star forming regions. At smaller scales (15″) FUV correlates poorly ($C_{coef} \sim 0.3$) with the dust tracers, a direct consequence of the absorption of FUV photons by dust. We find that the H I is reasonably well correlated with the 8μm emission ($C_{coef} \sim 0.6$) illustrating the fact that H I is mixed with PAH's. Interestingly, the H I map shows some correlation with the SF map ($C_{coef} \sim 0.4$) even though FUV and H I emissions were found to be completely uncorrelated ($C_{coef} \sim 0$).

Acknowledgements

First and foremost I would like to thank Prof. Elias Brinks for taking me on as a student and providing me with the opportunity to fulfil a dream. I would like to thank him for all the time, patience and encouragement he has provided throughout this research and for his kind and constant pressure, without which this study would have never materialized.

I am very grateful to Prof. Jim Hough for having the faith to offer me a place in the department, and for organising a University of Hertfordshire bursary to support my research, for which I am deeply indebted.

My deepest gratitude goes to my collaborators who have been a continual source of inspiration. I would like to deeply thank Prof. Fabian Walter for his support and invaluable comments throughout this project, Prof. Erwin De Blok for the opportunity to observe with the ATCA in Australia and Prof. Rob Kennicutt for his expertise and insight during the preparation of my first paper. Thanks to Antonio Usero for being an invaluable source of knowledge, Adam Leroy and Joshua Rich for their useful comments and discussions.

I would also like to thank my colleagues in CAR for their support and friendship. In particular, Volker Heesen (my second supervisor), Antonio Portas, Tom Scott and Dana Vicas for their advices and for being there all these years.

Of course, none of this would have been possible without the support and endless patience of my family, to whom this dissertation is dedicated to. Most importantly, my love and thanks go to my partner, Anna Mertziani, who has continually encouraged, supported and enabled me to pursue this project.

Contents

List of Figures

List of Tables

Chapter 1

Introduction

1.1 Overview

Observations of the Milky Way and nearby spiral galaxies have shown that most of the baryonic mass is condensed into stars. However, interstellar space is not entirely empty but filled with gas and interstellar dust amounting to about 10% on average of the stellar mass of the Galaxy and similar galaxies. The interstellar medium (ISM) is highly inhomogeneous with most of the mass concentrated in clouds occupying a small fraction of the total volume of a galaxy. Most of the interstellar gas is found in the galactic plane and the spiral arms and consequently the amount of stars and interstellar matter is about equal in these regions. In the local neighbourhood the mass contribution of the interstellar matter is around 30%. This medium is, however, extremely sparse with an average density of about one gas atom per cubic centimetre and 100 dust particles per cubic kilometre. As a result, it was completely overlooked by early astronomers and initially the only phenomenon directly available to visual observation were the diffuse bright nebulae and the partial extinction of starlight by "dark clouds" (e.g., Fig 1.1) in the visible structure of the Milky Way.

In 1811, William Herschel had already arrived at the conclusion that the abundance of nebulous matter must exceed all expectations but most astronomers were inclined to assume a completely empty space between the stars, in which the few objects, later known as gas- and dust-clouds, were only isolated phenomena. In 1904 J. Hartmann discovered a narrow absorption line of interstellar origin, the famous "stationary" calcium line in the spectrum of the spectroscopic binary star δ Orionis, which was recognized as important by only a few researchers and was at first explained as local absorption in the immediate neighbourhood of the star.

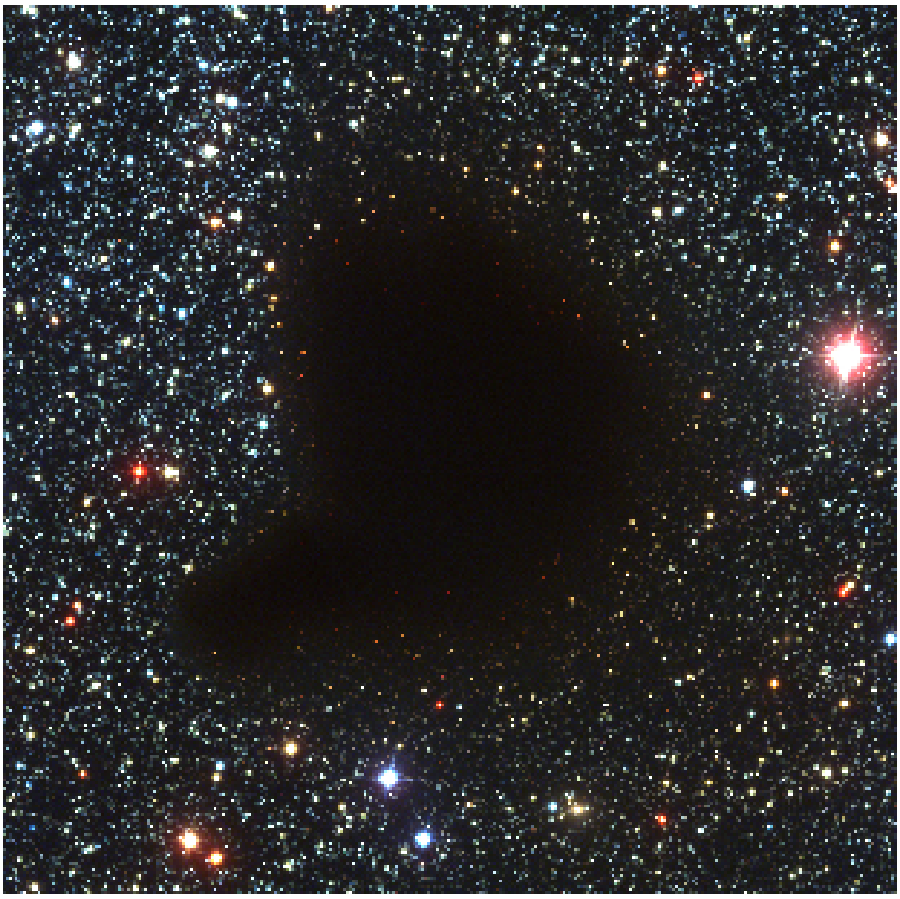

Figure 1.1: The dark molecular cloud Barnard 68 is an example of light absorption by dust grains. *Credit: FORS Team, 8.2-meter VLT Antu, ESO*

In the early years of the 20th century the prevailing view was that the ISM was homogeneous and diffuse, pervading space with near-constant density. This view was challenged in the late 1930's by the first high-resolution spectroscopy of bright stars that revealed that the so-called "stationary" lines were resolved into many narrower line components with different radial velocities. The complexity of the observed gas kinematics led to the recognition that the ISM was not homogeneous, but instead it was clumpy and organized into "clouds". The ISM suddenly became dynamic, with a kinetic energy density comparable to the thermal energy density (Dyson & Williams 1980).

The first convincing observational evidence on the nature of interstellar phenomena was produced by the introduction of photography into systematic observation of the sky. Long exposure photographs revealed a far clearer picture than could be obtained from visual observation. Many weak diffuse nebulae and dark clouds were discovered in the Milky Way and these dark patches were initially thought to be voids (Kwok 2007). Moreover, the photographs of spectra of diffuse nebulae showed that there were two different types: "emission nebulae", the optical radiation of which consisted of individual emission lines from atoms or ions, and "reflection nebulae" which simply reflected the light of neighbouring stars and therefore gave continuous spectra. In the dark clouds, on the other hand, a weakening of the continuous starlight was demonstrated (M. Wolf, 1923).

In 1930, Trumpler discovered that star clusters grew dimmer faster with distance than they would in a vacuum which revealed the existence of an absorbing and diffuse medium that absorbed starlight. The growing evidence for the existence of a general widespread interstellar medium led to a definitive change of approach: for gas components, the observation of a systematic increase in the strength of sharp interstellar absorption lines in stellar spectra with distance (Struve 1928), and for dust components, a comparison of photometric and geometric determinations of distance of open star clusters, from which resulted a general measure of interstellar extinction of almost one magnitude per one kpc. The year 1930 accordingly marked the approximate starting point of the study of interstellar matter as a new branch of astronomy.

Observationally, one of the most important tools in mapping the ISM is the 21–cm emission line of neutral hydrogen. Initially predicted by Hendrik van de Hulst in 1944 and independently detected by Ewen and Purcell at Harvard and Muller and Oort in 1951 this discovery marked the beginning of radio observations of the ISM in the Milky Way and nearby galaxies.

1.2 Gas

Evidence for the existence of interstellar gas comes mainly from spectroscopy by observing emission and absorption lines. The atoms and molecules in the ISM emit and absorb radiation corresponding to their different energy levels. As mentioned in the previous section, Johannes Hartmann observed absorption lines in the spectra of certain binary stars that were not Doppler shifted, as expected, by the motions of the stars. This proved that these lines came from gas clouds in the space between the Earth and the stars. In some stars, there were several lines, apparently formed in clouds moving with different velocities. The strongest lines in the visible region are those of neutral sodium and singly ionized calcium. In the ultraviolet region, the lines are more numerous with the strongest one being the Lyman line of hydrogen.

Stellar photons with energies higher than the Lyman limit (13.6 eV) can excite hydrogen atoms and thus ionize the gas. Based on optical and UV lines, it has been found that many atoms are ionized in interstellar space by stellar ultraviolet radiation, and to some extent, by cosmic rays. The density of interstellar matter is very low and as a result the free electrons only rarely encounter ions, and the gas remains ionized. Almost all elements from hydrogen to zinc (atomic number 30) and some additional heavier elements have been detected in the interstellar gas by absorption line observations in the visible and ultraviolet regime. The most abundant elements are hydrogen (about 70% by mass) and helium (almost 30% by mass) in agreement with stellar composition. However, heavier elements are significantly less abundant than in population I stars and must have been deposited in dust grains where they do not produce any absorption lines. This is supported by observations of dust poor regions where the element abundances in the gas are closer to solar.

The ISM is extremely inhomogeneous and in a dynamical state of constant change. Density, temperature, constitution of atoms, ions, and molecules, and its state of motion vary considerably from region to region. Many processes such as ultraviolet heating from stars in star-forming regions, supersonic expansion of shells of supernova explosions, and dynamical instabilities on every scale keep the ISM from a state of equilibrium. Under nearly all conditions, the ISM is either in a neutral state with a relatively small number of electrons and ions present, or it is in a state that is almost completely ionized. These two states can be further subdivided based on the physical state of hydrogen (Kulkarni & Heiles 1988).

In the neutral form the gas can be found in three different phases:

a) The molecular medium (MM), sometimes called the cold molecular neutral medium. It is in the form of cold dense molecular clouds and it is traced by molecular line emission. By measuring the intensity of spectral lines we know that its temperature is at most a few tens of degrees Kelvin, its mean volume density around 10^3 atoms cm^{-3} and it has a volume filling factor $f < 1\%$. The molecular clouds have typical sizes of ~ 40 pc and masses of order 10^5 $\mathcal{M}_\odot$ (Tielens 2005), deduced by measuring the sum of all line intensities. These are not in pressure equilibrium with other components of the ISM but self-gravitating. Consequently, their density varies considerably and in certain cases dense cores with densities of 10^4 cm^{-3} can form. These cores will eventually become new stars making molecular clouds the birthplaces of stars. Even though CO transitions are commonly used to trace this medium, more than 200 molecular species have been discovered with H_2 being the most abundant molecule. However, H_2 has extremely weak vibrational and rotational lines making it difficult to observe directly. Instead, the CO J=1–0 line at 2.6 mm is commonly used to indirectly detect interstellar H_2, which is thought to be the most abundant molecular species with an H_2/CO ratio of 10^4–10^5.

b) The cold (atomic) neutral medium (CNM), which is traced by the 21 cm hydrogen line, mainly when mapping H I in absorption and by UV absorption lines of various elements. Its temperature is typically around 100 K, its mean volume density ranges from 10 to 100 atoms cm^{-3} and its volume filling factor $f \approx 2-4\%$ (Kwok 2007). The morphology of the CNM is in the form of diffuse H I clouds with a typical size of 10 pc and mass of ~ 50 $\mathcal{M}_\odot$.

c) The warm neutral medium (WNM). Roughly half of all H I is WNM and can be observed using the 21 cm hydrogen line in emission. It has a low volume density ($n \approx 0.3$ cm^{-3}) and fills a substantial fraction of the interstellar volume ($f \geq 30\%$). The temperature of the WNM is of order 6000 K (Tielens 2005).

In the ionized state the ISM can be found in two different phases:

a) The warm ionized medium (WIM). This is a widely spread and diffuse medium traced by the Hα emission line and is also associated with distinct H II regions. The temperature of this medium is around 8000 K, its volume density is about 0.3 cm^{-3} and it has a volume filling factor of more than 15%. In the H II regions the density may range from 10 to 10^6 electrons cm^{-3} (Kwok 2007). The main source of ionization is considered to be ionizing photons from O and B stars and, to a lesser extent, due to shocks and collisions in the gas.

b) The hot ionized medium (HIM) which accounts for a large fraction ($f \leq$

50%) of the interstellar space and is also called "coronal gas". It is mainly associated with supernovae, and can be observed through diffuse soft X-ray emission and UV absorption lines of highly ionized elements (e.g., CIV, OVI, NV), which indicate a temperature of at least 2×10^5 K. It has a low density of about 10^{-3} electrons cm^{-3} (Kwok 2007) and consequently it does not contribute significantly to the total mass of the ISM. Most of this plasma is transferred to galaxy haloes through mechanical energy provided by supernovae and channelled through superbubbles of hot gas.

It has to be stated here that the aforementioned values are an approximation and represent the current theories and models of the ISM. A more detailed view of the current models is given in Section 1.4.

1.3 Dust

The under-abundance of elements heavier than He in the gas phase suggest that these might be in the form of grains. Historically, evidence of interstellar dust came from its starlight-obscuring effects and the need to correct for this by creating maps of local dust concentrations. We now know that these dark interstellar clouds are clouds of cold interstellar gas mixed with dust grains. The composition of dust grains is mainly carbon, silicon and iron-based, usually covered by a layer of ice (Draine 2003). They are macroscopic particles with typical sizes from a few molecules to 0.1μm and their origin is most likely AGB stars and supernovae.

Interstellar dust plays an important role in the physics of the interstellar medium, from the behaviour and chemistry of the gas, to the process of star formation. Dust grains shape the spectra of galaxies by attenuation of radiation at short wavelengths which is then re-radiated at longer wavelengths, mainly the far-infrared. In fact, at least 30% of the energy from stars is re-radiated in the infrared. The presence of dust grains in the ISM was initially inferred from this obscuration of stellar photons by Trumpler (1930). Most of the information on interstellar dust, such as the grain size distribution comes from studies of the "extinction" or "reddening" of starlight which is wavelength dependent. Analysis of spectral features is used to reveal the chemical composition of dust.

As mentioned earlier the ISM amounts to about 10% of the baryonic mass of the Galaxy. The gas–to–dust ratio is about 100:1 and consequently the abundance of dust is of order 0.1% of the total baryonic mass. However, dust grains absorb roughly 30–50% of starlight, a significant portion of the bolometric luminosity of

the Galaxy. In addition, dust plays an important role in the chemistry of the ISM. It is generally believed that almost all of the H_2 in the ISM is formed on the surface of dust grains. Indeed, the formation of other molecules might also take place in dust clouds (Draine 2011). By absorbing ultraviolet radiation from stars, dust grains can also prevent dissociation of molecules and thus allow for the formation of planetesimals and eventually planetary systems.

Dust can be observed indirectly, through extinction and reddening, and directly through electromagnetic radiation. Direct observations are mainly carried out in the infrared and consist of both continuum and emission line measurements. Continuum radiation at mid- to far-infrared is emitted by grains which are in radiative equilibrium with the radiation field whereas emission at near- to mid-infrared is mainly due to heating of smaller grains in non-equilibrium with the local radiation field (Mathis 1990). The emission spectra of dust grains is also determined by their temperature, however a substantial number of emission lines has not been identified as yet.

Infrared radiation is absorbed by water vapour in the Earth's atmosphere and consequently direct observations of dust started in the 1970's with the deployment of space infrared telescopes. The Infrared Astronomical Satellite (*IRAS*, 1983) mapped most of the sky at 12, 25, 60, and 100μm wavelengths, mapping the warm dust component of the ISM in the Galaxy and other nearby galaxies. The Infrared Space Observatory (*ISO*, 1995) mission provided pointed imaging and spectrophotometry from 2.5 to 240 μm and 2.5 to 196.8 μm respectively, and revealed the presence of intergalactic dust as well as ultra-luminous infrared galaxies (ULIRG's). These galaxies emit most of their energy output in the infrared due to large concentrations of dust heated by prodigious star formation.

In more recent years the *Spitzer* Space Telescope (2003) and the *Herschel* Space Observatory (2009) have set a new standard for studying the ISM, among many other fields, with high sensitivity and angular resolution observations. Some of the key results from *Spitzer* include the direct detection of dust-enshrouded star formation in galaxies up to a redshift of 3 and the detection of light from extrasolar planets (Deming et al. 2005; Charbonneau et al. 2005). *Herschel*, the largest space telescope ever launched, is already revolutionising the fields of star formation and chemistry of the ISM. Some of the recent results from *Herschel* include the detection of molecular oxygen in the Orion nebula (Goldsmith et al. 2011) and a cavity in the dust and gas cloud in NGC 1999 (Stanke et al. 2010), which provides new insights into the end of the star-forming process.

1.4 Models of the ISM

Over the last decades our understanding of the ISM in disc galaxies has changed considerably mainly due to new observations which cover the whole electromagnetic spectrum. The physical processes in the ISM were initially described by Spitzer (1956) who sketched a picture of the ISM in which all the gas is in pressure equilibrium. In his view, the H I clouds are confined within a pervasive ambient medium. This picture led Field et al. (1969) to suggest a two-phase model of the ISM where the cool (CNM) phase and the warm (WNM) phase are in pressure equilibrium and the thermal processes governing the ISM are heating by cosmic rays and X-rays and cooling through line emission and bremsstrahlung. Further observations of X-ray emission (Gorenstein et al. 1974; Burstein 1976), led McKee & Ostriker (1977) to add a third hot phase (HIM) and propose a three-phase model. In their view, the CNM is moderately clumpy with a scale height of about 140 parsecs, the warm component consists of the WNM (Lockman layer) which is quite tenuous with a scale height of about 500 parsecs (Lockman 1984) and the WIM (Reynolds layer) which is the diffuse ionized medium with a scale height of about 900 parsecs (Reynolds 1993), and the HIM which extends to scale heights of a few kpc. To explain the presence of this hot third component, Cox & Smith (1974) and McKee & Ostriker (1977) suggested supernova explosions in the disc as a possible mechanism able to provide the energy input for heating this component of the ISM. This hot gas can flow up into the halo of the galaxy where it eventually cools and falls back to the disc (Shapiro & Field 1976; Bregman 1980).

The picture of the ISM as it stands today has been referred to as "the Hamburger model of the Galaxy" (van der Hulst 1996). The OB associations in the midplane upset the layer of cool neutral gas and warm neutral and ionized gas through the effects of stellar winds and supernova explosions and heat up the halo of the disc. In addition, these two mechanisms produce filamentary structures, bubbles, and holes in the ISM therefore making it inhomogeneous and porous.

1.5 Energy Input in the ISM

Studies of neutral atomic hydrogen (H I) in nearby galaxies using synthesis instruments such as the Westerbork Synthesis Radio Telescope (WSRT), the Very Large Array (VLA), Australia Telescope Compact Array (ATCA) and more recently the Giant Metre–Wave Radio Telescope (GMRT) have shown the frothy structure of

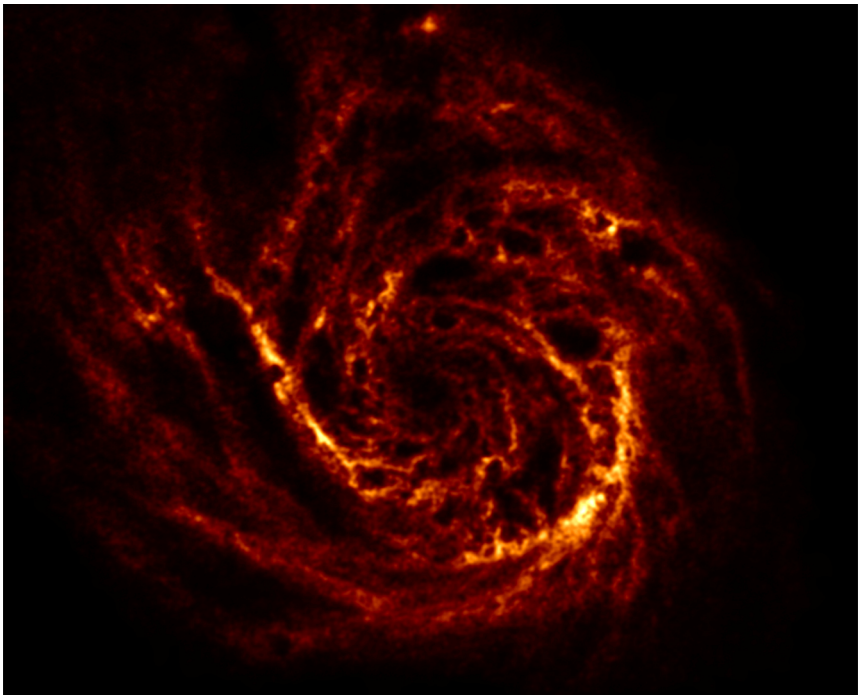

Figure 1.2: The neutral atomic hydrogen distribution in M101 shows a wealth of shell-like structures with a wide range of sizes. *Image credit: THINGS*

the interstellar medium (ISM). Filamentary structures characterize the gas distribution of the Galaxy and nearby galaxies (e.g., Fig 1.2) and have been referred to as the "cosmic bubble bath" (Brand & Zealey 1975) or the "violent interstellar medium" (McCray & Snow 1979). Particularly striking are elliptical features representing a deficiency of interstellar matter, usually bordered by neutral or ionized regions of higher density. These have been described as bubbles and shells, based on their appearance at different wavelengths. An example of such a structure can be seen in Fig 1.3.

These structures were first recognized as such in the Large Magellanic Cloud (LMC) by Westerlund & Mathewson (1966) and in the Small Magellanic Cloud (SMC) by Hindman (1967). The explanation put forward at the time was that these shells were the result of "super supernovae". In our own galaxy, there has long been evidence for shell-like structures. Heiles (1979, 1984) lists a number of early observations of expanding H I supershells in the Milky Way. As he emphasized "Identification of shells is a somewhat subjective process due to the fact that some shells are detected at only one velocity and for those shells that do change as a function of velocity usually only one hemisphere of the shell is observed". In addition, distances to these shells are very uncertain, which shifted the focus

Figure 1.3: An optical image of superbubble LHA 120-N 44 in the Large Magellanic Cloud surrounding the star cluster NGC 1929 taken with ESO's Very Large Telescope (VLT). *Image Credit: ESO/Manu Mejias*

Table 1.1. Previously published studies of H I holes in galaxies

Galaxy	FWHM beam (″)	FWHM beam (pc)	Velocity Resolution ($km\,s^{-1}$)	Reference
M 31	24×36	80×120	8.2	1, 2
M 33	12×24	40×40	8.2	3
M 101	13×16	500	8.2	4
Holmberg II	4.0×4.5	60	2.6	5
SMC	98	28	1.6	6, 7, 8
NGC 2403	9	144	6.2	9, 10
IC 10	4.7×5.0	44×20	12.2	11
IC 2574	6.4×5.9	100×91	2.6	12, 13
LMC	60	15	1.6	14
NGC 6822	42.4×12.0	100×29	1.6	15
DDO 47	7.8×7.2	150×140	2.6	16
Holmberg I	8.2×7.0	140×120	2.6	17
M 82	1.4×1.2	22×19	10.3	18
NGC 6946	12×14	350×400	4.1	19
DDO 43	14×11	375×290	2.6	20
DDO 88	14.5×13.1	520×470	2.6	21
NGC 1569	12.1×10.8	114×95	2.6	22
IC 1613	7.4×7.0	26×24	2.6	23

Note. — Where multiple studies exist for a galaxy, only the one with the best resolution and/or sensitivity is listed.

References. — (1) Brinks 1981; (2) Brinks & Bajaja 1986; (3) Deul & den Hartog 1990; (4) Kamphuis et al. 1991; (5) Puche et al. 1992; (6) Stanimirović 2007; (7) Stanimirović et al. 1999; (8) Hatzidimitriou et al. 2005; (9) Thilker et al. 1998; (10) Mashchenko et al. 1999; (11) Wilcots & Miller 1998; (12) Walter & Brinks 1999; (13) Rich et al. 2008; (14) Kim et al. 1999; (15) de Blok & Walter 2006; (16) Walter & Brinks 2001; (17) Ott et al. 2001; (18) Wills et al. 2002; (19) Boomsma et al. 2004; (20) Simpson et al. 2005b; (21) Simpson et al. 2005a; (22) Mühle et al. 2006; (23) Silich et al. 2006.

to nearby galaxies. At the time the work described in this thesis began, about a dozen galaxies had been observed at spatial and velocity resolutions adequate to map and analyse H I holes. They are listed in Table 1.1.

Following Chu et al. (2004) and references therein, bubbles and shells are assumed to be created by single stars, as a result of the combined effects of a stellar wind followed by the star exploding as a supernova. Superbubbles and supergiant shells are structures which have broken out of the disc of the galaxy and require multiple stars or some other mechanism for their formation. Since bubbles and shells appear as holes in maps of neutral hydrogen, we will be using this term throughout this thesis. As mentioned, stellar winds and supernovae from young massive stars in OB associations and Super Star Clusters (SSCs) are considered the main driving forces behind the creation of holes and shells whose radii can reach up to hundreds of parsecs (e.g., Weaver et al. 1977; McCray & Kafatos 1987). Recent observations and analysis of four nearby disc galaxies by

Relaño et al. (2007) has shown that Hα shells in giant H II regions are the likely progenitors of neutral hydrogen shells. In addition, Weisz et al. (2009a) found that H I holes in Holmberg II could in principle be the result of stellar feedback from multiple SF episodes, even though similar stellar populations were also found in regions where no H I holes were detected. However, a one to one correlation between H I holes and active star forming regions such as OB associations has not been established as yet. Moreover numerical models by Silich et al. (2008) suggest that the Hα shells studied by Relaño et al. (2007) cannot evolve into the largest H I shells observed unless a physical mechanism other than supernovae (SNe) is invoked.

The kinetic energies inferred on the basis of the typical expansion velocities measured (of order a few tens of $\mathrm{km\,s^{-1}}$) range from 10^{50} to 10^{54} erg. One of the problems of this "standard" theory of mechanical input is the existence of a growth-rate discrepancy. Observations show that shells are smaller than what is predicted by the theory of adiabatic evolution that assumes a hot ($\geq 10^6$ K), shock-heated interior whose pressure drives the shell growth (Pikel'Ner 1968; Castor et al. 1975; Dyson 1977). Oey (2007) suggests that this discrepancy can be attributed to one, or a combination of, the following reasons: an overestimate of the input power, an underestimate of the ambient density and/or pressure, enhanced radiative cooling in the interior of the bubbles, or the transfer of mechanical energy from the holes to cosmic rays through the strong MHD turbulence and magnetic fields that govern their interior. The inhomogeneity of the ISM could also be a factor in explaining this discrepancy.

Because of the failure to achieve a consensus on the hypothesis that star clusters power supergiant shells, several alternative explanations have been put forward to explain structures which are found in environments where star formation is suppressed or for those cases for which the energy requirement to create the structure is believed to far surpass what can be delivered by even a super star cluster (SSC). Among the mechanisms proposed are in-fall of high velocity clouds (e.g., Tenorio-Tagle & Bodenheimer 1988; Rand & Stone 1996; Santillán et al. 1999; Murray & Lin 2004), ram pressure enlarging embryonic shells (Bureau & Carignan 2002), and turbulence, coupled with cooling and gravitational instability (Wada et al. 2000; Dib & Burkert 2005). At one time even gamma-ray bursts have been invoked (Loeb & Perna 1998; Efremov et al. 1999; Perna & Raymond 2000).

The study of shells and supershells is relevant to many areas of galaxy research. Supergiant shells are linked to superbubble blow out and might lie at the origin

of a galactic fountain (Bregman 1980). If shells do indeed break out of the disc, the halo or in extreme cases even the intergalactic medium can be enriched by metals produced in the massive stars before they exploded as SNe (Tenorio-Tagle 2000). Numerical simulations and modelling suggest that actively star forming dwarf irregular galaxies are most prone to mass loss (Low & Ferrara 1999; Silich & Tenorio-Tagle 2001). Given that in the currently accepted ΛCDM cosmology dwarf galaxies dominated at large look-back times, this could explain the rapid enrichment and mixing of heavy elements shortly after the first galaxies were formed. On more local scales, H I holes play an important role in the evolution of the ISM and are ultimately linked to the process of star formation. Expanding holes compress their surrounding medium leading to conditions conducive to star formation (e.g., Tenorio-Tagle et al. 2005). Examples for this can be found in the LMC where CO observations point to the presence of molecular clouds on the rims of several supergiant shells (Yamaguchi et al. 2001). The Magellanic Clouds are not the only example. Leroy et al. (2006) show similar accumulations of molecular gas on the interface between two neighbouring shells in IC 10 which seemingly are running into each other. In other words, shells could be driving self-regulating (propagating or stochastic) star formation (Elmegreen et al. 2002). On yet smaller scales, the processes leading to shells and supergiant shells provide energy input on the largest turbulent scales which then cascade down to ever smaller scales. And finally, on a global scale, the star formation rate in disc galaxies is controlled by the Toomre gravitational instability parameter and the porosity of the ISM to supernova remnant heated-gas (Silk 1997). The energy input from SNe in the form of expanding shells (high porosity) provides positive feedback as it raises the velocity dispersion in the gas, shutting off further star formation until such time as the gas has cooled down, in a dynamical sense, and porosity decreases allowing SF to recommence. This implies a feedback loop which likely causes the ISM to have a one dimensional velocity dispersion of 6–10 $\mathrm{km\,s^{-1}}$ irrespective of galaxy type (Dib et al. 2006; Leroy et al. 2008; Tamburro et al. 2009).

1.6 A Multi-Wavelength View

To date, most studies on holes have been restricted to H I only, with the occasional reference to other wavelengths, mainly optical observations, such as Hα and OB associations. In the Galaxy, Pidopryhora et al. (2007) have recently detected a superbubble in both H I and Hα while in the Magellanic clouds Kennicutt et al.

(1995) detected nine supershells in Hα. Other examples include nearby dwarf galaxies (e.g., Martin 1998; Walter et al. 2002). However, there are currently no studies on the connection of H I holes with other components of the ISM, e.g., dust, molecular clouds and star formation sites. Such a comparison could lead to a better understanding of the dynamics of the ISM and in particular how stellar feedback shapes and affects certain ISM components. By looking at other wavelengths one would expect to see small (young) holes filled with Hα emission and a good fraction of medium aged holes filled with UV emission from less massive stars in OB associations, reinforcing the idea that holes are primarily formed as a result of intense star formation. In addition, current and recent star formation sites (as traced by Hα emission and UV) are expected to be found along the rims of some of the larger (older) holes. Molecular clouds, as traced by CO, should also be absent from the interior of H I holes and present on their rims where the gas is being compressed. This would be compatible with the idea of propagating star formation as was recently observed in a galactic bubble by Deharveng et al. (2009).

With the deployment of *Spitzer* and *Galaxy Evolution Explorer (GALEX)* high resolution observations of nearby galaxies are for the first time available, and a comparison between the various components of the ISM is now possible. Qualitatively it is straight forward and it can be done by visually describing and comparing maps of different wavelengths (e.g., Fig. 1.4). However, this method carries an unavoidable degree of subjectivity and is limited in terms of scale and detail.

A more robust way of comparing maps is to do so in a quantitative way and a few such attempts have been made. Of these the most widely used is wavelet analysis which allows the isolation of structures, such as spiral arms, filaments and clumps, from a map. In addition, this method characterizes a map based on features on different scales. Frick et al. (2001) utilised wavelets to investigate scale-by-scale correlations between maps of NGC 6946 in different spectral ranges. This method has since been used by Tabatabaei et al. (2007) and Dumas et al. (2011) to compare infrared and radio maps in M33 and M51 respectively. In a similar fashion, Hughes et al. (2006) used both wavelets and pixel–by–pixel correlation in order to compare the 1.4 GHz emission to 60μm emission in the LMC.

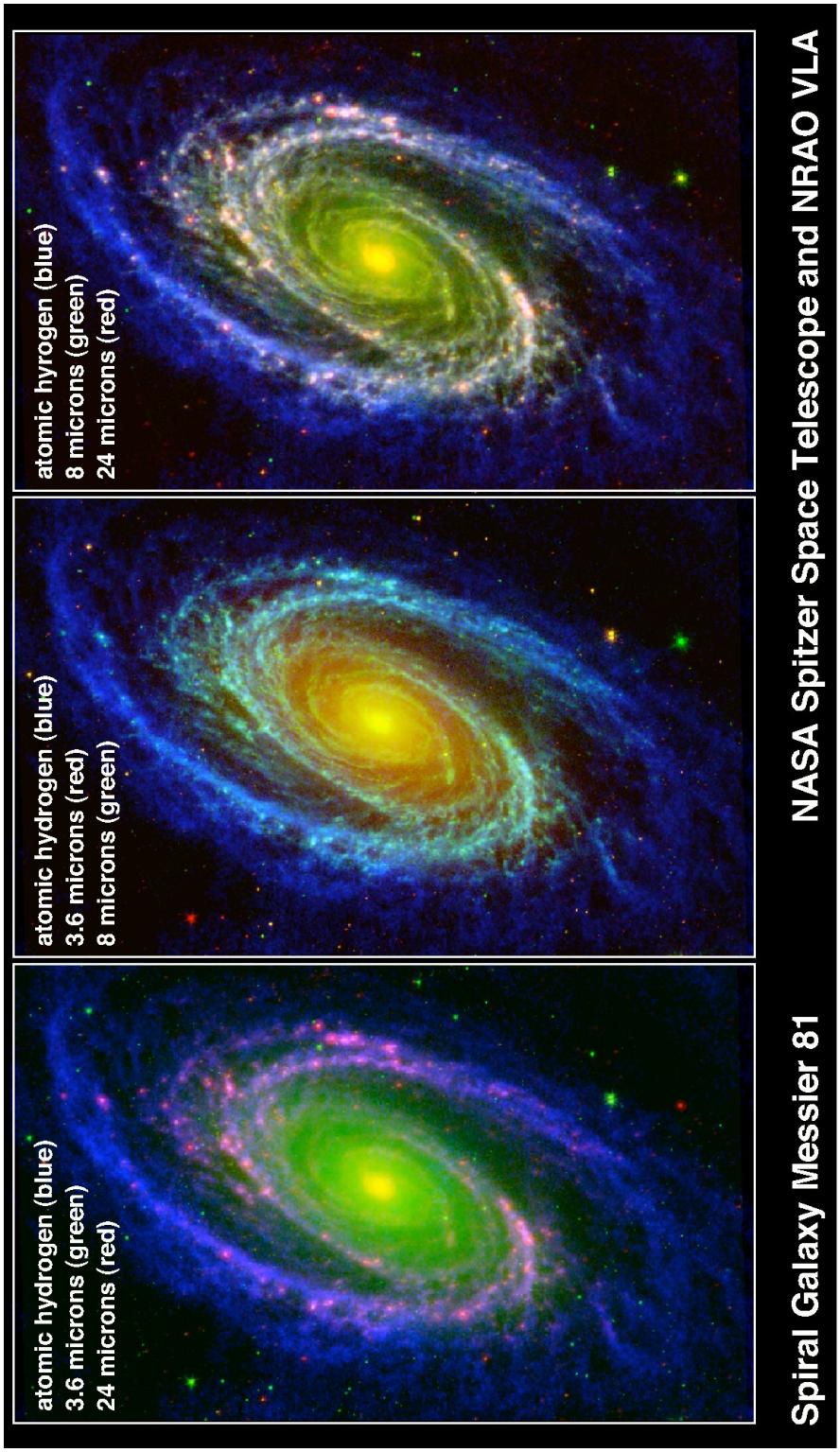

Figure 1.4: Composite images of M81 (NGC 3031) based on VLA H I and *Spitzer* 3.6μm, 8μm and 24μm observations.

1.7 THINGS and this Thesis

This work is primarily based on "The H I Nearby Galaxy Survey" (THINGS) a large program designed to investigate key characteristics related to galaxy morphology, star formation and mass distribution of galaxies across a range of Hubble type, metallicity, and current star formation rate. THINGS is based on 21–cm line observations of a sample of 34 nearby systems (2–15 Mpc). The observations were carried out with the National Radio Astronomy Observatory (NRAO) VLA in B, C, and D configurations totalling ~ 500 hours (including archival data) and are of high angular ($\approx 6''$) and velocity (2.6–5.2 $\mathrm{km\,s^{-1}}$) resolution. A summary of the observations is given in Walter et al. (2008). THINGS was designed to complement the *Spitzer* Infrared Nearby Galaxies Survey (SINGS; Kennicutt et al. 2003) and the *GALEX* Nearby Galaxies Survey (NGS; Gil de Paz et al. 2007) therefore providing us with multi-wavelength coverage of these galaxies. In addition, 18 galaxies from the THINGS sample have since been observed in CO as part of the Heterodyne Receiver Array CO Line Extragalactic Survey (HERACLES; Leroy et al. 2009). Consequently, this work utilises archival data from SINGS (infrared and Hα), NGS (UV) and HERACLES (CO).

The purpose of this thesis is to improve upon the status quo of hole analysis by adding 18 new galaxies and revisiting two (Holmberg II and IC 2574). All 20 galaxies were observed at similar angular and velocity resolution and down to similar detection thresholds as part of THINGS. The identification of H I holes will be carried out in a consistent manner in order to enable us for the first time to study these features in a systematic way across a variety of Hubble types. In particular, the aim is to get an insight on the overall properties of H I holes and explore the range of values that these can take. We expect to find constraints on the hole size, age and energy requirements, among others, and therefore identify the processes that influence their evolution in the ISM. Based on the typical number of holes detected in previous studies we anticipate to have a large sample of holes, which will allow us to establish relations between their properties in a statistical manner. Hole properties are expected to differ depending on the type of the host galaxy; theoretical models predict that holes in dwarf galaxies are more persistent compared with holes in spiral galaxies where shear can act as a destruction mechanism. Consequently, a comparison of the properties of holes across different galaxy types will give information on these mechanisms and their effects on shell formation and evolution. There has long been evidence for the relation between shell formation and star formation but this picture is often challenged. We aim to

address this issue by examining whether the creation of holes is compatible with this "standard model" over a range of galaxy types. In addition, the lack of a one-to-one correlation between massive stars in OB associations with the location of H I holes dictates the need for a method to compare structures at various wavelengths. Few such attempts have been made and with the recent availability of high-resolution maps across the EM spectrum such a tool could provide information on localised processes in the ISM. This thesis describes the development of a technique capable of comparing maps of different wavelengths in a quantitative manner and the application of this tool to NGC 2403.

In Chapter 2 we describe the method used to identify H I holes and present a catalogue of such structures detected in 20 nearby galaxies. We list a set of their observed and derived properties. A comparative analysis of the properties of H I holes and the impact these have on the host galaxies is presented in Chapter 3. In Chapter 4 we outline the development of a cross-correlation tool and give some first results from the application of this technique in a nearby galaxy. Finally, in Chapter 5 we present a summary and possible future directions as a result of this work.

Chapter 2

The Search for H I Holes

2.1 Observations

The present study is based on observations carried out within the framework of the THINGS project. For our analysis we selected 20 galaxies from the THINGS sample based on certain criteria. The basic criterion was to include at least one pair of galaxies from each Hubble type in order to be able to compare H I holes across all Hubble types. The galaxies in each pair were also selected to vary substantially in their star formation rates and H I masses and care was taken to select galaxies with sufficiently high signal-to-noise ratios. The list of selected galaxies is given in Table 2.1. In what follows we split our sample into dwarf and spiral galaxies based on their morphological type. All Irr and Magellanic type galaxies were classified as dwarfs.

The data reduction process is described in detail in Walter et al. (2008). The AIPS package was used to reduce the data for every galaxy and to create the datacubes. Two different weighting schemes were applied, *natural weighted* (NA, resulting in 'low' resolution, high sensitivity maps) and *robust weighted* (RO, resulting in higher resolution maps at the cost of increased noise), and a residual-flux rescaling method was performed on both versions of the cubes. For this study we used both the NA and RO cubes for the detection of the H I holes as is described in Section 2.3.1. This Chapter is based on the following paper: Bagetakos, I., Brinks, E., Walter, F., de Blok, W. J. G., Usero, A., Leroy, A. K., Rich, J. W., & Kennicutt, R. C. 2011, AJ, 141, 23. The work presented in this Chapter has been solely carried out by the author of this thesis. Brinks, E., Walter, F., and de Blok, W. J. G., provided the maps on which this work is based. Rich, J. and I independently analysed a small subset of galaxies in order to calibrate the qual-

Table 2.1. Characteristics of the galaxies in the sample

Name	Alternative Name	α(J2000) (h m s)	δ(J2000) ($^\circ$ $'$ $''$)	Type	D (Mpc)	Incl.[a] (deg)	PA[b] (deg)	H I Mass (10^8 $M_\odot$)	log(SFR) ($M_\odot$ yr^{-1})	log(D_{25}) ($0.1'$)	Resolution (pc)
NGC 628	M 74	01 36 41.8	+15 47 00.0	SA(s)c	7.3	7	20	38.0	0.08	1.99	218
NGC 2366	DDO 42	07 28 53.4	+69 12 51.1	IB(s)m	3.4	64	40	6.5	−1.02[c]	1.64	107
NGC 2403	···	07 36 51.1	+65 36 02.9	SAB(s)cd	3.2	63	124	25.8	−0.07	2.20	87
Holmberg II	DDO 50	08 19 05.0	+70 43 12.0	Im	3.4	41	177	5.9	−1.13	1.82	107
DDO 53	···	08 34 07.2	+66 10 54.0	Im	3.6	31	132	0.6	−2.10	0.89	103
NGC 2841	···	09 22 02.6	+50 58 35.4	SA(r)b	14.1	74	153	85.6	−0.70	1.80	405
Holmberg I	DDO 63	09 40 32.3	+71 10 56.0	IAB(s)m	3.8	12	50	1.4	−2.23	1.52	128
NGC 2976	···	09 47 15.3	+67 55 00.0	SAc	3.6	65	335	1.4	−0.98	1.90	87
NGC 3031	M 81	09 55 33.1	+69 03 54.7	SA(s)ab	3.6	59	330	36.3	0.03	2.33	132
NGC 3184	···	10 18 17.0	+41 25 28.0	SAB(rs)cd	11.1	16	179	30.6	0.16	1.87	281
IC 2574	DDO 81	10 28 27.7	+68 24 59.4	SAB(s)m	4.0	53	55	14.7	−0.93	2.11	111
NGC 3521	···	11 05 48.6	−00 02 09.2	SAB(rs)bc	10.7	73	340	80.2	0.52	1.92	376
NGC 3627	M 66	11 20 15.0	+12 59 29.6	SAB(s)b	9.3	62	173	8.2	0.39	2.01	249
NGC 4214	···	12 15 39.2	+36 19 37.0	IAB(s)m	2.9	44	65	4.1	−1.28	1.83	98
NGC 4449	···	12 28 11.9	+44 05 40.0	IBm	4.2	60	230	11.0	−0.33[d]	1.67	267
NGC 4736	M 94	12 50 53.0	+41 07 13.2	(R)SA(r)ab	4.7	41	296	4.0	−0.37	1.89	130
DDO 154	NGC 4789A	12 54 05.9	+27 09 09.9	IB(s)m	4.3	66	375	3.6	−2.44	1.29	147
NGC 5194	M 51	13 29 52.7	+47 11 43.0	SA(s)bc	8.0	42	172	25.4	0.78	1.89	221
NGC 6946	···	20 34 52.2	+60 09 14.4	SAB(rs)cd	5.9	33	243	41.5	0.68	2.06	135
NGC 7793	···	23 57 49.7	−32 35 27.9	SA(s)d	3.9	50	290	8.9	−0.29	2.02	142

Note. — All values taken from Walter et al. (2008) unless stated otherwise.

[a]Average inclination

[b]Average position angle

[c]Hunter & Elmegreen (2004)

[d]Hunter et al. (1999)

ity scale used to characterise the fidelity of individual features, Usero, Leroy and Kennicutt read and commented on earlier versions of the manuscript.

2.2 Global Characteristics

In order to derive some of the properties of the holes the scale height of the H I layer needs to be known. The scale height is the distance from the center of the plane to the region at which the mass density is 1/e of the maximum mass density. In an isothermal disc the scale height h is given by:

$$h = \frac{\sigma_v^2}{2\pi G\Sigma} \tag{2.1}$$

(van der Kruit 1988) where σ_v is the velocity dispersion, Σ the total mass surface density and the vertical distribution is a $\mathrm{sech}^2(z/2z_0)$. However, the disc of a galaxy consists of different components, stars and gas, which have different velocity dispersions, i.e., matter is not isothermal. In such a case where the gas is affected by the gravitational potential of the stars and its own self-gravity, its velocity dispersion is given by:

$$\sigma_{\mathrm{gas}}^2 = \frac{2\pi G\Sigma h_g^2}{h_g + h_*} \tag{2.2}$$

(Dopita & Ryder 1994) where h_g and h_* are the scale heights of gas and stars respectively. The 1σ line of sight velocity dispersion of the gas (σ_{gas}) was calculated by taking the FWHM of spectra in quiescent regions of the galaxy and was found to be of order $6-10\ \mathrm{km\,s^{-1}}$ consistent with what was found by Leroy et al. (2008) and Tamburro et al. (2009). We adopted a constant velocity dispersion for the gas for each of our targets. For h_* we used $h_* = h_R/7.3$ following Leroy et al. (2008), where h_R is the disc scale length. This average flattening ratio was measured by Kregel et al. (2002) assuming h_* does not vary with radius, which is a reasonable assumption. The total mass surface density was taken as the sum of the stars and gas (H I and H_2) mass surface densities (Leroy et al. 2008). The gas surface density is corrected to account for helium and metals. For the stars we used the 3.6μm surface brightness profile which traces the older stars and consequently the bulk of the star mass. In regular spirals, the effect of the dark matter halo on the scale height of the gas can be ignored to first order, because its effective contribution to the mass surface density within the typical radii dealt with is insignificant compared to that of baryonic matter. It should be noted that in the

case of dwarf galaxies the influence on scale height of the dark matter distribution becomes significant. In that case the approach by Dopita & Ryder (1994) would need to be replaced by a more sophisticated approach, such as the one proposed by Narayan & Jog (2002). This was recently pursued by us, the result of which has been published by Banerjee et al. (2011) (Appendix B).

The mass surface density decreases with radius, initially exponentially as it follows the light and gradually flattening well beyond R_{25} where H I dominates. The observed almost constant velocity dispersion of the gas combined with a radial decline in mass surface density implies that the gas layer flares, i.e., the scale height increases with radius. This is confirmed by observations of the Milky Way (Kalberla & Kerp 2009) and nearby galaxies (Brinks & Burton 1984; Sancisi et al. 2008). We therefore decided to use a radially dependent mass surface density to explicitly give radially dependent values for the scale height; an average value would introduce large uncertainties in the inner and outer parts of a galaxy. Fig. 2.1 illustrates the scale heights for all galaxies in our sample out to $1.2\,R_{25}$. The horizontal axis represents galactocentric radius normalised to R_{25}. The dotted lines correspond to the scale height calculated using Eq. 2 and the solid lines to a least squares best fit exponential function used to parametrize its behaviour. For galaxies for which the H I disc extends to more than $1.2\,R_{25}$ we extrapolated out to the edge of the H I disc at radius $R_{\rm max}$. It is clear that in the majority of objects the scale height increases exponentially with radius and the best fit function has the form:

$$h(r) \sim e^{(a\frac{R}{R_{25}})} \tag{2.3}$$

In dwarf galaxies the average exponent a is ~ 0.8, in early-type spirals it is ~ 3.6 and in late-type spirals it is ~ 2.3. At $R > R_{25}$ the scale height tends to flatten to some asymptotic value as the gas and dark matter dominate the matter distribution and therefore we decided to extrapolate using a logarithmic function of the form:

$$h(r) \sim ln(\frac{R}{R_{25}}) \tag{2.4}$$

This extrapolation only affects 3 galaxies (NGC 2403, NGC 4449 and NGC 4736) with a small number of holes.

The method described appears to underestimate the scale height in the inner part of spiral galaxies by up to a factor of 2; the diameter of fully contained H I holes in these inner parts was found to be consistently larger than the scale height. This can be understood as the velocity dispersion is dependent on radius

Table 2.2. Global derived characteristics of the galaxies in the sample

Galaxy	$R_{\rm max}$ (kpc)	$V_{\rm rot}$ (km s^{-1})	$\sigma_{\rm gas}$ (km s^{-1})	$<h>$ ($\times$100 pc)
(1)	(2)	(3)	(4)	(5)
NGC 628	20.0	213	7	4.9
NGC 2366	6.8	49	9	5.1
NGC 2403	16.3	138	8	3.6
Holmberg II	6.8	38	7	3.4
DDO 53	2.0	23	8	2.9
NGC 2841	46.0	282	9	4.8
Holmberg I	4.5	50	9	6.4
NGC 2976	2.5	74	9	1.2
NGC 3031	14.0	199	8	1.4
NGC 3184	18.1	207	7	3.1
IC 2574	9.3	70	7	2.9
NGC 3521	23.8	220	10	3.3
NGC 3627	7.8	203	13	1.4
NGC 4214	4.8	48	6	1.4
NGC 4449	5.1	42	10	4.0
NGC 4736	9.5	174	9	3.6
DDO 154	6.8	44	8	5.4
NGC 5194	11.9	137	14	1.6
NGC 6946	17.6	204	8	2.8
NGC 7793	7.8	119	8	2.6

Note. — (2) The maximum radius of the H I disk. (3) The rotation velocity of the galaxy at $R_{\rm max}$. (4) The velocity dispersion of the H I gas. (5) Average scale height over the H I disk.

as well (see e.g., Tamburro et al. 2009). The velocity dispersion tends to be higher in the inner disc due to the higher star formation and supernova rate. There is still considerable uncertainty surrounding this finding, a full analysis of which is beyond the scope of this thesis. The scale height is merely used to determine the volume density of the H I gas in the disc which in turn is used to determine the energy requirements of the holes. As is discussed later, the uncertainty in the volume density has the smallest effect on the calculation of these energies compared to other uncertainties. We therefore decided to adopt a constant gas velocity dispersion throughout each galaxy. Table 2.2 summarises the values adopted for all the galaxies in our sample. The scale height listed is an average over the entire H I disc. When deriving the properties for an H I hole, though, the scale height at the location of the hole was calculated.

2.3 The H I Hole Catalogues

2.3.1 Hole detection

Nearly all of the H I hole studies reported above are based on identifications made "by eye". This method carries selection biases which are difficult to quantify and is therefore subjective to a certain degree. To address this, several attempts have been made to create automated detection algorithms. The first such attempt was made by Thilker et al. (1998) who used models of expanding structures to identify shells in observed data cubes; they applied their code to NGC 2403. Mashchenko et al. (1999) refined the code to include more realistic three-dimensional hydrodynamical simulations of shells and revisited NGC 2403 where they detected 601 expanding shells. The same technique was also applied to the Canadian Galactic Plane Survey (CGPS) by Mashchenko & St-Louis (2002). These codes, although they are quite robust in discovering regular, expanding shells around young stars, fail to detect non-spherical or incomplete shells, which are the type of features we are predominantly finding in our data. A different approach to an automated procedure was proposed by Daigle et al. (2003) who used a neural networks algorithm to detect expanding shells based on velocity spectra. This method was successfully tested on data from the CGPS. More recently Ehlerová & Palouš (2005) developed a model independent algorithm which identifies H I holes as depressions in the channel maps without any constraints on the shape or expansion velocity of the hole, but requiring the hole is "complete". They applied this code to the Leiden–Dwingeloo Survey data and identified about 1000 structures in the Milky Way.

A cursory inspection of our data on galaxies in the Local Volume, with varying orientation parameters, sensitivity and linear resolution, quickly convinced us that none of the automated methods can be applied successfully to our entire sample. Any automated method would have to be fine-tuned to the characteristics of shells found in each individual galaxy thus reducing the consistency of that method. The human brain is superior when it comes to recognising irregular and open structures. In addition, the large majority of previous studies in this field were based on a "by eye" identification of H I holes and for reasons of consistency we therefore decided to identify the H I holes "by eye", despite the fact that this adds a level of subjectivity and is quite a time-consuming process.

The search for H I holes in the 20 THINGS galaxies was conducted with the

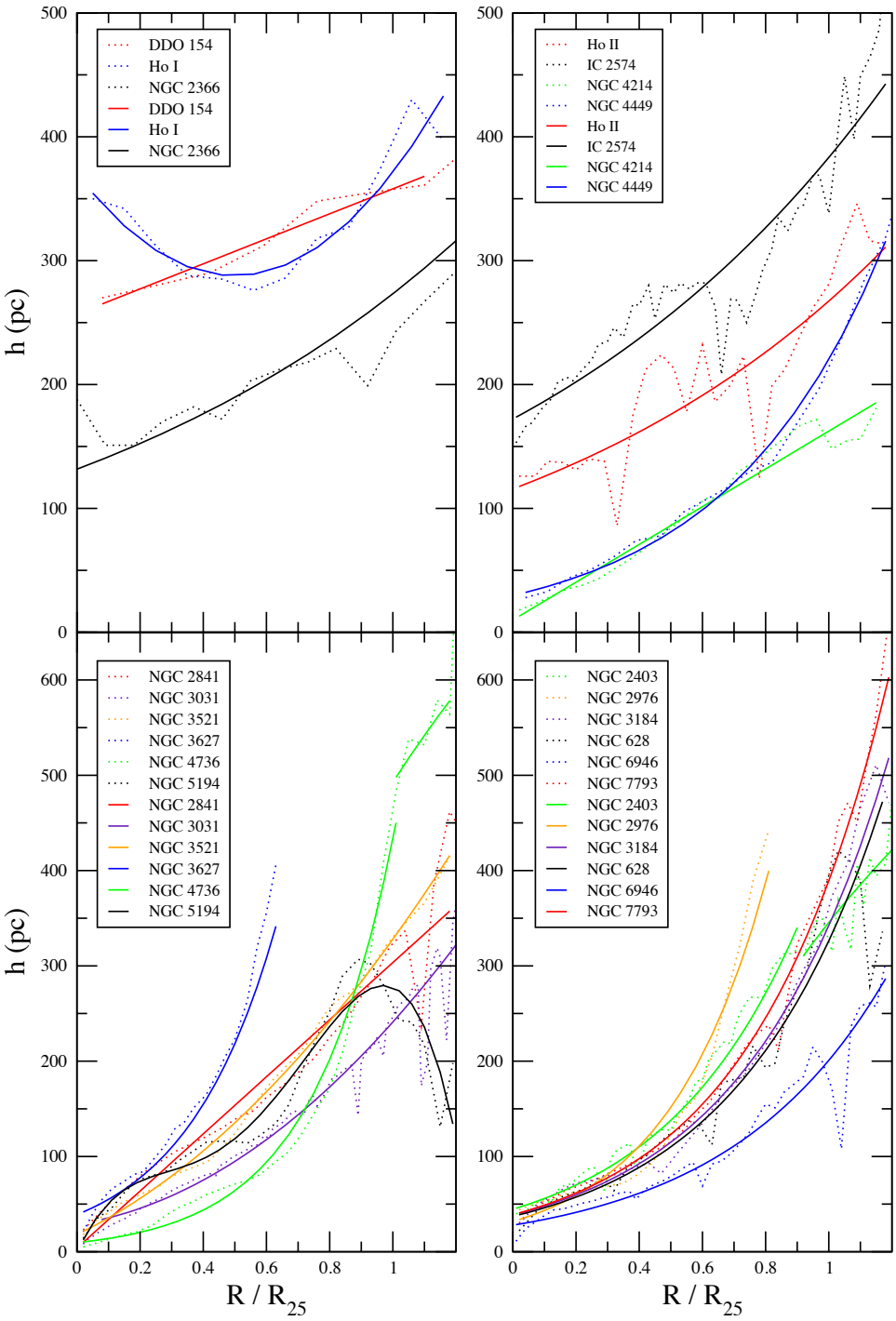

Figure 2.1: Scale heights as a function of galactocentric (R) radius normalised to R_{25} for dwarf galaxies (top panels), early-type (bottom left) and late-type (bottom right) spirals. The dotted lines correspond to the scale height calculated using Eq. 2 and the solid lines to a least squares best fit function.

KARMA[1] visualization software package which contains a large number of modules (tasks) several of which were used for this project. In particular, the task KVIS was used to display and investigate the integrated H I maps as well as digital movies of the data cube. The task KPVSLICE was also extensively used as it offers many ways to look at a data cube by producing interactive position-velocity (pV) cuts in any orientation through a data cube.

The detection process involved several steps which were followed in a consistent way for all 20 galaxies. First, the task KVIS was used to inspect the natural weighted integrated map for the most obvious, more extended structures. The second step was to search the higher resolution robust weighted integrated H I map for smaller holes. From these two steps we generated a list of candidate holes. The task KVIS was then used to inspect the natural weighted and robust weighted data cubes by displaying the channel maps sequentially, much like a movie. This was done for two reasons: although some of the holes are clearly visible in the integrated maps, many holes do not show up at all due, for example, to the inclination of the galaxy which means that holes along the line of sight tend to blend, or are "filled in" with emission at other velocities. Also, holes which are still fully contained within the H I disc can only be reliably detected in channel maps or pV diagrams. The second reason to display the channel maps as a movie was to discard holes that are chance superpositions of structures, such as parts of spiral arms, rather than genuine holes in the ISM. In order to set standard criteria to classify a feature as a genuine hole, we decided that a hole should be visible over at least 3 or 5 channels (depending on whether the velocity resolution is 5.2 or 2.6 $\mathrm{km\,s^{-1}}$, respectively), which is of order the full width at half maximum corresponding to the typical H I velocity dispersion encountered. This further eliminates spurious features.

In order to eliminate as much as possible any subjectivity, each hole in the revised list was examined individually using the task KPVSLICE. The signature of a hole in a pV diagram depends on the type of the hole as is discussed later, but overall this method is better suited for the detection of the smallest features. In addition, the inspection of pV diagrams is used to determine some of the basic properties of the holes, such as position, type, heliocentric and expansion velocities. For every feature detected, two sets of properties were determined. The first set involves the observed properties and the second set the derived proper-

[1]The KARMA visualization software package was developed by Richard Gooch, formerly of the Australia Telescope National Facility (ATNF).

ties. In addition, a quality ranking Q is assigned, which represents a (subjective) judgement regarding the probability of the feature being actually a shell in the H I distribution; its values range from 1 (low quality) to 9 (high quality). Even though this property is not directly quantifiable it depends on many aspects of the appearance of a hole and it follows certain criteria, each of which carries a Q value increment (given in parenthesis):

1. the hole must be present in at least 3 or 5 consecutive channel maps depending on whether the velocity resolution is 5.2 or 2.6 $\mathrm{km\,s^{-1}}$, respectively, (2-3 Q points)

2. the centre of the hole must remain stationary across the channel maps in which it is observed (2 Q points),

3. there must be sufficient contrast (at least a 50% drop in surface brightness) between the hole and its immediate surroundings (2-3 Q points),

4. the shape of the hole in position-velocity space must be clearly defined and adequately described by an ellipse (2 Q points).

Overall we detected more than 4000 candidate H I holes across the 20 galaxies. We decided to stay on the conservative side and only keep holes detected at high quality, i.e. above a certain threshold. This threshold was determined by comparing the holes we found in IC 2574 with those found in a parallel study by Rich et al. (2008). Both authors looked for holes independently assigning a quality parameter, Q value, to each hole. We then compared our catalogues based on the position and size of each hole. A hole was considered a match when its position was within half a beam size and its diameter agreed to better than 75%. From this comparison we found that over 75% of our $Q > 5$ holes had been identified by both authors and we therefore decided to use this value as our quality threshold. Once all the low Q holes were removed from our lists we were left with ~ 1000 H I holes.

2.3.2 Observed properties

In what follows we describe the observed characteristics of each hole.

1. The position of the centre of the hole in right ascension and declination (J2000 coordinates) determined by the (average) pixel where the flux density

is at a minimum. The uncertainty in the position is taken as half the robust beam size for each galaxy and is of order 3″.

2. The heliocentric velocity ($V_{\rm hel}$) of the hole. This was defined by the velocity channel in which the contrast between the H I hole and its rim was highest. The uncertainty here is equal to the velocity resolution (2.6 - 5.2 km s^{-1}).

3. The semi-major and semi-minor axes ($b_{\rm maj}$, $b_{\rm min}$) of the hole. To determine the major and minor axes, the approximate orientation of the hole was estimated and the task KPVSLICE was then used to draw cuts along these directions through the centre of the hole, either as seen directly on the integrated H I map or inferred from the pV diagram. These cuts revealed the decrease in H I at the position of the hole. The axes were taken as the FWHM of this depression. The uncertainty is of order half the robust beam size or 3″.

4. The axial ratio of the hole was defined by the ratio of minor axis to major axis. The uncertainty of the axial ratio determined by multiple independent measurements is of order 25%.

5. The position angle (PA) of the hole on the sky measured from north through east. Based on repeated independent measurements we estimate the uncertainty to be of order 20 degrees.

6. The type of the hole ($1-3$). Following Brinks & Bajaja (1986), the holes were assigned to one of three different types, based on their appearance in the pV diagrams (Fig. 2.2). A type 1 hole is a hole that has completely blown out of the disc of the galaxy, and therefore neither the approaching nor the receding sides of the hole can be observed as can be seen in Fig. 2.2, top. In a type 2 hole we only observe one side of the hole, which is usually seen in pV diagrams as a deviation toward either higher or lower velocities with respect to the velocity of the bulk of the H I within that area of the galaxy (Fig. 2.2, middle). Finally, in a type 3 hole we see both sides of the hole. Its signature in pV diagrams is that of an elliptical structure (Fig. 2.2, bottom). Typically, type 1 holes are larger than type 2 and 3 as they represent a later stage of bubble evolution i.e. type 3 holes are expected to evolve into type 1 (and possibly type 2) after growing.

7. The expansion velocity ($V_{\rm exp}$) of the hole. This was measured from the signature of the hole in the pV diagrams. For type 1 holes it is impossible

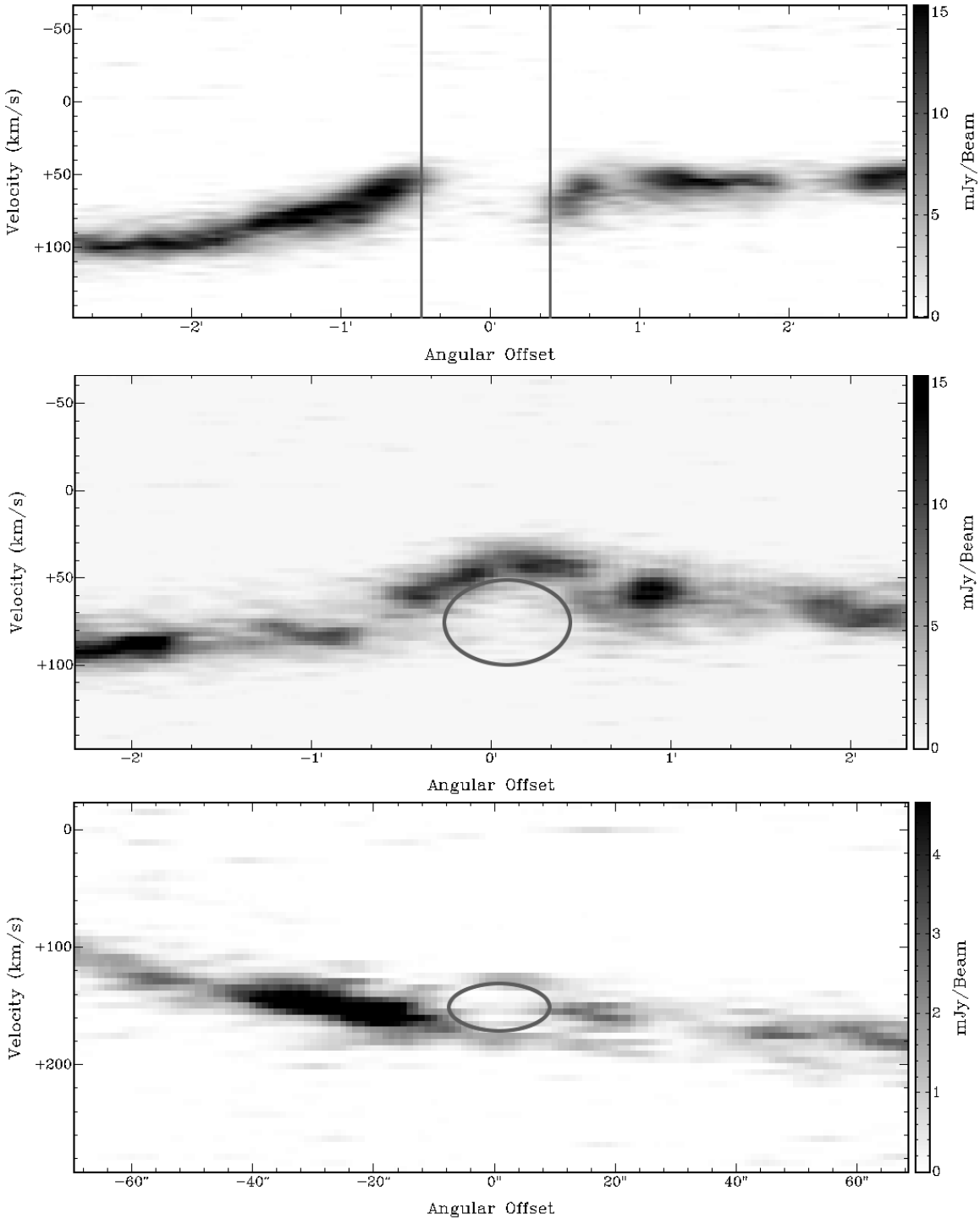

Figure 2.2: Examples of the appearance in pV diagrams of type 1 (top panel, hole no 21 in IC 2574), type 2 (middle, no 23 in IC 2574) and type 3 (bottom, no 90 in NGC 2403) holes as defined in Brinks & Bajaja (1986). The solid lines illustrate the position and shape of the holes in pV space.

to measure an expansion velocity. However, it is very likely that these have actually stalled and their final expansion velocity will be equal to the velocity dispersion of the gas. For type 2 holes the expansion velocity was taken as the difference between the velocity of the H I from that side of the hole which is seen to deviate from its measured velocity and the mean velocity of ambient gas surrounding the hole. In the case of type 3 holes, the expansion velocity was taken as half the difference between the velocity of the approaching and receding sides of the hole. We adopt an uncertainty that is equal to the velocity resolution (2.6 or 5.2 $\mathrm{km\,s^{-1}}$).

8. The average flux density (I) around the hole. This was determined by averaging the pixel values on the integrated H I map over an area around the hole, twice the area of the hole itself. This value is needed in order to derive the approximate density before the creation of the hole. Errors here are estimated to be of order 10% arising from the uncertainty on the position of the centre of the hole.

2.3.3 Derived properties

The observed characteristics have been used to determine the derived properties as described in the following:

1. The diameter (d) of the hole. Since most of the holes are not circular but elliptical, the diameter was defined using the geometric mean:

$$d = 2\sqrt{b_{\mathrm{maj}}\, b_{\mathrm{min}}} \tag{2.5}$$

where b_{maj} and b_{min} are the semi-major and semi-minor axis of the hole respectively. The uncertainty in d is of order 10%.

2. The kinetic age t of the hole. Assuming that over its lifetime the hole was expanding with V_{exp}, this is:

$$t_{\mathrm{kin}}\,[\mathrm{Myr}] = 0.978\frac{d/2}{V_{\mathrm{exp}}} \tag{2.6}$$

where d is the diameter of the hole in pc and V_{exp} is in $\mathrm{km\,s^{-1}}$. Since the expansion velocity was higher at earlier stages of the expansion, the kinetic age is an upper limit. Its statistical uncertainty is around 20%.

3. The H I column density ($N_{\rm HI}$) around the hole. The column density is given by:

$$N_{\rm HI}\,[{\rm cm}^{-2}] = 1.823 \times 10^{18} \sum T_{\rm B}\, dV \tag{2.7}$$

where $T_{\rm B}$ is the brightness temperature in units of Kelvin, V the velocity in $\rm km\,s^{-1}$ and the summation is over the velocity channels which contain signal. The relation between brightness temperature and flux density at 21–cm wavelength is given by:

$$T_{\rm B}\,[{\rm K}] = \frac{S}{1.66 \times 10^{-3}(B_{\rm maj}B_{\rm min})} \tag{2.8}$$

where $B_{\rm maj}$ and $B_{\rm min}$ are the FWHM of the beam respectively in arcsec and S is the flux in $\rm mJy\,beam^{-1}$. We calculated $T_{\rm B}$ from the average flux density (I) around the hole which we converted to Kelvin using the above equation.

4. The midplane H I volume density ($n_{\rm HI}$). This is given by:

$$n_{\rm HI}\,[{\rm cm}^{-3}] = \frac{N_{\rm HI}}{3.08 \times 10^{18}\, l(r)} \tag{2.9}$$

where $N_{\rm HI}$ is the column density in $\rm cm^{-2}$ and l is the effective thickness of the H I layer in pc which is assumed to have a Gaussian profile with a 1σ scale height h (see Section 2.2). Thus:

$$l(r)\,[{\rm pc}] = \frac{h\sqrt{2\pi}}{\cos i} \tag{2.10}$$

5. The volume (V) of the hole. For holes that are contained within the disc this is simply:

$$V\,[{\rm pc}^3] = (4/3)\pi(d/2)^3 \tag{2.11}$$

where d is the diameter of the hole in pc as given in Eq. (3). For holes that are larger than the thickness of the H I disc we assumed that holes have taken a cylindrical shape and therefore the volume is:

$$V\,[{\rm pc}^3] = 2\pi(d/2)^2\sqrt{8\ln 2}\,h \tag{2.12}$$

where h (in pc) is the 1σ scale height and the term $\sqrt{8\ln 2}\,h$ expresses the thickness of the disc.

6. Indicative H I mass ($M_{\rm HI}$). This is an estimate of the mass that filled the

hole, assuming the hole is spherical and completely empty and that the gas had a uniform distribution with volume density $n_{\rm HI}$ before the creation of the hole. In addition, assuming that only a small fraction of the surrounding H I is ionized, this value indicates the amount of H I mass which is expected to have been swept up to form a rim for those holes not blown out of the disc. $M_{\rm HI}$ was calculated using:

$$M_{\rm HI}\,[{\rm M}_\odot] = 2.9 \times 10^5\, n_{\rm HI}\, V \tag{2.13}$$

where $n_{\rm HI}$ is the volume density of the gas around the hole in cm^{-3} and V its volume in pc^3. The uncertainty of $M_{\rm HI}$ is around 30%.

7. The galactocentric distance (R) of the hole. This was calculated using:

$$R\,[{\rm pc}] = D \times 10^6 \sqrt{(x'')^2 + (y'')^2}\,{\rm pc} \tag{2.14}$$

where D is in Mpc and

$$x'' = x\sin\theta + y\cos\theta \tag{2.15}$$

$$y'' = \frac{y\sin\theta - x\cos\theta}{\cos i} \tag{2.16}$$

and

$$x = (\alpha - \alpha_0)\cos\delta_0 \tag{2.17}$$

$$y = \delta - \delta_0 \tag{2.18}$$

where θ is the position angle of the galaxy defined by the direction of the receding major axis, i its inclination, (α, δ) are the celestial coordinates of the centre of the hole and (α_0, δ_0) are the celestial coordinates of the centre of the galaxy (see Table 2.1).

8. The estimated energy requirements ($E_{\rm E}$) of the hole. Chevalier (1974) derived an equation for the energy requirements of an expanding shell, assuming an instantaneous energy deposition:

$$E_{\rm E}\,[{\rm erg}] = 5.3 \times 10^{43}\, n_{\rm o}^{1.12}\, (d/2)^{3.12}\, V_{\rm exp}^{1.4} \tag{2.19}$$

where $V_{\rm exp}$ is the expansion velocity in km s^{-1}, $n_{\rm o}$ is the density of the ambient medium in particles cm^{-3}, and d is the diameter of the hole in pc.

As was done in the case of M 31 (Brinks 1981), Ho II (Puche et al. 1992), IC 2574 (Walter & Brinks 1999) and DDO 47 (Walter & Brinks 2001), n_o was replaced by n_{HI}, which means we ignored contributions by He and H_2. In order to correct E_E for a He contribution, a factor of 1.5 would need to be applied. In addition to this systematic error, due to the large number of assumptions in Chevalier's' equation we estimate the random error in E_E to be of the order of 50%. An alternative method of deriving the energy requirements is the one presented in McCray & Kafatos (1987). We used their approach on our data and found that the agreement between the two methods is on average of order 15%. The equation derived by McCray & Kafatos (1987) strongly depends on the expansion velocity ($\propto d^2\, V_{exp}^3$) in contrast to the Chevalier equation which depends on the diameter of the hole. As the uncertainty in the expansion velocity is larger than the uncertainty in hole diameter and for reasons of consistency with previous studies on this subject we decided to derive energies using the Chevalier equation.

2.4 Description

In this section, we present each galaxy individually. We give a short description of each galaxy and an outline of our results. The complete hole catalogues are presented in Section 2.5, Tables 2.3–2.22. Each table has 14 columns: Column 1 is the number of each hole; Columns 2 and 3 the position (in α and δ in J2000.0); Column 4 the heliocentric velocity, V_{hel}, of the centre; Column 5 the type; Column 6 the diameter, d; Column 7 the expansion velocity, V_{exp}; Column 8 the position angle, $P.A.$; Column 9 the axial ratio of the hole, b_{min}/b_{maj}; Column 10 the galactocentric radius, R; Column 11 the volume density, $log(n_{HI})$, around the hole; Column 12 the kinetic age, t_{kin}; Column 13 the estimated energy requirement, $log(E_E)$; and Column 14 the estimated H I mass, $log(M_{HI})$, missing from the hole. Figures 2.3–2.28 in Section 2.6 show the detected H I holes overlaid as ellipses on the H I surface brightness maps.

NGC 628

NGC 628 is a grand-design Sc spiral galaxy located at a distance of 7.3 Mpc and is seen almost completely face-on. We detected 104 holes in its H I layer, with diameters ranging from 0.24 kpc (the resolution limit) to 2 kpc. Only a small fraction of these holes are type 3 ($\approx$ 5%). Several supershells were detected,

however 4 cases (holes number 24, 45, 47 and 99) are probably superpositions of 2 or more holes.

NGC 2366

NGC 2366 is a dwarf galaxy member of the M 81 group. It is considered to be a typical irregular galaxy and is characterized by a supergiant H II complex (NGC 2363) in the south-west (Yun 1999). We detected 26 holes in NGC 2366 but since this is a highly inclined system ($i = 63.8°$) we might be missing out on some features. All of the detected holes appear to be relatively young as their kinetic age was found to be between 6–38 Myr. In a previous H I study Hunter et al. (2001) searched for but did not detect any holes, however their spatial resolution was $\approx$ 260 pc, almost 2.5 times worse than our resolution.

NGC 2403

Another member of the M 81 group, NGC 2403, is a late-type spiral galaxy located at a distance of 3.2 Mpc. It has previously been studied by Thilker et al. (1998) and by Mashchenko et al. (1999) using an automated object recognition package who detected 50 and 601 holes respectively. Even though this galaxy is highly inclined ($i = 62.9°$), its close proximity and good resolution allowed us to detect 173 holes in its H I distribution. A few supershells were detected but the majority (81%) of the holes are smaller than 350 pc in diameter and younger than 20 Myr. There are also several special cases: some of the holes are most likely a superposition of two or more holes (holes number 51, 157 and 173); holes number 10, 43 have a peculiar signature in pV space.

Holmberg II

Holmberg II is a gas-rich dwarf galaxy located at a distance of 3.4 Mpc and is a member of the M 81 group of galaxies as well. An H I hole analysis was carried out by Puche et al. (1992) in which they found 51 holes across the entire face of this galaxy. We detected 39 holes in Holmberg II, the majority of which were also detected by Puche et al. (1992), all with very good agreement with respect to the position and size of the holes. The difference in the number of holes detected is due to our strict criteria of what constitutes a genuine hole as well as to the fact that several holes in our catalogue were classified as a superposition of two (or more) holes from the Puche et al. catalogue. As Figure 2.6 illustrates, these holes

dominate the H I distribution of Holmberg II. In addition several supershells were detected, the largest one (no 17) being over 2 kpc, one of the largest and oldest ($\sim$ 150 Myr) across the entire sample of holes. Note that hole no 37 is probably a superposition of two or more holes.

DDO 53

The dwarf irregular galaxy DDO 53 lies at a distance of 3.6 Mpc and also belongs to the M 81 group. It is the smallest galaxy in our sample with an H I radius of only 2 kpc. We detected 3 holes in its H I distribution, one of each type, with diameters in the range of 180-360 pc.

NGC 2841

NGC 2841 is an early-type Sc spiral and is the most distant galaxy in our sample located at 14.1 Mpc. The limited spatial resolution and the high inclination of this galaxy meant that we were only able to detect supershells of type 1. We found 15 H I holes and only one of these shows signs of expansion (number 10). In addition, holes number 4, 12 and 13 are possibly superpositions of holes. Hole no 5 is probably not a genuine hole but the result of the warp in the H I disc.

Holmberg I

Holmberg I is a dwarf irregular galaxy which forms part of the M 81 group of galaxies. Its H I distribution is dominated by a supergiant shell as was noted by Ott et al. (2001) which does not coincide with the kinetic centre of the galaxy. We detected 6 holes in this galaxy including the one detected by Ott et al. (2001). There is good agreement with respect to the position of this hole between both studies.

NGC 2976

The dwarf galaxy NGC 2976 is located at 3.6 Mpc and belongs to the M 81 group of galaxies. In NGC 2976 we found only 10 holes, which is not surprising given that this is one of the smallest galaxies in our sample with an H I disc radius of $R_{\rm max} = 2.5\,$kpc. No supershells were detected.

NGC 3031

NGC 3031, also known as M 81, is a grand design spiral galaxy located at a distance of 3.6 Mpc. The analysis of NGC 3031 revealed 321 H I holes, the largest number of holes detected in any of the galaxies in this sample. This is due to various factors such as its relatively large size, close proximity and high spatial resolution of the observations. We were able to detect holes down to ~ 80 pc which led to the detection of a wealth of small holes; almost 90% of the total holes detected have a size less than 200 pc. Only a handful of supershells were detected. The mean kinetic age is 7.8 Myr with 80% of the holes being younger than 9 Myr. Several features detected (holes no: 34, 72, 88, 93, 94, 97, 99, 102, 106, 109, 113, 114, 170, 255 and 273) are probably not genuine holes but the result of the warp in the H I disc. Due to its large angular size, M 81 was divided into 6 areas (Figures 2.11 – 2.17) to be able to show all detected holes.

NGC 3184

NGC 3184 is a spiral galaxy located at $D = 11.1$ Mpc and is viewed almost face-on. Its analysis revealed 40 H I holes, the majority of those being supershells (80%). This could be attributed to the large distance of this galaxy which only allowed us to detect holes with diameters larger than 400 pc. We failed to detect any type 3 holes, something which is expected since the scale height of the disc was found to be 250 pc, significantly smaller than our spatial resolution. Nevertheless, this is the largest number of supershells detected in any one galaxy. The mean kinetic age of the holes is also high (≈ 64 Myr). Note that hole number 13 is a superposition of 2 holes.

IC 2574

Another nearby ($D = 4.0$ Mpc) dwarf galaxy member of the M 81 group, IC 2574 hosts a relatively large number of H I holes (Walter & Brinks 1999). One particular hole (our hole no 21) has been extensively studied at different wavelengths from radio to X-ray (Stewart & Walter 2000; Cannon et al. 2005; Weisz et al. 2009a). These studies showed that there is a remnant star cluster in the centre of this hole and revealed evidence of propagating star formation along its rim. Here we report on 29 H I holes, compared to 48 holes detected by Walter & Brinks (1999) and 22 detected by Rich et al. (2008), the largest one being larger than 2 kpc in diameter. Almost all of the 29 holes we present here have been detected by Walter & Brinks

(1999). The difference in the total number of holes detected is due to the strict criteria we used to classify a structure as a genuine hole. Almost half of the holes (45%) show signs of expansion.

NGC 3521

Another distant galaxy in our sample, NGC 3521 is a spiral galaxy with a prominent bar located at a distance of 10.7 Mpc and viewed almost edge-on ($i = 72.7°$). The analysis of NGC 3521 revealed 13 holes in the H I distribution. The small number of holes detected and the lack of type 3 holes can be attributed to the large distance of this galaxy as well as its high inclination. All of the holes detected were consequently classified as supershells.

NGC 3627

NGC 3627 is a spiral galaxy at an adopted distance of $D = 9.3$ Mpc and is a member of the Leo Triplet. Its high inclination ($i = 61.8°$) meant we were only able to detect 18 holes in NGC 3627, two of them being type 3. One hole worth noting is hole no. 7 which has an unusually high expansion velocity of 65 $\mathrm{km\,s^{-1}}$, the highest observed in the entire sample.

NGC 4214

NGC 4214 is a nearby ($D = 2.9$ Mpc) dwarf irregular galaxy classified as a starburst galaxy. We found 56 H I holes in NGC 4214 with a wide range of sizes, from 0.11 to 1.2 kpc. Given the close proximity of this galaxy and consequently the high spatial resolution it is surprising that only about 7% of the holes detected are type 3. One possible explanation is that NGC 4214 has a low scale height and therefore holes can break out of the disc sooner.

NGC 4449

Another dwarf irregular galaxy, NGC 4449, is located at a distance of $D = 4.2$ Mpc. It has a very extended H I structure reaching out to 6 times the Holmberg radius. The R_{max} radius for this galaxy was taken at the edge of the H I disc thus excluding this structure. What is also unusual about NGC 4449 is that it has two counter-rotating gas systems (Hunter et al. 1998). We detected 20 H I holes in NGC 4449, most of them located within R_{25} and 6 located in the extended structure outside the R_{max} radius.

NGC 4736

NGC 4736 is a ringed spiral galaxy located at $D = 4.7$ Mpc: we found 23 holes in its H I distribution. The range of their diameters is quite small (0.21-0.45 kpc) and they are young holes ($t_{\rm kin} < 22$ Myr). As Figure 2.24 illustrates, the majority of the holes are located at small galactocentric radii and only type 1 holes lie at larger galactocentric radii. Finally note that hole number 11 is probably a superposition of 2 holes.

DDO 154

The gas-rich dwarf galaxy DDO 154 is a nearby galaxy with a very extended and warped H I disc. Hoffman et al. (2001) found 2 holes in the H I distribution which were also detected in our analysis. We report here on a total of 9 holes. The scale height of DDO 154 was found to be ≈ 500 pc which explains why holes can grow to a relatively large diameter before breaking out of the disc, as is the case with shell number 6 (≈ 400 pc).

NGC 5194

NGC 5194 is a grand-design spiral galaxy at a distance of $D = 8.0$ Mpc which is undergoing interaction with NGC 5195. We report 47 holes in NGC 5194 with only one type 3 hole detected. Most of the holes are in fact supershells, with one of those (no 5) being a superposition of two or more holes.

NGC 6946

Located at a distance of 5.9 Mpc, NGC 6946 is a large spiral galaxy seen almost face-on. Previous H I studies by Kamphuis & Sancisi (1993) and Boomsma (2007) revealed 19 and 121 H I holes respectively. We detected 56 holes, a subset of those detected by Boomsma (2007). There is excellent agreement for holes larger than 700 pc between our samples but not for smaller ones. This is due to the strict criteria ($Q > 5$) we applied on holes whose size is comparable to the resolution limit. NGC 6946 hosts the largest hole in our sample (no 58) with a size of 2.1 kpc and energy requirements in excess of 4×10^{54} erg, which corresponds to ~ 4000 SNe. Most of the holes detected (84%) are type 1, with two holes (no 15 and 16) appearing as a superposition of more than one hole.

NGC 7793

A member of the Sculptor group, NGC 7793 is an Sd spiral galaxy at $D = 3.9$ Mpc. A detailed analysis revealed 27 H I holes distributed almost uniformly across the H I disc with sizes ranging from 0.19 to 1.05 kpc.

2.5 Tables

Table 2.3. NGC 628 hole properties

No	α (h m s)	δ ($^\circ$ $'$ $''$)	$V_{\rm hel}$ (km s^{-1})	*Type* (1 − 3)	d (pc)	$V_{\rm exp}$ (km s^{-1})	*P.A.* ($^\circ$)	*Axial Ratio*	R (kpc)	$log(n_{\rm HI})$ (cm^{-3})	$t_{\rm kin}$ (Myr)	$log(E_{\rm E})$ (10^{50} erg)	$log(M_{\rm HI})$ (10^4 M$_\odot$)
1	1 36 20.1	15 43 45.2	645	1	520	7	109	0.7	13.1	-1.1	36	1.2	1.2
2	1 36 20.2	15 45 07.7	650	1	849	7	0	1.0	11.8	-1.0	59	2.0	1.9
3	1 36 23.4	15 43 43.6	639	1	575	7	149	0.5	11.7	-0.9	40	1.6	1.6
4	1 36 24.0	15 44 30.1	639	2	546	10	126	0.8	10.5	-0.7	27	1.9	1.6
5	1 36 24.1	15 50 55.6	665	2	459	7	0	0.9	12.4	-0.8	32	1.4	1.3
6	1 36 24.3	15 44 13.6	639	2	520	7	114	0.7	10.7	-0.7	36	1.7	1.6
7	1 36 24.6	15 47 15.1	650	1	720	7	13	0.8	8.9	-0.4	50	2.4	2.5
8	1 36 24.8	15 44 51.1	632	1	582	7	81	0.8	9.9	-0.6	41	1.9	2.3
9	1 36 26.2	15 45 25.5	639	1	513	7	87	0.9	8.7	-0.5	36	1.9	2.2
10	1 36 26.3	15 49 12.0	650	3	475	7	148	0.8	9.3	-0.3	33	2.0	1.9
11	1 36 27.0	15 45 28.5	639	1	411	7	0	0.6	8.2	-0.4	29	1.7	1.5
12	1 36 27.1	15 48 48.0	655	1	442	7	31	0.9	8.5	-0.3	31	1.9	2.2
13	1 36 27.6	15 51 10.5	670	1	613	7	9	0.8	11.5	-0.7	43	1.8	1.7
14	1 36 28.1	15 48 34.5	655	1	336	7	128	0.9	7.9	-0.2	23	1.6	1.5
15	1 36 28.3	15 49 06.0	657	1	936	7	0	0.6	8.3	-0.3	65	2.9	2.9
16	1 36 28.3	15 52 31.5	676	1	548	7	82	0.6	13.7	-1.0	38	1.4	1.3
17	1 36 28.5	15 51 25.5	673	1	700	7	161	0.7	11.7	-0.8	49	2.0	1.9
18	1 36 28.7	15 46 42.0	642	1	878	7	65	0.8	6.7	-0.2	61	3.0	2.8
19	1 36 29.3	15 44 37.4	639	2	838	10	78	0.5	8.1	-0.4	41	2.9	2.7
20	1 36 29.3	15 50 35.9	663	1	685	7	11	0.6	10.0	-0.6	48	2.1	2.4
21	1 36 29.9	15 44 40.4	642	1	548	7	54	0.9	7.8	-0.3	38	2.1	2.3
22	1 36 30.3	15 45 17.9	634	1	657	7	124	0.7	6.9	-0.2	46	2.5	2.5
23	1 36 30.3	15 49 05.9	657	1	407	7	112	0.9	7.4	-0.1	28	2.0	2.3
24	1 36 30.4	15 46 14.9	637	1	1777	7	145	0.4	6.1	-0.5	124	3.6	3.4
25	1 36 30.5	15 51 02.9	663	2	664	10	172	0.7	10.4	-0.6	32	2.3	2.4
26	1 36 31.1	15 48 26.9	652	1	814	7	0	1.0	6.3	-0.1	57	2.9	2.7
27	1 36 31.4	15 47 20.9	652	1	585	7	111	0.6	5.4	-0.2	41	2.4	2.3

Table 2.3 (cont'd)

No	α (h m s)	δ ($^\circ$ $'$ $''$)	$V_{\rm hel}$ (km s^{-1})	*Type* (1 − 3)	d (pc)	$V_{\rm exp}$ (km s^{-1})	*P.A.* ($^\circ$)	*Axial Ratio*	R (kpc)	$log(n_{\rm HI})$ (cm^{-3})	$t_{\rm kin}$ (Myr)	$log(E_{\rm E})$ (10^{50} erg)	$log(M_{\rm HI})$ (10^4 M$_\odot$)
28	1 36 31.6	15 42 44.9	634	1	455	7	105	0.7	10.4	-0.8	32	1.4	1.3
29	1 36 32.1	15 50 46.4	670	2	439	7	164	0.8	9.5	-0.6	31	1.6	1.5
30	1 36 32.3	15 43 38.9	637	2	617	13	118	0.8	8.6	-0.3	23	2.7	2.5
31	1 36 32.8	15 47 46.4	655	1	901	7	49	0.9	4.9	-0.2	63	3.0	2.6
32	1 36 32.8	15 50 05.9	668	1	1938	7	0	0.8	8.1	-0.4	135	3.8	3.4
33	1 36 33.2	15 46 56.8	650	1	743	7	0	1.0	4.5	-0.1	52	2.8	2.5
34	1 36 33.2	15 51 50.8	670	2	368	8	104	0.8	11.2	-0.7	22	1.3	1.2
35	1 36 33.2	15 51 07.3	670	1	490	7	137	0.8	9.8	-0.6	34	1.7	1.6
36	1 36 33.4	15 46 14.8	642	1	822	7	126	0.6	4.6	-0.1	57	3.0	2.6
37	1 36 34.3	15 45 43.3	629	1	484	7	89	0.6	4.7	-0.1	34	2.2	2.2
38	1 36 34.7	15 45 11.8	634	1	649	7	102	0.4	5.3	-0.1	45	2.6	2.5
39	1 36 35.0	15 47 20.8	655	1	888	7	0	0.7	3.6	-0.1	62	3.1	2.6
40	1 36 35.4	15 45 49.3	629	1	475	7	83	0.6	4.1	-0.1	33	2.2	2.1
41	1 36 35.4	15 49 25.3	668	1	758	7	71	0.6	6.1	-0.2	53	2.7	2.6
42	1 36 35.5	15 50 31.3	676	1	633	7	41	0.8	8.2	-0.3	44	2.4	2.5
43	1 36 36.2	15 44 04.3	637	3	319	8	0	1.0	6.8	-0.1	19	1.7	2.0
44	1 36 36.5	15 51 04.3	673	1	575	7	100	0.5	9.1	-0.5	40	2.1	2.3
45	1 36 37.1	15 49 05.7	670	1	2123	7	49	0.4	5.1	-0.5	148	3.8	3.6
46	1 36 38.1	15 52 22.2	678	2	619	8	61	0.9	11.6	-0.7	38	2.0	1.8
47	1 36 39.1	15 44 05.7	629	1	1226	7	98	0.5	6.3	-0.3	86	3.2	3.2
48	1 36 39.2	15 48 14.7	670	1	704	7	169	0.8	3.0	0.1	49	3.0	2.6
49	1 36 39.8	15 45 52.2	626	1	621	7	0	0.6	2.6	0.1	43	2.8	2.4
50	1 36 40.2	15 45 19.1	634	1	582	7	101	0.8	3.7	-0.1	41	2.5	2.3
51	1 36 40.2	15 50 16.2	678	1	562	7	0	0.8	7.0	-0.2	39	2.3	2.4
52	1 36 40.3	15 48 35.6	676	1	613	7	114	0.8	3.5	0.2	43	2.9	2.5
53	1 36 40.4	15 43 37.1	639	2	505	13	104	0.7	7.2	-0.3	19	2.5	2.3
54	1 36 41.0	15 53 04.1	678	1	649	7	69	0.6	12.9	-0.9	45	1.7	1.7

Table 2.3 (cont'd)

No	α (h m s)	δ ($^\circ$ $'$ $''$)	$V_{\rm hel}$ (km s^{-1})	*Type* (1 − 3)	d (pc)	$V_{\rm exp}$ (km s^{-1})	*P.A.* ($^\circ$)	*Axial Ratio*	R (kpc)	$log(n_{\rm HI})$ (cm^{-3})	$t_{\rm kin}$ (Myr)	$log(E_{\rm E})$ (10^{50} erg)	$log(M_{\rm HI})$ (10^4 M$_\odot$)
55	1 36 41.6	15 44 16.1	639	3	336	7	97	0.9	5.9	0.0	23	1.9	2.1
56	1 36 41.6	15 45 26.6	634	1	565	7	99	0.9	3.3	-0.1	39	2.5	2.2
57	1 36 41.6	15 48 13.1	678	2	613	5	94	0.8	2.6	0.1	60	2.6	2.4
58	1 36 42.7	15 50 56.6	683	1	882	7	21	0.9	8.4	-0.5	62	2.6	2.6
59	1 36 42.8	15 42 22.1	629	1	490	7	0	0.8	9.9	-0.9	34	1.4	1.4
60	1 36 43.0	15 40 56.6	645	1	530	7	0	0.9	12.9	-1.2	37	1.1	1.1
61	1 36 44.1	15 45 49.0	645	1	759	7	55	0.9	2.8	0.0	53	3.0	2.5
62	1 36 44.4	15 45 20.5	637	1	510	7	119	0.8	3.8	0.0	36	2.5	2.3
63	1 36 44.9	15 44 29.5	637	1	653	7	38	0.9	5.6	0.1	46	2.8	2.7
64	1 36 45.2	15 49 05.5	678	3	423	13	69	0.8	4.8	0.1	16	2.7	2.3
65	1 36 45.4	15 49 46.0	676	2	534	10	119	0.6	6.2	-0.2	26	2.5	2.3
66	1 36 45.6	15 50 40.0	678	1	613	7	121	0.8	8.0	-0.5	43	2.1	2.3
67	1 36 46.3	15 43 26.5	632	2	657	12	112	0.7	8.1	-0.3	27	2.7	2.5
68	1 36 47.4	15 43 44.4	642	1	751	7	101	0.5	7.5	-0.2	52	2.7	2.7
69	1 36 47.8	15 45 11.4	645	1	1782	7	49	0.6	4.9	0.0	125	4.1	3.4
70	1 36 48.0	15 46 27.9	645	2	338	12	106	0.5	3.4	0.1	14	2.3	2.0
71	1 36 48.0	15 49 15.9	681	1	700	7	96	0.7	5.8	0.0	49	2.9	2.7
72	1 36 48.1	15 48 06.9	673	1	720	7	106	0.8	4.0	0.1	50	3.0	2.6
73	1 36 48.6	15 47 17.4	670	1	1413	7	130	0.5	3.5	0.0	99	3.8	3.1
74	1 36 49.2	15 44 35.4	639	1	490	7	67	0.8	6.4	-0.3	34	2.1	2.2
75	1 36 49.2	15 48 51.9	689	2	884	13	105	0.4	5.4	0.1	33	3.6	2.9
76	1 36 50.4	15 43 27.8	645	2	501	7	91	0.5	8.8	-0.4	35	1.9	2.2
77	1 36 50.5	15 46 30.8	660	1	1573	7	164	0.7	4.6	0.0	110	4.0	3.3
78	1 36 50.5	15 50 03.8	681	1	562	7	104	0.8	7.9	-0.3	39	2.3	2.4
79	1 36 50.6	15 52 26.3	681	1	530	7	108	0.9	12.4	-0.9	37	1.4	1.4
80	1 36 51.1	15 45 33.8	647	2	490	9	149	0.8	5.7	0.0	27	2.5	2.3
81	1 36 52.4	15 46 57.8	668	3	577	5	152	0.7	5.4	0.0	56	2.4	2.5

Table 2.3 (cont'd)

No	α (h m s)	δ ($^\circ$ $'$ $''$)	$V_{\rm hel}$ (km s^{-1})	*Type* (1 − 3)	d (pc)	$V_{\rm exp}$ (km s^{-1})	*P.A.* ($^\circ$)	*Axial Ratio*	R (kpc)	$log(n_{\rm HI})$ (cm^{-3})	$t_{\rm kin}$ (Myr)	$log(E_{\rm E})$ (10^{50} erg)	$log(M_{\rm HI})$ (10^4 M$_\odot$)
82	1 36 52.8	15 46 02.3	660	1	548	7	151	0.6	6.1	-0.1	38	2.4	2.4
83	1 36 53.0	15 47 42.8	673	2	425	13	0	1.0	6.0	-0.1	16	2.4	2.2
84	1 36 53.6	15 44 15.7	647	1	425	7	0	1.0	8.4	-0.4	30	1.7	1.6
85	1 36 54.2	15 48 32.2	670	2	490	13	133	0.8	7.2	-0.1	18	2.6	2.4
86	1 36 54.6	15 47 20.2	665	1	822	7	113	0.4	6.6	-0.1	57	2.9	2.8
87	1 36 54.8	15 47 02.2	676	2	960	21	168	0.7	7.0	-0.2	22	3.7	2.9
88	1 36 55.5	15 47 50.2	665	2	725	8	124	0.5	7.3	-0.2	44	2.7	2.6
89	1 36 55.8	15 43 14.2	637	1	475	7	71	0.5	10.8	-0.8	33	1.5	1.4
90	1 36 56.4	15 48 20.1	678	1	751	7	82	0.5	8.1	-0.3	52	2.6	2.6
91	1 36 56.8	15 46 32.1	668	2	637	14	0	1.0	7.8	-0.2	22	2.9	2.6
92	1 36 57.3	15 45 54.6	655	1	795	7	146	0.6	8.3	-0.3	56	2.7	2.7
93	1 36 57.5	15 44 44.1	645	2	442	10	123	0.9	9.4	-0.4	22	2.0	1.6
94	1 36 58.2	15 43 00.6	639	2	625	5	141	0.5	11.9	-0.8	61	1.6	1.7
95	1 36 58.4	15 42 32.1	639	1	470	7	111	0.7	12.8	-0.9	33	1.3	1.2
96	1 36 59.0	15 46 38.1	663	1	749	7	135	0.6	8.9	-0.2	52	2.7	2.8
97	1 36 59.3	15 50 20.0	676	1	610	7	122	0.4	11.4	-1.0	43	1.6	1.5
98	1 36 59.5	15 47 15.5	673	1	1001	7	130	0.8	9.1	-0.3	70	2.9	3.0
99	1 36 59.8	15 52 54.5	670	1	1938	7	112	0.5	15.6	-0.9	135	3.3	3.1
100	1 37 00.7	15 48 54.5	673	1	725	7	114	0.5	10.5	-0.8	51	2.0	2.4
101	1 37 01.3	15 48 20.0	665	1	548	7	134	0.6	10.4	-0.6	38	1.8	1.7
102	1 37 02.0	15 44 45.5	652	1	510	7	120	0.8	11.5	-0.7	36	1.6	1.5
103	1 37 02.6	15 50 48.4	668	1	490	7	100	0.8	13.4	-1.2	34	1.1	1.0
104	1 37 03.7	15 46 15.4	660	2	825	13	101	0.5	11.4	-0.6	31	2.8	2.8
105	1 37 03.9	15 47 30.4	663	2	419	10	116	0.7	11.4	-0.7	20	1.6	1.3
106	1 37 06.8	15 45 52.8	655	1	470	7	119	0.7	13.3	-1.0	33	1.2	1.2

Table 2.4. NGC 2366 hole properties

No	α (h m s)	δ ($^\circ$ $'$ $''$)	$V_{\rm hel}$ (km s^{-1})	*Type* (1 − 3)	d (pc)	$V_{\rm exp}$ (km s^{-1})	*P.A.* (°)	*Axial Ratio*	R (kpc)	$log(n_{\rm HI})$ (cm^{-3})	$t_{\rm kin}$ (Myr)	$log(E_{\rm E})$ (10^{50} erg)	$log(M_{\rm HI})$ (10^4 M$_\odot$)
1	7 28 23.3	69 12 03.9	58	1	412	9	133	0.7	4.2	-1.0	22	1.2	1.0
2	7 28 30.7	69 10 13.0	61	1	418	9	31	0.6	3.3	-0.7	23	1.5	1.2
3	7 28 31.0	69 08 50.5	58	1	693	9	31	0.8	5.0	-1.2	38	1.6	1.4
4	7 28 33.2	69 10 34.0	66	3	250	9	0	1.0	2.9	-0.5	14	1.0	0.8
5	7 28 35.4	69 11 20.6	63	1	515	9	16	0.8	2.3	-0.3	28	2.3	2.0
6	7 28 37.2	69 09 32.6	56	1	391	9	48	0.7	4.2	-1.0	21	1.1	0.9
7	7 28 41.6	69 12 07.1	94	2	500	10	0	1.0	1.4	-0.2	24	2.4	2.5
8	7 28 42.8	69 11 04.1	94	2	300	24	0	1.0	2.2	-0.2	6	2.2	1.3
9	7 28 43.3	69 13 05.6	102	1	469	9	154	0.7	1.9	-0.3	26	2.1	1.8
10	7 28 43.9	69 12 29.6	100	3	350	12	0	1.0	1.3	-0.2	14	2.0	1.6
11	7 28 44.5	69 10 34.1	89	2	400	20	0	1.0	3.0	-0.4	10	2.2	1.5
12	7 28 50.1	69 11 20.6	85	3	208	10	65	0.9	2.1	-0.1	10	1.3	1.0
13	7 28 54.0	69 10 37.1	92	1	693	9	7	0.8	3.7	-0.7	38	2.3	2.0
14	7 28 54.9	69 10 29.6	81	1	540	9	14	0.9	4.0	-0.7	29	1.8	1.6
15	7 28 55.4	69 12 52.1	105	1	510	9	0	0.6	0.3	0.1	28	2.7	2.6
16	7 28 56.3	69 12 07.1	105	3	300	16	0	1.0	1.6	-0.1	9	2.2	1.5
17	7 28 57.7	69 14 49.1	128	1	312	9	156	0.5	2.8	-0.5	17	1.3	1.1
18	7 28 58.0	69 11 23.6	102	1	587	9	4	0.8	2.9	-0.4	32	2.3	2.0
19	7 28 59.7	69 13 11.6	128	1	450	9	0	1.0	0.8	0.1	24	2.5	2.5
20	7 29 00.8	69 15 13.1	141	1	550	9	0	1.0	3.2	-0.6	30	2.0	1.8
21	7 29 05.3	69 14 56.6	136	3	275	10	156	0.9	2.6	-0.5	13	1.3	1.0
22	7 29 06.2	69 15 34.1	130	2	350	16	0	1.0	3.4	-0.6	11	1.8	1.2
23	7 29 06.4	69 14 05.6	149	2	258	14	44	0.9	1.7	-0.3	9	1.6	1.1
24	7 29 12.1	69 14 23.6	143	2	349	11	124	0.8	2.3	-0.5	16	1.7	1.3
25	7 29 13.8	69 13 25.1	136	1	274	9	46	0.8	2.8	-0.6	15	1.0	0.8
26	7 29 16.3	69 15 20.5	156	3	242	10	67	0.9	3.2	-0.5	12	1.0	0.7

Table 2.5. NGC 2403 hole properties

No	α (h m s)	δ ($^\circ$ $'$ $''$)	$V_{\rm hel}$ (km s^{-1})	*Type* (1 – 3)	d (pc)	$V_{\rm exp}$ (km s^{-1})	*P.A.* ($^\circ$)	*Axial Ratio*	R (kpc)	$log(n_{\rm HI})$ (cm^{-3})	$t_{\rm kin}$ (Myr)	$log(E_{\rm E})$ (10^{50} erg)	$log(M_{\rm HI})$ (10^4 M$_\odot$)
1	7 35 13.9	65 37 04.3	61	1	272	15	26	0.8	12.8	-1.4	9	0.5	0.0
2	7 35 17.0	65 36 53.2	66	2	159	15	174	0.6	12.5	-1.4	5	-0.2	-0.6
3	7 35 18.3	65 38 04.2	56	1	179	8	110	0.9	11.3	-1.4	11	-0.5	-0.6
4	7 35 20.7	65 40 32.1	20	1	232	8	105	0.8	10.1	-1.2	14	0.0	0.0
5	7 35 20.8	65 38 26.1	46	1	223	8	79	0.7	10.7	-1.3	14	-0.1	-0.2
6	7 35 20.8	65 41 34.1	25	1	232	8	32	0.8	10.2	-1.3	14	0.0	-0.1
7	7 35 23.4	65 36 08.0	71	2	220	10	166	0.6	12.4	-1.3	11	0.1	-0.2
8	7 35 29.1	65 39 25.8	30	1	302	8	85	0.8	9.2	-1.2	18	0.4	0.4
9	7 35 31.5	65 35 46.8	82	2	191	16	5	0.7	11.7	-1.2	6	0.2	-0.3
10	7 35 35.5	65 38 22.6	56	3	162	17	35	0.8	8.8	-0.9	5	0.4	-0.1
11	7 35 39.3	65 42 27.5	25	1	1239	8	15	0.8	9.4	-1.3	76	2.2	2.4
12	7 35 39.4	65 34 24.5	87	1	265	8	25	0.5	12.3	-1.2	16	0.2	0.2
13	7 35 39.8	65 37 44.5	41	1	239	8	123	0.7	8.6	-1.0	15	0.4	0.3
14	7 35 40.6	65 35 47.4	71	3	248	13	98	0.8	10.3	-1.1	9	0.6	0.2
15	7 35 42.8	65 37 20.3	51	1	255	8	150	0.7	8.5	-1.1	16	0.3	0.2
16	7 35 44.5	65 40 26.3	25	1	216	8	74	0.8	7.6	-1.2	13	0.0	-0.1
17	7 35 45.3	65 35 16.2	92	2	286	22	41	0.6	10.3	-1.1	6	1.1	0.4
18	7 35 47.4	65 33 26.1	102	1	248	8	160	0.8	12.5	-1.3	15	0.0	0.0
19	7 35 47.5	65 36 42.1	61	1	245	25	89	0.7	8.4	-1.0	5	1.1	0.3
20	7 35 48.6	65 38 37.1	30	1	475	8	110	0.5	7.0	-0.9	29	1.4	1.3
21	7 35 48.8	65 36 20.1	66	2	187	21	0	1.0	8.6	-1.0	4	0.6	-0.1
22	7 35 49.1	65 42 08.1	25	1	197	8	17	0.6	8.7	-1.2	12	-0.1	-0.2
23	7 35 52.5	65 29 22.9	123	1	452	8	37	0.7	18.4	-2.0	28	0.1	0.1
24	7 35 53.6	65 38 55.9	30	2	202	15	69	0.9	6.4	-0.9	7	0.6	0.2
25	7 35 55.7	65 38 28.8	41	2	220	16	58	0.6	6.2	-0.8	7	0.9	0.3
26	7 35 58.0	65 39 29.7	15	1	286	8	8	0.4	6.1	-0.8	17	0.8	0.7
27	7 35 59.8	65 32 44.6	113	1	646	8	160	0.8	11.9	-1.3	39	1.4	1.3

Table 2.5 (cont'd)

No	α (h m s)	δ ($^\circ$ $'$ $''$)	$V_{\rm hel}$ (km s^{-1})	*Type* (1 − 3)	d (pc)	$V_{\rm exp}$ (km s^{-1})	*P.A.* ($^\circ$)	*Axial Ratio*	R (kpc)	$log(n_{\rm HI})$ (cm^{-3})	$t_{\rm kin}$ (Myr)	$log(E_{\rm E})$ (10^{50} erg)	$log(M_{\rm HI})$ (10^4 M$_\odot$)
28	7 36 01.9	65 35 37.5	87	2	281	16	0	1.0	7.5	-1.0	9	1.0	0.5
29	7 36 02.2	65 37 18.5	41	1	197	8	2	0.6	5.8	-0.8	12	0.3	0.2
30	7 36 02.8	65 33 55.5	113	3	187	15	0	1.0	9.7	-1.0	6	0.5	0.0
31	7 36 04.2	65 35 55.4	71	1	165	8	26	0.6	6.8	-0.9	10	-0.1	-0.2
32	7 36 04.4	65 36 35.4	71	1	248	8	22	0.8	6.1	-0.9	15	0.6	0.5
33	7 36 05.1	65 35 23.4	92	1	280	16	51	0.6	7.4	-1.0	9	0.9	0.4
34	7 36 05.4	65 40 49.3	35	1	752	8	29	0.8	6.8	-0.9	46	2.0	2.2
35	7 36 07.6	65 36 12.2	71	1	169	15	69	0.7	6.0	-0.8	6	0.5	0.0
36	7 36 08.5	65 36 51.2	61	3	192	18	15	0.4	5.3	-0.7	5	0.9	0.3
37	7 36 11.4	65 37 22.0	51	2	237	21	2	0.5	4.6	-0.4	6	1.6	0.9
38	7 36 11.4	65 39 07.0	41	2	264	21	9	0.4	4.8	-0.5	6	1.6	0.9
39	7 36 13.2	65 39 10.0	46	3	156	20	0	1.0	4.8	-0.5	4	0.9	0.2
40	7 36 15.3	65 37 16.8	56	3	162	15	2	0.8	4.1	-0.4	5	0.9	0.4
41	7 36 17.3	65 40 10.7	46	1	755	8	65	0.7	5.8	-0.7	46	2.3	2.4
42	7 36 17.7	65 36 29.7	61	2	215	21	102	0.5	4.3	-0.4	5	1.4	0.7
43	7 36 18.2	65 36 39.7	61	3	179	21	71	0.9	4.1	-0.8	4	0.8	0.1
44	7 36 18.8	65 32 26.6	123	2	194	16	171	0.8	10.0	-1.1	6	0.4	-0.1
45	7 36 18.9	65 30 16.6	133	3	169	8	24	0.7	13.7	-1.2	10	-0.3	-0.4
46	7 36 19.6	65 31 10.6	128	1	197	8	70	0.6	12.0	-1.3	12	-0.3	-0.3
47	7 36 20.0	65 33 20.6	113	2	1080	20	68	0.7	8.4	-0.9	26	3.0	2.6
48	7 36 20.3	65 38 40.6	51	2	223	16	5	0.7	3.9	-0.3	7	1.4	0.8
49	7 36 21.4	65 35 10.5	97	1	156	8	0	1.0	5.4	-0.7	10	0.1	0.0
50	7 36 21.8	65 39 08.5	46	3	172	18	0	1.0	4.4	-0.4	5	1.0	0.4
51	7 36 22.9	65 35 34.4	87	1	204	8	77	0.6	4.6	-0.6	12	0.6	0.5
52	7 36 23.1	65 37 30.4	56	2	169	15	172	0.7	3.1	-0.2	6	1.2	0.6
53	7 36 23.8	65 31 34.4	144	1	149	8	42	0.5	10.9	-1.2	9	-0.6	-0.6
54	7 36 24.6	65 40 32.3	62	2	219	11	0	1.0	6.4	-0.7	10	0.7	0.4

Table 2.5 (cont'd)

No	α (h m s)	δ ($^\circ$ $'$ $''$)	$V_{\rm hel}$ (km s^{-1})	*Type* (1 − 3)	d (pc)	$V_{\rm exp}$ (km s^{-1})	*P.A.* ($^\circ$)	*Axial Ratio*	R (kpc)	$log(n_{\rm HI})$ (cm^{-3})	$t_{\rm kin}$ (Myr)	$log(E_{\rm E})$ (10^{50} erg)	$log(M_{\rm HI})$ (10^4 M$_\odot$)
55	7 36 26.7	65 35 59.2	82	3	318	15	62	0.8	3.6	-0.3	10	1.9	1.7
56	7 36 28.3	65 28 46.1	154	1	153	8	21	0.7	15.3	-1.4	9	-0.7	-0.7
57	7 36 29.1	65 38 09.1	56	1	541	8	42	0.8	3.0	-0.3	33	2.2	2.1
58	7 36 29.3	65 31 50.0	139	2	219	6	0	1.0	9.8	-1.1	18	0.0	0.1
59	7 36 29.7	65 36 18.0	71	1	204	8	18	0.6	2.8	-0.3	12	0.9	0.7
60	7 36 29.9	65 27 20.0	154	1	194	8	17	0.8	17.6	-1.7	12	-0.6	-0.6
61	7 36 29.9	65 39 35.0	66	1	312	8	72	0.6	5.0	-0.7	19	1.0	0.9
62	7 36 29.9	65 40 58.0	56	2	187	11	74	0.4	7.3	-0.8	8	0.4	0.1
63	7 36 31.7	65 31 25.9	154	2	156	10	0	1.0	10.2	-1.1	8	-0.2	-0.4
64	7 36 31.9	65 34 47.9	113	1	802	8	92	0.9	4.5	-0.5	49	2.6	2.5
65	7 36 32.9	65 35 38.8	82	1	232	8	2	0.6	3.1	-0.3	14	1.1	1.4
66	7 36 33.4	65 28 14.8	159	1	219	8	0	1.0	15.7	-1.4	13	-0.2	-0.2
67	7 36 33.5	65 38 38.8	61	3	202	15	155	0.9	3.6	-0.5	7	1.1	0.6
68	7 36 33.9	65 30 46.8	149	1	195	8	140	0.9	11.1	-1.1	12	-0.1	-0.1
69	7 36 34.1	65 33 12.8	144	1	707	8	62	0.8	6.8	-0.8	43	2.1	2.3
70	7 36 35.6	65 38 35.7	61	3	125	16	0	1.0	3.6	-0.4	4	0.5	0.0
71	7 36 36.3	65 40 24.7	77	3	245	16	10	0.7	6.7	-1.0	8	0.9	0.3
72	7 36 37.6	65 35 33.6	108	2	277	11	38	0.7	2.6	-0.2	12	1.6	1.5
73	7 36 38.5	65 38 27.5	66	1	221	8	104	0.5	3.5	-0.3	14	1.0	0.9
74	7 36 39.7	65 36 10.4	92	2	279	15	169	0.8	1.5	-0.1	9	2.0	1.6
75	7 36 40.5	65 32 14.4	159	1	218	8	70	0.9	7.8	-1.1	13	0.1	0.1
76	7 36 41.0	65 37 34.4	77	1	761	8	60	0.7	2.1	-0.2	47	2.8	2.4
77	7 36 41.8	65 32 39.3	154	1	1160	8	22	0.9	7.0	-0.7	71	2.8	2.8
78	7 36 42.2	65 39 50.3	71	2	187	16	19	0.4	6.1	-0.6	6	0.9	0.4
79	7 36 43.7	65 41 27.2	82	1	678	8	146	0.7	9.0	-1.1	41	1.7	1.5
80	7 36 43.9	65 37 12.2	77	3	172	13	0	1.0	1.6	-0.1	6	1.2	1.1
81	7 36 44.3	65 36 50.1	71	1	229	8	44	0.7	1.1	0.0	14	1.4	1.4

Table 2.5 (cont'd)

No	α (h m s)	δ ($^\circ$ $'$ $''$)	$V_{\rm hel}$ (km s^{-1})	*Type* (1 − 3)	d (pc)	$V_{\rm exp}$ (km s^{-1})	*P.A.* ($^\circ$)	*Axial Ratio*	R (kpc)	$log(n_{\rm HI})$ (cm^{-3})	$t_{\rm kin}$ (Myr)	$log(E_{\rm E})$ (10^{50} erg)	$log(M_{\rm HI})$ (10^4 M$_\odot$)
82	7 36 46.1	65 38 04.0	82	1	218	8	26	0.9	3.2	-0.4	13	0.9	0.8
83	7 36 47.2	65 36 31.0	97	2	199	20	22	0.5	0.7	0.0	5	1.8	1.2
84	7 36 48.2	65 32 18.9	169	1	209	8	13	0.6	6.9	-0.9	13	0.3	0.2
85	7 36 48.3	65 34 51.9	144	3	288	13	65	0.9	2.4	-0.1	11	1.9	1.6
86	7 36 48.3	65 34 27.9	149	1	194	8	66	0.8	3.1	-0.1	12	1.0	0.8
87	7 36 49.3	65 40 51.8	82	2	288	24	68	0.9	8.4	-1.0	6	1.3	0.5
88	7 36 49.5	65 38 28.8	113	1	331	8	86	0.7	4.2	-0.5	20	1.4	1.7
89	7 36 50.0	65 35 21.8	169	2	194	20	9	0.8	1.3	0.0	5	1.7	1.3
90	7 36 50.6	65 34 57.7	159	3	218	26	25	0.9	2.0	-0.2	4	1.8	1.3
91	7 36 51.3	65 27 24.7	175	1	218	8	39	0.9	15.4	-1.2	13	0.1	0.0
92	7 36 51.4	65 30 24.7	180	2	146	11	31	0.7	10.1	-1.1	7	-0.2	-0.5
93	7 36 51.5	65 40 42.7	97	3	187	20	0	1.0	8.4	-1.0	5	0.6	-0.1
94	7 36 51.8	65 37 25.7	102	1	854	8	171	0.6	2.5	-0.2	52	2.9	2.5
95	7 36 52.4	65 29 34.6	169	1	191	8	32	0.7	11.5	-1.2	12	-0.2	-0.2
96	7 36 53.8	65 32 08.5	180	2	309	11	151	0.7	6.7	-0.8	14	1.1	0.8
97	7 36 53.9	65 34 07.5	190	2	207	11	52	0.7	3.2	-0.4	9	1.0	0.7
98	7 36 55.1	65 34 38.4	175	1	618	8	56	0.5	2.2	-0.2	38	2.6	2.2
99	7 36 55.2	65 29 53.4	175	1	172	8	0	1.0	10.7	-1.2	11	-0.2	-0.3
100	7 36 55.3	65 35 20.4	185	1	284	8	62	0.7	1.0	0.0	17	1.7	1.6
101	7 36 58.0	65 36 04.2	154	2	172	15	0	1.0	1.0	0.0	6	1.4	1.2
102	7 36 58.5	65 39 43.2	113	1	675	8	8	0.8	7.3	-0.7	41	2.1	2.4
103	7 36 58.6	65 39 53.2	113	1	223	21	73	0.7	7.6	-1.0	5	0.8	0.2
104	7 36 59.0	65 37 01.1	133	1	265	8	59	0.9	2.6	-0.1	16	1.5	1.6
105	7 36 59.8	65 28 05.1	180	1	216	8	88	0.8	13.5	-1.4	13	-0.3	-0.3
106	7 37 00.5	65 35 39.0	195	1	234	8	152	0.9	1.1	0.0	14	1.5	1.4
107	7 37 00.8	65 39 37.0	118	1	327	8	113	0.9	7.3	-0.8	20	1.0	0.8
108	7 37 01.2	65 34 39.0	190	1	232	32	38	0.6	2.0	-0.2	4	2.0	1.3

Table 2.5 (cont'd)

No	α (h m s)	δ ($^\circ$ $'$ $''$)	$V_{\rm hel}$ (km s^{-1})	*Type* (1 − 3)	d (pc)	$V_{\rm exp}$ (km s^{-1})	*P.A.* ($^\circ$)	*Axial Ratio*	R (kpc)	$log(n_{\rm HI})$ (cm^{-3})	$t_{\rm kin}$ (Myr)	$log(E_{\rm E})$ (10^{50} erg)	$log(M_{\rm HI})$ (10^4 M$_\odot$)
109	7 37 01.6	65 29 32.9	180	1	213	8	174	0.6	10.7	-1.2	13	-0.1	-0.1
110	7 37 01.7	65 28 49.9	185	1	202	8	45	0.9	12.0	-1.3	12	-0.2	-0.3
111	7 37 02.4	65 35 22.9	195	1	274	15	130	0.6	1.3	0.0	9	2.0	1.6
112	7 37 03.5	65 34 54.8	206	3	203	16	0	1.0	1.7	-0.1	6	1.5	1.3
113	7 37 04.5	65 39 50.8	128	2	153	20	34	0.7	8.1	-0.8	4	0.5	-0.2
114	7 37 05.3	65 36 59.6	154	3	187	10	110	0.8	3.4	-0.2	9	1.1	0.8
115	7 37 05.4	65 37 23.7	149	1	304	8	86	0.9	4.0	-0.3	19	1.4	1.7
116	7 37 05.5	65 29 59.7	190	1	178	15	48	0.8	9.7	-1.2	6	0.2	-0.3
117	7 37 06.8	65 31 41.6	211	2	279	16	2	0.8	6.6	-0.7	9	1.3	0.8
118	7 37 08.3	65 37 29.5	144	1	363	8	31	0.7	4.5	-0.4	22	1.6	1.9
119	7 37 08.5	65 40 12.5	123	1	216	8	31	0.8	9.2	-1.0	13	0.2	0.1
120	7 37 09.1	65 32 07.4	206	2	324	25	150	0.6	5.8	-0.7	6	1.8	1.0
121	7 37 10.6	65 35 20.3	200	2	241	21	134	0.8	2.2	0.0	6	2.0	1.6
122	7 37 13.0	65 34 35.1	211	3	162	16	163	0.8	2.5	-0.2	5	1.1	0.5
123	7 37 13.4	65 30 31.1	206	1	181	8	24	0.6	8.3	-1.0	11	0.0	-0.1
124	7 37 13.5	65 33 25.1	226	1	353	8	42	0.4	3.7	-0.2	22	1.8	1.9
125	7 37 13.5	65 40 00.1	133	1	701	8	156	0.6	9.4	-1.0	43	1.8	1.6
126	7 37 14.0	65 33 26.0	226	1	478	8	13	0.7	3.7	-0.1	29	2.3	2.3
127	7 37 15.2	65 27 39.9	190	1	1777	8	142	0.9	13.1	-1.4	109	2.6	2.7
128	7 37 15.4	65 32 20.9	226	1	749	8	20	0.6	5.2	-0.5	46	2.5	2.5
129	7 37 16.5	65 36 01.8	180	2	143	20	159	0.6	3.6	-0.3	3	1.0	0.3
130	7 37 17.3	65 34 48.8	216	1	276	8	70	0.5	2.9	-0.4	17	1.3	1.5
131	7 37 17.3	65 34 32.8	216	1	784	8	3	0.5	2.9	-0.1	48	2.9	2.6
132	7 37 18.1	65 34 31.7	221	1	209	8	172	0.8	3.0	-0.4	13	0.9	0.7
133	7 37 19.1	65 37 26.7	139	2	223	20	53	0.7	5.9	-0.6	5	1.2	0.5
134	7 37 19.1	65 37 14.7	144	3	108	23	154	0.8	5.6	-0.6	2	0.4	-0.4
135	7 37 19.5	65 36 21.6	164	3	239	21	124	0.7	4.4	-0.5	6	1.5	0.8

Table 2.5 (cont'd)

No	α (h m s)	δ ($^\circ$ $'$ $''$)	$V_{\rm hel}$ (km s^{-1})	*Type* (1 − 3)	d (pc)	$V_{\rm exp}$ (km s^{-1})	*P.A.* ($^\circ$)	*Axial Ratio*	R (kpc)	$log(n_{\rm HI})$ (cm^{-3})	$t_{\rm kin}$ (Myr)	$log(E_{\rm E})$ (10^{50} erg)	$log(M_{\rm HI})$ (10^4 M$_\odot$)
136	7 37 19.6	65 30 37.6	216	3	146	10	165	0.7	7.8	-0.7	7	0.1	-0.1
137	7 37 20.4	65 36 50.2	175	1	358	8	119	0.8	5.2	-0.6	22	1.3	1.2
138	7 37 22.1	65 35 32.4	221	2	248	10	72	0.6	3.9	-0.2	12	1.5	1.1
139	7 37 22.3	65 29 08.4	206	1	187	8	0	1.0	10.2	-1.2	11	-0.1	-0.2
140	7 37 22.4	65 39 27.4	139	1	363	8	5	0.6	9.6	-1.2	22	0.8	0.7
141	7 37 22.8	65 36 12.4	190	3	207	26	60	0.7	4.7	-0.6	4	1.4	0.5
142	7 37 23.1	65 35 59.3	180	2	187	26	0	1.0	4.5	-0.4	4	1.4	0.5
143	7 37 24.2	65 31 43.2	231	1	132	8	4	0.9	6.0	-0.9	8	-0.3	-0.4
144	7 37 25.7	65 34 52.1	216	2	242	15	65	0.9	4.0	-0.3	8	1.5	0.9
145	7 37 26.4	65 38 55.1	139	1	204	16	18	0.5	9.2	-1.2	6	0.4	-0.1
146	7 37 28.0	65 32 27.9	237	1	437	8	9	0.7	5.2	-0.7	27	1.6	1.8
147	7 37 28.3	65 38 46.9	144	1	187	18	13	0.6	9.2	-1.0	5	0.5	-0.1
148	7 37 28.9	65 39 20.9	133	1	209	8	124	0.6	10.2	-1.2	13	0.0	-0.1
149	7 37 29.0	65 37 37.9	175	2	204	26	174	0.5	7.5	-0.8	4	1.1	0.3
150	7 37 31.9	65 34 54.6	221	1	226	8	22	0.6	4.8	-0.6	14	0.8	0.6
151	7 37 32.8	65 28 42.5	216	1	1108	8	0	1.0	10.5	-1.3	68	2.1	2.4
152	7 37 34.2	65 36 24.4	180	1	169	20	140	0.7	6.6	-0.8	4	0.6	0.0
153	7 37 34.4	65 34 09.4	237	1	191	8	3	0.7	4.8	-0.7	12	0.3	0.2
154	7 37 34.6	65 32 06.4	237	1	249	8	68	0.9	5.8	-1.0	15	0.3	0.2
155	7 37 35.6	65 32 45.3	247	1	261	8	171	0.7	5.3	-0.9	16	0.6	0.5
156	7 37 37.4	65 31 56.1	237	1	254	8	5	0.5	6.1	-1.0	16	0.4	0.3
157	7 37 38.6	65 35 23.0	206	1	711	8	120	0.7	6.1	-0.8	43	2.0	2.2
158	7 37 38.8	65 31 28.0	237	1	181	8	59	0.6	6.6	-1.1	11	-0.1	-0.2
159	7 37 39.4	65 37 02.0	180	2	179	11	61	0.9	8.1	-0.8	8	0.4	0.1
160	7 37 40.7	65 33 41.8	237	1	1048	8	145	0.7	5.5	-0.7	64	2.7	2.6
161	7 37 42.9	65 36 36.7	190	2	169	25	39	0.7	8.1	-0.8	3	0.8	0.0
162	7 37 43.6	65 34 26.6	226	1	199	8	66	0.5	6.1	-0.9	12	0.2	0.1

Table 2.5 (cont'd)

No	α (h m s)	δ ($^\circ$ $'$ $''$)	$V_{\rm hel}$ (km s^{-1})	*Type* (1 − 3)	d (pc)	$V_{\rm exp}$ (km s^{-1})	*P.A.* ($^\circ$)	*Axial Ratio*	R (kpc)	$log(n_{\rm HI})$ (cm^{-3})	$t_{\rm kin}$ (Myr)	$log(E_{\rm E})$ (10^{50} erg)	$log(M_{\rm HI})$ (10^4 M$_\odot$)
163	7 37 47.8	65 32 30.2	242	1	241	8	89	0.8	6.4	-0.9	15	0.5	0.4
164	7 37 49.6	65 32 24.0	242	1	665	8	81	0.8	6.6	-0.8	41	1.9	2.2
165	7 37 52.8	65 34 43.8	221	3	159	10	105	0.6	7.6	-0.9	8	0.1	-0.2
166	7 38 00.0	65 29 55.0	242	1	201	8	33	0.7	9.0	-1.4	12	-0.3	-0.4
167	7 38 02.2	65 31 26.8	247	1	319	8	153	0.9	8.1	-1.0	20	0.8	0.7
168	7 38 04.0	65 27 27.6	237	3	187	11	0	1.0	12.0	-1.3	8	-0.2	-0.4
169	7 38 06.4	65 32 48.4	247	2	197	20	96	0.6	8.4	-1.0	5	0.6	-0.1
170	7 38 07.8	65 31 42.3	247	1	159	8	4	0.6	8.6	-1.2	10	-0.4	-0.4
171	7 38 10.3	65 29 04.0	247	1	403	8	133	0.8	10.3	-1.1	25	0.9	0.8
172	7 38 10.4	65 33 58.0	221	1	599	8	145	0.7	9.4	-0.8	37	1.9	1.7
173	7 38 15.2	65 30 31.5	247	1	1501	8	15	0.7	9.7	-1.2	92	2.6	2.7
174	7 38 17.2	65 28 53.3	252	1	155	8	6	0.8	10.9	-1.4	9	-0.7	-0.7
175	7 38 28.2	65 30 34.2	247	1	245	8	87	0.7	10.9	-1.2	15	0.1	0.1

Table 2.6. HolmbergII hole properties

No	α (h m s)	δ ($^\circ$ $'$ $''$)	$V_{\rm hel}$ ($\rm km\,s^{-1}$)	*Type* (1 – 3)	d (pc)	$V_{\rm exp}$ ($\rm km\,s^{-1}$)	*P.A.* ($^\circ$)	*Axial Ratio*	R (kpc)	$log(n_{\rm HI})$ ($\rm cm^{-3}$)	$t_{\rm kin}$ (Myr)	$log(E_{\rm E})$ (10^{50} erg)	$log(M_{\rm HI})$ ($10^4\,\rm M_\odot$)
1	8 18 22.2	70 44 13.1	148	1	1260	7	162	0.5	4.7	-0.9	88	2.7	2.8
2	8 18 28.9	70 42 20.3	161	1	1400	7	89	0.8	4.0	-0.7	98	3.0	3.0
3	8 18 34.5	70 40 32.0	166	1	287	7	168	0.8	4.3	-0.6	20	0.9	0.9
4	8 18 40.1	70 41 36.3	164	1	731	7	112	0.7	3.2	-0.5	51	2.4	2.6
5	8 18 42.4	70 40 58.6	166	1	412	7	89	0.6	3.3	-0.5	29	1.6	1.5
6	8 18 48.8	70 43 40.3	156	1	486	7	84	0.7	1.8	-0.1	34	2.2	2.4
7	8 18 50.3	70 45 59.8	143	2	279	10	0	1.0	3.1	-0.4	14	1.3	1.0
8	8 18 52.0	70 42 46.2	156	3	345	10	0	1.0	1.5	-0.1	17	2.0	2.1
9	8 18 52.8	70 44 26.6	143	3	279	10	0	1.0	1.8	-0.2	14	1.6	1.3
10	8 18 55.4	70 38 50.5	179	1	1187	7	54	0.7	4.5	-0.7	83	2.8	2.9
11	8 18 58.1	70 45 38.4	133	1	556	7	93	0.6	2.5	-0.3	39	2.2	2.4
12	8 18 58.4	70 42 56.3	159	3	403	11	130	0.7	0.8	0.0	18	2.4	2.3
13	8 18 59.0	70 44 57.8	135	1	838	7	0	1.0	1.8	-0.2	59	2.9	2.8
14	8 19 00.1	70 42 26.2	164	2	318	15	19	0.8	0.9	-0.1	10	2.2	2.0
15	8 19 01.0	70 46 35.2	128	3	362	8	0	1.0	3.4	-0.4	22	1.5	1.3
16	8 19 03.6	70 43 27.5	151	1	761	7	154	0.7	0.3	0.0	53	3.0	2.8
17	8 19 05.4	70 41 24.4	171	1	2110	7	47	0.7	1.8	-0.3	147	4.0	3.5
18	8 19 07.9	70 46 00.3	135	1	737	7	24	0.5	2.8	-0.4	52	2.5	2.6
19	8 19 13.1	70 44 24.0	140	1	1107	7	95	0.6	1.5	-0.2	77	3.2	3.0
20	8 19 14.8	70 45 25.4	148	3	329	12	0	1.0	2.5	-0.3	13	1.8	1.4
21	8 19 15.3	70 45 01.4	138	3	378	9	0	1.0	2.1	-0.3	21	1.8	1.5
22	8 19 16.5	70 46 50.8	138	1	403	7	115	0.7	3.8	-0.5	28	1.5	1.4
23	8 19 18.4	70 43 20.7	153	2	738	16	110	0.9	1.5	-0.1	23	3.3	2.8
24	8 19 21.9	70 48 14.5	133	1	640	7	0	0.7	5.4	-0.9	45	1.7	1.6
25	8 19 22.7	70 47 18.9	133	1	325	7	131	0.4	4.5	-0.7	23	1.0	1.0
26	8 19 23.9	70 43 29.3	143	1	483	7	26	0.7	2.1	-0.2	34	2.2	2.4
27	8 19 25.5	70 42 14.2	166	1	312	7	0	1.0	2.4	0.0	22	1.7	1.6

Table 2.6 (cont'd)

No	α (h m s)	δ ($^\circ$ $'$ $''$)	$V_{\rm hel}$ (km s^{-1})	*Type* (1 − 3)	d (pc)	$V_{\rm exp}$ (km s^{-1})	*P.A.* ($^\circ$)	*Axial Ratio*	R (kpc)	$log(n_{\rm HI})$ (cm^{-3})	$t_{\rm kin}$ (Myr)	$log(E_{\rm E})$ (10^{50} erg)	$log(M_{\rm HI})$ (10^4 M$_\odot$)
28	8 19 26.3	70 41 05.2	177	3	263	11	0	1.0	3.1	-0.3	12	1.5	1.1
29	8 19 26.6	70 45 29.2	143	1	479	7	117	0.7	3.3	-0.5	33	1.8	1.7
30	8 19 28.3	70 44 38.1	151	2	318	13	68	0.8	2.9	-0.3	12	1.8	1.3
31	8 19 28.8	70 43 38.0	148	1	491	7	113	0.8	2.6	-0.2	34	2.1	2.4
32	8 19 30.3	70 39 52.9	174	1	1282	7	0	1.0	4.2	-0.6	90	2.9	3.0
33	8 19 34.8	70 41 21.1	171	3	531	20	19	0.8	3.6	-0.4	13	2.7	1.9
34	8 19 35.1	70 45 04.6	153	1	657	7	126	0.7	3.8	-0.5	46	2.2	2.5
35	8 19 35.9	70 46 33.1	143	1	1330	7	131	0.9	4.8	-0.8	93	2.8	3.0
36	8 19 40.3	70 42 07.3	164	3	424	14	168	0.8	3.9	-0.5	15	2.1	1.5
37	8 19 40.7	70 46 02.8	143	1	1778	7	138	0.5	4.8	-0.9	124	3.1	3.4
38	8 19 43.2	70 43 11.6	161	1	789	7	0	1.0	4.1	-0.5	55	2.5	2.7
39	8 19 44.0	70 43 55.0	166	2	474	18	72	0.8	4.3	-0.4	13	2.4	1.7
40	8 19 45.8	70 45 42.9	143	1	1267	7	151	0.7	5.1	-0.8	89	2.7	2.9

Table 2.7. DDO 53 hole properties

No	α (h m s)	δ ($^\circ$ $'$ $''$)	$V_{\rm hel}$ ($\rm km\,s^{-1}$)	*Type* (1 – 3)	d (pc)	$V_{\rm exp}$ ($\rm km\,s^{-1}$)	*P.A.* ($^\circ$)	*Axial Ratio*	R (kpc)	$log(n_{\rm HI})$ ($\rm cm^{-3}$)	$t_{\rm kin}$ (Myr)	$log(E_{\rm E})$ (10^{50} erg)	$log(M_{\rm HI})$ ($10^4\,\rm M_\odot$)
1	8 34 10.0	66 10 38.0	17	1	363	8	44	0.7	0.4	-0.2	22	1.8	1.6
2	8 34 11.7	66 10 42.5	22	2	309	8	148	0.8	0.6	-0.4	19	1.4	1.2
3	8 34 12.2	66 11 18.5	17	3	179	10	145	0.3	1.3	-0.4	9	0.7	0.5

Table 2.8. NGC 2841 hole properties

No	α (h m s)	δ ($^\circ$ $'$ $''$)	$V_{\rm hel}$ (km s^{-1})	*Type* (1 − 3)	d (pc)	$V_{\rm exp}$ (km s^{-1})	*P.A.* ($^\circ$)	*Axial Ratio*	R (kpc)	$log(n_{\rm HI})$ (cm^{-3})	$t_{\rm kin}$ (Myr)	$log(E_{\rm E})$ (10^{50} erg)	$log(M_{\rm HI})$ (10^4 M$_\odot$)
1	9 21 36.4	51 06 55.8	379	1	1333	9	161	1.0	38.4	-2.0	72	1.8	1.7
2	9 21 36.9	51 02 25.8	539	1	1136	9	163	0.5	34.3	-1.5	62	1.9	1.7
3	9 21 40.3	51 07 58.9	363	1	1597	9	162	0.8	44.6	-2.0	87	2.0	1.8
4	9 21 44.5	51 01 40.9	384	1	1264	9	0	0.9	23.0	-1.2	69	2.5	2.6
5	9 21 45.0	51 01 10.9	405	1	1253	9	145	0.8	23.5	-1.3	68	2.3	2.1
6	9 21 45.6	51 01 57.4	374	1	886	9	31	0.9	21.0	-1.2	48	2.0	1.7
7	9 21 47.1	51 02 21.4	363	1	1474	9	108	0.5	19.4	-1.2	80	2.7	2.6
8	9 21 52.1	50 59 50.0	441	1	1421	9	75	0.8	15.0	-1.2	77	2.7	2.6
9	9 21 52.6	50 59 33.5	472	1	1242	9	162	0.7	15.1	-1.1	68	2.6	2.5
10	9 21 57.4	50 59 24.5	425	3	1127	28	0	0.9	6.6	-0.7	20	3.5	2.4
11	9 22 00.9	51 02 39.5	487	1	1055	9	153	0.8	28.3	-1.7	57	1.7	1.5
12	9 22 05.8	50 52 53.0	782	1	1666	9	118	0.8	38.6	-2.0	91	2.1	2.4
13	9 22 10.2	50 52 03.5	824	1	1136	9	134	0.5	38.3	-1.7	62	1.7	1.5
14	9 22 16.3	50 56 53.0	834	1	1450	9	126	0.7	19.6	-1.2	79	2.7	2.6
15	9 22 17.7	50 56 07.9	886	1	917	9	57	0.8	19.7	-1.2	50	2.0	2.2
16	9 22 31.8	50 50 15.3	886	1	991	9	88	0.9	39.2	-1.7	54	1.5	1.3

Table 2.9. Holmberg I hole properties

No	α (h m s)	δ ($^\circ$ $'$ $''$)	$V_{\rm hel}$ ($\rm km\,s^{-1}$)	*Type* (1 – 3)	d (pc)	$V_{\rm exp}$ ($\rm km\,s^{-1}$)	*P.A.* ($^\circ$)	*Axial Ratio*	R (kpc)	$log(n_{\rm HI})$ ($\rm cm^{-3}$)	$t_{\rm kin}$ (Myr)	$log(E_{\rm E})$ (10^{50} erg)	$log(M_{\rm HI})$ ($10^4\,\rm M_\odot$)
1	9 40 13.6	71 11 29.3	130	1	491	6	123	0.8	1.8	-0.6	40	1.6	1.6
2	9 40 22.1	71 12 03.5	146	2	195	16	13	0.9	1.6	-0.3	6	1.3	0.7
3	9 40 28.6	71 12 07.7	138	3	363	12	45	1.0	1.4	-0.3	15	1.9	1.5
4	9 40 30.0	71 11 03.2	135	1	744	6	4	1.0	0.2	-0.4	61	2.4	2.8
5	9 40 33.6	71 12 49.5	153	3	418	12	45	0.6	2.1	-0.6	17	1.9	1.4
6	9 40 59.1	71 12 36.3	138	1	668	6	45	0.8	3.1	-1.4	54	1.1	1.1

Table 2.10. NGC 2976 hole properties

No	α (h m s)	δ ($^\circ$ $'$ $''$)	$V_{\rm hel}$ (km s^{-1})	*Type* (1 − 3)	d (pc)	$V_{\rm exp}$ (km s^{-1})	*P.A.* ($^\circ$)	*Axial Ratio*	R (kpc)	$log(n_{\rm HI})$ (cm^{-3})	$t_{\rm kin}$ (Myr)	$log(E_{\rm E})$ (10^{50} erg)	$log(M_{\rm HI})$ (10^4 M$_\odot$)
1	9 47 06.0	67 54 13.5	-7	1	158	9	0	0.6	2.7	-1.0	9	-0.2	-0.3
2	9 47 07.8	67 56 55.5	59	1	140	9	104	0.5	2.2	-0.7	8	0.0	-0.2
3	9 47 11.0	67 55 58.5	59	1	169	12	44	0.7	1.1	0.1	7	1.4	1.3
4	9 47 11.6	67 54 15.0	-17	2	179	15	62	0.8	1.6	-0.4	6	1.0	0.5
5	9 47 13.7	67 54 48.0	-2	2	155	15	0	1.0	0.5	0.2	5	1.5	1.2
6	9 47 13.7	67 55 46.5	28	1	187	9	155	0.7	0.9	0.1	10	1.3	1.4
7	9 47 14.5	67 55 55.5	39	3	127	23	150	0.7	1.2	0.0	3	1.3	0.4
8	9 47 14.8	67 54 57.0	-2	1	158	9	78	0.4	0.1	0.4	9	1.4	1.2
9	9 47 19.6	67 53 42.0	-63	2	134	15	135	0.6	1.5	0.1	4	1.1	0.6
10	9 47 21.4	67 54 24.0	-33	3	164	15	17	0.9	1.0	0.2	5	1.6	1.5
11	9 47 23.8	67 53 03.0	-63	1	239	9	81	0.8	2.2	-0.9	13	0.5	0.3
12	9 47 27.5	67 54 43.5	-33	1	190	9	0	1.0	2.4	-0.7	10	0.5	0.3
13	9 47 28.9	67 55 18.0	-7	1	206	9	93	0.8	3.1	-1.2	11	0.0	-0.1

Table 2.11. NGC 3031 hole properties

No	α (h m s)	δ ($^\circ$ $'$ $''$)	$V_{\rm hel}$ (km s^{-1})	*Type* (1 – 3)	d (pc)	$V_{\rm exp}$ (km s^{-1})	*P.A.* ($^\circ$)	*Axial Ratio*	R (kpc)	$log(n_{\rm HI})$ (cm^{-3})	$t_{\rm kin}$ (Myr)	$log(E_{\rm E})$ (10^{50} erg)	$log(M_{\rm HI})$ (10^4 M$_\odot$)
1	9 53 56.2	69 12 36.5	119	2	131	12	79	0.5	14.2	-0.7	5	0.1	-0.3
2	9 53 58.8	69 13 44.0	132	2	140	8	26	0.8	14.3	-0.7	9	0.0	-0.1
3	9 53 59.4	69 13 26.0	119	1	155	8	35	0.5	14.1	-0.8	10	0.0	-0.1
4	9 54 00.8	69 13 50.0	127	1	86	8	164	0.7	14.2	-0.7	5	-0.7	-0.8
5	9 54 02.7	69 13 08.0	114	1	179	8	16	0.6	13.7	-0.9	11	0.1	0.0
6	9 54 04.5	69 13 12.4	122	1	140	8	170	0.8	13.5	-0.8	9	-0.2	-0.3
7	9 54 05.1	69 14 04.9	135	1	147	8	98	0.7	13.9	-0.7	9	0.1	-0.1
8	9 54 11.3	69 13 46.8	132	2	108	8	86	0.7	13.3	-0.7	7	-0.4	-0.5
9	9 54 24.8	69 13 28.4	132	1	193	8	0	0.5	12.0	-0.7	12	0.4	0.2
10	9 54 28.7	69 13 58.4	143	3	140	8	174	0.8	12.2	-0.7	9	0.0	-0.1
11	9 54 33.9	69 14 08.7	135	3	91	8	175	0.3	12.2	-0.6	6	-0.5	-0.6
12	9 54 34.6	69 05 35.6	78	1	131	8	70	0.5	8.7	-0.4	8	0.2	0.1
13	9 54 35.0	69 14 25.1	132	3	86	10	46	0.7	12.4	-0.3	4	-0.1	-0.4
14	9 54 35.2	69 05 28.1	76	1	143	8	132	0.5	8.6	-0.2	9	0.5	0.3
15	9 54 36.3	69 05 16.1	65	3	100	13	26	0.8	8.6	-0.2	4	0.4	-0.1
16	9 54 36.5	69 07 34.1	117	2	129	8	87	0.4	8.0	-0.2	8	0.4	0.2
17	9 54 36.5	69 04 07.1	45	1	226	8	141	0.7	9.3	-0.4	14	1.0	0.8
18	9 54 37.1	69 07 17.5	114	1	262	8	45	0.8	7.9	-0.3	16	1.3	1.1
19	9 54 39.6	69 08 35.4	143	3	129	8	16	0.7	7.8	-0.2	8	0.4	0.2
20	9 54 40.4	69 03 15.9	21	3	102	8	42	0.6	9.2	-0.2	6	0.1	-0.1
21	9 54 41.3	69 04 10.0	40	3	122	8	135	0.8	8.5	0.0	7	0.5	0.3
22	9 54 42.2	69 04 23.4	40	3	136	14	54	0.6	8.1	0.0	5	1.1	0.5
23	9 54 42.7	69 04 24.9	40	1	118	8	57	0.6	8.1	0.0	7	0.5	0.3
24	9 54 43.6	69 09 08.4	153	2	124	8	33	0.6	7.6	-0.3	8	0.3	0.1
25	9 54 43.7	69 05 38.4	81	2	118	11	121	0.8	7.2	-0.2	5	0.5	0.2
26	9 54 43.9	69 13 39.9	135	2	154	8	25	0.6	11.4	-0.6	9	0.2	0.1
27	9 54 44.8	69 06 17.3	107	2	96	13	0	0.8	6.9	-0.1	4	0.4	0.0

Table 2.11 (cont'd)

No	α (h m s)	δ ($^\circ$ $'$ $''$)	$V_{\rm hel}$ (km s^{-1})	*Type* (1 − 3)	d (pc)	$V_{\rm exp}$ (km s^{-1})	*P.A.* ($^\circ$)	*Axial Ratio*	R (kpc)	$log(n_{\rm HI})$ (cm^{-3})	$t_{\rm kin}$ (Myr)	$log(E_{\rm E})$ (10^{50} erg)	$log(M_{\rm HI})$ (10^4 M$_\odot$)
28	9 54 45.4	69 13 56.3	135	2	111	11	133	0.6	11.7	-0.4	5	0.2	-0.2
29	9 54 46.6	69 03 42.8	9	2	96	10	165	0.8	7.8	0.0	5	0.4	0.1
30	9 54 46.6	69 03 51.8	9	2	132	12	0	0.9	7.7	0.0	5	1.0	0.5
31	9 54 47.1	69 06 23.3	107	3	143	8	12	0.5	6.5	0.1	9	0.8	0.6
32	9 54 47.3	69 02 08.2	-14	3	104	8	125	0.7	9.1	-0.2	6	0.2	0.0
33	9 54 47.9	69 03 02.2	1	1	274	8	0	0.5	8.2	0.0	17	1.6	1.4
34	9 54 48.7	69 01 42.7	-19	3	104	8	178	0.7	9.3	-0.3	6	0.0	-0.1
35	9 54 48.8	69 07 11.2	135	2	111	8	54	0.6	6.3	0.0	7	0.4	0.3
36	9 54 49.2	69 00 15.7	-39	1	157	8	56	0.3	10.8	-0.6	10	0.2	0.1
37	9 54 49.3	69 06 20.2	91	2	106	11	0	1.0	6.2	0.1	5	0.7	0.3
38	9 54 49.4	69 13 45.7	130	2	114	8	171	0.9	11.5	-0.5	7	-0.1	-0.2
39	9 54 49.6	69 05 21.7	65	2	106	10	10	0.6	6.4	0.0	5	0.5	0.2
40	9 54 49.7	69 04 48.7	32	1	172	8	57	0.7	6.6	-0.1	11	0.9	0.7
41	9 54 49.8	69 09 33.7	163	1	124	8	77	0.5	7.3	-0.3	8	0.3	0.1
42	9 54 50.1	69 09 17.1	171	2	147	10	61	0.7	7.1	-0.2	7	0.7	0.4
43	9 54 50.7	69 13 21.6	135	2	86	10	176	0.7	11.0	-0.6	4	-0.5	-0.7
44	9 54 51.6	69 03 54.6	6	2	117	8	135	0.7	6.9	-0.2	7	0.3	0.1
45	9 54 52.0	69 01 26.1	-37	2	117	13	100	0.7	9.0	-0.1	4	0.7	0.2
46	9 54 52.3	69 01 11.0	-45	3	93	8	113	0.6	9.3	-0.1	6	0.0	-0.1
47	9 54 53.4	69 00 59.0	-47	2	106	10	166	0.4	9.3	-0.2	5	0.3	0.0
48	9 54 53.7	69 08 33.5	163	1	334	8	0	0.9	6.3	-0.1	20	1.8	1.8
49	9 54 54.8	69 00 59.0	-50	2	109	13	137	0.5	9.1	-0.1	4	0.5	0.1
50	9 54 55.6	69 01 27.4	-47	2	155	10	132	0.5	8.4	-0.1	8	0.9	0.6
51	9 54 56.4	69 09 48.4	166	1	309	8	133	0.6	7.1	-0.3	19	1.5	1.7
52	9 54 56.4	69 00 09.4	-63	2	86	8	120	0.7	9.8	-0.1	5	-0.1	-0.2
53	9 54 56.4	69 08 28.9	163	1	193	8	39	0.5	6.0	0.0	12	1.1	0.9
54	9 54 56.5	69 01 54.4	-42	3	106	10	100	0.4	7.8	0.0	5	0.5	0.2

Table 2.11 (cont'd)

No	α (h m s)	δ ($^\circ$ $'$ $''$)	$V_{\rm hel}$ (km s^{-1})	*Type* (1 − 3)	d (pc)	$V_{\rm exp}$ (km s^{-1})	*P.A.* ($^\circ$)	*Axial Ratio*	R (kpc)	$log(n_{\rm HI})$ (cm^{-3})	$t_{\rm kin}$ (Myr)	$log(E_{\rm E})$ (10^{50} erg)	$log(M_{\rm HI})$ (10^4 M$_\odot$)
55	9 54 56.7	69 00 55.9	-63	3	123	10	0	1.0	8.8	-0.1	6	0.7	0.3
56	9 54 56.8	69 13 21.4	135	3	86	9	42	0.7	11.0	-0.4	5	-0.3	-0.5
57	9 54 57.1	69 01 37.9	-55	3	99	8	54	0.6	8.0	-0.1	6	0.2	0.1
58	9 54 57.1	69 08 58.9	168	1	106	8	0	1.0	6.4	0.0	6	0.4	0.2
59	9 54 57.4	69 13 15.4	130	2	108	15	80	0.7	10.9	-0.3	4	0.5	-0.1
60	9 54 57.6	69 02 00.3	-55	2	93	15	133	0.6	7.6	-0.2	3	0.4	-0.2
61	9 54 57.7	68 59 54.3	-75	3	92	8	0	0.9	9.9	-0.1	6	0.1	-0.1
62	9 54 57.8	69 14 18.4	127	1	136	8	145	0.6	12.2	-0.4	8	0.2	0.1
63	9 54 58.2	69 01 51.3	-65	1	136	8	40	0.9	7.6	-0.1	8	0.5	0.4
64	9 54 58.4	69 01 18.3	-63	2	114	18	0	0.9	8.2	-0.1	3	0.9	0.2
65	9 54 58.4	69 01 24.3	-73	1	93	8	132	0.6	8.1	-0.1	6	0.1	-0.1
66	9 54 58.6	69 13 01.8	132	3	104	8	58	0.7	10.7	-0.3	6	0.0	-0.1
67	9 54 58.8	68 59 21.3	-81	3	104	10	89	0.7	10.4	-0.3	5	0.2	-0.1
68	9 54 58.8	69 13 19.8	125	3	95	8	146	0.7	11.1	-0.4	6	-0.2	-0.3
69	9 54 59.5	69 01 24.3	-60	2	140	18	61	0.8	7.9	-0.2	4	1.0	0.4
70	9 54 59.7	69 00 13.8	-83	2	96	8	0	0.8	9.2	-0.1	6	0.1	0.0
71	9 55 00.2	68 59 27.2	-83	2	112	10	101	0.5	10.1	-0.2	5	0.3	0.1
72	9 55 00.8	68 59 16.7	-91	2	104	10	150	0.7	10.2	-0.2	5	0.3	0.0
73	9 55 00.8	69 13 13.7	130	3	126	15	152	0.7	10.9	-0.3	4	0.7	0.1
74	9 55 01.2	69 01 03.2	-78	1	136	8	76	0.6	8.1	-0.2	8	0.5	0.3
75	9 55 01.4	69 07 07.7	145	1	127	8	68	0.6	4.8	-0.1	8	0.5	0.4
76	9 55 01.4	68 59 46.7	-91	1	140	8	162	0.8	9.5	-0.1	9	0.6	0.4
77	9 55 01.7	68 59 37.7	-88	1	157	8	90	0.8	9.7	-0.2	10	0.7	0.6
78	9 55 01.8	69 00 45.2	-78	2	111	10	76	0.6	8.3	-0.3	5	0.3	0.0
79	9 55 02.0	69 13 12.2	122	2	136	10	124	0.6	10.9	-0.3	7	0.5	0.2
80	9 55 02.3	69 10 48.2	153	2	160	13	0	0.7	8.0	-0.2	6	1.0	0.5
81	9 55 02.7	69 08 39.2	163	3	118	8	44	0.5	5.8	0.0	7	0.5	0.4

Table 2.11 (cont'd)

No	α (h m s)	δ ($^\circ$ $'$ $''$)	$V_{\rm hel}$ ($\rm km\,s^{-1}$)	*Type* (1 − 3)	d (pc)	$V_{\rm exp}$ ($\rm km\,s^{-1}$)	*P.A.* (°)	*Axial Ratio*	R (kpc)	$log(n_{\rm HI})$ ($\rm cm^{-3}$)	$t_{\rm kin}$ (Myr)	$log(E_{\rm E})$ (10^{50} erg)	$log(M_{\rm HI})$ ($10^4\,\rm M_\odot$)
82	9 55 03.1	68 58 10.6	-96	1	123	8	90	0.9	11.2	-0.6	8	-0.1	-0.2
83	9 55 03.4	69 13 13.6	119	2	91	8	98	0.8	11.0	-0.4	6	-0.3	-0.4
84	9 55 03.9	69 00 01.6	-88	3	86	8	120	0.7	8.8	-0.2	5	-0.1	-0.2
85	9 55 04.2	69 00 22.6	-93	1	104	8	68	0.7	8.4	-0.2	6	0.1	-0.1
86	9 55 04.5	69 13 25.6	114	2	120	8	23	0.6	11.3	-0.6	7	-0.2	-0.3
87	9 55 05.4	69 07 22.6	158	1	133	8	20	0.6	4.6	0.0	8	0.6	0.5
88	9 55 05.4	68 58 37.5	-111	2	101	12	0	0.9	10.4	-0.2	4	0.3	-0.1
89	9 55 05.5	68 59 43.5	-93	2	149	13	79	0.9	9.0	-0.2	6	0.9	0.4
90	9 55 05.9	69 13 21.0	114	1	218	8	120	0.5	11.2	-0.5	13	0.8	0.6
91	9 55 06.7	69 09 09.0	166	2	138	8	83	0.7	6.1	-0.1	8	0.6	0.4
92	9 55 06.9	68 59 30.0	-104	2	106	13	128	0.6	9.1	-0.3	4	0.4	-0.1
93	9 55 07.4	68 58 31.5	-106	3	149	8	45	0.9	10.2	-0.2	9	0.6	0.4
94	9 55 07.4	68 58 39.0	-109	3	132	9	61	0.9	10.1	-0.2	7	0.5	0.2
95	9 55 07.5	69 11 36.0	148	2	124	8	28	0.6	9.0	-0.3	8	0.2	0.1
96	9 55 08.1	69 09 46.4	158	1	175	8	144	0.8	6.8	-0.3	11	0.8	0.6
97	9 55 08.2	68 57 56.9	-101	3	114	12	1	0.9	10.9	-0.3	5	0.4	0.0
98	9 55 08.3	68 59 53.9	-119	1	93	8	93	0.6	8.4	-0.3	6	-0.2	-0.3
99	9 55 08.8	68 58 38.8	-104	3	93	10	168	0.6	9.9	-0.3	5	0.0	-0.2
100	9 55 08.9	68 59 35.8	-114	2	131	8	120	0.6	8.7	-0.4	8	0.2	0.1
101	9 55 09.0	69 13 35.9	114	1	147	8	120	0.7	11.7	-0.5	9	0.3	0.2
102	9 55 09.6	68 58 07.3	-114	3	100	17	156	0.8	10.5	-0.2	3	0.5	-0.1
103	9 55 09.8	69 10 05.8	158	3	104	10	38	0.7	7.2	-0.2	5	0.3	0.0
104	9 55 09.9	69 10 58.4	148	1	302	8	27	0.7	8.3	-0.4	18	1.3	1.2
105	9 55 10.1	69 09 29.8	161	1	143	8	68	0.5	6.5	-0.4	9	0.4	0.2
106	9 55 10.2	68 58 19.4	-114	3	110	12	149	0.9	10.1	-0.2	4	0.4	0.0
107	9 55 10.3	69 12 35.9	117	1	122	8	1	0.8	10.4	-0.3	7	0.2	0.0
108	9 55 10.4	69 12 52.4	122	2	108	10	39	0.7	10.8	-0.2	5	0.3	0.0

Table 2.11 (cont'd)

No	α (h m s)	δ ($^\circ$ $'$ $''$)	$V_{\rm hel}$ (km s^{-1})	*Type* (1 − 3)	d (pc)	$V_{\rm exp}$ (km s^{-1})	*P.A.* ($^\circ$)	*Axial Ratio*	R (kpc)	$log(n_{\rm HI})$ (cm^{-3})	$t_{\rm kin}$ (Myr)	$log(E_{\rm E})$ (10^{50} erg)	$log(M_{\rm HI})$ (10^4 M$_\odot$)
109	9 55 10.5	68 58 28.2	-114	2	104	16	25	0.7	9.9	-0.2	3	0.5	-0.1
110	9 55 10.5	68 58 59.7	-119	2	109	8	83	0.8	9.2	-0.2	7	0.2	0.1
111	9 55 11.0	68 55 31.2	-111	2	135	8	36	0.3	13.7	-0.8	8	-0.2	-0.3
112	9 55 11.4	69 08 53.8	158	2	175	10	61	0.8	5.8	0.1	9	1.3	1.0
113	9 55 11.5	68 58 13.2	-109	2	92	18	129	0.9	10.1	-0.2	3	0.5	-0.2
114	9 55 11.8	68 57 44.7	-124	2	113	13	132	0.7	10.7	-0.3	4	0.4	0.0
115	9 55 12.1	69 09 47.8	158	1	127	8	69	0.8	6.9	-0.2	8	0.4	0.2
116	9 55 12.1	68 55 23.7	-114	1	100	8	90	0.5	13.8	-0.7	6	-0.6	-0.6
117	9 55 13.2	69 13 02.7	117	2	145	13	151	0.6	11.1	-0.2	5	0.9	0.4
118	9 55 13.6	69 07 58.1	166	1	122	8	94	0.8	4.7	0.0	7	0.6	0.4
119	9 55 16.0	69 12 32.5	104	3	118	11	137	0.6	10.6	-0.1	5	0.6	0.2
120	9 55 16.5	69 12 22.0	107	3	93	8	48	0.6	10.4	-0.4	6	-0.3	-0.4
121	9 55 16.7	68 56 52.0	-135	3	100	10	68	0.8	11.3	-0.4	5	0.0	-0.2
122	9 55 17.2	69 10 04.0	148	2	154	8	44	0.6	7.4	-0.1	9	0.7	0.6
123	9 55 17.2	69 07 53.5	145	2	108	11	21	0.7	4.7	0.0	5	0.6	0.2
124	9 55 17.2	69 13 04.0	112	2	127	11	107	0.8	11.4	-0.2	6	0.6	0.3
125	9 55 17.6	69 08 44.5	156	2	160	8	80	0.7	5.7	0.2	10	1.1	0.9
126	9 55 18.0	69 07 28.0	161	1	129	8	90	0.7	4.2	-0.1	8	0.5	0.4
127	9 55 21.2	68 57 32.3	-145	1	127	8	67	0.8	9.9	-0.3	8	0.2	0.1
128	9 55 21.4	69 07 14.3	150	1	167	8	111	0.9	3.9	-0.1	10	0.9	1.1
129	9 55 21.5	68 57 53.3	-142	1	152	8	12	0.5	9.4	-0.4	9	0.4	0.2
130	9 55 21.9	69 01 51.8	-104	2	112	8	52	0.5	4.1	0.0	7	0.5	0.3
131	9 55 22.3	68 54 33.7	-127	1	109	8	127	0.8	13.8	-0.9	7	-0.6	-0.6
132	9 55 22.4	68 55 36.7	-127	1	193	8	51	0.5	12.3	-0.8	12	0.3	0.2
133	9 55 22.5	68 56 18.7	-153	3	111	9	73	0.6	11.5	-0.3	6	0.2	0.0
134	9 55 23.9	69 07 33.6	132	1	132	8	157	0.9	4.4	-0.1	8	0.6	0.4
135	9 55 24.9	69 11 54.6	88	1	111	8	52	0.6	10.3	-0.3	7	0.2	0.0

Table 2.11 (cont'd)

No	α (h m s)	δ ($^\circ$ $'$ $''$)	$V_{\rm hel}$ (km s^{-1})	*Type* (1 − 3)	d (pc)	$V_{\rm exp}$ (km s^{-1})	*P.A.* ($^\circ$)	*Axial Ratio*	R (kpc)	$log(n_{\rm HI})$ (cm^{-3})	$t_{\rm kin}$ (Myr)	$log(E_{\rm E})$ (10^{50} erg)	$log(M_{\rm HI})$ (10^4 M$_\odot$)
136	9 55 25.7	69 13 42.6	96	2	114	10	0	1.0	12.8	-0.7	6	-0.2	-0.5
137	9 55 26.1	69 11 42.6	88	1	118	8	57	0.6	10.1	-0.3	7	0.1	0.0
138	9 55 26.2	69 08 08.0	130	3	104	8	16	0.7	5.3	0.2	6	0.6	0.4
139	9 55 27.6	68 57 11.0	-163	1	201	8	73	0.8	9.7	-0.5	12	0.6	0.5
140	9 55 28.2	69 12 56.0	86	1	136	8	108	0.6	11.9	-0.5	8	0.2	0.1
141	9 55 28.3	68 55 57.5	-163	1	154	8	65	0.4	11.3	-0.6	9	0.2	0.1
142	9 55 28.5	69 11 29.0	88	1	93	8	100	0.6	10.0	-0.4	6	-0.3	-0.4
143	9 55 28.7	69 07 26.0	107	3	121	8	148	0.5	4.5	0.0	7	0.6	0.4
144	9 55 28.7	69 07 51.5	104	3	118	8	119	0.6	5.1	0.1	7	0.7	0.5
145	9 55 28.8	69 11 03.5	91	2	103	13	26	0.5	9.4	-0.5	4	0.1	-0.4
146	9 55 32.3	69 12 10.8	83	3	111	8	150	0.6	11.3	-0.3	7	0.1	-0.1
147	9 55 32.9	69 07 25.7	96	2	96	10	50	0.5	4.8	0.1	5	0.5	0.2
148	9 55 33.0	69 11 00.2	83	1	193	8	143	0.5	9.7	-0.5	12	0.6	0.5
149	9 55 33.2	69 10 31.7	96	1	137	8	111	0.5	9.1	-0.5	8	0.2	0.1
150	9 55 33.4	68 56 49.7	-181	1	179	8	107	0.6	9.6	-0.5	11	0.5	0.3
151	9 55 34.1	68 55 33.1	-176	1	109	8	12	0.8	11.3	-0.6	7	-0.3	-0.4
152	9 55 34.4	69 08 06.1	104	1	155	8	11	0.5	5.8	-0.2	10	0.6	0.5
153	9 55 35.0	68 56 19.6	-173	3	124	10	90	0.4	10.2	-0.7	6	0.0	-0.3
154	9 55 36.4	68 55 24.0	-178	1	123	8	0	1.0	11.3	-0.4	8	0.1	0.0
155	9 55 36.5	69 00 04.3	-189	1	133	8	1	0.6	4.9	-0.1	8	0.6	0.4
156	9 55 36.8	69 12 06.0	73	1	131	8	169	0.5	11.5	-0.4	8	0.2	0.0
157	9 55 36.8	69 12 16.5	73	1	124	8	179	0.6	11.8	-0.5	8	0.0	-0.1
158	9 55 37.5	68 56 11.9	-184	1	124	8	62	0.5	10.2	-0.6	8	-0.1	-0.2
159	9 55 37.5	69 11 18.0	78	3	183	14	2	0.8	10.5	-0.1	6	1.3	0.8
160	9 55 38.3	69 10 60.0	76	3	149	15	45	0.9	10.2	-0.1	5	1.1	0.5
161	9 55 39.5	68 56 02.8	-189	2	161	8	21	0.6	10.2	-0.5	10	0.4	0.2
162	9 55 41.2	68 56 02.8	-191	2	140	8	124	0.8	10.1	-0.6	9	0.1	0.0

Table 2.11 (cont'd)

No	α (h m s)	δ ($^\circ$ $'$ $''$)	$V_{\rm hel}$ (km s^{-1})	*Type* (1 − 3)	d (pc)	$V_{\rm exp}$ (km s^{-1})	*P.A.* ($^\circ$)	*Axial Ratio*	R (kpc)	$log(n_{\rm HI})$ (cm^{-3})	$t_{\rm kin}$ (Myr)	$log(E_{\rm E})$ (10^{50} erg)	$log(M_{\rm HI})$ (10^4 M$_\odot$)
163	9 55 41.4	69 12 20.8	73	1	108	8	39	0.7	12.3	-0.7	7	-0.4	-0.5
164	9 55 41.7	68 56 37.2	-194	2	92	8	53	0.9	9.3	-0.7	6	-0.6	-0.7
165	9 55 42.5	68 55 41.7	-186	2	179	12	129	0.8	10.5	-0.6	7	0.7	0.3
166	9 55 43.4	68 54 34.1	-163	1	140	8	21	0.8	11.9	-0.7	9	-0.1	-0.2
167	9 55 44.6	68 58 14.1	-212	1	92	8	86	0.9	6.9	-0.4	6	-0.2	-0.4
168	9 55 45.6	68 56 19.0	-202	2	149	8	21	0.5	9.4	-0.7	9	0.1	0.0
169	9 55 46.7	68 58 32.3	-222	1	110	8	89	0.9	6.4	-0.2	7	0.2	0.1
170	9 55 46.7	69 09 58.0	52	3	129	12	22	0.7	9.6	-0.1	5	0.8	0.3
171	9 55 47.8	68 56 42.9	-207	1	236	8	66	0.8	8.8	-0.7	14	0.6	0.5
172	9 55 48.1	69 12 11.4	63	1	96	8	130	0.8	12.8	-0.7	6	-0.6	-0.6
173	9 55 48.1	68 56 24.9	-214	1	308	8	2	0.9	9.2	-0.7	19	1.0	0.9
174	9 55 48.2	69 00 16.7	-230	1	92	8	34	0.9	4.2	-0.1	6	0.1	0.0
175	9 55 48.5	69 10 54.9	55	3	110	8	103	0.9	11.2	-0.2	7	0.2	0.0
176	9 55 49.6	69 05 56.3	14	1	109	8	139	0.5	4.8	0.0	7	0.4	0.2
177	9 55 51.2	69 07 17.2	45	1	224	8	44	0.5	6.7	-0.3	14	1.0	0.8
178	9 55 51.3	68 58 53.9	-243	1	127	8	154	0.8	5.9	-0.1	8	0.5	0.3
179	9 55 51.8	68 58 08.1	-232	1	97	8	0	1.0	6.8	-0.3	6	-0.1	-0.2
180	9 55 51.9	69 11 12.7	47	1	129	8	66	0.7	11.9	-0.5	8	0.1	0.0
181	9 55 52.5	68 58 41.8	-235	1	185	8	3	0.9	6.1	-0.1	11	1.0	0.8
182	9 55 52.8	69 06 56.1	37	1	128	8	76	0.9	6.5	-0.3	8	0.3	0.1
183	9 55 55.9	69 09 49.9	27	3	137	11	25	0.5	10.6	-0.2	6	0.7	0.4
184	9 55 56.4	69 11 04.9	42	1	127	8	41	0.6	12.3	-0.6	8	0.0	-0.2
185	9 55 56.5	69 09 36.4	27	3	118	8	109	0.8	10.4	-0.2	7	0.3	0.1
186	9 55 57.3	69 09 43.9	21	3	107	8	0	1.0	10.6	-0.2	7	0.1	0.0
187	9 55 57.8	69 00 21.3	-238	1	392	8	79	0.5	4.4	-0.3	24	1.9	1.7
188	9 55 58.4	69 11 18.3	52	3	104	11	61	0.7	12.8	-0.7	5	-0.3	-0.5
189	9 55 58.7	69 00 43.8	-240	1	143	8	122	0.5	4.2	-0.2	9	0.6	0.9

Table 2.11 (cont'd)

No	α (h m s)	δ ($^\circ$ $'$ $''$)	$V_{\rm hel}$ ($\rm km\,s^{-1}$)	*Type* (1 − 3)	d (pc)	$V_{\rm exp}$ ($\rm km\,s^{-1}$)	*P.A.* ($^\circ$)	*Axial Ratio*	R (kpc)	$log(n_{\rm HI})$ ($\rm cm^{-3}$)	$t_{\rm kin}$ (Myr)	$log(E_{\rm E})$ (10^{50} erg)	$log(M_{\rm HI})$ ($10^4\,\rm M_\odot$)
190	9 55 59.7	69 04 10.7	-65	3	124	8	116	0.6	4.6	0.1	8	0.7	0.5
191	9 55 59.8	69 09 07.7	19	3	109	8	169	0.5	10.1	-0.1	7	0.3	0.1
192	9 56 03.2	68 59 15.3	-240	2	158	12	0	1.0	5.7	0.0	6	1.1	0.7
193	9 56 03.4	69 06 59.9	-16	1	154	8	65	0.6	8.1	-0.3	9	0.6	0.4
194	9 56 03.4	68 58 22.3	-248	1	147	8	88	0.7	6.5	-0.3	9	0.4	0.3
195	9 56 03.8	68 55 05.9	-220	2	104	8	125	0.7	10.3	-0.6	6	-0.3	-0.4
196	9 56 03.8	69 10 02.9	32	2	104	11	107	0.7	11.9	-0.5	5	0.0	-0.3
197	9 56 03.9	69 02 46.4	-148	1	123	8	0	1.0	4.5	-0.1	8	0.5	0.3
198	9 56 04.0	68 58 35.9	-245	1	363	8	147	0.7	6.3	-0.1	22	1.9	1.9
199	9 56 04.7	69 08 14.9	1	3	100	8	89	0.8	9.8	0.0	6	0.3	0.1
200	9 56 04.8	69 08 49.4	21	2	162	8	130	0.5	10.5	-0.2	10	0.7	0.5
201	9 56 05.1	69 10 43.4	42	3	122	8	45	0.8	12.9	-0.6	7	-0.1	-0.2
202	9 56 05.5	68 59 19.3	-240	1	193	8	89	0.8	5.8	-0.1	12	1.1	0.9
203	9 56 05.5	69 09 46.3	24	1	93	8	78	0.6	11.8	-0.5	6	-0.3	-0.4
204	9 56 06.2	68 59 25.2	-240	2	106	8	0	1.0	5.7	0.0	6	0.4	0.2
205	9 56 07.0	69 08 46.3	11	2	95	8	63	0.7	10.7	-0.3	6	-0.1	-0.2
206	9 56 07.9	69 08 58.2	21	2	106	12	171	0.6	11.1	-0.3	4	0.3	-0.1
207	9 56 08.2	69 02 46.1	-140	1	126	8	53	0.7	5.2	0.0	8	0.6	0.4
208	9 56 08.7	68 59 55.1	-232	1	168	8	84	0.5	5.6	0.0	10	1.0	0.8
209	9 56 08.8	68 52 25.1	-194	3	124	8	169	0.5	13.6	-0.9	8	-0.4	-0.5
210	9 56 08.9	69 07 28.1	-21	3	86	8	158	0.7	9.4	-0.2	5	-0.1	-0.2
211	9 56 08.9	69 08 10.1	-6	2	161	8	177	0.6	10.3	-0.1	10	0.8	0.6
212	9 56 09.0	69 06 08.6	-21	3	145	13	101	0.8	8.0	0.0	5	1.0	0.6
213	9 56 09.4	69 05 53.6	-32	3	143	8	106	0.5	7.8	0.0	9	0.8	0.6
214	9 56 09.8	69 09 47.6	19	1	122	8	115	0.8	12.4	-0.6	7	-0.1	-0.2
215	9 56 10.2	69 00 26.6	-220	1	123	8	0	1.0	5.5	0.0	8	0.6	0.4
216	9 56 10.3	69 07 29.6	-19	2	142	10	37	0.4	9.7	-0.2	7	0.7	0.4

Table 2.11 (cont'd)

No	α (h m s)	δ ($^\circ$ $'$ $''$)	$V_{\rm hel}$ (km s^{-1})	*Type* (1 − 3)	d (pc)	$V_{\rm exp}$ (km s^{-1})	*P.A.* ($^\circ$)	*Axial Ratio*	R (kpc)	$log(n_{\rm HI})$ (cm^{-3})	$t_{\rm kin}$ (Myr)	$log(E_{\rm E})$ (10^{50} erg)	$log(M_{\rm HI})$ (10^4 M$_\odot$)
217	9 56 10.4	68 54 24.9	-204	3	160	15	150	0.4	11.1	-0.5	5	0.7	0.2
218	9 56 10.7	68 56 33.9	-235	2	142	8	52	0.7	8.6	-0.4	9	0.4	0.2
219	9 56 10.8	69 01 47.4	-166	1	109	8	170	0.5	5.3	-0.2	7	0.2	0.0
220	9 56 11.1	68 59 25.0	-238	3	96	8	39	0.8	6.1	0.1	6	0.4	0.2
221	9 56 11.2	69 06 18.9	-29	3	123	13	0	1.0	8.5	0.1	5	0.9	0.5
222	9 56 11.2	69 08 39.9	16	1	143	8	156	0.5	11.2	-0.4	9	0.3	0.2
223	9 56 11.3	69 02 56.4	-122	2	104	8	42	0.7	5.8	-0.2	6	0.2	0.0
224	9 56 11.3	69 00 45.9	-204	1	165	8	2	0.7	5.5	-0.2	10	0.8	0.6
225	9 56 11.3	68 59 34.0	-235	3	88	8	0	1.0	6.0	0.1	5	0.2	0.0
226	9 56 11.8	69 00 25.0	-217	2	96	10	61	0.8	5.7	0.2	5	0.6	0.2
227	9 56 11.8	68 58 51.9	-253	1	261	8	105	0.5	6.5	-0.2	16	1.3	1.6
228	9 56 12.2	69 00 02.4	-225	2	106	8	0	1.0	5.9	0.0	6	0.4	0.2
229	9 56 12.3	69 04 29.4	-63	1	118	8	35	0.6	7.0	-0.3	7	0.2	0.1
230	9 56 12.7	68 59 44.4	-230	2	147	8	50	0.7	6.1	-0.1	9	0.7	0.5
231	9 56 12.8	69 01 51.9	-160	1	102	8	31	0.6	5.7	-0.2	6	0.1	0.0
232	9 56 13.0	69 03 21.8	-104	1	236	8	54	0.6	6.3	-0.1	14	1.4	1.6
233	9 56 13.0	69 01 00.8	-194	1	226	8	48	0.7	5.7	-0.2	14	1.2	1.4
234	9 56 13.4	69 00 17.2	-222	2	165	10	121	0.7	5.9	0.0	8	1.2	0.8
235	9 56 13.5	69 05 08.3	-75	3	109	16	69	0.8	7.7	0.1	3	1.0	0.4
236	9 56 13.8	69 00 39.7	-207	2	122	11	44	0.8	5.8	0.0	5	0.8	0.4
237	9 56 13.9	69 07 24.8	-24	3	111	8	100	0.6	10.1	-0.3	7	0.1	-0.1
238	9 56 14.0	69 06 03.8	-55	3	149	15	5	0.9	8.7	0.1	5	1.4	0.8
239	9 56 14.1	68 59 49.9	-232	1	136	8	142	0.6	6.2	-0.1	8	0.6	0.4
240	9 56 14.1	69 05 23.3	-63	3	114	10	7	0.9	8.1	0.2	6	0.8	0.5
241	9 56 14.2	69 05 33.8	-57	3	114	8	38	0.9	8.2	0.2	7	0.7	0.5
242	9 56 14.3	69 08 24.8	9	1	226	8	29	0.7	11.3	-0.5	14	0.9	0.7
243	9 56 14.5	69 05 42.7	-55	3	123	8	28	0.9	8.4	0.2	8	0.8	0.6

Table 2.11 (cont'd)

No	α (h m s)	δ ($^\circ$ $'$ $''$)	$V_{\rm hel}$ (km s^{-1})	*Type* (1 − 3)	d (pc)	$V_{\rm exp}$ (km s^{-1})	*P.A.* ($^\circ$)	*Axial Ratio*	R (kpc)	$log(n_{\rm HI})$ (cm^{-3})	$t_{\rm kin}$ (Myr)	$log(E_{\rm E})$ (10^{50} erg)	$log(M_{\rm HI})$ (10^4 M$_\odot$)
244	9 56 14.6	69 02 15.7	-145	1	368	8	18	0.8	6.0	-0.1	22	2.0	2.0
245	9 56 15.0	69 03 36.7	-96	1	111	8	57	0.6	6.8	-0.1	7	0.3	0.2
246	9 56 15.4	69 05 51.7	-73	2	105	10	122	0.8	8.7	0.1	5	0.6	0.3
247	9 56 15.4	69 06 24.7	-37	2	114	10	160	0.9	9.3	-0.2	6	0.4	0.1
248	9 56 15.5	69 00 45.8	-202	2	175	13	50	0.8	6.0	0.0	7	1.4	0.9
249	9 56 15.7	69 02 39.6	-124	1	190	8	75	0.7	6.4	0.0	12	1.1	0.9
250	9 56 15.7	69 03 02.1	-109	2	104	8	20	0.7	6.6	0.0	6	0.3	0.2
251	9 56 16.1	69 05 09.6	-68	3	117	13	48	0.7	8.1	0.0	4	0.8	0.3
252	9 56 16.2	68 52 05.0	-202	2	86	8	20	0.7	13.8	-0.9	5	-0.9	-1.0
253	9 56 16.9	68 57 12.5	-248	2	146	8	121	0.5	8.2	-0.5	9	0.3	0.1
254	9 56 17.2	69 05 02.1	-68	3	135	8	20	0.7	8.2	-0.1	8	0.6	0.4
255	9 56 17.6	69 03 56.0	-104	3	102	13	41	0.6	7.4	-0.2	4	0.4	0.0
256	9 56 17.6	69 00 26.0	-225	2	96	10	87	0.8	6.4	0.1	5	0.5	0.2
257	9 56 17.7	68 58 39.5	-253	1	126	8	104	0.7	7.1	-0.4	8	0.2	0.0
258	9 56 17.8	69 01 28.8	-176	1	88	8	0	1.0	6.3	0.0	5	0.1	-0.1
259	9 56 17.8	68 54 09.5	-217	2	142	8	123	0.7	11.4	-0.6	9	0.1	0.0
260	9 56 18.2	69 00 18.4	-217	2	106	10	0	1.0	6.5	0.0	5	0.5	0.2
261	9 56 18.3	69 05 21.4	-78	1	92	8	23	0.9	8.7	-0.2	6	0.0	-0.2
262	9 56 18.4	69 05 31.9	-73	3	90	8	24	0.6	8.9	0.0	5	0.2	0.0
263	9 56 18.9	69 01 44.8	-176	2	86	13	55	0.7	6.6	0.0	3	0.4	-0.1
264	9 56 19.1	69 06 12.4	-45	1	104	8	128	0.7	9.7	-0.1	6	0.2	0.0
265	9 56 19.3	69 00 45.4	-209	1	175	8	90	0.8	6.6	0.0	11	1.0	0.8
266	9 56 19.5	69 03 57.5	-104	2	136	15	150	0.6	7.7	0.0	4	1.1	0.5
267	9 56 19.5	68 54 09.3	-220	1	129	8	169	0.7	11.4	-0.7	8	-0.1	-0.2
268	9 56 19.5	69 06 01.9	-60	3	145	8	26	0.8	9.5	0.0	9	0.8	0.6
269	9 56 19.7	69 03 18.4	-130	2	123	18	0	1.0	7.4	0.1	3	1.2	0.5
270	9 56 20.0	69 05 09.4	-81	1	124	8	148	0.5	8.8	-0.2	8	0.4	0.2

Table 2.11 (cont'd)

No	α (h m s)	δ ($^\circ$ $'$ $''$)	$V_{\rm hel}$ (km s^{-1})	*Type* (1 − 3)	d (pc)	$V_{\rm exp}$ (km s^{-1})	*P.A.* ($^\circ$)	*Axial Ratio*	R (kpc)	$log(n_{\rm HI})$ (cm^{-3})	$t_{\rm kin}$ (Myr)	$log(E_{\rm E})$ (10^{50} erg)	$log(M_{\rm HI})$ (10^4 M$_\odot$)
271	9 56 20.0	69 05 18.4	-81	2	129	16	121	0.7	8.9	-0.2	4	0.8	0.3
272	9 56 20.4	69 02 31.8	-155	2	96	15	61	0.8	7.1	0.0	3	0.6	0.1
273	9 56 20.7	69 04 16.9	-106	2	102	8	160	0.6	8.2	-0.2	6	0.1	-0.1
274	9 56 21.0	68 58 19.7	-245	1	361	8	115	0.5	7.6	-0.4	22	1.6	1.7
275	9 56 21.3	69 04 49.7	-96	3	100	8	24	0.8	8.7	0.0	6	0.3	0.2
276	9 56 21.6	69 00 27.2	-212	3	193	8	64	0.8	6.9	-0.2	12	1.0	0.8
277	9 56 21.7	69 03 42.2	-122	2	126	8	79	0.7	7.9	0.0	8	0.6	0.5
278	9 56 21.7	69 00 00.2	-220	1	572	8	78	0.5	7.0	-0.2	35	2.4	2.3
279	9 56 22.0	69 01 43.7	-178	3	140	8	6	0.8	7.0	-0.1	9	0.7	0.5
280	9 56 22.0	69 03 58.7	-114	1	224	8	18	0.6	8.2	-0.1	14	1.3	1.1
281	9 56 22.1	69 02 21.2	-171	2	111	13	29	0.6	7.3	0.0	4	0.7	0.2
282	9 56 23.2	69 02 39.1	-155	1	155	8	83	0.5	7.6	-0.1	10	0.8	0.6
283	9 56 23.4	68 57 55.5	-243	3	131	8	91	0.6	8.1	-0.3	8	0.4	0.2
284	9 56 23.6	69 04 57.1	-91	1	157	8	138	0.8	9.2	-0.2	10	0.7	0.5
285	9 56 24.4	69 02 27.0	-160	2	111	8	112	0.6	7.7	-0.2	7	0.2	0.1
286	9 56 24.4	69 04 57.0	-91	1	206	8	145	0.8	9.4	-0.2	13	1.0	0.9
287	9 56 25.4	68 59 36.0	-227	1	155	8	52	0.5	7.5	-0.3	10	0.5	0.4
288	9 56 25.5	68 54 34.5	-212	2	165	10	93	0.7	11.1	-0.6	8	0.5	0.2
289	9 56 25.5	69 02 48.0	-153	1	111	8	2	0.6	8.0	-0.1	7	0.3	0.2
290	9 56 25.7	69 04 33.0	-101	2	129	15	63	0.7	9.3	-0.1	4	0.9	0.3
291	9 56 25.8	69 06 22.5	-37	3	88	10	13	0.8	10.9	-0.2	4	0.1	-0.2
292	9 56 25.9	68 57 58.4	-238	1	93	8	17	0.6	8.3	-0.4	6	-0.2	-0.3
293	9 56 26.2	69 05 10.4	-83	3	111	8	73	0.6	9.8	-0.3	7	0.1	0.0
294	9 56 26.2	69 02 07.4	-168	2	129	8	44	0.7	7.8	-0.3	8	0.3	0.1
295	9 56 26.7	68 55 46.3	-222	1	204	8	115	0.6	10.0	-0.7	13	0.5	0.4
296	9 56 27.0	69 03 23.9	-135	3	122	8	49	0.8	8.6	-0.1	7	0.4	0.3
297	9 56 27.1	69 03 56.9	-119	3	106	8	90	0.6	9.0	0.1	6	0.5	0.3

Table 2.11 (cont'd)

No	α (h m s)	δ ($^\circ$ $'$ $''$)	$V_{\rm hel}$ (km s^{-1})	*Type* (1 − 3)	d (pc)	$V_{\rm exp}$ (km s^{-1})	*P.A.* (°)	*Axial Ratio*	R (kpc)	$log(n_{\rm HI})$ (cm^{-3})	$t_{\rm kin}$ (Myr)	$log(E_{\rm E})$ (10^{50} erg)	$log(M_{\rm HI})$ (10^4 M$_\odot$)
298	9 56 27.6	68 54 19.3	-212	2	122	8	84	0.8	11.4	-0.5	7	0.0	-0.1
299	9 56 27.9	69 05 08.8	-81	1	122	8	164	0.8	10.1	-0.4	7	0.1	0.0
300	9 56 28.2	69 01 41.8	-173	2	447	13	31	0.8	8.0	-0.4	17	2.2	2.0
301	9 56 28.6	69 02 55.3	-142	2	111	8	109	0.6	8.6	-0.2	7	0.2	0.1
302	9 56 28.7	69 05 07.3	-81	1	143	8	80	0.5	10.2	-0.4	9	0.3	0.2
303	9 56 29.0	69 05 23.7	-65	1	136	8	160	0.8	10.5	-0.5	8	0.2	0.1
304	9 56 29.4	69 04 40.2	-88	1	106	8	52	0.4	10.0	-0.4	6	-0.1	-0.2
305	9 56 29.5	69 02 46.2	-142	2	111	20	131	0.6	8.7	-0.2	3	0.8	0.1
306	9 56 30.1	69 06 38.7	34	1	161	8	12	0.6	11.8	-0.4	10	0.5	0.4
307	9 56 30.3	69 04 50.6	-83	2	101	8	149	0.9	10.2	-0.4	6	-0.2	-0.3
308	9 56 31.4	69 05 14.5	-63	2	122	8	100	0.8	10.7	-0.4	7	0.1	0.0
309	9 56 31.5	68 54 09.9	-214	1	155	8	65	0.5	11.7	-0.7	10	0.1	0.0
310	9 56 31.8	69 04 01.0	-114	2	126	8	11	0.7	9.8	-0.3	8	0.3	0.1
311	9 56 31.9	69 04 11.5	-104	3	104	8	7	0.7	10.0	-0.3	6	0.0	-0.1
312	9 56 31.9	69 04 34.0	-83	2	147	8	68	0.7	10.3	-0.3	9	0.4	0.3
313	9 56 32.7	69 05 53.5	-42	2	102	13	144	0.6	11.5	-0.4	4	0.2	-0.2
314	9 56 32.8	69 06 34.0	-34	2	111	11	141	0.6	12.2	-0.4	5	0.1	-0.2
315	9 56 33.9	69 04 27.9	-81	1	122	8	35	0.8	10.5	-0.4	7	0.1	0.0
316	9 56 34.6	69 03 30.8	-114	1	123	8	0	1.0	9.9	-0.6	8	-0.1	-0.2
317	9 56 36.2	68 56 09.7	-212	2	117	10	74	0.7	10.3	-0.5	6	0.1	-0.2
318	9 56 38.2	68 54 38.0	-209	1	180	8	145	0.5	11.6	-0.7	11	0.3	0.2
319	9 56 39.1	69 05 35.0	-47	1	93	8	38	0.6	12.3	-0.6	6	-0.5	-0.6
320	9 56 41.3	68 55 09.3	-212	1	221	8	124	0.7	11.4	-0.6	14	0.7	0.6
321	9 56 41.7	69 00 43.8	-163	1	129	8	42	0.7	9.8	-0.6	8	0.0	-0.1

Table 2.12. NGC 3184 hole properties

No	α (h m s)	δ ($^\circ$ $'$ $''$)	$V_{\rm hel}$ ($\rm km\,s^{-1}$)	*Type* (1 − 3)	d (pc)	$V_{\rm exp}$ ($\rm km\,s^{-1}$)	*P.A.* ($^\circ$)	*Axial Ratio*	R (kpc)	$log(n_{\rm HI})$ ($\rm cm^{-3}$)	$t_{\rm kin}$ (Myr)	$log(E_{\rm E})$ (10^{50} erg)	$log(M_{\rm HI})$ ($10^4\,\rm M_\odot$)
1	10 18 04.9	41 25 32.5	586	1	823	7	152	0.7	7.6	-0.2	58	2.9	2.8
2	10 18 05.3	41 26 41.5	566	1	944	7	12	0.6	8.3	-0.2	66	3.0	2.9
3	10 18 05.4	41 23 37.0	625	1	856	7	0	0.5	9.4	-0.4	60	2.7	2.7
4	10 18 05.7	41 25 01.0	594	2	798	13	5	0.6	7.3	-0.2	30	3.2	2.7
5	10 18 06.4	41 25 59.5	576	1	798	7	162	0.6	6.9	-0.1	56	3.0	2.8
6	10 18 06.5	41 27 25.0	550	1	944	7	12	0.6	9.2	-0.5	66	2.7	2.7
7	10 18 07.6	41 26 05.5	571	1	742	7	104	0.5	6.2	0.0	52	2.9	2.7
8	10 18 08.5	41 22 26.5	646	1	923	7	117	0.7	11.2	-0.7	64	2.4	2.6
9	10 18 09.7	41 24 17.5	620	1	1251	7	62	0.7	5.9	-0.1	87	3.5	3.0
10	10 18 11.0	41 23 46.0	628	2	681	13	103	0.6	6.6	-0.2	26	2.9	2.5
11	10 18 13.7	41 25 49.0	573	1	1046	7	57	0.9	2.3	0.0	73	3.4	2.7
12	10 18 14.2	41 22 53.5	646	1	1196	7	57	0.7	8.5	-0.3	84	3.2	3.0
13	10 18 14.4	41 23 29.5	643	1	1630	7	70	0.8	6.6	-0.5	114	3.5	3.3
14	10 18 14.5	41 28 16.0	537	1	1109	7	71	0.7	9.2	-0.4	78	3.0	2.9
15	10 18 16.0	41 27 17.5	548	1	1636	7	62	0.5	5.9	-0.1	114	3.9	3.3
16	10 18 16.4	41 26 17.5	560	1	535	7	51	0.8	2.7	0.1	37	2.6	2.3
17	10 18 17.2	41 24 10.0	633	1	941	7	68	0.9	4.2	0.0	66	3.2	2.7
18	10 18 18.0	41 25 07.0	604	1	1483	7	166	0.7	1.2	0.1	104	3.9	3.0
19	10 18 19.6	41 24 14.5	628	1	995	7	90	0.9	4.3	0.0	70	3.3	2.8
20	10 18 20.0	41 28 20.5	535	1	484	7	0	1.0	9.5	-0.4	34	1.9	2.2
21	10 18 20.4	41 23 32.5	635	1	1179	7	168	0.8	6.5	-0.1	82	3.4	3.0
22	10 18 20.4	41 25 28.0	594	1	685	7	83	0.5	2.1	-0.1	48	2.8	2.3
23	10 18 20.4	41 28 46.0	535	1	1424	7	58	0.9	10.9	-0.7	100	3.1	3.0
24	10 18 21.3	41 25 08.5	602	1	1027	7	146	0.5	2.9	0.0	72	3.4	2.8
25	10 18 21.7	41 27 47.5	537	1	813	7	60	0.6	8.1	-0.2	57	2.8	2.8
26	10 18 22.0	41 26 40.0	563	1	1368	7	93	0.6	5.0	0.0	96	3.7	3.1
27	10 18 22.9	41 24 47.5	612	2	1149	20	0	0.8	4.3	0.0	28	4.1	2.9

Table 2.12 (cont'd)

No	α (h m s)	δ ($^\circ$ $'$ $''$)	$V_{\rm hel}$ (km s^{-1})	*Type* (1 − 3)	d (pc)	$V_{\rm exp}$ (km s^{-1})	*P.A.* ($^\circ$)	*Axial Ratio*	R (kpc)	$log(n_{\rm HI})$ (cm^{-3})	$t_{\rm kin}$ (Myr)	$log(E_{\rm E})$ (10^{50} erg)	$log(M_{\rm HI})$ (10^4 M$_\odot$)
28	10 18 23.3	41 28 23.5	545	2	805	8	0	0.9	10.2	-0.5	49	2.6	2.6
29	10 18 23.4	41 23 40.0	630	1	1021	7	29	0.9	7.3	-0.2	71	3.1	2.9
30	10 18 23.7	41 26 20.5	566	1	484	7	0	1.0	5.1	0.0	34	2.4	2.3
31	10 18 25.0	41 27 16.0	545	1	742	7	44	0.5	7.7	-0.2	52	2.7	2.6
32	10 18 25.2	41 25 29.5	592	1	559	7	41	0.8	5.2	0.0	39	2.5	2.4
33	10 18 26.0	41 22 41.5	641	1	646	7	0	1.0	10.6	-0.6	45	2.1	2.4
34	10 18 26.8	41 26 32.5	560	1	1370	7	0	0.5	7.0	-0.2	96	3.6	3.2
35	10 18 26.8	41 27 05.5	555	1	1154	7	121	0.9	8.2	-0.3	81	3.2	3.0
36	10 18 28.0	41 25 46.0	581	1	1032	7	156	0.7	7.0	-0.2	72	3.2	2.9
37	10 18 28.6	41 25 19.0	602	2	646	15	0	1.0	7.4	-0.2	21	2.9	2.5
38	10 18 28.9	41 24 29.5	617	1	1180	7	78	0.4	8.1	-0.4	82	3.1	2.9
39	10 18 30.0	41 26 31.0	568	1	874	7	102	0.5	8.7	-0.2	61	2.9	2.8
40	10 18 32.5	41 24 44.4	607	1	1142	7	148	0.7	10.0	-0.7	80	2.8	2.7

Table 2.13. IC 2574 hole properties

No	α (h m s)	δ ($^\circ$ $'$ $''$)	$V_{\rm hel}$ (km s^{-1})	*Type* (1 − 3)	d (pc)	$V_{\rm exp}$ (km s^{-1})	*P.A.* ($^\circ$)	*Axial Ratio*	R (kpc)	$log(n_{\rm HI})$ (cm^{-3})	$t_{\rm kin}$ (Myr)	$log(E_{\rm E})$ (10^{50} erg)	$log(M_{\rm HI})$ (10^4 M$_\odot$)
1	10 27 30.6	68 21 29.2	4	1	1078	7	27	0.9	7.4	-0.6	75	2.8	3.0
2	10 27 34.1	68 20 32.2	0	3	429	10	0	1.0	7.8	-0.7	21	1.7	1.4
3	10 27 45.8	68 24 36.5	19	3	351	17	0	1.0	4.8	-0.5	10	1.9	1.2
4	10 27 47.2	68 22 47.0	19	2	541	10	12	0.6	5.1	-0.4	26	2.2	1.9
5	10 27 47.4	68 21 20.0	9	1	468	7	0	1.0	6.1	-0.5	33	1.8	1.7
6	10 27 54.0	68 24 16.9	25	3	509	10	143	0.7	3.9	-0.5	25	2.1	1.7
7	10 27 56.1	68 23 49.9	30	1	2021	7	30	0.7	3.7	-0.4	141	3.8	3.5
8	10 27 59.4	68 24 30.3	25	1	565	7	123	0.7	3.2	-0.6	39	1.9	2.2
9	10 28 03.4	68 28 10.7	53	1	734	7	89	0.8	5.7	-0.7	51	2.1	2.4
10	10 28 09.7	68 23 24.1	30	1	661	7	99	0.9	2.7	-0.4	46	2.4	2.5
11	10 28 16.3	68 25 25.5	43	1	604	7	26	0.7	1.6	-0.4	42	2.3	2.4
12	10 28 19.3	68 24 23.9	43	3	430	13	19	0.7	1.1	-0.3	16	2.3	2.2
13	10 28 22.9	68 27 10.3	45	1	1886	7	166	0.7	3.2	-0.5	132	3.7	3.4
14	10 28 23.0	68 22 38.8	30	3	331	13	0	1.0	3.2	-0.4	12	1.7	1.3
15	10 28 23.6	68 25 02.8	48	3	548	5	77	0.6	0.5	-0.2	54	2.1	2.4
16	10 28 23.9	68 24 22.3	50	2	453	10	29	0.6	0.9	-0.3	22	2.2	2.2
17	10 28 25.0	68 25 55.2	43	3	466	9	118	0.8	1.4	-0.4	25	2.0	2.2
18	10 28 30.8	68 25 53.6	50	1	807	7	17	0.9	1.2	-0.3	56	2.7	2.7
19	10 28 37.1	68 26 59.4	61	2	390	16	0	1.0	2.7	-0.4	12	2.1	1.5
20	10 28 37.2	68 24 44.4	53	1	897	7	120	0.8	1.2	-0.3	63	2.9	2.9
21	10 28 43.2	68 28 12.7	66	1	894	7	88	0.7	4.4	-0.4	63	2.8	2.9
22	10 28 43.3	68 26 15.7	61	1	692	7	45	0.7	2.3	-0.3	48	2.5	2.6
23	10 28 43.7	68 27 36.7	76	2	702	36	0	1.0	3.7	-0.3	10	3.5	2.7
24	10 28 47.8	68 25 06.5	71	1	413	7	81	0.7	2.3	-0.1	29	2.0	1.8
25	10 28 47.9	68 29 03.5	76	1	493	7	58	0.6	5.6	-0.5	34	1.8	1.7
26	10 28 50.4	68 26 22.9	68	1	1061	7	53	0.9	2.9	-0.3	74	3.1	3.0
27	10 29 09.2	68 23 29.7	71	3	320	7	173	0.8	5.6	-0.4	22	1.4	1.3

Table 2.13 (cont'd)

No	α (h m s)	δ (° ′ ″)	$V_{\rm hel}$ (km s^{-1})	*Type* (1 − 3)	d (pc)	$V_{\rm exp}$ (km s^{-1})	*P.A.* (°)	*Axial Ratio*	R (kpc)	$log(n_{\rm HI})$ (cm^{-3})	$t_{\rm kin}$ (Myr)	$log(E_{\rm E})$ (10^{50} erg)	$log(M_{\rm HI})$ (10^4 M$_\odot$)

Table 2.14. NGC 3521 hole properties

No	α (h m s)	δ ($^\circ$ $'$ $''$)	$V_{\rm hel}$ ($\rm km\,s^{-1}$)	*Type* (1 – 3)	d (pc)	$V_{\rm exp}$ ($\rm km\,s^{-1}$)	*P.A.* ($^\circ$)	*Axial Ratio*	R (kpc)	$log(n_{\rm HI})$ ($\rm cm^{-3}$)	$t_{\rm kin}$ (Myr)	$log(E_{\rm E})$ (10^{50} erg)	$log(M_{\rm HI})$ ($10^4\,\rm M_\odot$)
1	11 05 42.2	0 00 15.0	944	1	828	10	161	0.9	11.5	-0.5	41	2.8	2.7
2	11 05 42.7	0 00 10.5	970	1	794	10	131	0.7	10.3	-0.5	39	2.7	2.6
3	11 05 43.0	0 01 55.5	996	1	660	10	126	0.5	13.5	-0.8	32	2.1	1.8
4	11 05 45.8	0 01 28.5	939	1	672	10	146	0.9	5.1	0.1	33	3.1	2.6
5	11 05 47.8	0 02 46.5	727	1	603	10	129	0.6	4.6	0.1	29	3.0	2.5
6	11 05 48.0	0 01 07.5	981	1	676	10	139	0.6	3.9	0.1	33	3.2	2.6
7	11 05 48.1	0 02 54.0	696	1	934	10	0	1.0	4.7	0.1	46	3.6	2.9
8	11 05 50.0	0 04 16.5	597	2	928	16	131	0.8	7.8	-0.2	28	3.5	2.9
9	11 05 52.1	0 04 31.5	597	1	1011	10	95	1.0	7.8	-0.2	49	3.3	2.9
10	11 05 53.4	0 03 19.5	701	1	1205	10	126	0.6	9.0	-0.3	59	3.5	3.1
11	11 05 54.1	0 05 42.0	597	1	1122	10	145	0.7	11.9	-0.6	55	3.1	2.9
12	11 05 57.2	0 03 55.5	385	1	1137	10	88	0.8	16.6	-0.9	56	2.7	2.8
13	11 05 59.0	0 06 13.5	628	1	921	10	146	0.7	18.6	-1.0	45	2.3	2.0

Table 2.15. NGC 3627 hole properties

No	α (h m s)	δ ($^\circ$ $'$ $''$)	$V_{\rm hel}$ (km s^{-1})	*Type* (1 – 3)	d (pc)	$V_{\rm exp}$ (km s^{-1})	*P.A.* ($^\circ$)	*Axial Ratio*	R (kpc)	$log(n_{\rm HI})$ (cm^{-3})	$t_{\rm kin}$ (Myr)	$log(E_{\rm E})$ (10^{50} erg)	$log(M_{\rm HI})$ (10^4 M$_\odot$)
1	11 20 13.1	12 57 01.0	849	1	466	13	160	0.8	7.8	-0.7	18	1.9	1.4
2	11 20 13.2	13 00 01.0	616	1	425	13	142	0.9	2.6	0.0	16	2.6	2.0
3	11 20 14.3	13 01 13.0	554	1	359	13	0	1.0	4.7	-0.6	14	1.6	1.5
4	11 20 14.4	13 00 44.5	554	2	538	30	0	1.0	3.4	0.1	9	3.5	2.4
5	11 20 15.0	13 00 17.5	590	2	626	15	148	0.9	2.2	0.1	20	3.2	2.4
6	11 20 15.4	12 58 07.0	859	1	538	13	0	1.0	3.7	-0.1	20	2.7	2.2
7	11 20 15.5	12 58 41.5	844	2	987	65	0	1.0	2.2	-0.4	7	4.2	2.8
8	11 20 15.6	13 00 56.5	548	3	401	13	175	0.8	4.3	-0.1	15	2.3	2.0
9	11 20 15.8	13 01 35.5	564	1	560	13	124	0.9	6.1	-0.7	21	2.2	2.0
10	11 20 16.0	12 58 28.0	885	2	569	13	145	0.3	2.9	0.0	21	2.9	2.3
11	11 20 16.8	12 59 37.0	688	1	648	13	154	0.6	2.6	-0.1	24	3.1	2.3
12	11 20 16.8	13 00 01.0	647	2	741	12	168	0.6	3.0	-0.1	30	3.2	2.5
13	11 20 17.1	12 59 04.0	792	3	381	30	0	0.9	2.9	0.0	6	2.9	2.0
14	11 20 17.5	13 01 22.0	569	1	628	13	0	1.0	6.8	-0.7	24	2.3	2.2
15	11 20 18.2	12 58 28.0	859	2	557	13	123	0.8	4.8	-0.3	21	2.6	2.2
16	11 20 18.6	12 58 43.0	819	1	538	13	0	1.0	5.0	-0.3	20	2.5	2.2
17	11 20 19.5	12 59 02.5	761	1	444	13	173	0.5	6.2	-0.5	17	2.1	2.0
18	11 20 20.5	12 59 34.0	719	1	404	13	0	1.0	7.6	-0.7	15	1.7	1.3

Table 2.16. NGC 4214 hole properties

No	α (h m s)	δ ($^\circ$ $'$ $''$)	$V_{\rm hel}$ (km s^{-1})	*Type* (1 − 3)	d (pc)	$V_{\rm exp}$ (km s^{-1})	*P.A.* ($^\circ$)	*Axial Ratio*	R (kpc)	$log(n_{\rm HI})$ (cm^{-3})	$t_{\rm kin}$ (Myr)	$log(E_{\rm E})$ (10^{50} erg)	$log(M_{\rm HI})$ (10^4 M$_\odot$)
1	12 15 15.4	36 19 49.4	266	2	368	13	55	0.8	4.5	-0.6	14	1.7	1.2
2	12 15 16.2	36 19 08.9	266	1	342	6	14	0.6	4.2	-0.5	28	1.2	1.2
3	12 15 16.2	36 20 08.9	261	2	498	10	11	0.6	4.6	-0.6	24	1.9	1.6
4	12 15 19.3	36 19 43.4	258	3	257	10	0	1.0	3.7	-0.4	13	1.3	1.0
5	12 15 22.5	36 18 56.9	258	1	382	6	51	0.8	3.0	-0.6	31	1.2	1.7
6	12 15 26.5	36 25 06.0	285	1	298	6	60	0.8	6.7	-1.4	24	0.0	0.1
7	12 15 28.3	36 17 21.0	271	1	433	6	46	0.5	2.8	-0.4	35	1.6	1.9
8	12 15 28.6	36 18 27.0	262	1	812	6	52	0.9	2.1	-0.4	66	2.5	2.4
9	12 15 28.7	36 16 15.0	270	1	717	6	144	0.8	3.8	-0.5	58	2.2	2.4
10	12 15 29.2	36 21 21.0	279	1	296	15	134	0.8	3.0	-0.2	10	1.9	1.4
11	12 15 31.3	36 21 13.5	266	1	296	24	97	0.8	2.6	-0.1	6	2.3	1.9
12	12 15 32.4	36 20 27.0	258	1	419	6	121	0.7	1.8	0.0	34	2.1	2.2
13	12 15 32.8	36 22 34.5	294	1	401	6	112	0.7	3.8	-0.4	33	1.6	1.6
14	12 15 33.0	36 22 06.0	288	3	114	15	0	1.0	3.2	-0.2	4	0.7	0.1
15	12 15 35.4	36 17 42.0	275	2	385	12	0	1.0	2.1	-0.3	16	2.1	1.9
16	12 15 35.4	36 19 30.0	271	1	228	6	30	0.9	0.7	0.4	19	1.7	1.7
17	12 15 35.5	36 23 48.0	296	1	448	6	156	0.9	5.0	-0.7	37	1.3	1.3
18	12 15 35.8	36 18 13.5	269	1	428	6	0	1.0	1.5	0.0	35	2.1	2.1
19	12 15 35.8	36 23 18.0	296	2	524	11	94	0.7	4.4	-0.6	23	2.0	2.1
20	12 15 36.0	36 14 51.0	287	1	360	6	121	0.8	5.3	-1.0	29	0.8	0.8
21	12 15 37.8	36 16 57.0	275	1	619	6	65	0.7	3.0	-0.4	50	2.2	2.3
22	12 15 37.8	36 17 22.5	270	1	403	6	176	0.8	2.5	-0.3	33	1.7	2.0
23	12 15 39.4	36 22 07.5	303	1	304	6	37	0.8	2.8	-0.3	25	1.2	1.2
24	12 15 39.5	36 18 48.0	288	3	207	20	0	0.9	0.9	0.5	5	2.4	1.8
25	12 15 39.5	36 24 25.5	300	1	403	6	119	0.6	5.4	-0.8	33	1.1	1.1
26	12 15 39.9	36 23 06.0	306	1	640	6	137	0.5	3.9	-0.6	52	1.9	2.2
27	12 15 40.0	36 19 21.0	305	1	270	25	75	0.6	0.7	0.4	5	2.8	1.8

Table 2.16 (cont'd)

No	α (h m s)	δ ($^\circ$ $'$ $''$)	$V_{\rm hel}$ (km s^{-1})	*Type* (1 − 3)	d (pc)	$V_{\rm exp}$ (km s^{-1})	*P.A.* ($^\circ$)	*Axial Ratio*	R (kpc)	$log(n_{\rm HI})$ (cm^{-3})	$t_{\rm kin}$ (Myr)	$log(E_{\rm E})$ (10^{50} erg)	$log(M_{\rm HI})$ (10^4 M$_\odot$)
28	12 15 40.2	36 23 01.5	307	1	397	6	144	0.6	3.8	-0.6	32	1.3	1.3
29	12 15 40.6	36 21 10.5	314	1	506	6	15	0.7	1.7	0.0	41	2.3	2.3
30	12 15 41.0	36 16 03.0	292	1	212	6	46	0.8	4.1	-0.6	17	0.5	0.6
31	12 15 41.0	36 16 37.5	288	1	491	6	141	0.9	3.5	-0.4	40	1.8	2.1
32	12 15 41.4	36 18 21.0	287	1	131	6	132	0.6	1.6	0.1	11	0.6	0.6
33	12 15 41.6	36 20 09.0	325	1	412	6	81	0.6	1.1	0.0	34	2.1	2.0
34	12 15 41.7	36 21 51.0	311	1	327	6	12	0.8	2.5	-0.4	27	1.3	1.7
35	12 15 42.4	36 17 58.5	296	1	376	6	145	0.8	2.1	0.0	31	1.9	2.1
36	12 15 43.7	36 19 31.5	310	1	327	6	50	0.8	0.9	0.3	27	2.1	2.0
37	12 15 45.3	36 19 54.0	294	1	342	6	104	0.9	0.4	0.8	28	2.7	2.3
38	12 15 45.6	36 18 51.0	302	1	171	6	0	1.0	1.6	0.1	14	1.0	0.9
39	12 15 45.9	36 15 36.0	300	1	1229	6	136	0.6	5.0	-0.8	100	2.6	2.7
40	12 15 46.5	36 18 54.0	314	1	335	6	19	0.7	1.7	0.1	27	1.8	2.0
41	12 15 46.7	36 19 06.0	320	2	321	20	0	1.0	1.7	0.1	8	2.5	2.0
42	12 15 46.8	36 21 45.0	323	1	655	6	165	0.6	2.5	-0.4	53	2.2	2.3
43	12 15 46.9	36 18 30.0	334	1	171	6	0	1.0	2.1	0.0	14	0.8	0.8
44	12 15 47.3	36 16 37.5	300	1	340	6	134	0.6	4.0	-0.4	28	1.3	1.3
45	12 15 47.6	36 20 27.0	332	1	401	6	179	0.7	1.6	-0.1	33	1.9	2.0
46	12 15 49.9	36 18 30.0	325	1	413	6	70	0.7	2.6	-0.2	34	1.8	2.1
47	12 15 49.9	36 22 54.0	312	2	347	4	172	0.5	3.8	-0.6	42	0.9	1.1
48	12 15 53.0	36 22 09.0	319	1	513	6	0	1.0	3.4	-0.5	42	1.7	2.0
49	12 15 53.8	36 20 31.5	324	1	299	6	0	1.0	2.7	-0.4	24	1.2	1.2
50	12 15 53.8	36 21 28.5	324	1	382	6	74	0.8	3.0	-0.5	31	1.4	1.8
51	12 15 54.8	36 19 11.9	332	1	368	6	151	0.5	3.0	-0.4	30	1.5	1.9
52	12 15 54.9	36 17 29.9	312	3	278	10	107	1.0	4.3	-0.7	14	1.0	0.7
53	12 15 55.3	36 20 23.9	331	1	765	6	96	0.8	2.9	-0.4	62	2.4	2.5
54	12 15 56.3	36 20 28.4	324	1	476	6	90	0.9	3.1	-0.5	39	1.6	2.0

Table 2.16 (cont'd)

No	α (h m s)	δ ($^\circ$ $'$ $''$)	$V_{\rm hel}$ ($\rm km\,s^{-1}$)	*Type* (1 – 3)	d (pc)	$V_{\rm exp}$ ($\rm km\,s^{-1}$)	*P.A.* ($^\circ$)	*Axial Ratio*	R (kpc)	$log(n_{\rm HI})$ ($\rm cm^{-3}$)	$t_{\rm kin}$ (Myr)	$log(E_{\rm E})$ (10^{50} erg)	$log(M_{\rm HI})$ ($10^4\,\rm M_\odot$)
55	12 15 56.9	36 16 53.9	318	1	342	6	0	1.0	5.0	-0.9	28	0.7	0.8
56	12 16 00.6	36 19 37.4	319	1	302	6	39	0.7	4.0	-0.7	25	0.8	0.9

Table 2.17. NGC 4449 hole properties

No	α (h m s)	δ ($^\circ$ $'$ $''$)	$V_{\rm hel}$ ($\rm km\,s^{-1}$)	*Type* (1 − 3)	d (pc)	$V_{\rm exp}$ ($\rm km\,s^{-1}$)	*P.A.* ($^\circ$)	*Axial Ratio*	R (kpc)	$log(n_{\rm HI})$ ($\rm cm^{-3}$)	$t_{\rm kin}$ (Myr)	$log(E_{\rm E})$ (10^{50} erg)	$log(M_{\rm HI})$ ($10^4\,\rm M_\odot$)
1	12 27 44.9	44 04 53.1	267	1	550	10	7	0.9	8.1	-2.0	27	0.5	0.4
2	12 27 50.3	44 02 50.2	247	1	600	10	0	0.8	5.9	-2.0	29	0.7	0.5
3	12 27 51.0	44 02 50.3	236	1	716	10	122	0.7	5.9	-2.0	35	0.9	0.7
4	12 28 04.1	44 04 58.0	180	2	784	26	124	0.9	2.0	-0.1	15	3.6	2.6
5	12 28 07.9	44 03 22.0	195	3	458	20	38	0.9	4.0	-0.7	11	2.2	1.4
6	12 28 08.3	44 04 43.0	190	1	798	10	44	0.8	1.5	0.1	39	3.3	2.7
7	12 28 09.5	44 05 58.0	206	1	735	10	0	1.0	1.3	0.1	36	3.2	2.6
8	12 28 10.1	44 06 04.0	211	1	901	10	25	0.6	1.5	0.1	44	3.5	2.8
9	12 28 10.3	44 06 10.0	211	3	424	22	127	0.8	1.7	-0.1	9	2.8	2.1
10	12 28 10.9	44 05 05.5	211	1	604	10	29	0.7	1.0	0.3	30	3.2	2.5
11	12 28 13.1	44 03 43.1	195	1	577	10	63	0.6	4.2	-1.0	28	1.6	1.4
12	12 28 13.8	44 04 55.1	216	2	233	26	148	0.8	2.0	0.0	4	2.1	1.2
13	12 28 14.8	44 06 05.6	242	2	540	30	85	0.6	0.8	0.4	9	3.8	2.5
14	12 28 16.2	44 05 25.1	226	1	326	10	0	0.9	1.8	0.1	16	2.1	2.0
15	12 28 16.6	44 05 49.1	216	1	725	10	0	0.7	1.4	0.2	35	3.3	2.7
16	12 28 24.4	44 05 38.6	195	3	439	28	0	1.0	4.2	-1.0	8	1.9	1.0
17	12 28 25.0	44 07 23.6	190	1	586	10	145	0.8	3.6	-1.4	29	1.3	1.1
18	12 28 32.9	44 04 47.6	169	1	875	10	51	0.6	8.1	-1.7	43	1.5	1.2
19	12 28 33.2	44 03 58.1	164	1	574	10	47	0.7	9.4	-2.0	28	0.7	0.5
20	12 28 49.1	44 08 13.0	154	1	477	10	20	0.8	10.1	-2.0	23	0.1	0.0

Table 2.18. NGC 4736 hole properties

No	α (h m s)	δ ($^\circ$ $'$ $''$)	$V_{\rm hel}$ (km s^{-1})	*Type* (1 − 3)	d (pc)	$V_{\rm exp}$ (km s^{-1})	*P.A.* ($^\circ$)	*Axial Ratio*	R (kpc)	$log(n_{\rm HI})$ (cm^{-3})	$t_{\rm kin}$ (Myr)	$log(E_{\rm E})$ (10^{50} erg)	$log(M_{\rm HI})$ (10^4 M$_\odot$)
1	12 50 30.9	41 08 57.0	407	1	371	9	2	0.8	6.1	-1.3	20	0.7	0.6
2	12 50 37.2	41 11 13.6	370	1	262	9	176	0.6	7.3	-1.5	14	0.0	-0.1
3	12 50 39.1	41 04 15.1	339	1	359	9	134	0.8	7.0	-1.5	19	0.3	0.2
4	12 50 39.3	41 04 46.6	339	1	381	9	163	0.8	6.2	-1.5	21	0.5	0.4
5	12 50 41.1	41 07 36.1	401	1	364	9	151	0.7	3.1	-0.4	20	1.6	1.6
6	12 50 44.6	41 07 27.1	401	2	414	20	42	0.8	2.3	0.0	10	2.8	1.9
7	12 50 45.0	41 06 57.1	386	2	361	26	0	1.0	2.3	0.1	7	2.8	1.8
8	12 50 45.2	41 07 46.6	407	3	303	15	23	0.8	2.3	0.1	10	2.2	1.6
9	12 50 45.8	41 07 54.1	422	2	350	15	0	0.9	2.1	0.1	11	2.5	1.8
10	12 50 47.1	41 07 10.6	376	2	439	30	0	0.9	1.6	0.5	7	3.6	2.1
11	12 50 47.6	41 06 57.1	376	1	254	9	155	0.6	1.6	-0.3	14	1.3	1.0
12	12 50 47.9	41 07 22.6	401	3	226	16	0	1.0	1.3	0.6	7	2.5	1.6
13	12 50 48.9	41 06 40.7	345	1	350	9	133	0.6	1.6	0.5	19	2.6	2.0
14	12 50 49.6	41 08 40.7	396	1	332	9	121	0.7	2.5	-0.1	18	1.8	1.6
15	12 50 50.7	41 06 28.7	303	3	417	20	40	0.4	1.5	0.5	10	3.4	2.1
16	12 50 52.1	41 06 33.2	283	1	235	9	64	0.8	1.2	0.8	13	2.4	1.8
17	12 50 54.7	41 07 10.7	200	2	452	10	0	1.0	0.5	0.9	22	3.5	2.2
18	12 50 56.0	41 06 24.2	215	1	212	9	28	0.7	1.5	0.6	12	2.1	1.6
19	12 50 58.6	41 07 36.1	267	2	271	21	12	0.6	1.8	0.3	6	2.6	1.6
20	12 50 59.2	41 05 57.1	226	1	244	9	0	0.7	2.4	-0.1	13	1.4	1.3
21	12 50 59.2	41 07 25.6	262	2	341	26	1	0.6	1.9	0.3	6	3.0	1.8
22	12 50 59.3	41 07 48.1	283	3	212	11	134	0.7	2.3	0.4	9	1.9	1.7
23	12 51 02.4	41 07 01.6	226	2	339	15	0	1.0	2.7	0.0	11	2.3	1.8
24	12 51 20.4	41 10 03.0	257	1	300	9	50	0.7	9.9	-1.5	16	0.1	0.0

Table 2.19. DDO 154 hole properties

No	α (h m s)	δ ($^\circ$ $'$ $''$)	$V_{\rm hel}$ ($\rm km\,s^{-1}$)	*Type* (1 – 3)	d (pc)	$V_{\rm exp}$ ($\rm km\,s^{-1}$)	*P.A.* ($^\circ$)	*Axial Ratio*	R (kpc)	$log(n_{\rm HI})$ ($\rm cm^{-3}$)	$t_{\rm kin}$ (Myr)	$log(E_{\rm E})$ (10^{50} erg)	$log(M_{\rm HI})$ ($10^4\,\rm M_\odot$)
1	12 53 56.7	27 07 53.0	411	1	472	8	53	0.7	3.2	-1.0	29	1.3	1.2
2	12 53 58.6	27 07 53.0	400	1	685	8	110	0.8	2.6	-1.0	42	1.8	1.7
3	12 54 03.0	27 07 54.5	400	1	460	8	118	0.7	2.3	-0.8	28	1.5	1.3
4	12 54 03.1	27 09 17.0	380	1	361	8	162	0.8	1.6	-0.7	22	1.2	1.1
5	12 54 06.3	27 08 21.5	382	1	604	8	139	0.9	2.2	-0.8	37	1.9	1.7
6	12 54 07.6	27 09 53.0	362	3	396	6	0	1.0	1.3	-0.8	32	1.1	1.2
7	12 54 08.4	27 09 14.0	372	2	454	13	163	0.8	1.1	-0.6	17	1.9	1.5
8	12 54 15.6	27 11 02.0	328	2	271	13	0	1.0	3.6	-1.1	10	0.7	0.3
9	12 54 15.9	27 09 41.0	354	1	416	8	173	0.9	4.1	-1.2	25	1.0	0.8

Table 2.20. NGC 5194 hole properties

No	α (h m s)	δ ($^\circ$ $'$ $''$)	$V_{\rm hel}$ (km s^{-1})	*Type* (1 – 3)	d (pc)	$V_{\rm exp}$ (km s^{-1})	*P.A.* ($^\circ$)	*Axial Ratio*	R (kpc)	$log(n_{\rm HI})$ (cm^{-3})	$t_{\rm kin}$ (Myr)	$log(E_{\rm E})$ (10^{50} erg)	$log(M_{\rm HI})$ (10^4 M$_\odot$)
1	13 29 33.2	47 11 43.4	473	1	1344	14	161	0.8	8.2	-0.7	47	3.3	2.8
2	13 29 35.7	47 09 59.9	483	1	368	14	135	0.9	8.2	-0.4	13	2.0	1.4
3	13 29 35.7	47 10 32.9	462	1	349	14	0	1.0	7.7	-0.4	12	1.9	1.4
4	13 29 39.8	47 09 31.5	499	1	828	32	93	0.8	7.5	-0.4	13	3.5	2.7
5	13 29 40.4	47 10 24.0	488	1	1903	14	23	0.8	6.0	-0.1	116	4.2	3.9
6	13 29 41.7	47 08 36.0	509	1	658	20	103	0.5	8.6	-0.5	16	2.9	2.5
7	13 29 41.7	47 12 48.0	400	1	349	14	0	1.0	5.2	-0.1	12	2.2	2.0
8	13 29 42.7	47 12 19.5	416	1	717	14	80	0.9	4.4	-0.2	25	3.1	2.5
9	13 29 43.0	47 12 07.5	411	2	795	20	134	1.0	4.2	-0.1	19	3.6	2.6
10	13 29 43.2	47 08 10.5	525	2	546	20	127	0.6	9.2	-0.4	13	2.7	2.4
11	13 29 44.6	47 08 22.5	494	2	459	20	10	0.7	8.6	-0.5	11	2.4	1.6
12	13 29 44.6	47 12 52.5	400	1	641	14	94	0.6	4.3	-0.1	22	3.0	2.4
13	13 29 44.9	47 11 09.0	473	1	886	14	25	0.6	3.5	-0.2	31	3.4	2.6
14	13 29 45.2	47 09 13.5	525	2	523	20	34	0.9	6.8	-0.5	13	2.6	2.2
15	13 29 46.4	47 09 54.0	514	1	290	14	0	0.9	5.0	-0.1	10	2.0	1.9
16	13 29 47.7	47 09 00.0	530	1	308	14	0	0.8	6.7	-0.4	11	1.7	1.1
17	13 29 47.9	47 13 12.0	390	1	407	14	0	0.9	4.0	0.0	14	2.6	2.2
18	13 29 48.2	47 15 16.5	390	1	895	14	12	0.7	8.5	-0.8	31	2.7	2.4
19	13 29 48.5	47 10 01.5	525	1	839	14	157	0.7	4.4	-0.1	29	3.4	2.7
20	13 29 48.8	47 13 42.0	375	1	815	14	53	0.7	4.9	0.0	29	3.5	2.9
21	13 29 48.9	47 08 58.5	525	1	705	14	132	0.7	6.6	-0.4	25	2.8	2.5
22	13 29 49.5	47 12 13.5	406	2	728	25	62	0.7	1.8	0.0	14	3.7	2.5
23	13 29 50.4	47 15 39.0	390	1	537	14	155	0.8	9.2	-0.9	19	1.9	1.4
24	13 29 50.8	47 13 19.5	375	2	754	20	78	0.9	3.7	-0.1	18	3.5	2.6
25	13 29 50.8	47 15 21.0	395	1	753	14	137	0.4	8.5	-0.9	26	2.4	2.2
26	13 29 51.9	47 09 03.0	525	1	839	14	102	0.7	6.2	-0.4	29	3.1	2.7
27	13 29 51.9	47 12 12.0	406	3	435	18	60	0.6	1.2	0.0	12	2.8	2.0

Table 2.20 (cont'd)

No	α (h m s)	δ ($^\circ$ $'$ $''$)	$V_{\rm hel}$ (km s^{-1})	*Type* (1 − 3)	d (pc)	$V_{\rm exp}$ (km s^{-1})	*P.A.* ($^\circ$)	*Axial Ratio*	R (kpc)	$log(n_{\rm HI})$ (cm^{-3})	$t_{\rm kin}$ (Myr)	$log(E_{\rm E})$ (10^{50} erg)	$log(M_{\rm HI})$ (10^4 M$_\odot$)
28	13 29 52.4	47 09 58.5	535	1	872	14	173	1.0	4.1	-0.2	31	3.3	2.6
29	13 29 52.6	47 11 18.0	504	2	688	20	165	0.7	1.1	0.0	17	3.5	2.4
30	13 29 52.7	47 14 27.0	364	1	407	14	61	0.9	6.3	-0.3	14	2.3	2.2
31	13 29 53.8	47 11 10.5	504	2	713	26	12	0.5	1.3	0.0	13	3.7	2.5
32	13 29 53.8	47 13 12.0	390	1	862	14	126	0.7	3.5	-0.2	30	3.3	2.6
33	13 29 55.7	47 13 22.5	390	1	523	14	41	0.9	4.1	-0.2	18	2.6	2.2
34	13 29 55.7	47 15 42.0	395	1	711	14	57	0.8	9.4	-0.9	25	2.3	2.1
35	13 29 56.0	47 11 09.0	514	2	562	26	131	0.9	1.9	0.0	11	3.3	2.3
36	13 29 58.0	47 11 39.0	468	2	756	26	0	1.0	2.3	-0.1	14	3.7	2.5
37	13 29 58.5	47 09 40.5	540	1	694	28	133	0.8	5.3	-0.3	12	3.4	2.5
38	13 29 58.5	47 10 42.0	514	2	465	16	0	1.0	3.3	-0.1	14	2.7	2.1
39	13 29 58.8	47 12 46.5	411	1	744	14	116	0.7	3.6	-0.1	26	3.2	2.5
40	13 29 59.1	47 15 24.0	400	1	340	14	70	0.6	9.1	-0.6	12	1.6	1.1
41	13 29 59.7	47 10 52.5	514	2	562	11	77	0.5	3.4	-0.1	25	2.7	2.3
42	13 30 00.2	47 09 46.5	525	2	475	30	63	0.7	5.4	-0.2	8	3.0	2.2
43	13 30 00.8	47 07 39.0	509	2	713	16	131	0.5	10.0	-0.6	22	2.7	2.4
44	13 30 01.6	47 10 09.0	519	2	688	31	0	0.7	5.2	-0.1	11	3.6	2.6
45	13 30 01.9	47 13 22.5	421	2	665	26	1	0.7	5.5	-0.1	13	3.5	2.6
46	13 30 02.6	47 11 24.0	509	1	956	14	80	0.6	4.2	-0.1	33	3.6	2.8
47	13 30 02.7	47 10 27.0	504	2	598	25	39	0.8	5.1	-0.1	12	3.3	2.5
48	13 30 06.1	47 11 04.5	499	2	871	15	81	0.9	5.8	-0.2	28	3.3	2.8

Table 2.21. NGC 6946 hole properties

No	α (h m s)	δ ($^\circ$ $'$ $''$)	$V_{\rm hel}$ ($\rm km\,s^{-1}$)	*Type* (1 − 3)	d (pc)	$V_{\rm exp}$ ($\rm km\,s^{-1}$)	*P.A.* ($^\circ$)	*Axial Ratio*	R (kpc)	$log(n_{\rm HI})$ ($\rm cm^{-3}$)	$t_{\rm kin}$ (Myr)	$log(E_{\rm E})$ (10^{50} erg)	$log(M_{\rm HI})$ ($10^4\,\rm M_\odot$)
1	20 33 46.1	60 09 27.5	145	1	970	8	166	0.5	14.9	-1.0	59	2.2	2.0
2	20 34 07.2	60 09 40.0	132	1	892	8	156	0.8	10.3	-0.6	55	2.6	2.6
3	20 34 11.5	60 06 29.6	158	1	1695	8	117	0.6	9.9	-0.5	104	3.5	3.1
4	20 34 13.2	60 08 52.2	145	2	543	15	177	0.9	8.6	-0.2	18	2.7	2.3
5	20 34 18.5	60 08 47.7	142	3	198	10	93	0.8	7.5	0.0	10	1.3	1.0
6	20 34 19.5	60 07 37.3	153	1	1138	8	148	0.7	7.5	-0.1	70	3.5	3.0
7	20 34 19.6	60 09 31.3	137	1	1222	8	123	0.8	7.4	0.0	75	3.7	3.2
8	20 34 20.6	60 10 16.3	122	1	485	8	130	0.9	7.7	0.1	30	2.6	2.5
9	20 34 20.8	60 11 14.8	99	1	543	8	169	0.4	8.8	-0.1	33	2.5	2.5
10	20 34 22.7	60 08 25.3	145	3	303	18	178	0.6	6.6	0.1	8	2.4	2.0
11	20 34 25.5	60 04 43.3	145	1	590	8	64	0.7	10.1	-0.5	36	2.2	2.3
12	20 34 25.7	60 08 26.8	147	1	735	8	128	0.7	5.9	0.2	45	3.2	2.8
13	20 34 26.1	60 11 10.3	88	2	858	21	56	0.4	7.7	0.0	20	3.8	2.9
14	20 34 26.9	60 06 31.4	160	1	1854	8	102	0.6	7.3	-0.1	113	4.1	3.4
15	20 34 28.7	60 09 43.4	117	1	1445	8	42	0.8	5.4	-0.4	88	3.5	3.4
16	20 34 30.1	60 09 05.9	117	1	1317	8	50	0.8	4.9	-0.4	81	3.3	3.3
17	20 34 30.9	60 10 35.9	104	2	483	16	95	0.8	5.9	0.2	15	3.1	2.5
18	20 34 33.1	60 08 20.9	150	1	726	8	24	0.8	4.4	0.2	44	3.2	2.7
19	20 34 33.2	60 04 31.4	135	1	454	8	62	0.8	9.9	-0.3	28	2.0	2.2
20	20 34 34.9	60 14 26.9	39	1	505	8	62	0.5	12.0	-0.5	31	1.9	1.7
21	20 34 35.0	60 02 34.4	119	1	527	8	122	0.9	13.5	-0.9	32	1.6	1.4
22	20 34 37.7	60 15 33.0	47	1	1329	8	65	0.7	13.9	-0.8	81	2.9	3.0
23	20 34 39.6	60 06 31.5	140	1	697	8	64	0.8	5.8	0.1	43	3.0	2.6
24	20 34 39.8	60 04 24.0	112	1	966	8	179	0.8	9.8	-0.3	59	3.0	2.9
25	20 34 40.1	60 09 49.5	94	1	454	8	0	0.6	3.2	0.3	28	2.7	2.2
26	20 34 41.6	60 06 03.0	114	1	286	8	0	1.0	6.7	0.1	17	1.8	1.9
27	20 34 43.8	60 05 24.0	109	1	297	8	0	0.8	7.7	0.1	18	1.9	2.0

Table 2.21 (cont'd)

No	α (h m s)	δ ($^\circ$ $'$ $''$)	$V_{\rm hel}$ (km s^{-1})	*Type* (1 − 3)	d (pc)	$V_{\rm exp}$ (km s^{-1})	*P.A.* ($^\circ$)	*Axial Ratio*	R (kpc)	$log(n_{\rm HI})$ (cm^{-3})	$t_{\rm kin}$ (Myr)	$log(E_{\rm E})$ (10^{50} erg)	$log(M_{\rm HI})$ (10^4 M$_\odot$)
28	20 34 44.4	60 11 57.0	21	1	558	8	0	1.0	6.1	0.1	34	2.7	2.5
29	20 34 46.4	60 02 37.5	101	1	531	8	58	0.7	13.3	-0.8	32	1.6	1.5
30	20 34 46.8	60 03 06.0	96	1	739	8	37	0.8	12.4	-0.7	45	2.2	2.5
31	20 34 47.2	60 05 34.5	104	2	652	11	121	0.8	7.4	0.1	29	3.1	2.7
32	20 34 50.4	60 16 01.5	21	1	809	8	66	0.8	13.9	-0.7	49	2.3	2.1
33	20 34 52.2	60 10 39.0	19	1	623	8	35	0.8	2.8	0.3	38	3.1	2.4
34	20 34 54.6	60 11 27.0	-10	1	1371	8	60	0.3	4.4	0.2	84	4.0	3.2
35	20 34 59.2	60 07 21.0	52	1	1084	8	26	0.9	4.4	0.2	66	3.8	3.0
36	20 35 00.6	60 10 58.5	-25	1	640	8	167	0.8	3.7	0.3	39	3.1	2.6
37	20 35 02.6	60 06 39.0	62	3	198	12	0	0.8	6.1	0.1	8	1.6	1.6
38	20 35 05.8	60 05 52.5	55	2	483	21	99	0.8	8.0	-0.1	11	2.9	2.3
39	20 35 07.7	60 06 58.4	32	1	502	8	90	0.4	6.2	0.1	31	2.6	2.4
40	20 35 08.3	60 06 04.4	42	1	572	8	45	0.6	7.9	0.0	35	2.6	2.5
41	20 35 08.3	60 10 59.9	-51	1	742	8	0	0.7	4.6	0.3	45	3.3	2.8
42	20 35 08.9	60 07 19.4	24	1	569	8	48	0.8	5.9	0.2	35	2.8	2.5
43	20 35 12.4	60 02 50.9	60	1	660	8	111	0.7	14.6	-1.0	40	1.8	1.6
44	20 35 13.1	60 07 14.9	11	1	321	8	3	0.6	6.7	0.1	20	2.0	2.0
45	20 35 13.1	60 09 49.4	-43	1	578	8	162	0.7	4.7	0.3	35	3.0	2.6
46	20 35 13.7	60 11 07.4	-66	1	841	8	111	0.7	5.6	0.1	51	3.3	2.8
47	20 35 15.3	60 07 59.9	-2	1	495	8	129	0.6	6.2	0.1	30	2.5	2.3
48	20 35 17.1	60 09 25.4	-43	3	309	15	0	0.7	5.6	0.3	10	2.5	2.1
49	20 35 18.9	60 10 22.3	-61	1	646	8	68	0.6	6.1	0.2	40	3.0	2.7
50	20 35 20.3	60 04 52.3	34	1	1072	8	16	0.5	11.8	-0.5	66	2.9	2.9
51	20 35 21.0	60 10 14.8	-64	1	1384	8	144	0.9	6.5	0.1	85	3.9	3.2
52	20 35 21.9	60 07 49.3	-15	1	526	8	107	0.5	7.7	-0.2	32	2.3	2.3
53	20 35 27.2	60 13 32.7	-53	1	1759	8	67	0.5	10.8	-0.8	108	3.3	3.0
54	20 35 29.2	60 08 22.2	-33	1	713	8	171	0.9	8.8	-0.3	44	2.6	2.5

Table 2.21 (cont'd)

No	α (h m s)	δ ($^\circ$ $'$ $''$)	$V_{\rm hel}$ (km s^{-1})	*Type* (1 – 3)	d (pc)	$V_{\rm exp}$ (km s^{-1})	*P.A.* ($^\circ$)	*Axial Ratio*	R (kpc)	$log(n_{\rm HI})$ (cm^{-3})	$t_{\rm kin}$ (Myr)	$log(E_{\rm E})$ (10^{50} erg)	$log(M_{\rm HI})$ (10^4 M$_\odot$)
55	20 35 29.3	60 05 07.2	19	1	846	8	133	0.7	12.8	-0.7	52	2.4	2.6
56	20 35 31.5	60 03 14.6	34	1	508	8	88	0.7	16.3	-1.1	31	1.2	1.1
57	20 35 35.4	60 09 10.1	-40	1	916	8	55	0.6	9.7	-0.6	56	2.7	2.5
58	20 35 38.2	60 07 40.0	-20	1	2141	8	37	0.9	11.3	-0.7	131	3.7	3.3

Table 2.22. NGC 7793 hole properties

No	α (h m s)	δ ($^\circ$ $'$ $''$)	$V_{\rm hel}$ (km s^{-1})	*Type* (1 − 3)	d (pc)	$V_{\rm exp}$ (km s^{-1})	*P.A.* ($^\circ$)	*Axial Ratio*	R (kpc)	$log(n_{\rm HI})$ (cm^{-3})	$t_{\rm kin}$ (Myr)	$log(E_{\rm E})$ (10^{50} erg)	$log(M_{\rm HI})$ (10^4 M$_\odot$)
1	23 57 29.1	-32 35 04.4	310	1	443	8	22	0.8	5.2	-0.6	27	1.7	1.5
2	23 57 35.5	-32 35 57.0	286	1	754	8	10	0.7	3.9	-0.2	46	2.8	2.7
3	23 57 35.7	-32 34 58.5	302	1	313	8	174	0.6	3.5	0.0	19	1.8	2.0
4	23 57 36.7	-32 35 46.5	286	1	852	8	64	0.9	3.5	-0.1	52	3.1	2.8
5	23 57 37.5	-32 33 07.5	291	2	336	16	13	0.7	4.3	-0.4	10	2.0	1.4
6	23 57 41.1	-32 33 60.0	299	2	401	13	45	0.6	2.7	0.0	15	2.5	2.2
7	23 57 41.4	-32 37 07.5	253	1	189	8	0	0.8	3.9	-0.1	12	1.0	0.8
8	23 57 43.3	-32 36 33.0	248	1	434	8	175	0.4	2.7	0.0	27	2.3	2.2
9	23 57 43.5	-32 34 18.0	279	3	511	7	26	0.7	2.2	0.1	36	2.6	2.4
10	23 57 45.0	-32 35 39.0	260	2	557	14	18	0.8	1.3	0.3	19	3.3	2.5
11	23 57 46.7	-32 34 06.0	253	2	491	10	34	0.7	2.2	0.2	24	2.8	2.4
12	23 57 48.1	-32 35 28.5	237	2	381	16	11	0.6	0.4	0.4	12	3.0	2.1
13	23 57 49.5	-32 35 27.0	227	3	313	7	14	0.9	0.3	0.4	22	2.3	2.0
14	23 57 52.7	-32 35 48.0	204	1	396	8	90	0.8	0.8	0.3	24	2.5	2.2
15	23 57 54.0	-32 37 40.5	186	1	360	8	138	0.6	3.5	-0.1	22	1.9	2.1
16	23 57 55.2	-32 34 51.0	186	1	496	8	0	0.5	2.0	0.1	30	2.6	2.3
17	23 57 55.6	-32 37 42.0	178	1	197	8	0	0.8	3.6	-0.2	12	1.0	0.8
18	23 57 57.4	-32 37 52.5	175	1	386	8	48	0.8	4.0	-0.4	24	1.7	2.0
19	23 57 57.9	-32 34 54.0	186	1	521	8	10	0.6	2.6	0.1	32	2.7	2.5
20	23 57 59.6	-32 37 25.5	162	3	335	10	54	0.5	3.6	-0.3	16	1.8	1.9
21	23 58 03.6	-32 33 15.0	188	2	510	16	43	0.9	5.8	-0.7	16	2.1	1.5
22	23 58 03.7	-32 35 03.0	157	2	426	8	0	0.9	3.9	-0.3	26	1.9	2.1
23	23 58 06.3	-32 34 01.4	178	1	1056	8	15	0.7	5.5	-0.6	65	2.8	2.9
24	23 58 09.5	-32 36 23.9	142	1	706	8	79	0.8	4.9	-0.5	43	2.4	2.5
25	23 58 10.8	-32 37 59.9	152	2	432	13	0	0.8	5.9	-0.8	16	1.7	1.2
26	23 58 11.2	-32 36 01.4	147	1	483	8	179	1.0	5.4	-0.6	30	1.8	1.6
27	23 58 15.8	-32 37 11.8	150	1	528	8	153	0.8	6.6	-0.9	32	1.5	1.4

Table 2.22 (cont'd)

No	α (h m s)	δ (° ′ ″)	$V_{\rm hel}$ (km s^{-1})	*Type* (1 − 3)	d (pc)	$V_{\rm exp}$ (km s^{-1})	*P.A.* (°)	*Axial Ratio*	R (kpc)	$log(n_{\rm HI})$ (cm^{-3})	$t_{\rm kin}$ (Myr)	$log(E_{\rm E})$ (10^{50} erg)	$log(M_{\rm HI})$ (10^4 M$_\odot$)

2.6 Figures

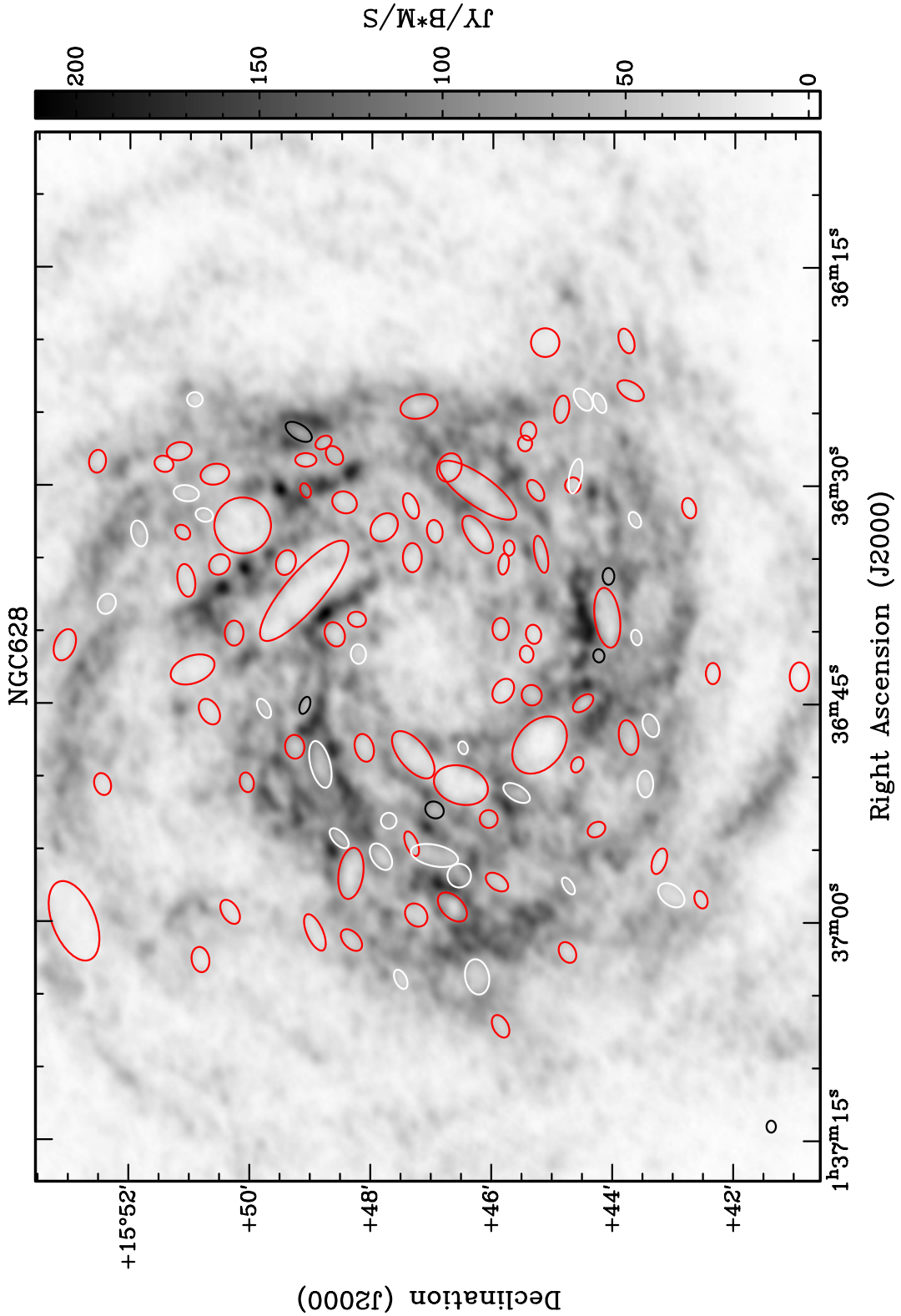

Figure 2.3: Position of the H I holes in NGC 628. The colours illustrate the different type of the holes: red - type 1, white - type 2 and black - type3. The gray-scale map is a linear representation of the H I surface brightness map and the size of the beam is illustrated in the bottom left corner.

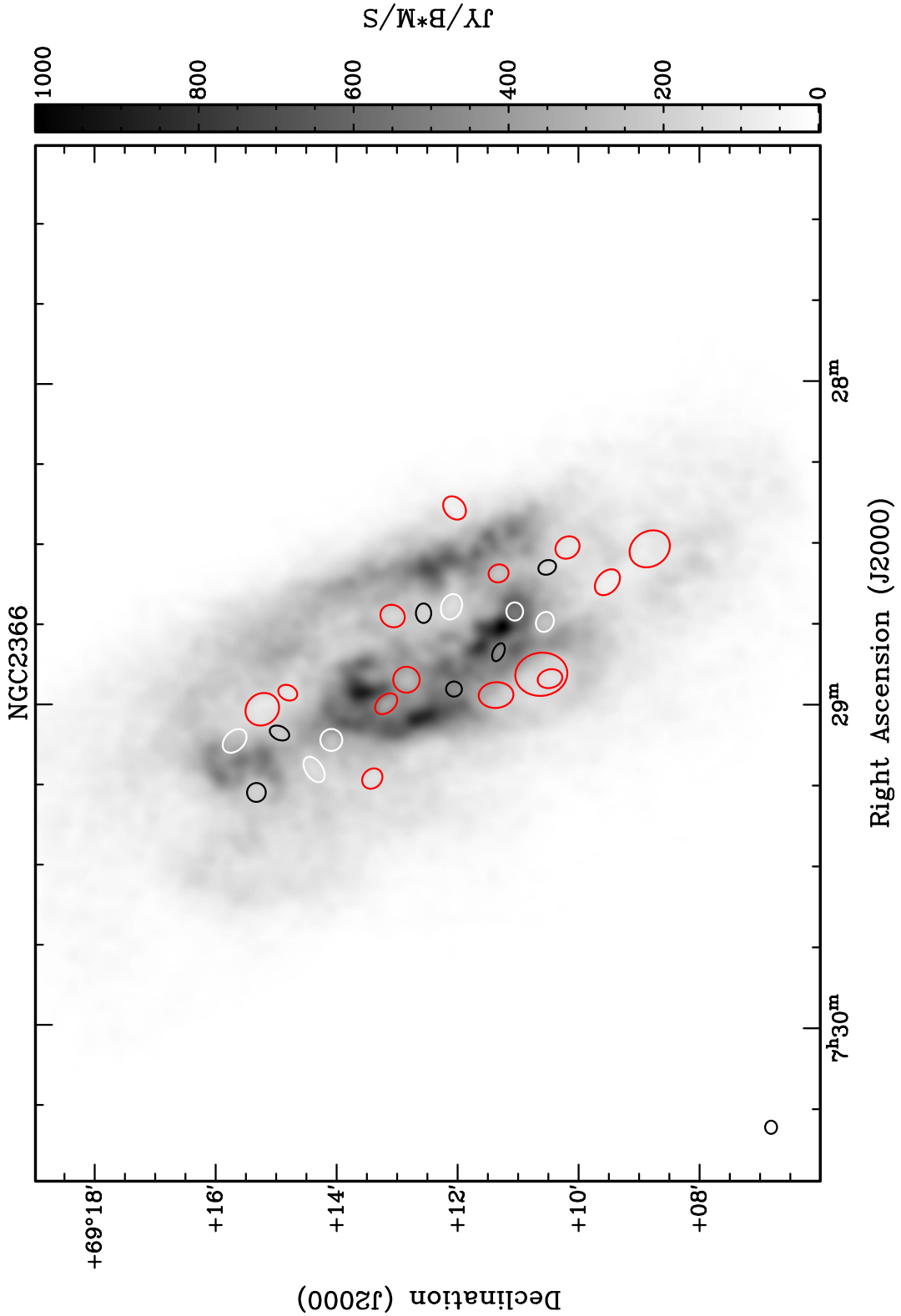

Figure 2.4: Position of the H I holes in NGC 2366. The colours illustrate the different type of the holes: red - type 1, white - type 2 and black - type3. The gray-scale map is a linear representation of the H I surface brightness map.

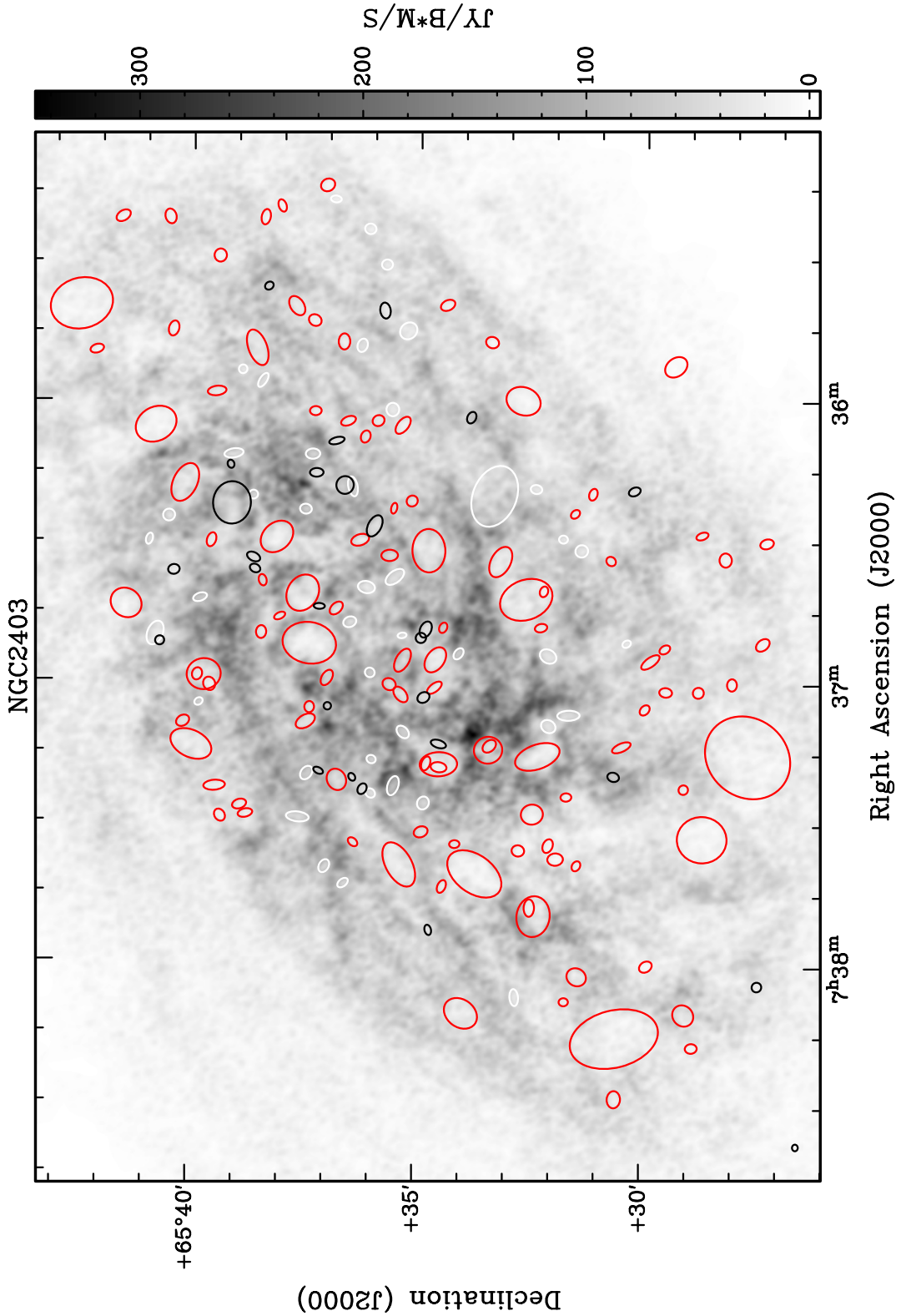

Figure 2.5: Position of the H I holes in NGC 2403. The colours illustrate the different type of the holes: red - type 1, white - type 2 and black - type3. The gray-scale map is a linear representation of the H I surface brightness map and the size of the beam is illustrated in the bottom left corner.

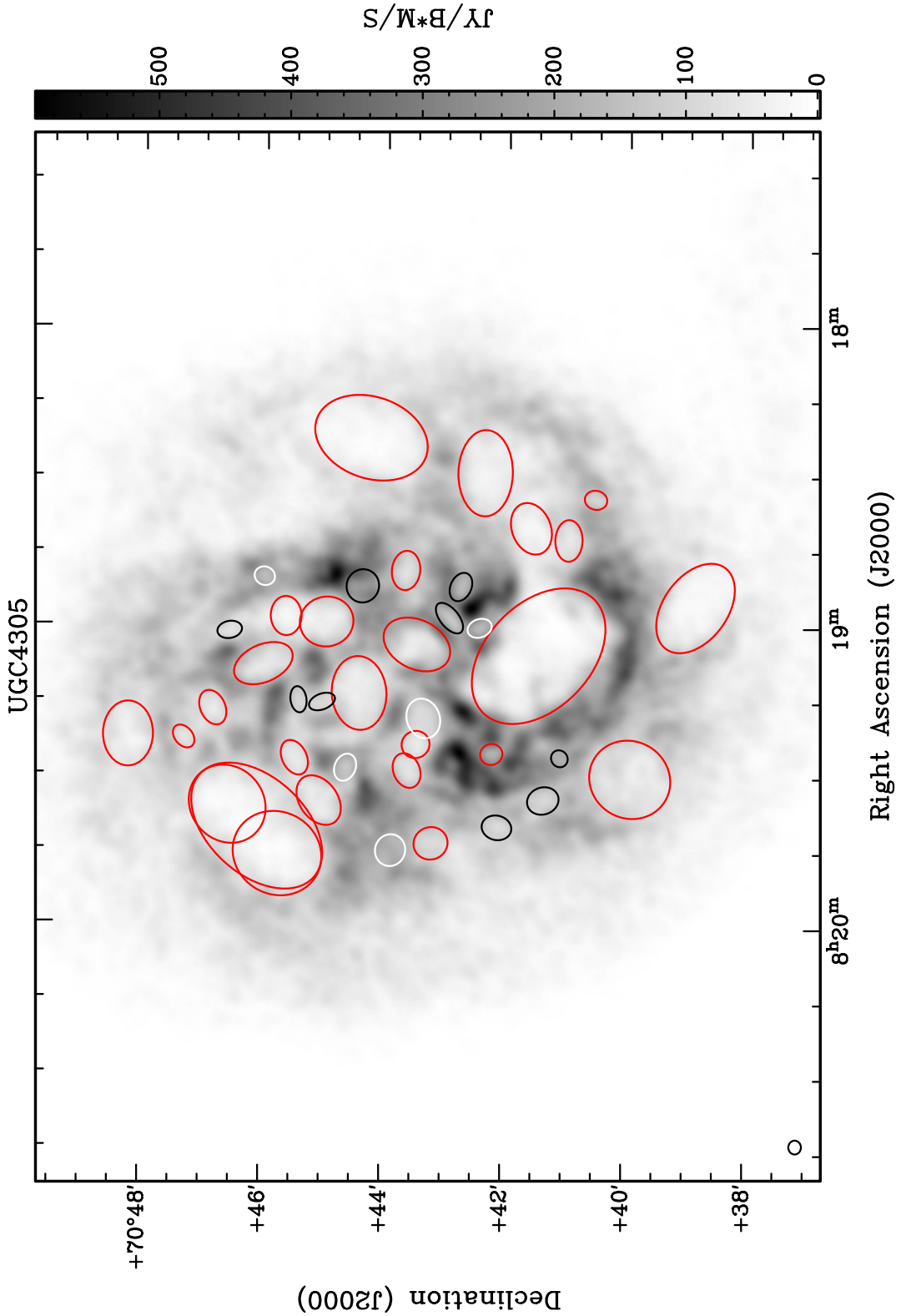

Figure 2.6: Position of the H I holes in Holmberg II. The colours illustrate the different type of the holes: red - type 1, white - type 2 and black - type3. The gray-scale map is a linear representation of the H I surface brightness map and the size of the beam is illustrated in the bottom left corner.

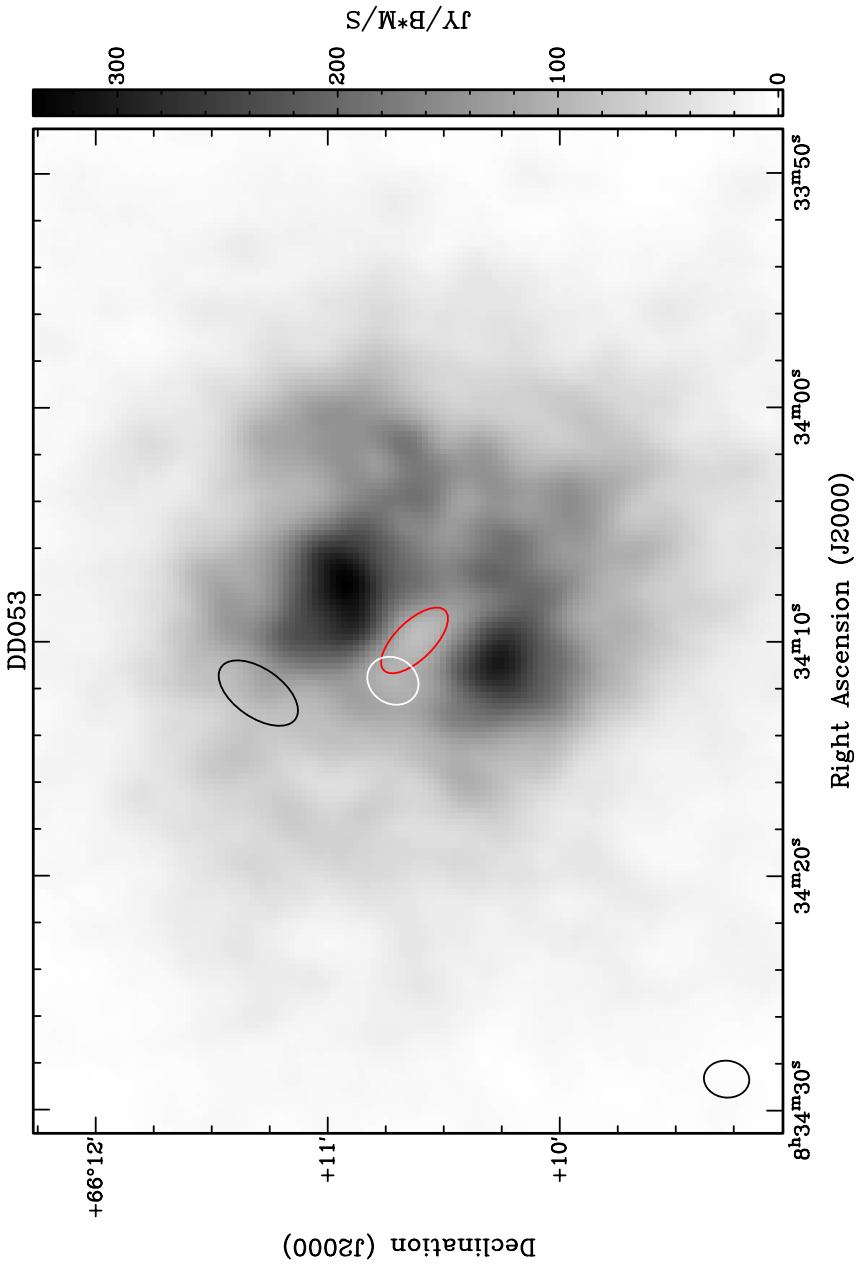

Figure 2.7: Position of the H I holes in DDO 53. The colours illustrate the different type of the holes: red - type 1, white - type 2 and black - type3. The gray-scale map is a linear representation of the H I surface brightness map and the size of the beam is illustrated in the bottom left corner.

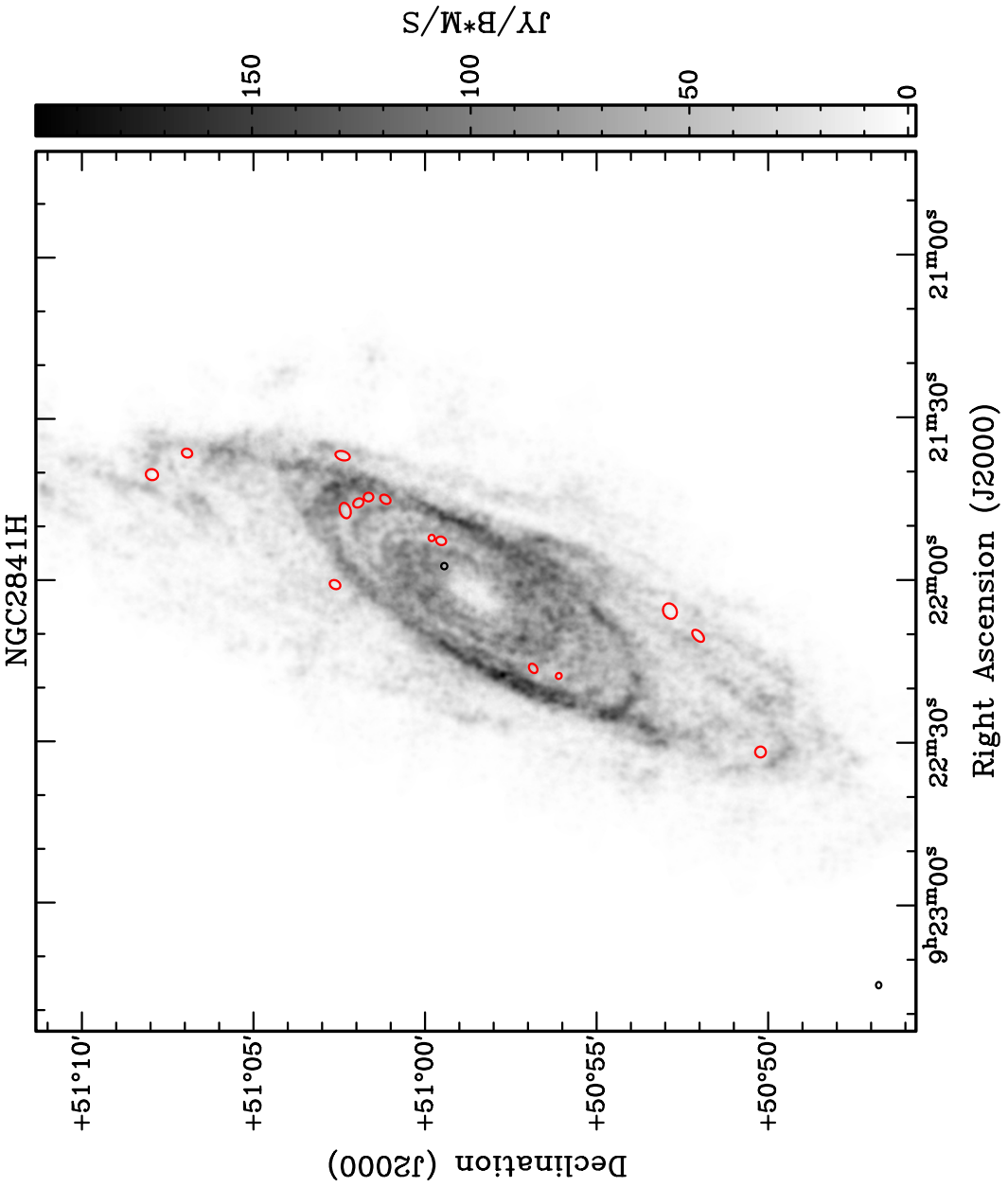

Figure 2.8: Position of the H I holes in NGC 2841. The colours illustrate the different type of the holes: red - type 1, white - type 2 and black - type3. The gray-scale map is a linear representation of the H I surface brightness map and the size of the beam is illustrated in the bottom left corner.

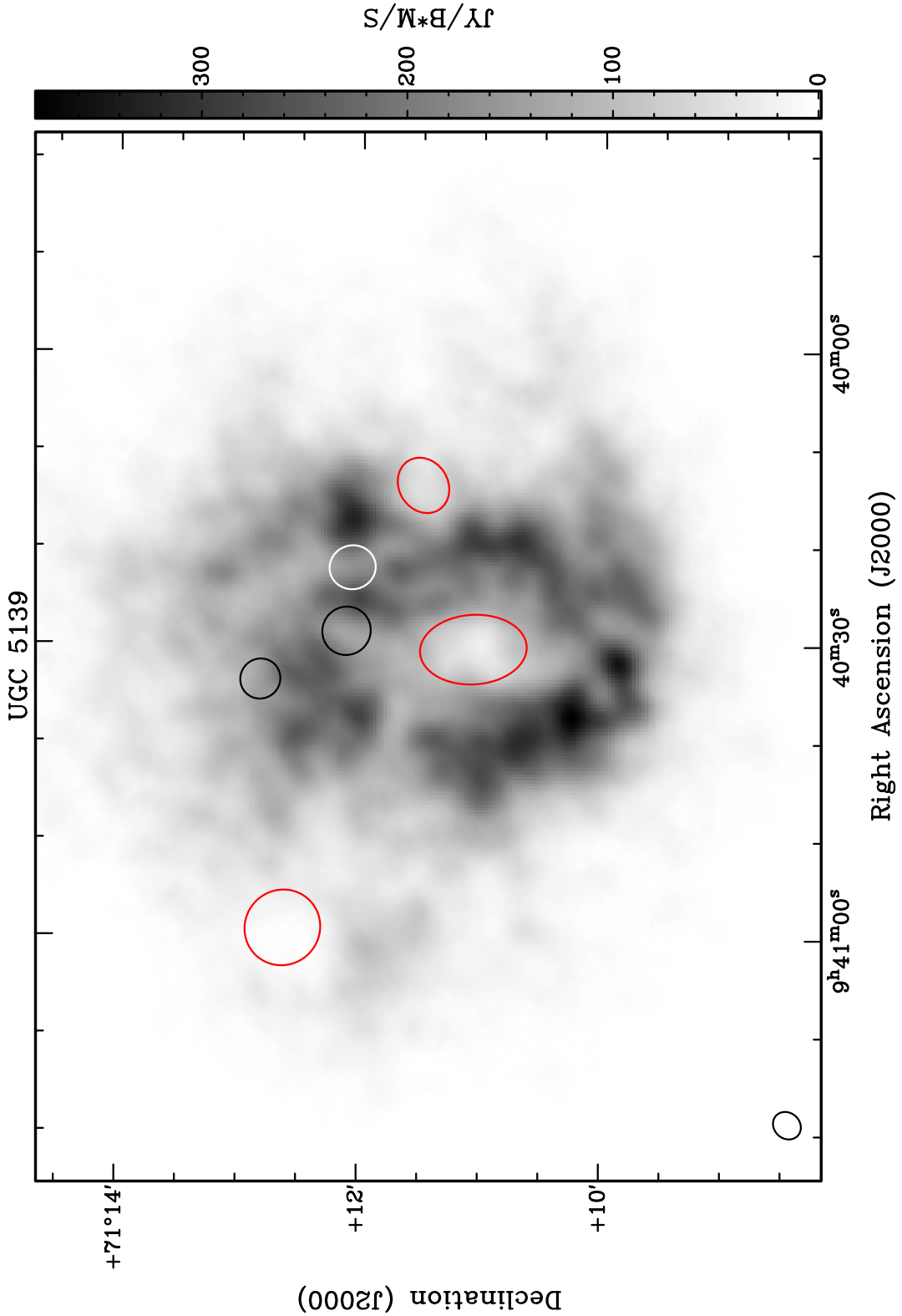

Figure 2.9: Position of the H I holes in Holmberg I. The colours illustrate the different type of the holes: red - type 1, white - type 2 and black - type3. The gray-scale map is a linear representation of the H I surface brightness map and the size of the beam is illustrated in the bottom left corner.

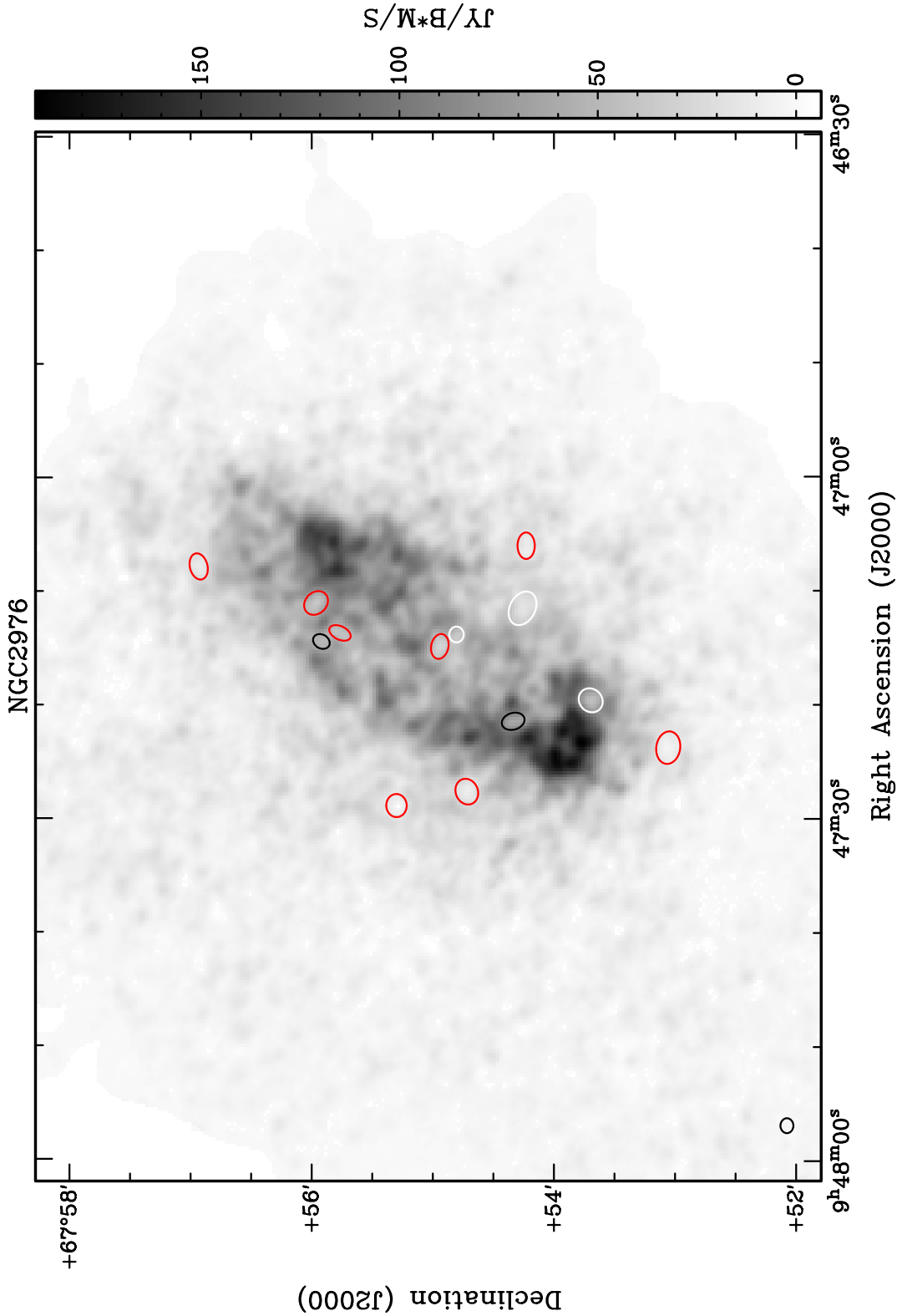

Figure 2.10: Position of the H I holes in NGC 2976. The colours illustrate the different type of the holes: red - type 1, white - type 2 and black - type3. The gray-scale map is a linear representation of the H I surface brightness map and the size of the beam is illustrated in the bottom left corner.

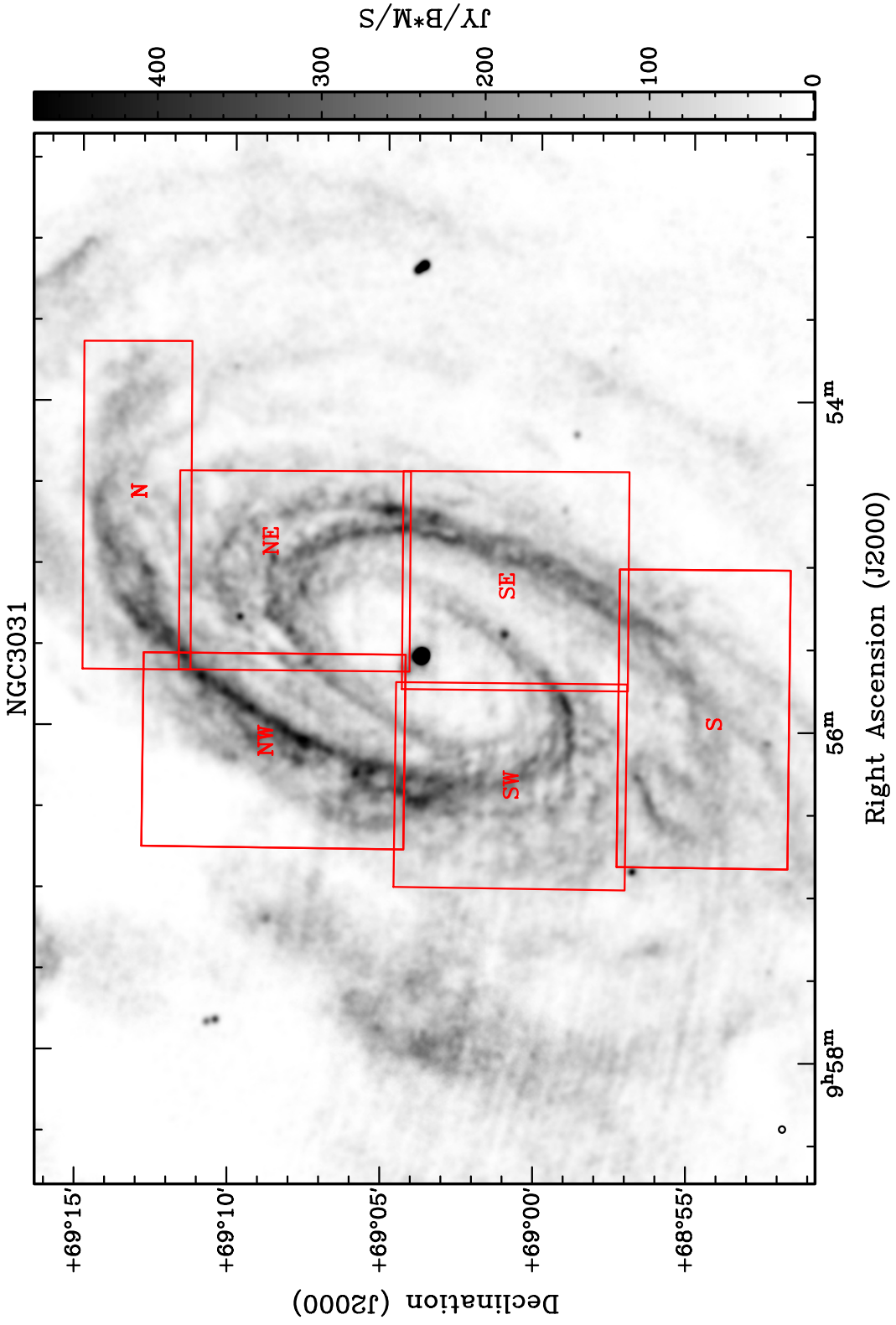

Figure 2.11: NGC 3031 divided into 6 fields. The gray-scale map is a linear representation of the H I surface brightness map and the size of the beam is illustrated in the bottom left corner.

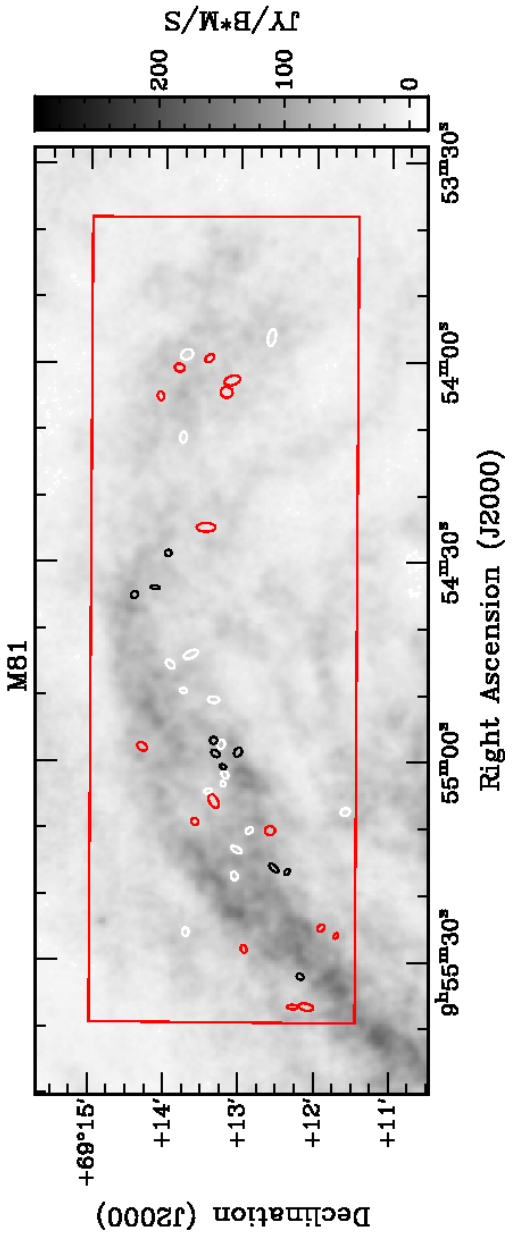

Figure 2.12: Position of the H I holes in the north field of NGC 3031. The colours illustrate the different type of the holes: red - type 1, white - type 2 and black - type3. The gray-scale map is a linear representation of the H I surface brightness map.

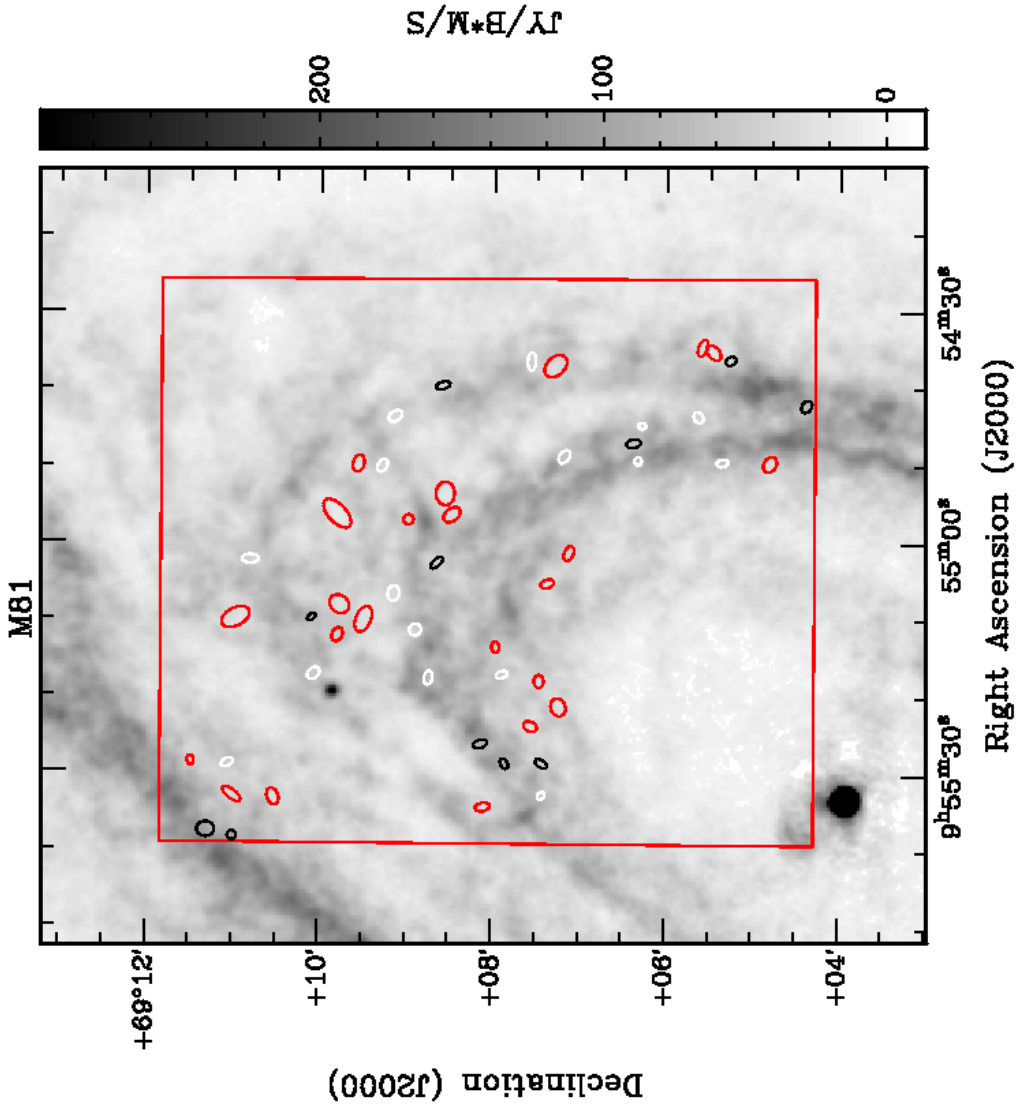

Figure 2.13: Position of the H I holes in the north–east field of NGC 3031. The colours illustrate the different type of the holes: red - type 1, white - type 2 and black - type3. The gray-scale map is a linear representation of the H I surface brightness map.

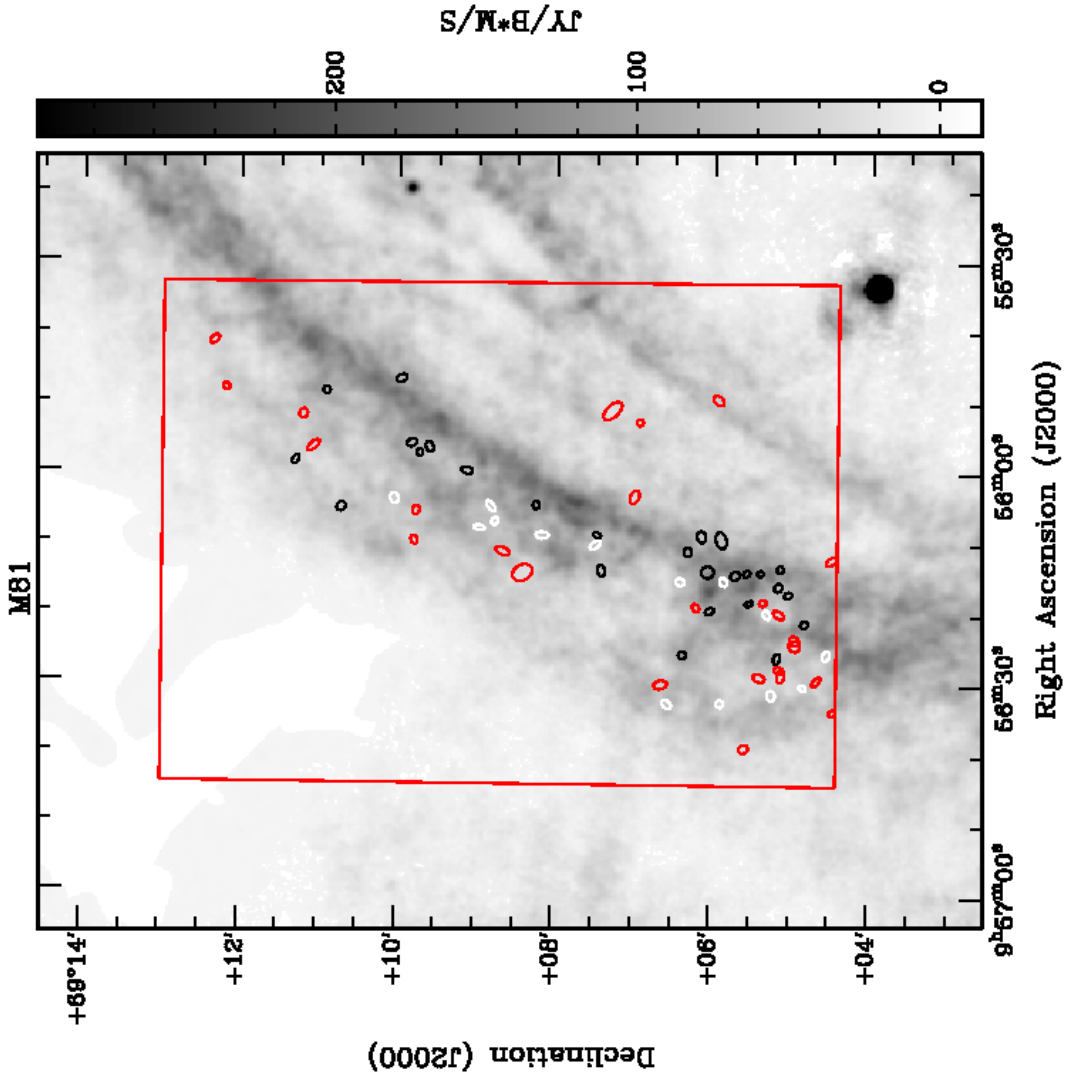

Figure 2.14: Position of the H I holes in the north–west field of NGC 3031. The colours illustrate the different type of the holes: red - type 1, white - type 2 and black - type3. The gray-scale map is a linear representation of the H I surface brightness map.

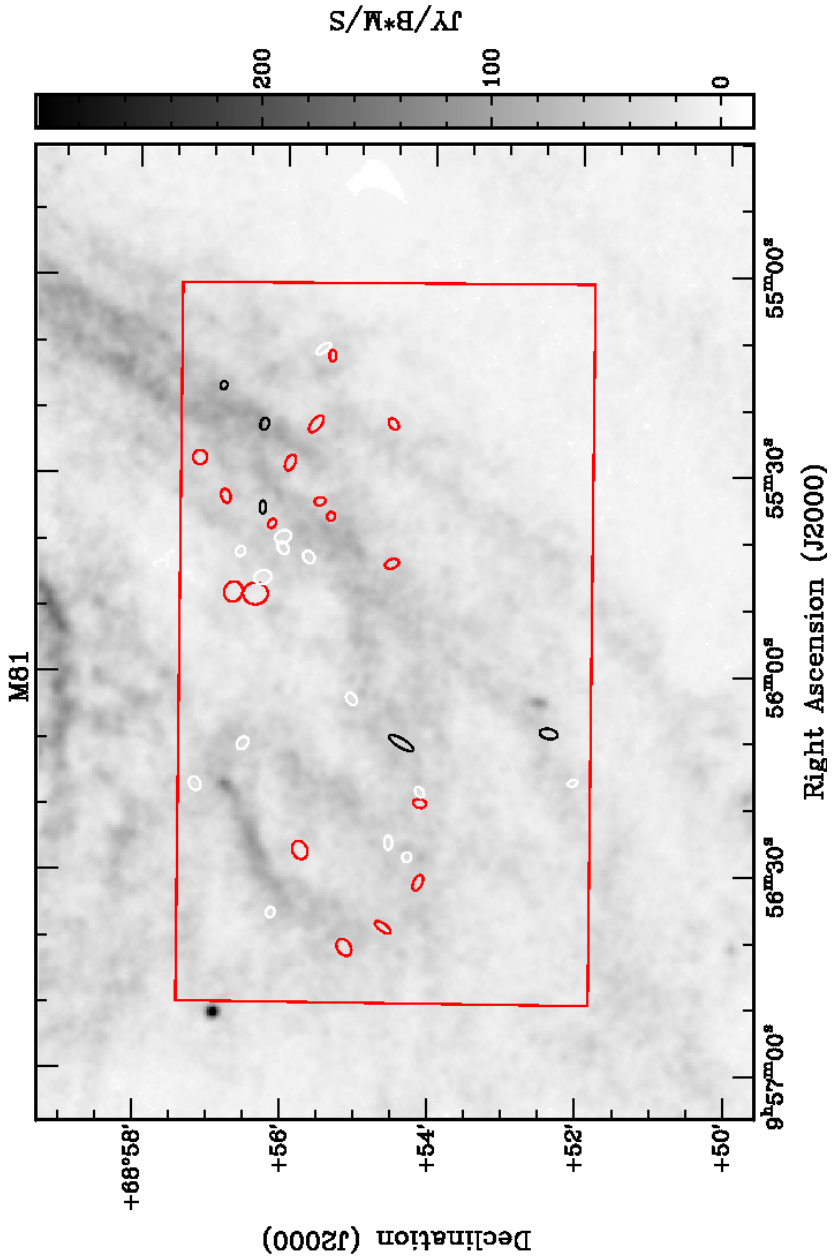

Figure 2.15: Position of the H I holes in the south field of NGC 3031. The colours illustrate the different type of the holes: red - type 1, white - type 2 and black - type3. The gray-scale map is a linear representation of the H I surface brightness map.

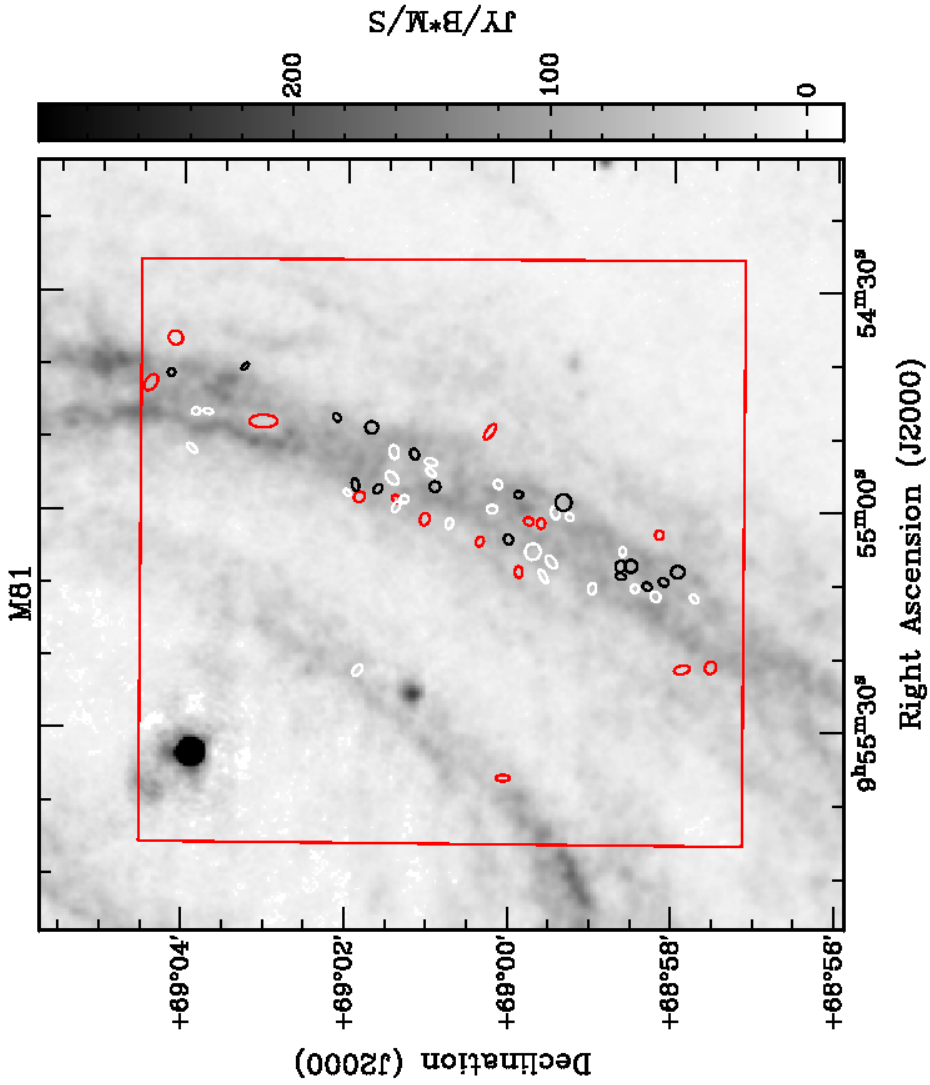

Figure 2.16: Position of the H I holes in the south–east field of NGC 3031. The colours illustrate the different type of the holes: red - type 1, white - type 2 and black - type3. The gray-scale map is a linear representation of the H I surface brightness map.

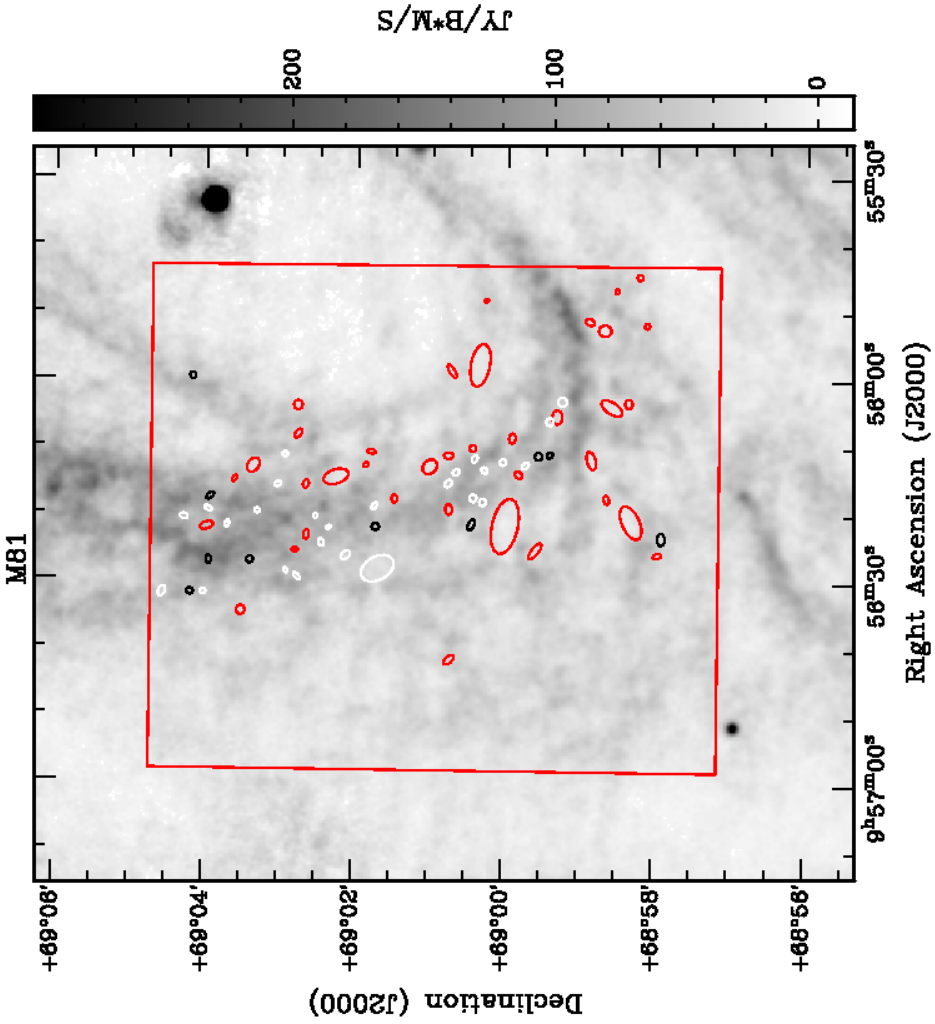

Figure 2.17: Position of the H I holes in the south–west field of NGC 3031. The colours illustrate the different type of the holes: red - type 1, white - type 2 and black - type3. The gray-scale map is a linear representation of the H I surface brightness map.

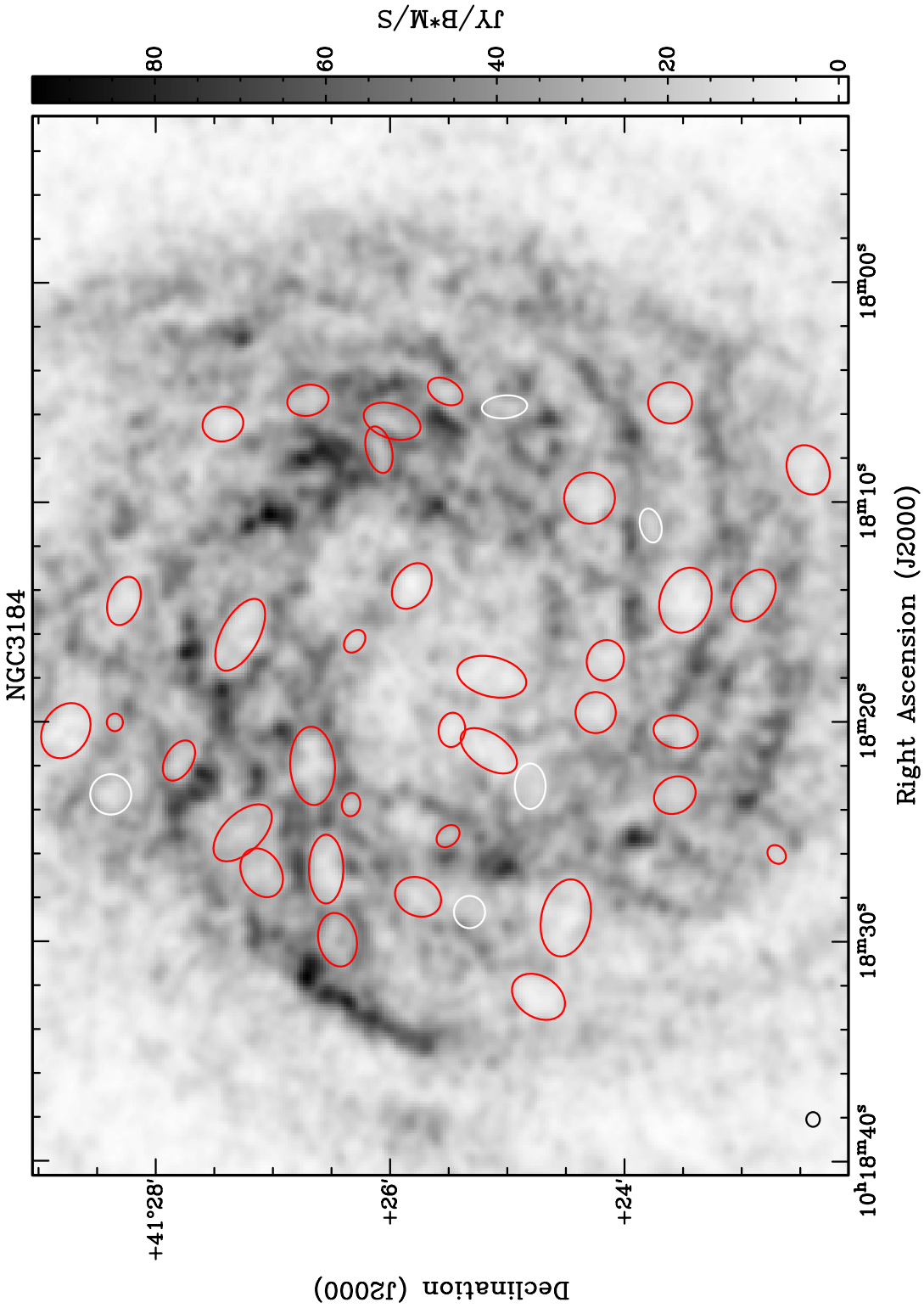

Figure 2.18: Position of the H I holes in NGC 3184. The colours illustrate the different type of the holes: red - type 1, white - type 2 and black - type3. The gray-scale map is a linear representation of the H I surface brightness map and the size of the beam is illustrated in the bottom left corner.

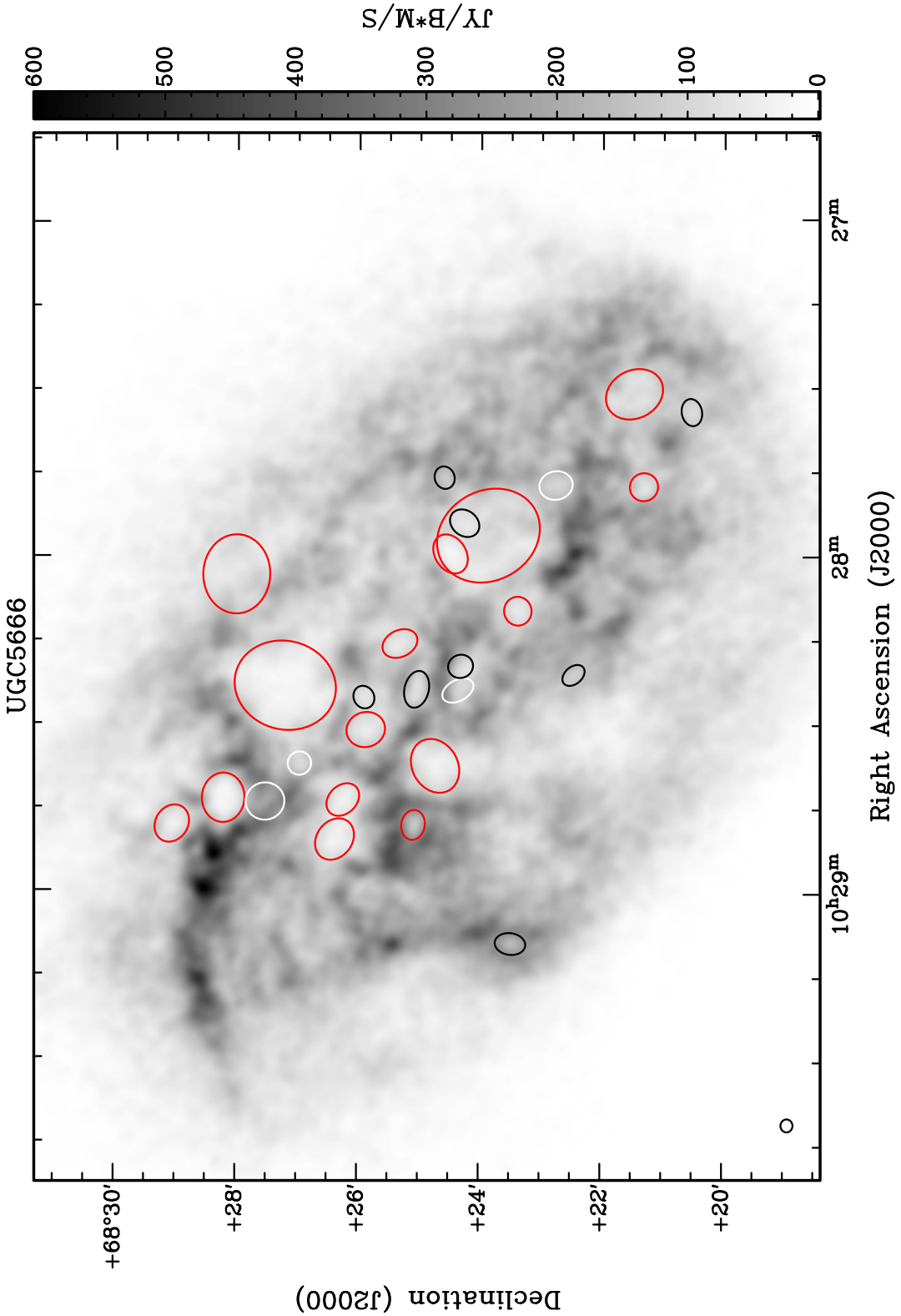

Figure 2.19: Position of the H I holes in IC 2574. The colours illustrate the different type of the holes: red - type 1, white - type 2 and black - type3. The gray-scale map is a linear representation of the H I surface brightness map and the size of the beam is illustrated in the bottom left corner.

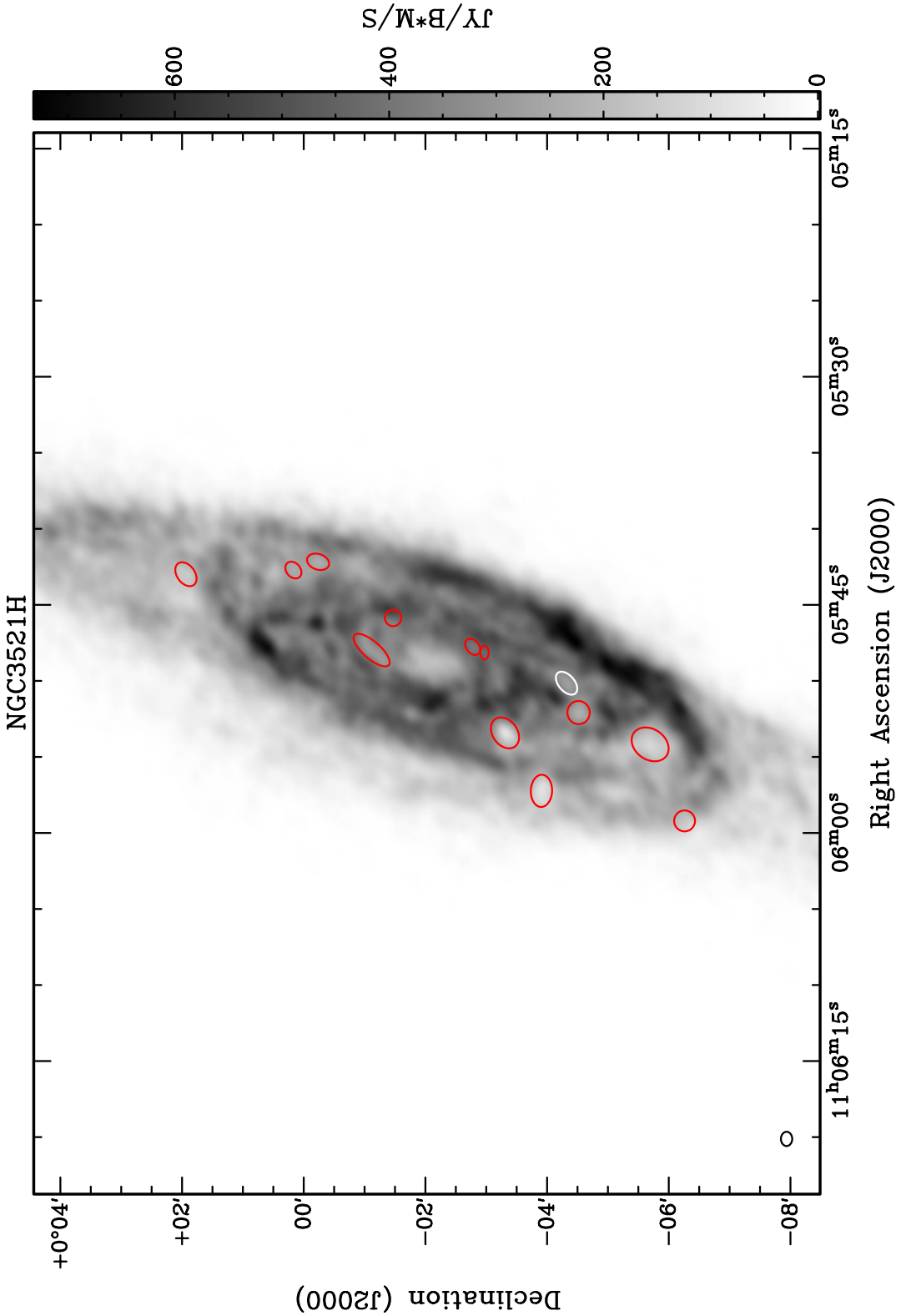

Figure 2.20: Position of the H I holes in NGC 3521. The colours illustrate the different type of the holes: red - type 1, white - type 2 and black - type3. The gray-scale map is a linear representation of the H I surface brightness map and the size of the beam is illustrated in the bottom left corner.

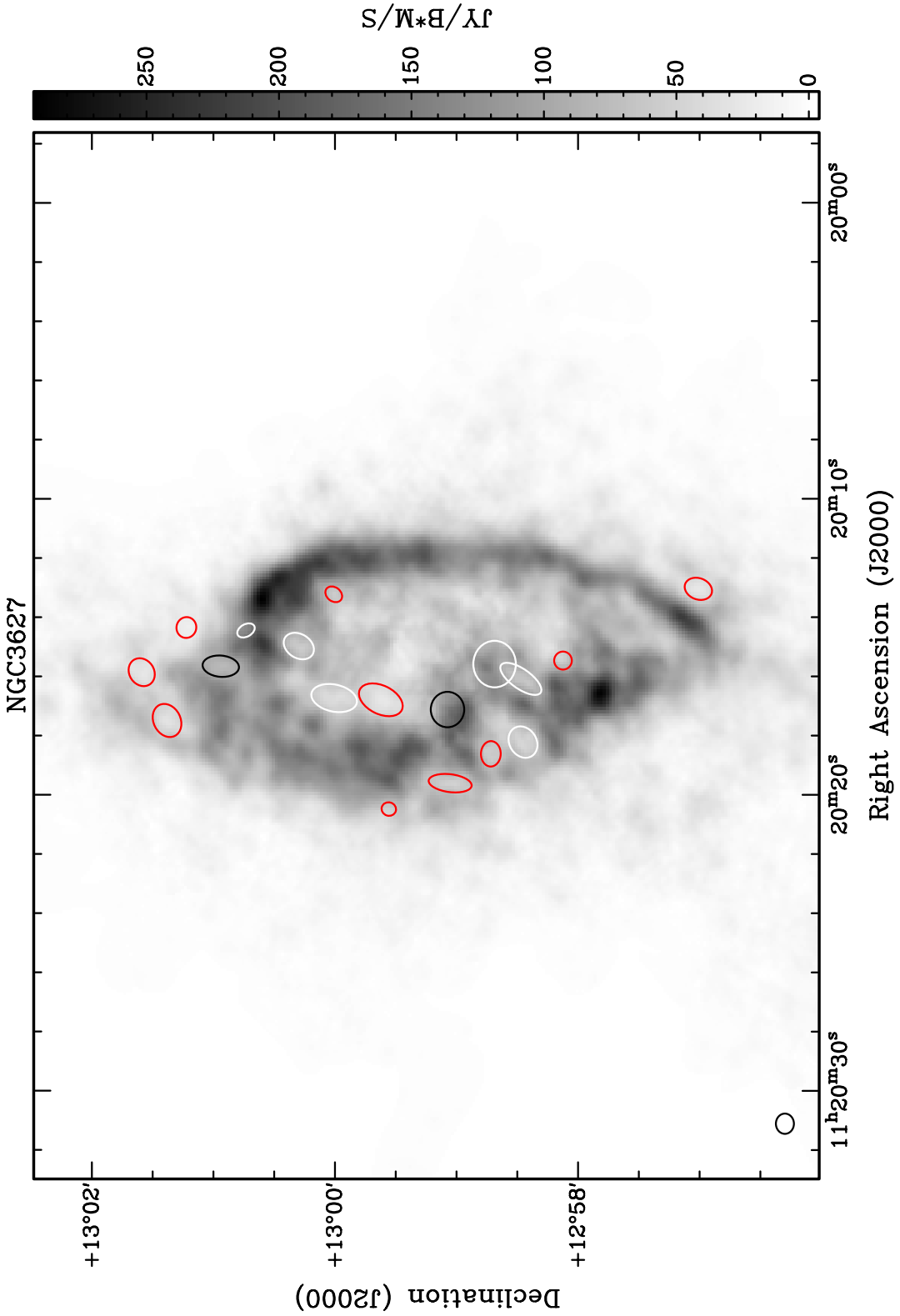

Figure 2.21: Position of the H I holes in NGC 3627. The colours illustrate the different type of the holes: red - type 1, white - type 2 and black - type3. The gray-scale map is a linear representation of the H I surface brightness map and the size of the beam is illustrated in the bottom left corner.

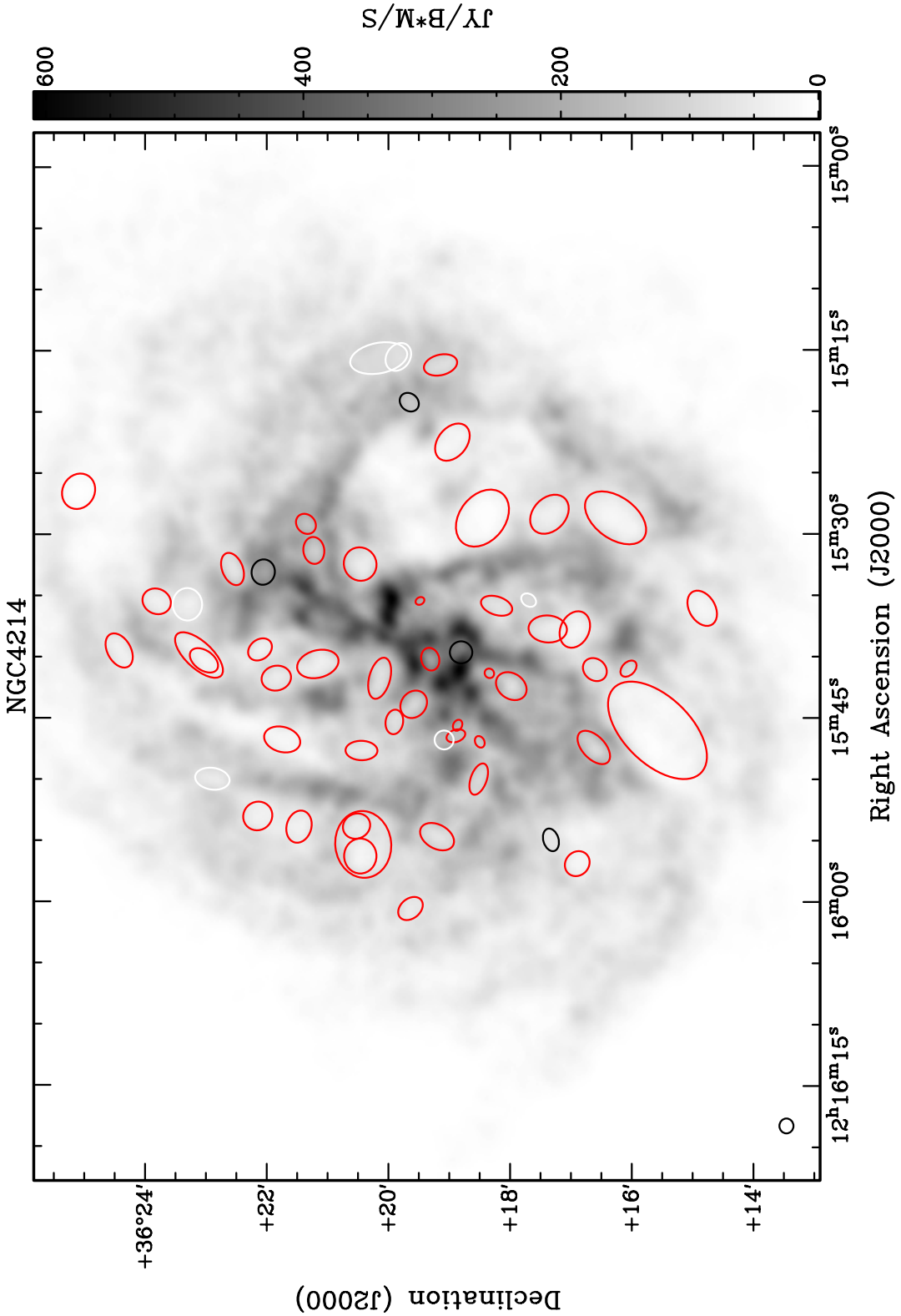

Figure 2.22: Position of the H I holes in NGC 4214. The colours illustrate the different type of the holes: red - type 1, white - type 2 and black - type3. The gray-scale map is a linear representation of the H I surface brightness map and the size of the beam is illustrated in the bottom left corner.

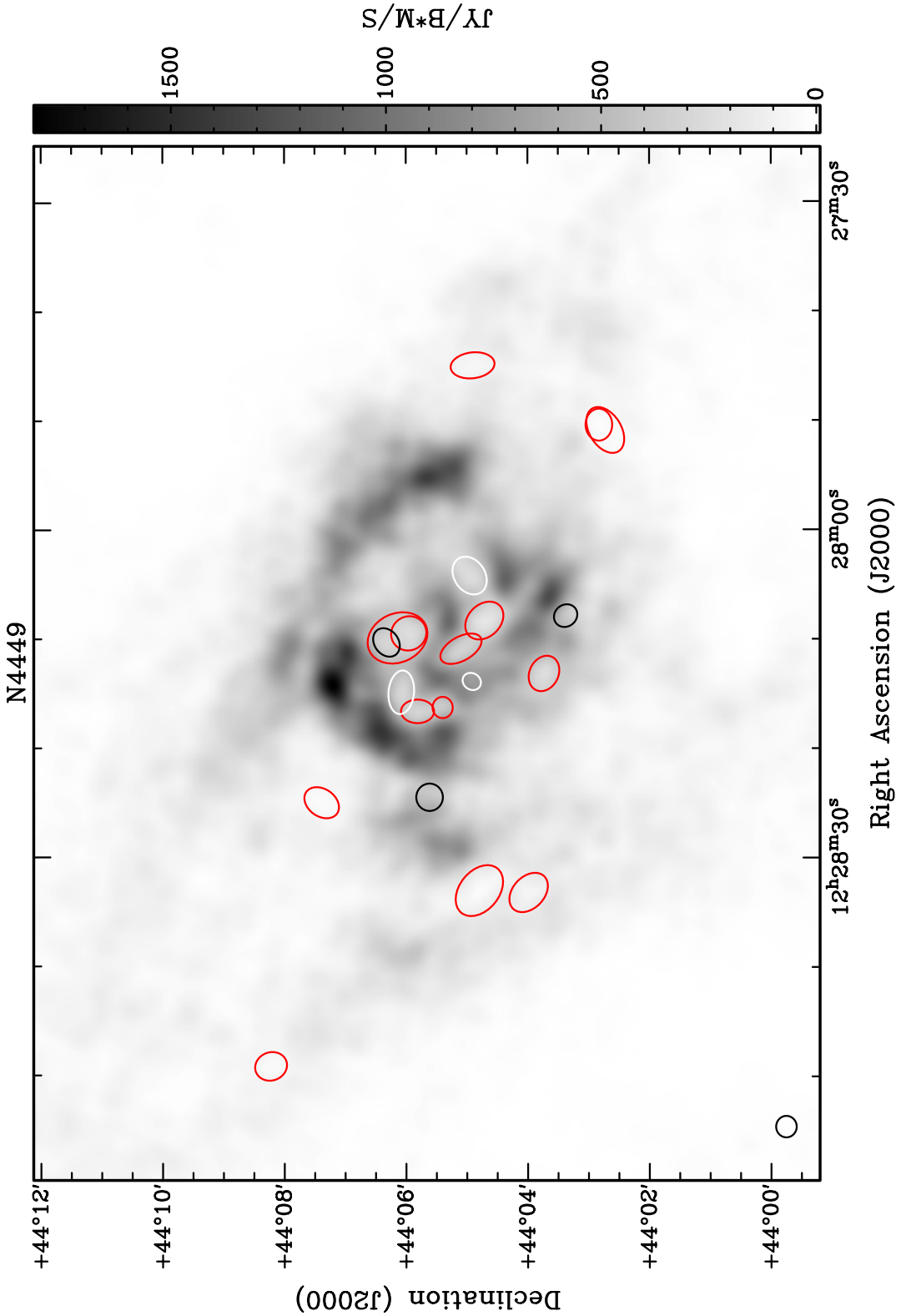

Figure 2.23: Position of the H I holes in NGC 4449. The colours illustrate the different type of the holes: red - type 1, white - type 2 and black - type3. The gray-scale map is a linear representation of the H I surface brightness map and the size of the beam is illustrated in the bottom left corner.

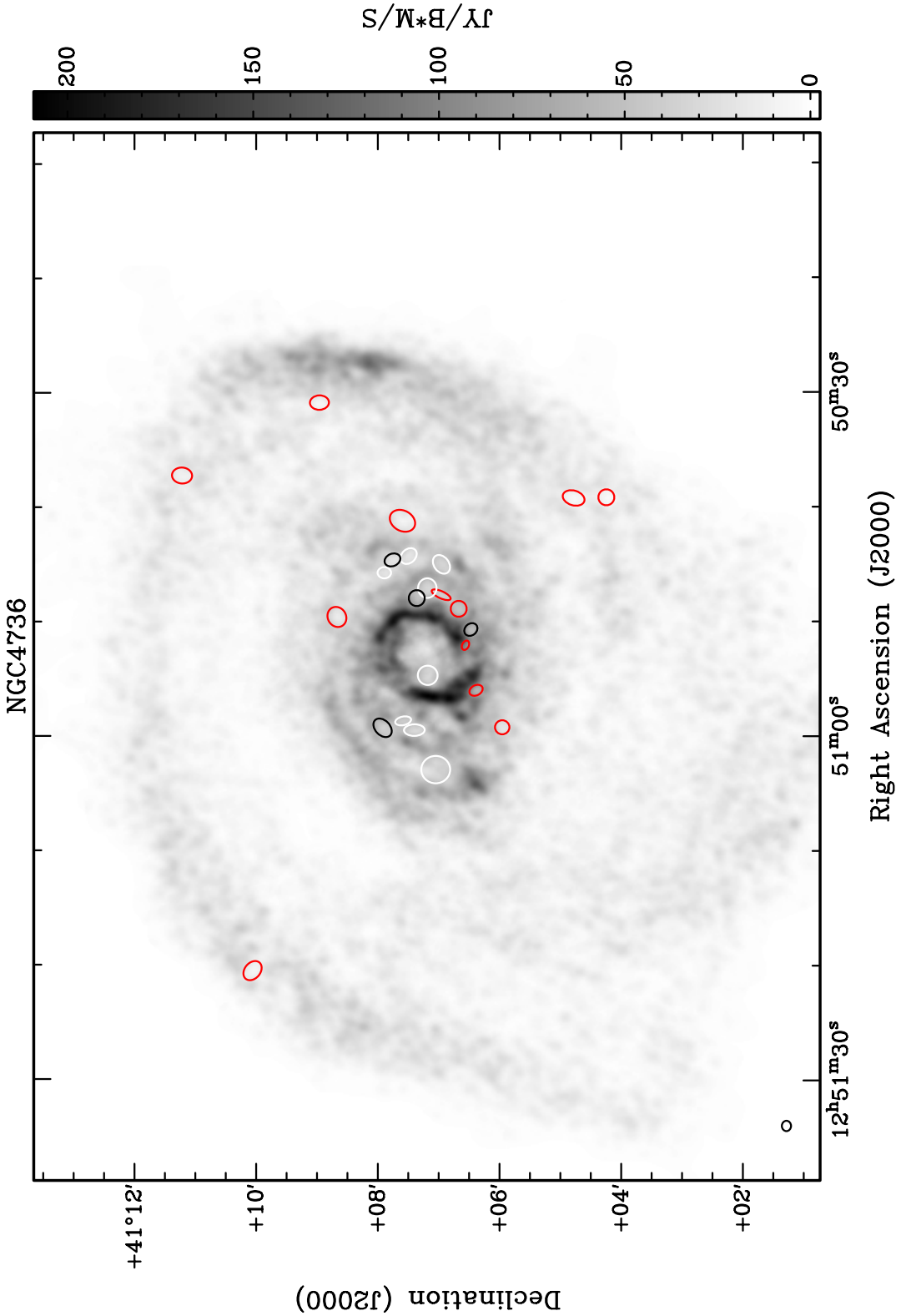

Figure 2.24: Position of the H I holes in NGC 4736. The colours illustrate the different type of the holes: red - type 1, white - type 2 and black - type3. The gray-scale map is a linear representation of the H I surface brightness map and the size of the beam is illustrated in the bottom left corner.

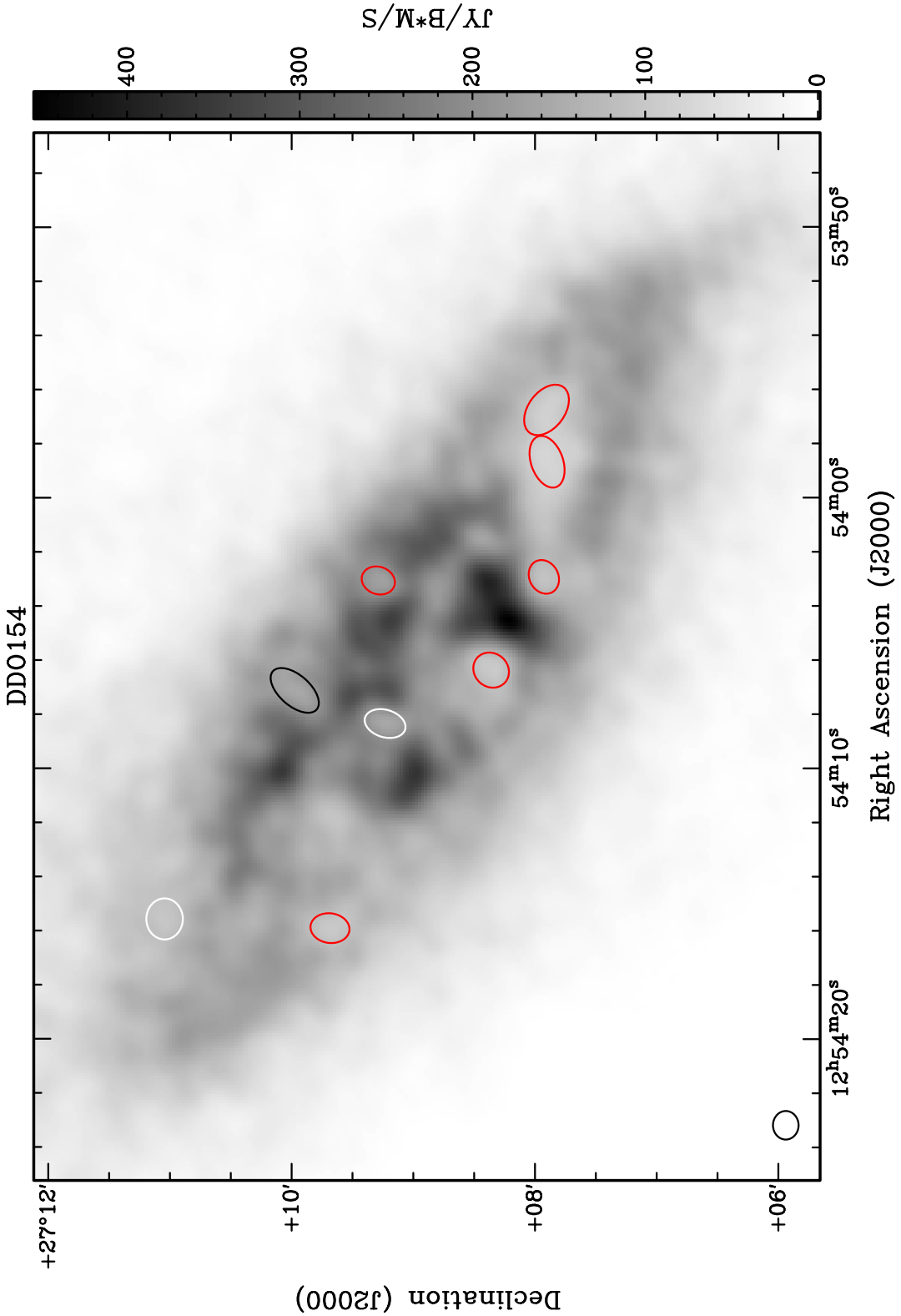

Figure 2.25: Position of the H I holes in DDO 154. The colours illustrate the different type of the holes: red - type 1, white - type 2 and black - type3. The gray-scale map is a linear representation of the H I surface brightness map and the size of the beam is illustrated in the bottom left corner.

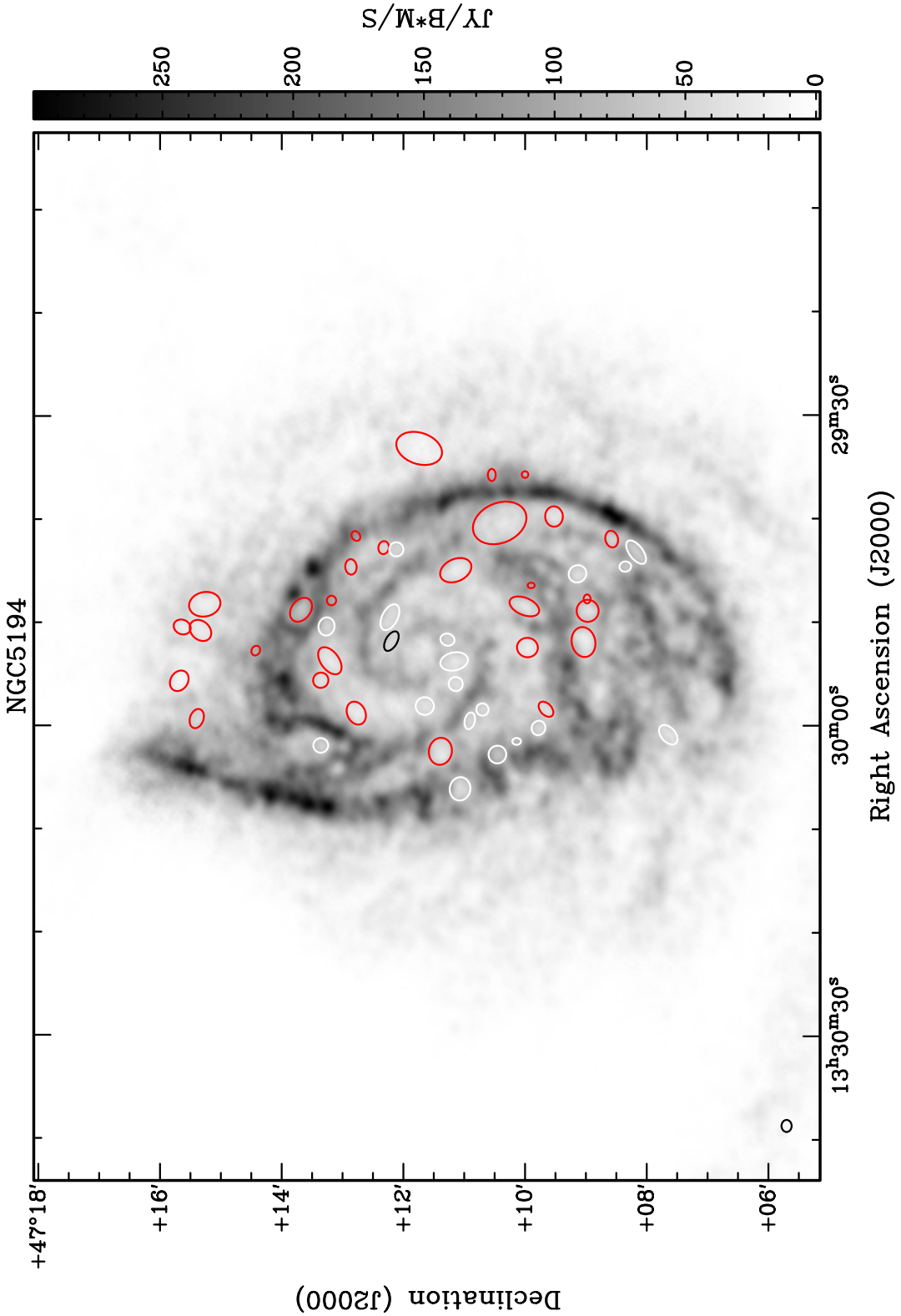

Figure 2.26: Position of the H I holes in NGC 5194. The colours illustrate the different type of the holes: red - type 1, white - type 2 and black - type3. The gray-scale map is a linear representation of the H I surface brightness map and the size of the beam is illustrated in the bottom left corner.

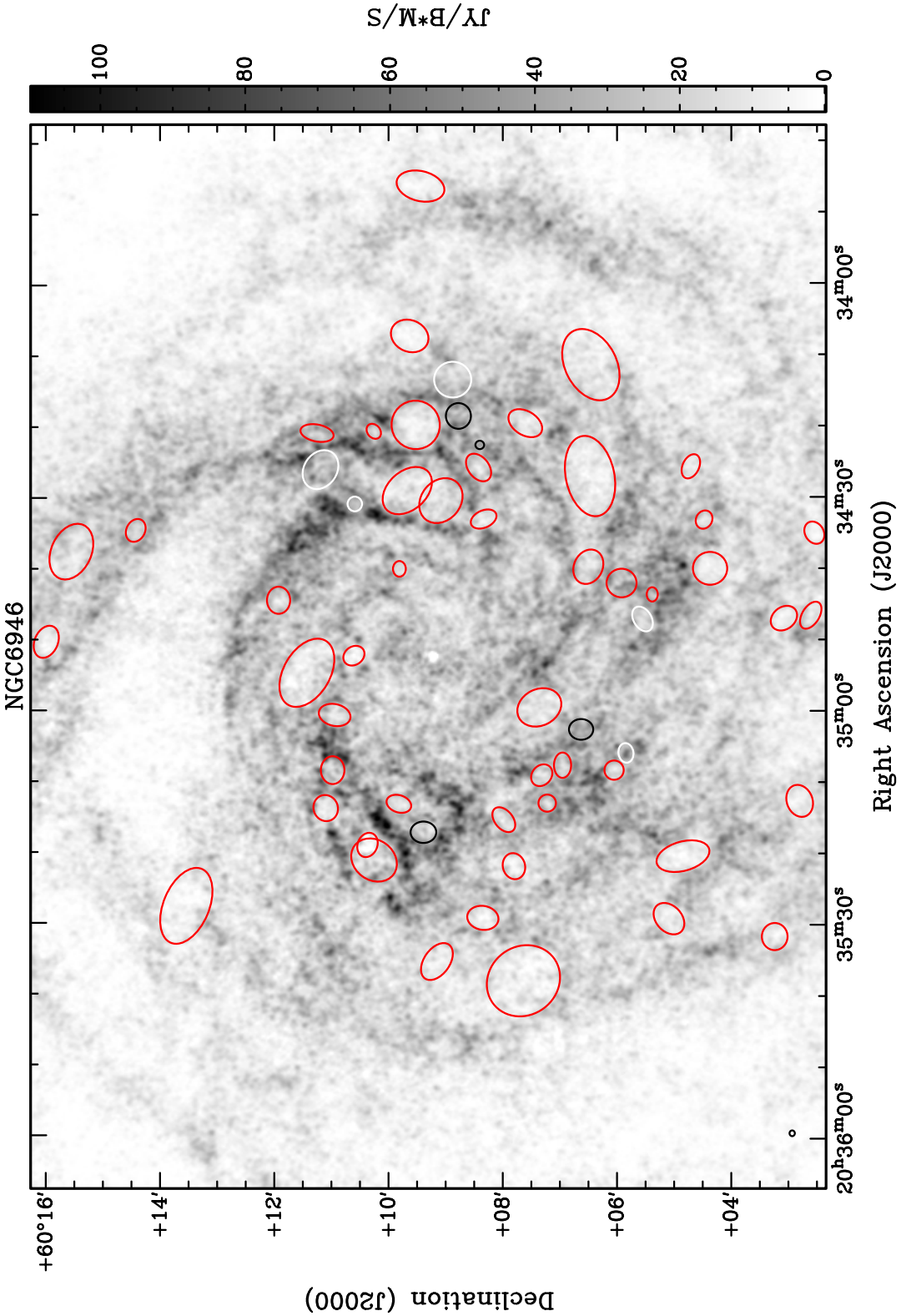

Figure 2.27: Position of the H I holes in NGC 6946. The colours illustrate the different type of the holes: red - type 1, white - type 2 and black - type3. The gray-scale map is a linear representation of the H I surface brightness map and the size of the beam is illustrated in the bottom left corner.

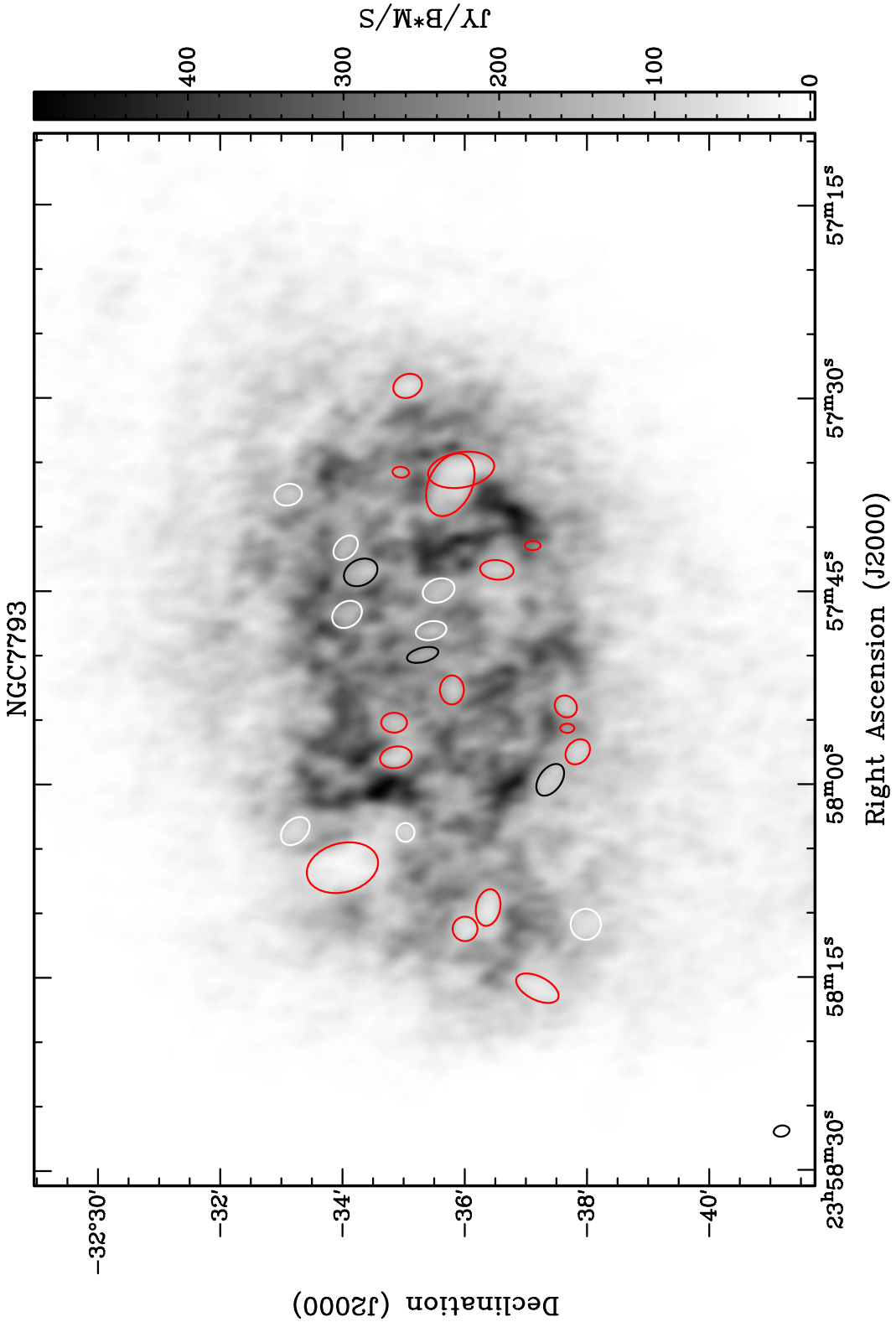

Figure 2.28: Position of the H I holes in NGC 7793. The colours illustrate the different type of the holes: red - type 1, white - type 2 and black - type3. The gray-scale map is a linear representation of the H I surface brightness map and the size of the beam is illustrated in the bottom left corner.

2.7 Summary

In this Chapter we presented a catalogue of H I holes in 20 nearby galaxies, which form part of the THINGS project. Our sample consists of 12 spiral and 8 dwarf galaxies selected to span a range of properties, notably star formation rates, Hubble type and high spatial resolution. We used the KARMA package for the identification of features in the H I distribution and catalogued more than 4000 candidate holes. The identification was done "by eye" and a set of criteria implemented on a quality ranking scale was applied to each candidate. We compared the candidate holes in IC 2574 with those catalogued in a parallel study by Rich et al. (2008) and decided on a threshold above which we classified a candidate as a genuine hole. On application of this quality threshold we ended up with the 1000 most promising holes across the whole sample of galaxies.

We determined a set of observed properties for each hole including its size, expansion velocity, axial ratio and type as was done in previous studies in this field. In order to be able to carry a comparative analysis of these structures we derived a number of properties such as kinetic age, indicative H I mass, galactocentric radius and energy requirement for each hole. For the calculation of the indicative H I mass and energy requirement the midplane H I volume density ($n_{\rm HI}$) and therefore the scale height of the H I disc needed to be calculated. For the scale height we used the approach of Dopita & Ryder (1994) and derived the scale height as a function of galactocentric radius for each galaxy. As predicted, we found that dwarf galaxies have a thicker gas disc and in spirals the H I disc tends to flare in the outskirts. We presented the full catalogue of H I holes, maps of their distribution and a short description for each galaxy. We will now proceed to the comparative analysis of these structures.

Chapter 3

Analysis of H I Holes

3.1 Comparative Analysis

In this Chapter we will analyse the results presented in Chapter 2, focusing on a comparative analysis of the entire sample. The work presented here is based on the Bagetakos et al. (2011) paper and has been carried out by the author of this thesis. Valuable feedback and comments were provided by the co-authors. Table 3.1 provides a basic summary of the properties of the holes on a per galaxy basis and lists, among other things, the range of H I hole diameters, expansion velocities, and kinetic ages. The number of holes detected in each galaxy varies substantially. This variation is partly due to the difference in spatial resolution at which each galaxy was observed. Specifically, the number of type 3 holes detected is greatly affected by resolution. As these holes are fully contained within the H I disc their diameter is typically less than 300 pc, the resolution limit in some of the more distant galaxies. In the case of spiral galaxies the lack of H I in between the spiral arms sometimes appears as an H I hole. These inter-arm regions in general do not constitute genuine holes and therefore have not been included in any comparative analysis. This is also the case for features that resemble holes in pV diagrams, and consequently were assigned a high Q value, but are the result of a warped disc or for holes which are superpositions of 2 or more holes.

For the first time we are now able to undertake a comparative study of the small scale structure of the ISM, in a systematic way and across Hubble type. The homogeneity of our sample allows us to perform a number of analyses which we present here in three sections. The first section includes a comparison of the properties of the holes in each galaxy; the second section compares these properties across the galaxies in our sample; the third section searches for global trends and

Table 3.1. Summary of basic properties of H I holes across the sample of galaxies

Name	No	d (kpc)	$V_{\rm exp}$ (km s^{-1})	$t_{\rm kin}$ (Myr)	type 1 (%)	type 2 (%)	type 3 (%)
NGC 628	102	0.32-1.94	5-21	14-135	70	25	5
NGC 2366	26	0.21-0.69	9-24	6-38	54	23	23
NGC 2403	173	0.10-1.78	6-32	2-109	62	24	14
Holmberg II	39	0.26-2.11	7-20	10-147	64	13	23
DDO 53	3	0.18-0.36	8-10	9-22	33	33	33
NGC 2841	15	0.89-1.67	9-28	20-91	93	0	7
Holmberg I	6	0.19-0.74	6-16	6-61	50	17	33
NGC 2976	13	0.13-0.24	9-23	3-13	62	23	15
NGC 3031	306	0.09-0.57	8-20	3-35	43	34	23
NGC 3184	39	0.48-1.64	7-20	21-114	87	13	0
IC 2574	27	0.32-2.02	5-36	9-141	55	15	30
NGC 3521	13	0.60-1.20	10-16	28-59	92	8	0
NGC 3627	17	0.36-0.74	12-30	6-30	59	29	12
NGC 4214	56	0.11-1.23	4-25	4-100	82	11	7
NGC 4449	20	0.23-0.90	10-30	4-44	70	15	15
NGC 4736	23	0.21-0.45	9-30	6-22	48	35	17
DDO 154	9	0.27-0.68	6-13	10-42	67	22	11
NGC 5194	47	0.29-1.34	8-32	8-82	60	38	2
NGC 6946	56	0.20-2.14	8-21	8-131	84	9	7
NGC 7793	27	0.10-1.06	7-16	10-65	59	30	11

Note. — Col 1: Galaxy name; Col 2: number of HI holes; Cols 3–5: the minimum and maximum, indicating the range of hole diameters, hole expansion velocities, and kinetic age, respectively; Cols 6–8: the percentage of type 1, 2, and 3 holes detected.

correlations with, e.g., Hubble type, luminosity, etc. We then proceed to test the hypothesis that H I holes are compatible with being a direct result of massive star formation. In what follows we decided to exclude the dwarf galaxy DDO 53 as this has only 3 detected H I holes. We also exclude those few H I holes which in the discussion of the individual galaxies were flagged as being superpositions or potentially not genuine holes. These holes are marked with an asterisk in Tables 2.3–2.22.

3.1.1 Overall properties of the holes

The set of figures we will describe next shows the number distributions of the observed and derived properties of the holes. We start with showing the diameter distribution of the holes in order to investigate if there are any obvious trends regarding their size distribution, both within a galaxy as well as from target to target. The result is shown in Fig. 3.1 which shows a mosaic of 20 panels, each panel showing a histogram representing the relative (normalised) frequency distribution as a function of diameter of each of the 19 targets, plus a final panel showing

the distribution summing over all targets. The bins are 200 pc in size. There are obvious differences among the galaxies. However, in this and subsequent figures one has to guard against selection effects. The absence of small diameter holes in some targets is due to their larger relative distance which sets a lower limit to the linear resolution. We therefore add a vertical dotted line to indicate the resolution limit for each galaxy. In galaxies where there is a gap between the resolution limit and the smallest hole detected this is attributed to other factors, such as the signal to noise ratio (e.g. NGC 3184), and the inclination of the object under study (e.g. NGC 2841 and NGC 3521). In these three cases holes with diameters close to the resolution limit were indeed detected, albeit with low quality values. The large diameter end of the distributions varies greatly among the galaxies. In three cases, NGC 2976, NGC 3031, and NGC 4736, we see a sharp cut-off at around 400 pc which, at first glance, does not seem to correlate with galaxy type or any other global property. On the other hand it appears that Scd type galaxies tend to have small numbers of large (> 1 kpc) holes in their H I distribution. We return to this below.

The relative number distribution of the expansion velocities is plotted in Figure 3.2. The bins correspond to $2\,\mathrm{km\,s^{-1}}$ and only holes for which an expansion velocity could be measured are plotted. The distributions appear to vary significantly among the galaxies mainly because of small number statistics.

Figure 3.3 shows the relative number distribution of the kinetic ages of the holes in the 19 galaxies in a format similar to Fig. 3.1. The bins measure 10^7 yr. The shaded histograms correspond to those holes for which an expansion velocity could be measured, i.e. types 2 and 3. For type 1 holes, which are likely to have stalled, we adopted a lower limit to the expansion velocity which was set to the one-dimensional velocity dispersion of the gas. The kinetic age distributions are similar to those of the diameters of the holes which is to be expected since the kinetic age is derived from the diameter and the expansion velocity which, across the targets, has a small range. M 81 (NGC 3031) shows a quite striking distribution. As mentioned in the previous paragraph, this galaxy predominantly has small holes. Their ages are all below 40 Myr. One possible explanation is that M 81 is actively interacting with M 82 and NGC 3077: numerical models by Yun (1999) provide an estimate of 2.2×10^8 yr for the most recent perigalacticon and it is conceivable that this interaction eventually set off a sequence of events which led to a phase of enhanced star formation 0.5×10^8 yr ago, leading to the current abundance of small, young H I holes. Similarly, NGC 2976 appears to

have had a star formation episode $1 - 2 \times 10^7$ yr ago triggered by gas in-fall from an intergalactic cloud generated during encounters between members of the M 81 group (Bronkalla et al. 1992).

The relative number distribution of the characteristic energies required to create the holes is shown in Fig. 3.4. The energies are binned logarithmically. It is evident that nearly all distributions fall in a range that spans 3 orders of magnitude. The shift towards higher energies for the galaxies NGC 2841, NGC 3184 and NGC 3521 is a selection effect due to their relative large distance which reduces the linear resolution and sensitivity to pick up small holes. In the case of NGC 3627 the shift towards higher energies is due to the fact that this galaxy has the highest velocity dispersion, which is likely driven by the central bar, and hence the energies of all type 1 holes have probably been overestimated.

Figure 3.5 shows the relative number distribution of the indicative H I masses, binned logarithmically. The shape of these distributions is dominated by the diameter distribution of the holes, as the volume densities are showing a much smaller range of values (2σ from ~ 0.1 to $\sim 0.7\,\mathrm{cm}^{-3}$). The indicative masses span a range of $(2 \times 10^3\,M_\odot - 3 \times 10^7\,M_\odot)$. Apart from NGC 2403, NGC 2976 and NGC 3031 which have their distributions skewed towards smaller mass values, all other galaxies cover the same range.

The radial location of the holes in the disc of the host galaxy is illustrated in Figure 3.6. The horizontal axis represents the galactocentric distance normalised to the maximum extent of the H I disc, R_{max} (given in Tab. 2.2), in bins of size $0.1R_{\mathrm{max}}$. From this figure it is evident that wherever there is H I, holes are found, even in the outskirts of galaxies. The vertical line in the figure indicates the location of R_{25}, confirming the finding that holes are found well beyond the main optical body of a galaxy. The number of holes *per area* has its peak near the centre, though, as can be seen in Fig. 3.7 which shows the log of the number of holes per kpc^2 as a function of R/R_{max}. The surface number density of H I holes is fairly constant or slightly drops out to R_{25}, beyond which radius it drops significantly in most of the galaxies.

Finally, Figure 3.8 illustrates the relative number distribution of the axial ratio of the holes in each galaxy. It appears that dwarf galaxies have rounder holes, on average, than spirals (the mean axial ratio for dwarfs is 0.80 and 0.71 for spirals, confirmed by a Mann-Whitney test with $p < 0.0005$). This was first observed in Holmberg II by Puche et al. (1992) and explained by Walter & Brinks (1999) and Brinks et al. (2002) as follows. Within R_{25} the H I disc in a dwarf is intrinsically

thicker than in spirals (see Table 2.2) which prevents holes from blowing out at an early stage. Holes will therefore remain intrinsically spherical and the apparent axial ratio of an intrinsically spherical hole is not affected by the inclination of the host galaxy. Holes in spiral galaxies will tend to break out of the disc, leaving an approximately circular feature in the plane of the galaxy which, when seen under an angle, will appear elliptical. As will be discussed below another possible explanation for this trend is the effect that shear plays on the appearance of holes.

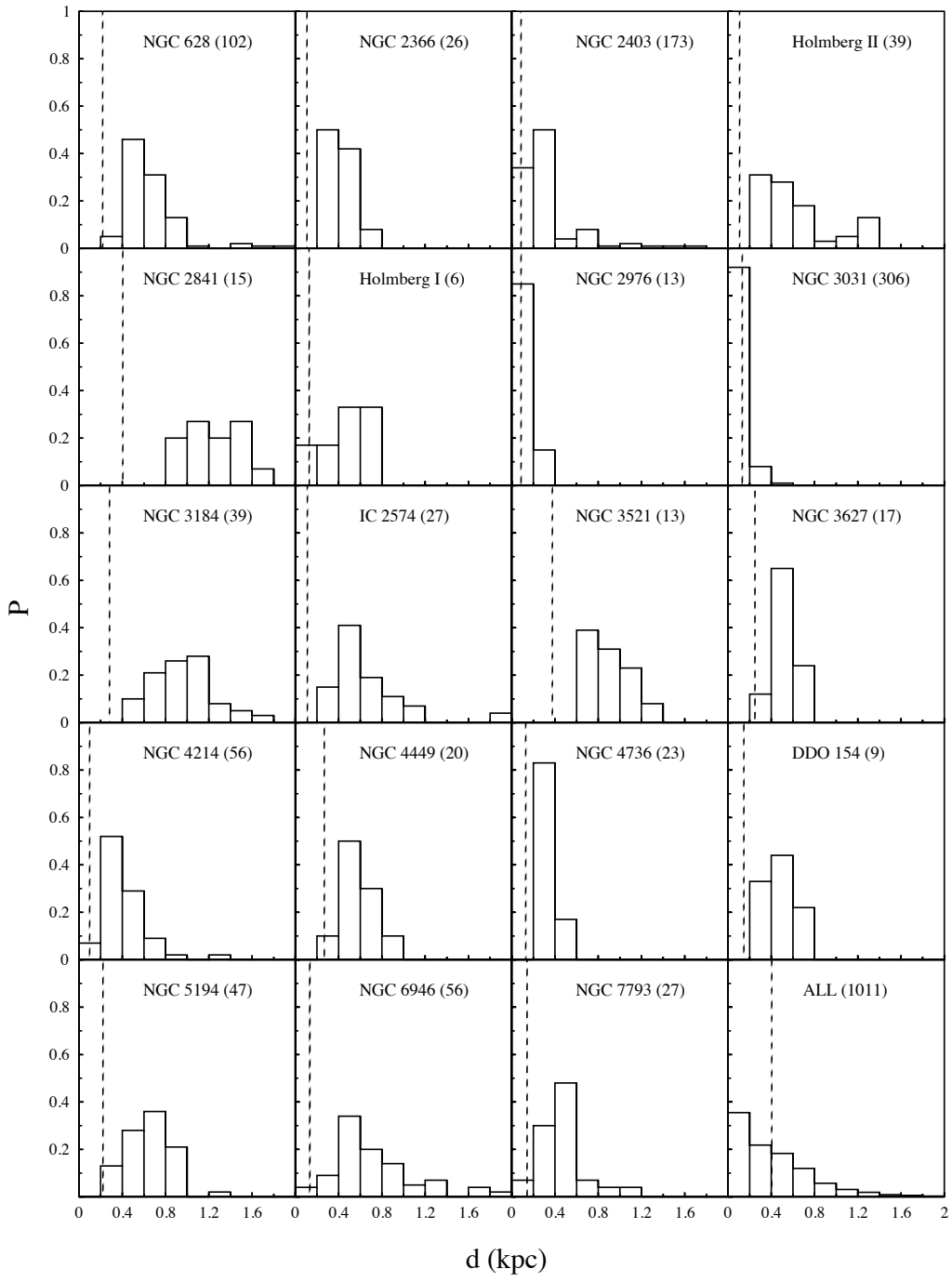

Figure 3.1: Relative number distribution of the diameters of the holes. The vertical dashed line indicates the lower limit set by the linear resolution. Each panel lists the galaxy it refers to and the last panel shows all holes as well as the worst linear resolution across the entire sample (dashed line). The number in parentheses indicates the total number of holes represented by the histogram.

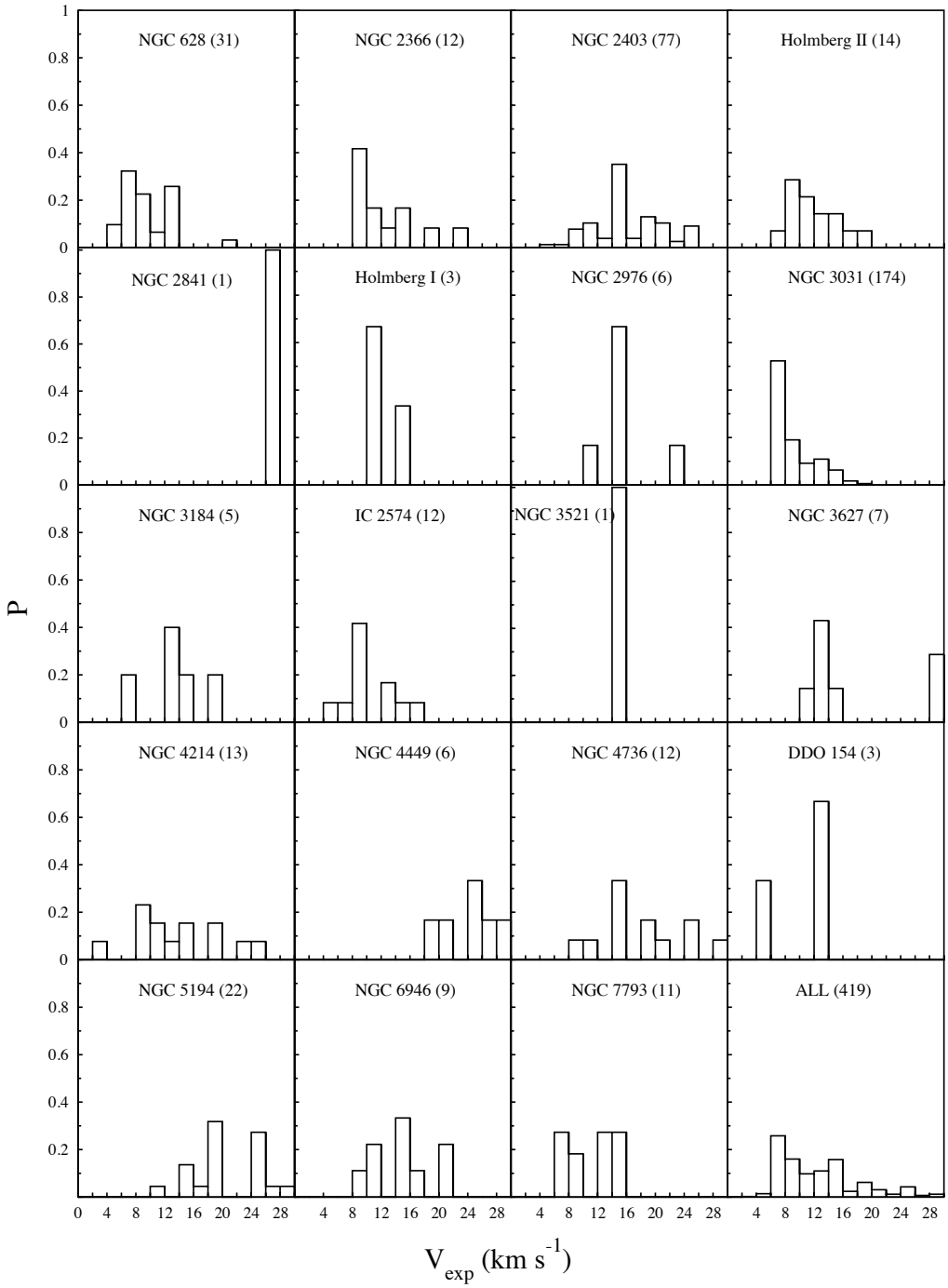

Figure 3.2: Relative number distribution of the expansion velocities of the expanding holes. Each panel lists the galaxy it refers to; the number in parentheses indicates the total number of holes represented by the histogram. The sharp cut-off point at $\sim 5\,\mathrm{km\,s^{-1}}$ is due to our velocity resolution.

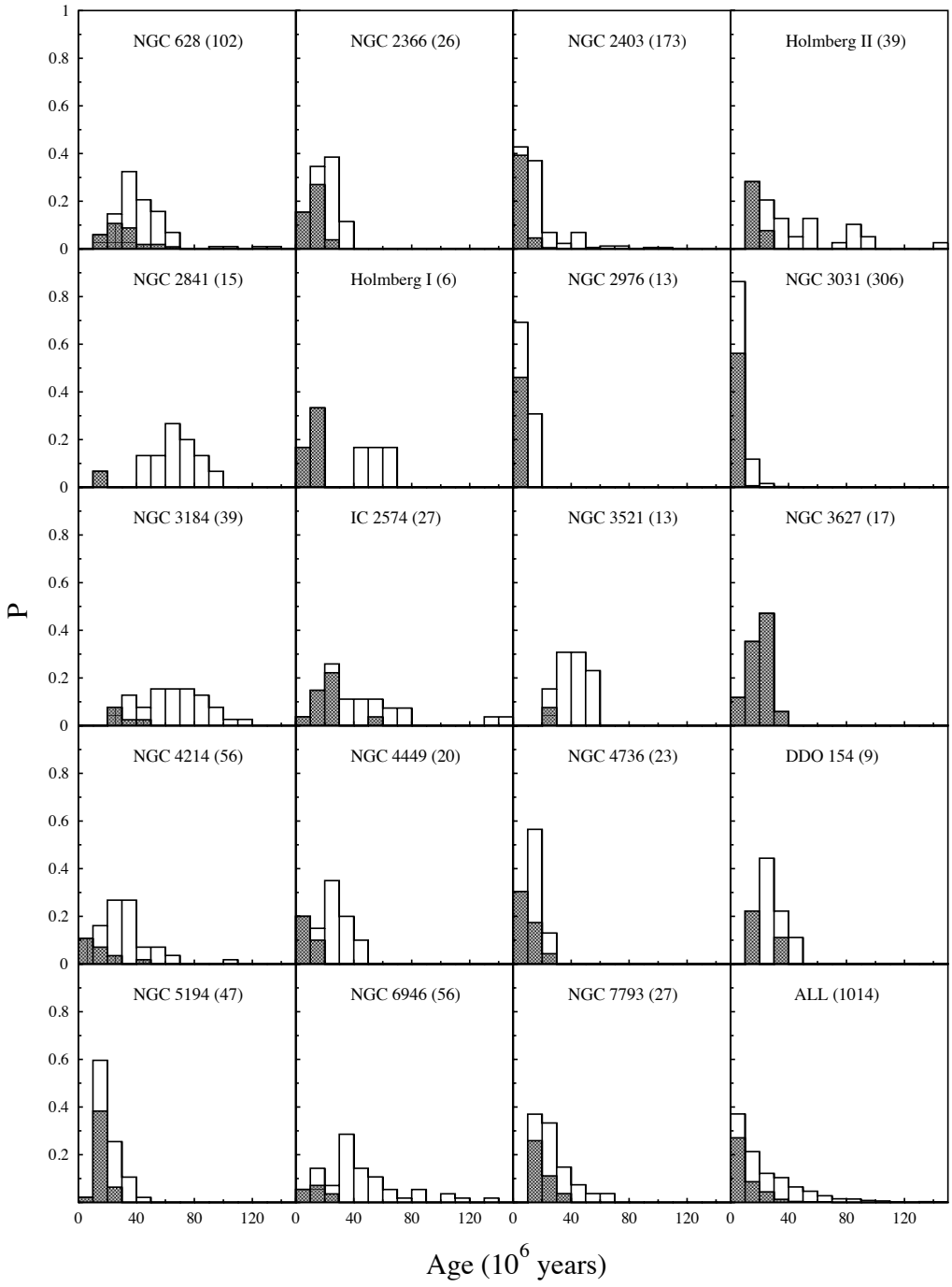

Figure 3.3: Relative number distribution of the kinetic ages of the holes. The shaded areas represent the fraction of holes for which an expansion velocity was measured (types 2 and 3). In the other cases we assumed an expansion velocity equal to the velocity dispersion. Each panel lists the galaxy it refers to; the number in parentheses indicates the total number of holes represented by the histogram.

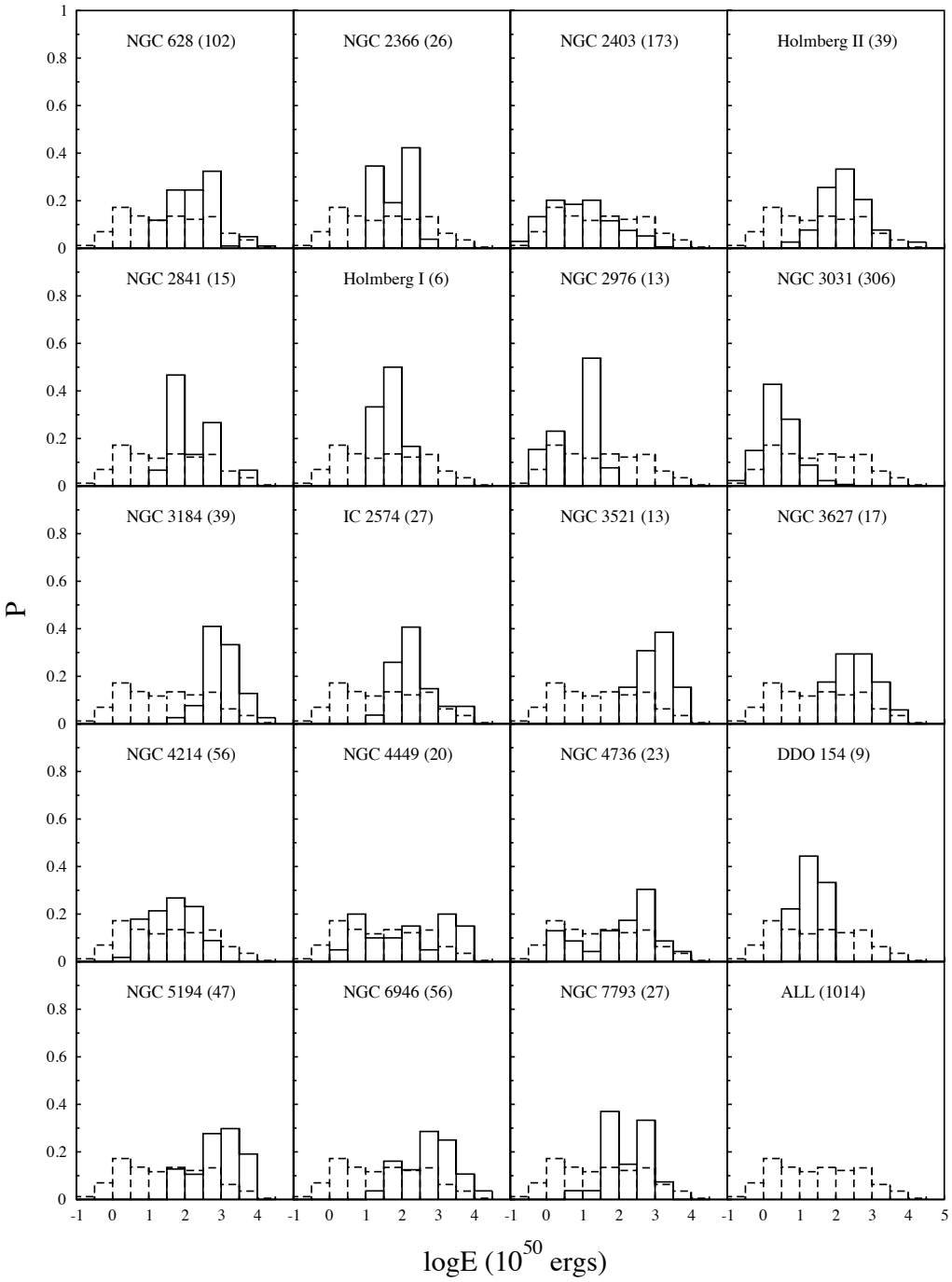

Figure 3.4: Relative number distribution of the energy requirements to create the holes. Note that the horizontal axis is binned logarithmically. The bottom right panel shows the distribution of all holes combined. This dashed histogram is repeated for reference in each of the other panels. Each panel lists the galaxy it refers to; the number in parentheses indicates the total number of holes represented by the histogram.

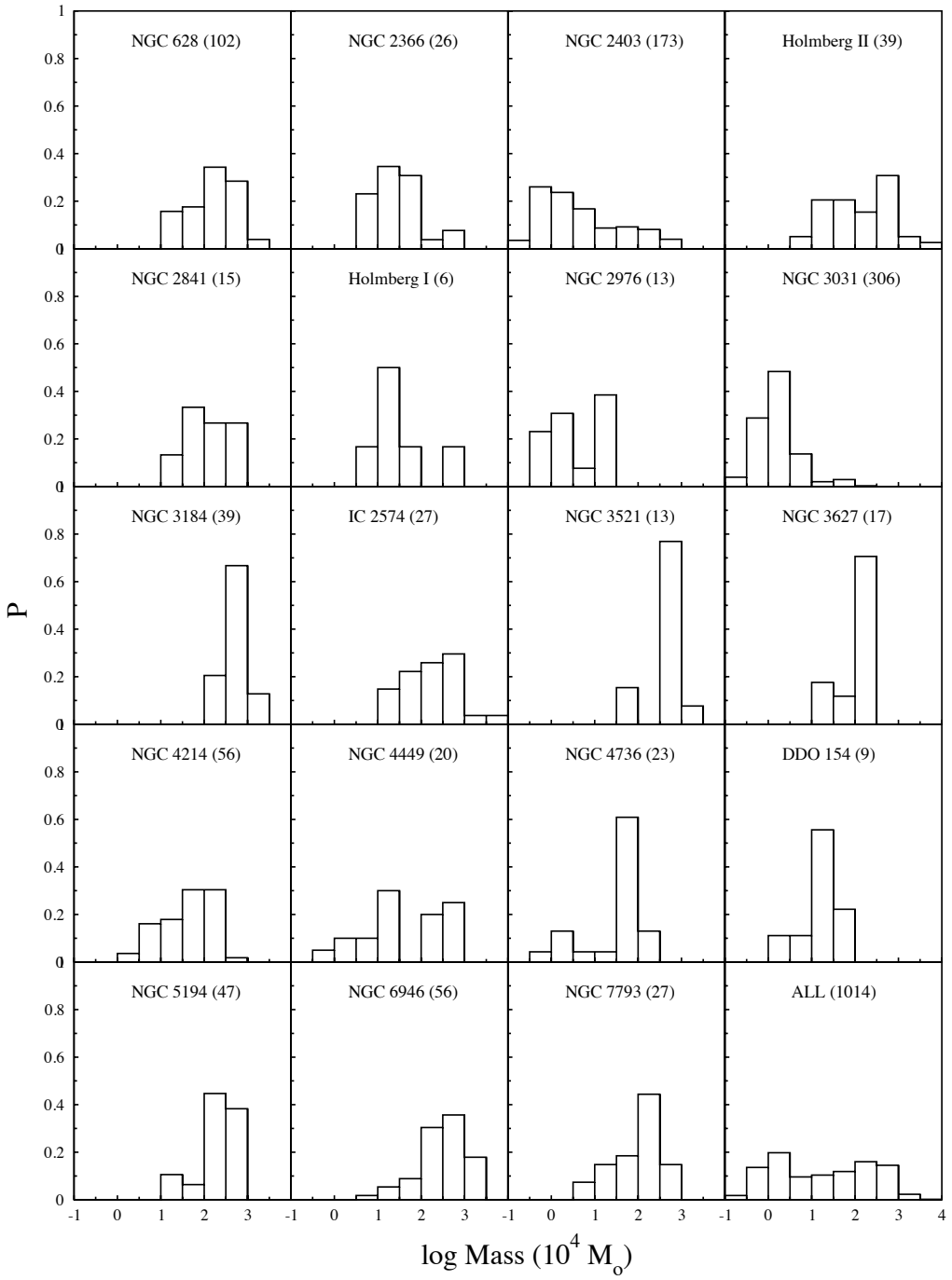

Figure 3.5: Relative number distribution of the indicative H I masses of the holes in logarithmic bins. Each panel lists the galaxy it refers to; the number in parentheses indicates the total number of holes represented by the histogram.

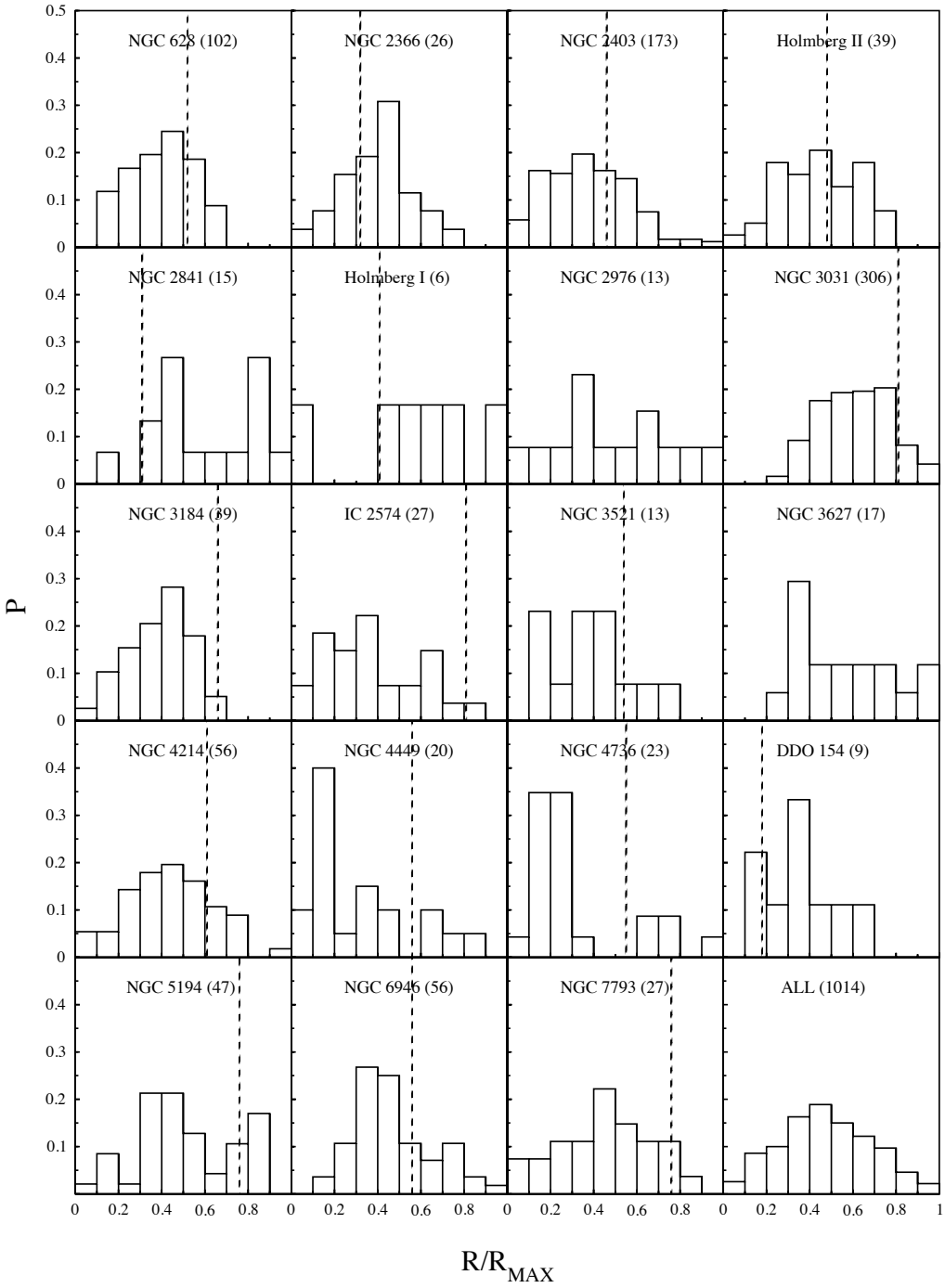

Figure 3.6: Relative radial number distribution of the H I holes. The x–axis represents the relative galactocentric radius of an H I hole with respect to the largest extent of the H I disc of the host galaxy, $R_{\rm max}$. The dashed vertical line indicates for each galaxy the corresponding location of R_{25}. The bottom right panel shows the distribution of all holes combined. Each panel lists the galaxy it refers to; the number in parentheses indicates the total number of holes represented by the histogram. Overall 77% of the holes are located within R_{25} and 23% outside.

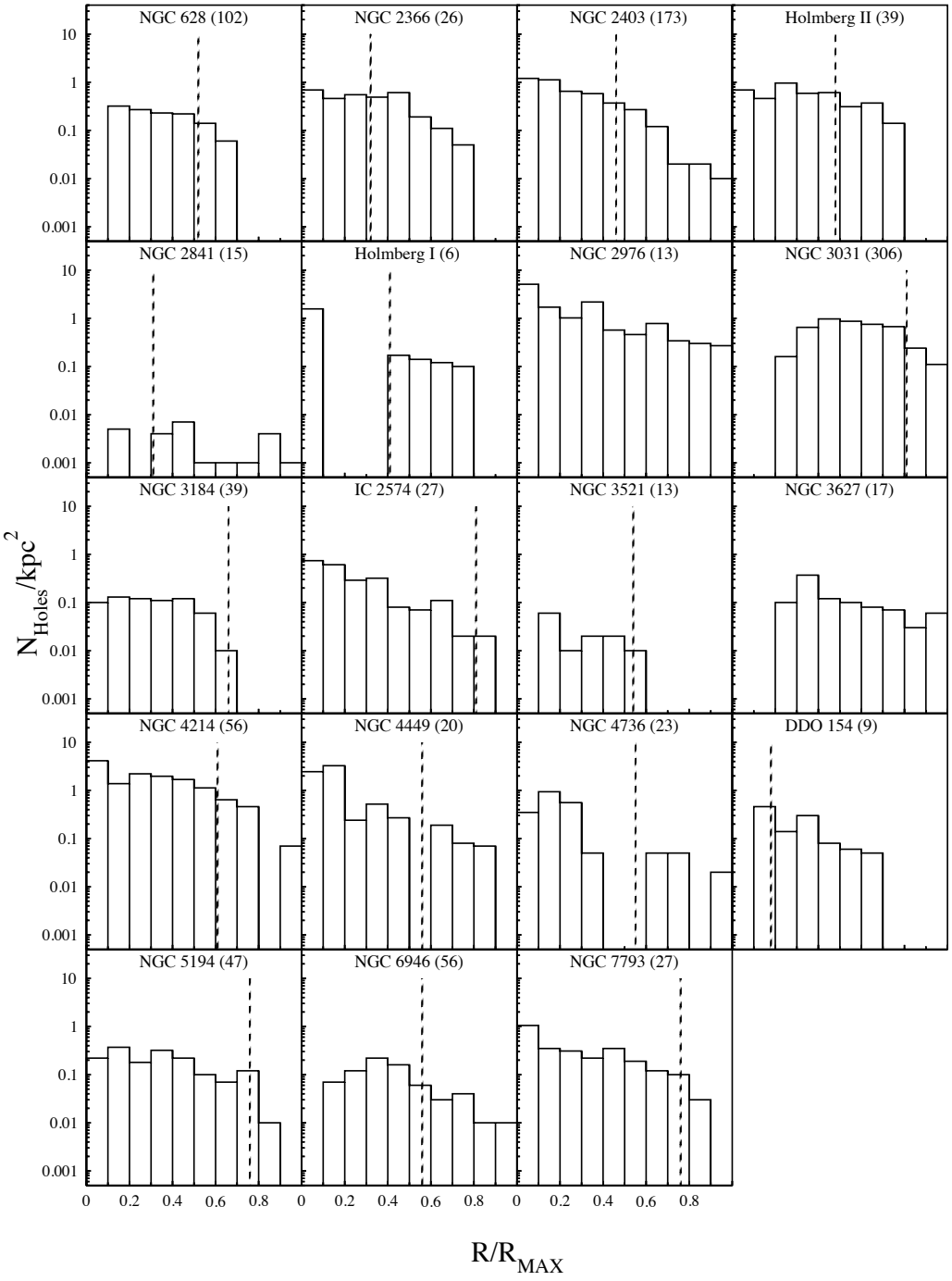

Figure 3.7: As Fig. 3.6 but showing the number of H I holes per kpc^2 as a function of galactocentric radius normalised by $R_{\rm max}$. The dashed vertical line indicates for each galaxy the corresponding location of R_{25}. The y–axis is plotted on a logarithmic scale.

3.1.2 Relations between hole properties

The trend that dwarf galaxies tend to have rounder holes on average is also evident in Figure 3.9 which presents the axial ratio vs. the diameter of the holes. The last panel in this figure shows the entire sample of holes from which can be seen that there are few, if any, round holes larger than 1 kpc. For holes smaller than 1 kpc we see that the axial ratio takes the whole range of values indicative of the different factors that determine the axial ratio. This is the first of the next series of figures where we search for correlations between two observed and/or derived properties among the holes detected in each of the 19 targets.

Figure 3.10 is a scatter diagram of axial ratio vs. galactocentric radius. Shear at a point R_o with respect to a neighbouring point at distance ΔR in a differentially rotating disc is given by:

$$S[\mathrm{km\,s^{-1}\,kpc^{-1}}] = \frac{1}{2}(\frac{V_o}{R_o} - \frac{\Delta V}{\Delta R}) \tag{3.1}$$

where V_o is the velocity at R_o, ΔR is the distance between the points and ΔV the difference in velocity between these two points. The last term in equation 18 is zero for a flat rotation curve ($\Delta V = 0$). Using the rotation curves of galaxies (where applicable) we calculated values for shear between points separated by $\sim 0.05\%\, R_{\mathrm{max}}$ as illustrated in Fig. 3.10 (red line). The shear gradient is typically 10–50 $\mathrm{km\,s^{-1}\,kpc^{-1}}$, the upper boundary being typical for Sa galaxies, later types reaching half this value. This is enough to turn an originally circular structure of 500 pc diameter, into an elliptical feature with axial ratio of ~ 0.5 within 50 Myr. The range in shear gradient listed is what one expects to find between the outer and inner regions of a spiral galaxy, the inner regions having the highest values (not considering the very inner solid body part). Most dwarf galaxies are dominated by solid body rotation, so shear is absent. One would therefore naïvely expect holes at larger radii to be rounder than holes at smaller radii. However no such trend is apparent in the galaxies shown in Fig. 3.10. This null result does not imply, though, that shear is not important in spirals. Holes are supposedly continuously formed, and more so within R_{25}, which means that there will be many young, and therefore round H I holes populating the inner regions of galaxies. In the outer regions, some holes might be sufficiently long-lived for the more modest shear there to have an observable effect. One would therefore expect a relation of axial ratio with kinetic age in the sense that on average older holes in shear dominated, i.e., spiral galaxies, are less round than younger ones

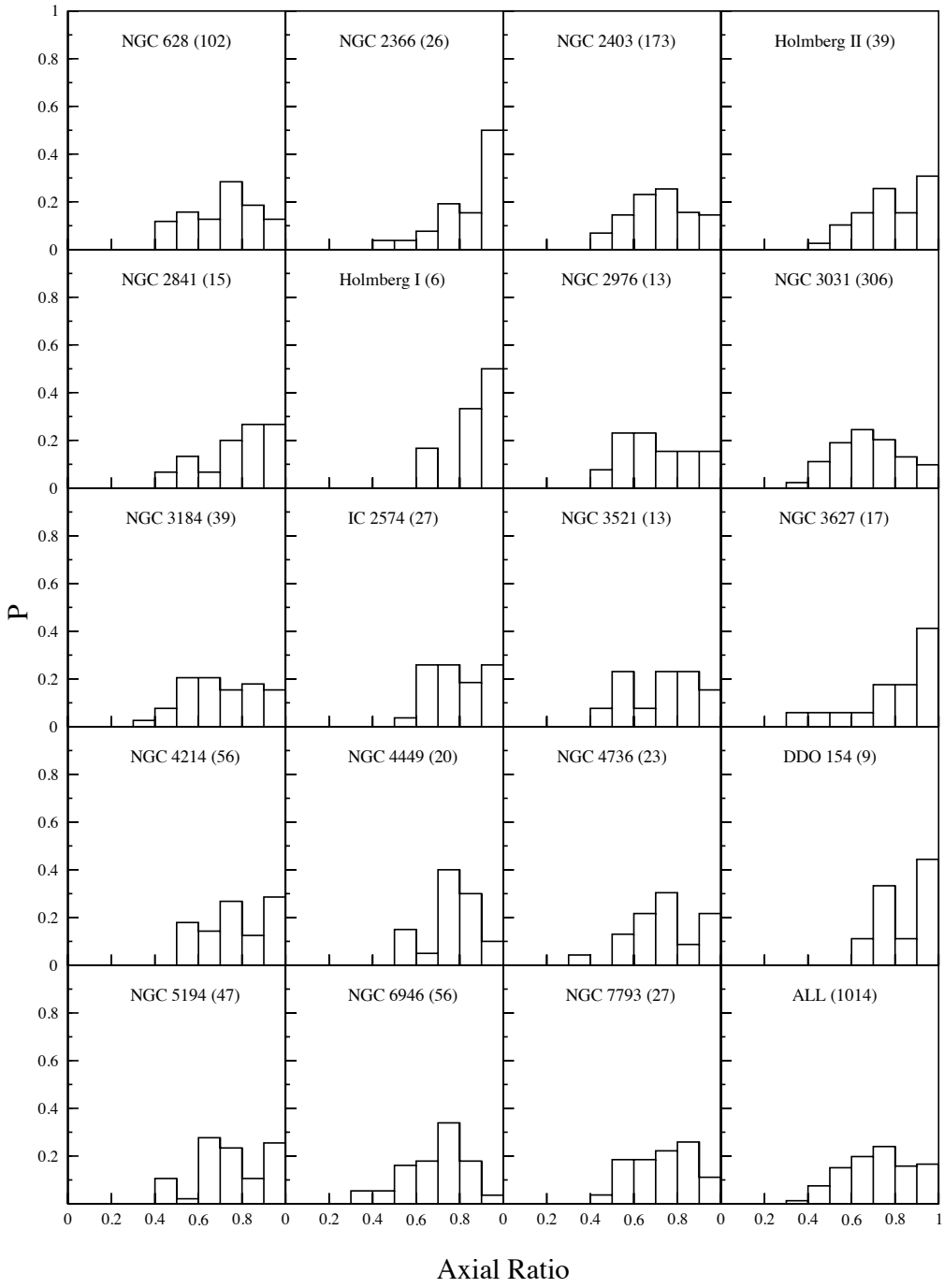

Figure 3.8: Relative number distribution of the axial ratios of the holes. The bottom right panel shows the distribution of all holes combined. Each panel lists the galaxy it refers to; the number in parentheses indicates the total number of holes represented by the histogram.

(Silich & Mashchenko 1996; Elmegreen et al. 2002). This is investigated in the next figure, Fig. 3.11. Except for some of the dwarf galaxies, where shear is not that important, only 5% of holes older than 50 Myr are round (average axial ratio is 0.70). In the case of younger holes, the entire range of axial ratio is found, as expected, as one gets a mix of young, round holes in low shear environments with elliptical ones that find themselves in regions of high shear. The destructive role of shear is also illustrated in Fig. 3.12 where the diameter of holes is plotted against shear for galaxies for which it could be measured. There is a clear negative correlation (Spearman's $\rho = -0.41$, $p < 0.0001$) between shear and the diameter of holes, i.e., in environments where shear is higher than ~ 15 km s^{-1} kpc^{-1} no holes larger than 1 kpc were found.

It is not just shear which defines the observed axial ratio of an H I hole. The axial ratio of those holes which have blown out and those that have lost their initial spherical shape due to shear depends crucially on viewing angle. The inclination should cause the major axis of holes to be aligned with the major axis of the disc. We also know that holes do not live in isolation and that two neighbouring spherical holes can merge to form a larger elliptical one. All these effects will tend to wash out whatever trend of axial ratio there might be with radius. However, there are some conclusions which can be drawn from Figs. 3.8–3.11: i) H I holes in dwarfs are rounder than in spirals (see Section 3.1.3); ii) blow-out holes in spirals are not circular as we do not observe any alignment between the major axis of the holes and the major axis of the disc (if anything, cursory inspection of the figures in Section 2.6 suggests the holes align with the spiral arm structure); iii) there is a sharp cut-off to the axial ratio at a level of 0.4. Regarding iii), in the identification process there was no requirement for holes to be less flattened than a certain value. The sharp lower envelope at 0.4 suggests then, that structures more elongated than that become difficult to identify as holes.

The diameter of a hole versus its position in the host galaxy is shown in Figure 3.13 where the horizontal axis represents the galactocentric distance as a fraction of the H I disc radius. In the case of dwarf galaxies there is a tendency for large holes to be located at larger galactocentric radii however, this is not a statistically significant result (Spearman's $\rho = 0.03$, $p = 0.68$). In spiral galaxies, no such trend is seen (Spearman's $\rho = -0.09$, $p = 0.01$). This is somewhat contrary to expectations. As we have explained in Section 2.2, galaxy discs flare at large radius. One would therefore expect holes to be able to grow to larger diameters before breaking out and subsequently stalling, considering that the ambient

density also drops with radius. The lack of finding a corresponding trend in the diameters of holes could be due to a variety of factors, one being that there is a growing incompleteness of finding holes in the very low H I surface brightness outer regions of spirals. Alternatively, we know that star formation is inefficient at large radii (e.g., Kennicutt 1989; Martin & Kennicutt 2001; Schaye 2004; Thornley et al. 2006; Bigiel et al. 2008; Leroy et al. 2008) and consequently the number of stars more massive than 8 $M_{\odot}$ which are formed co-spatially decreases, reducing the total energy deposited after their demise as supernovae, resulting in holes of more modest diameter. Another possible explanation is that the ambient density drops significantly perpendicular to the disc of the galaxy and therefore holes will tend to be elongated in this direction. Consequently, even though these chimney-like structures will be intrinsically larger in the direction perpendicular to the disc, when viewed inclined, they might appear to have a lower ellipticity and mimic spherical features.

Figure 3.14 shows the diameter of a hole versus its expansion velocity for those holes for which we could measure this, i.e., types 2 and 3. Contrary to the findings by Stanimirović (2007) we do not find a clear trend of increasing expansion velocity with increasing size (Spearman's $\rho = 0.40$, $p < 0.0001$). However, Stanimirović (2007) were able to detect holes down to 15 pc where this trend is strongest. We should also like to note that their result is based on just one interacting system, the LMC/SMC. There are examples in Figure 3.14 of individual galaxies which show a similar trend, such as Ho II and NGC 4736. However, this trend does not dominate across galaxies. This is also illustrated in Fig. 3.15 where we plot on a log–log scale expansion velocity versus hole diameter for all expanding holes across the entire sample of galaxies. In this figure the straight lines correspond to lines of constant age, drawn at (0.5, 1, and 5) $\times 10^7$ yr. Assuming Chevalier's single blast approximation and, for simplicity a constant ambient density of $n_{\circ} = 1.0\,\mathrm{cm}^{-3}$, we can draw curves of constant required energy. There are two competing mechanisms which both contribute to the way the points are distributed in Figs. 3.14 and 3.15. Once a supernova has gone off, the ejecta which initially move at high speeds will slow down as they interact with the surrounding circumstellar medium and ISM, eventually entering the snowplough phase which is when we tend to identify them as H I holes. One would therefore expect larger holes to have lower expansion velocities. On the other hand, as long as stars from the parent OB association go off as SNe, energy is continuously deposited and, if the expanding shell has not yet suffered blow-out, will maintain an over-pressure within the shell which in turn

will keep up an accelerated flow. The latter mechanism is more likely to dominate in the smaller, younger holes. It is then interesting to note that the distribution of points in our Fig. 3.15 agrees with the corresponding graph in Stanimirović (2007) if one restricts the comparison to holes larger than 100 pc. In other words we hypothesize that the relation found by these authors is possibly a consequence of the smaller holes still harbouring supernova activity.

In Figure 3.16 the energy requirement of each hole versus its radial distance is presented. The radial distribution is normalised by the radius of the H I disc, $R_{\rm max}$. In ten, mostly spiral galaxies there appears to be a trend of higher energy holes to be located at smaller galactocentric radius (Spearman's $\rho = -0.44$, $p < 0.0001$). Further analysis showed that in all galaxies, apart from NGC 4214, the average energy requirement is higher for holes lying within R_{25} ($E_{\rm E} = 2.1 \times 10^{52}$ erg) than for those outside this radius ($E_{\rm E} = 1.0 \times 10^{52}$ erg). This might be due to the fact that the external pressure is higher within R_{25}. First of all the gas density is higher near the centre, as can be verified in the paper by Leroy et al. (2008). Secondly, the SFR is higher in the central regions than in the outskirts which translates into more holes being created (cf., Fig. 3.7), increasing the velocity dispersion and hence pressure of the gas.

We also investigated the following relations, but there do not seem to be any trends of expansion velocity with either of axial ratio, displaced mass, energy required to produce the hole, or with galactocentric radius. Neither is there any relation linking kinetic age with position from the centre in a galaxy.

3.1.3 Comparison of properties across the THINGS sample

As was mentioned earlier, we selected 20 galaxies out of the 34 available. We ensured that we had 2 galaxies per Hubble type. Within each Hubble type, we tried to select galaxies which differed in some property, such as SFR, to explore as wide a parameter space as possible. If we look at the distribution of the kinetic age of the holes across the sample, we find a trend which becomes more obvious if we group the galaxies in terms of early-type, late-type and dwarf galaxies as illustrated in Fig. 3.17. The mean kinetic age shifts towards higher values when we move from early-type spirals ($\overline{t_{\rm kin}} = 13.9$ Myr) to late-type ($\overline{t_{\rm kin}} = 31.6$ Myr) to dwarf galaxies ($\overline{t_{\rm kin}} = 32.5$ Myr). A Mann–Whitney test confirms the difference between early-type and late-type spirals ($\rho < 0.0001$) as well as the difference between late-type

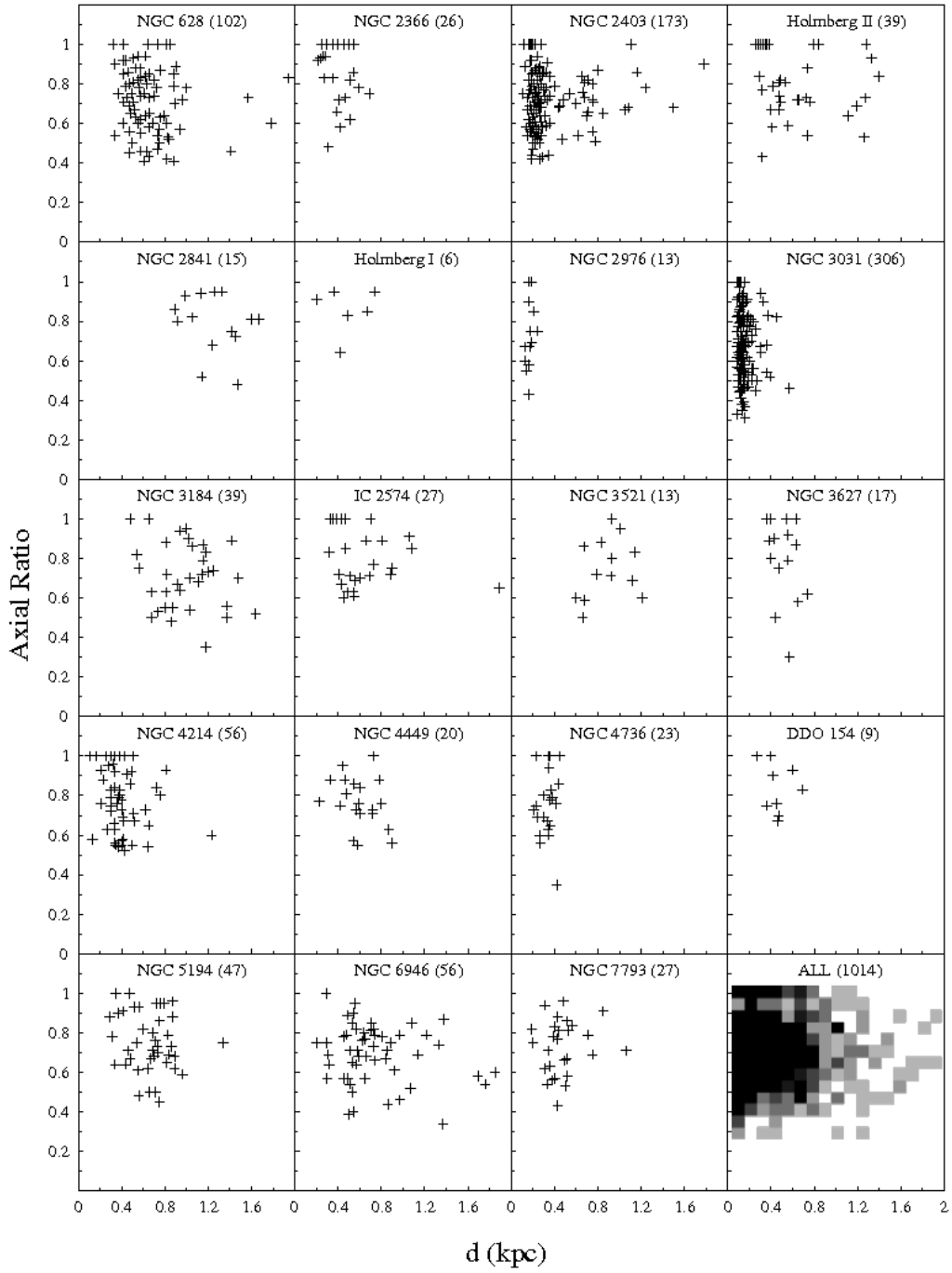

Figure 3.9: Axial ratio vs. diameter of the H I holes. The bottom right panel shows the accumulated result for all galaxies where, rather than plotting individual values we present the data binned and in the form of a density plot. Each panel lists the galaxy it refers to; the number in parentheses indicates the total number of holes represented by the histogram.

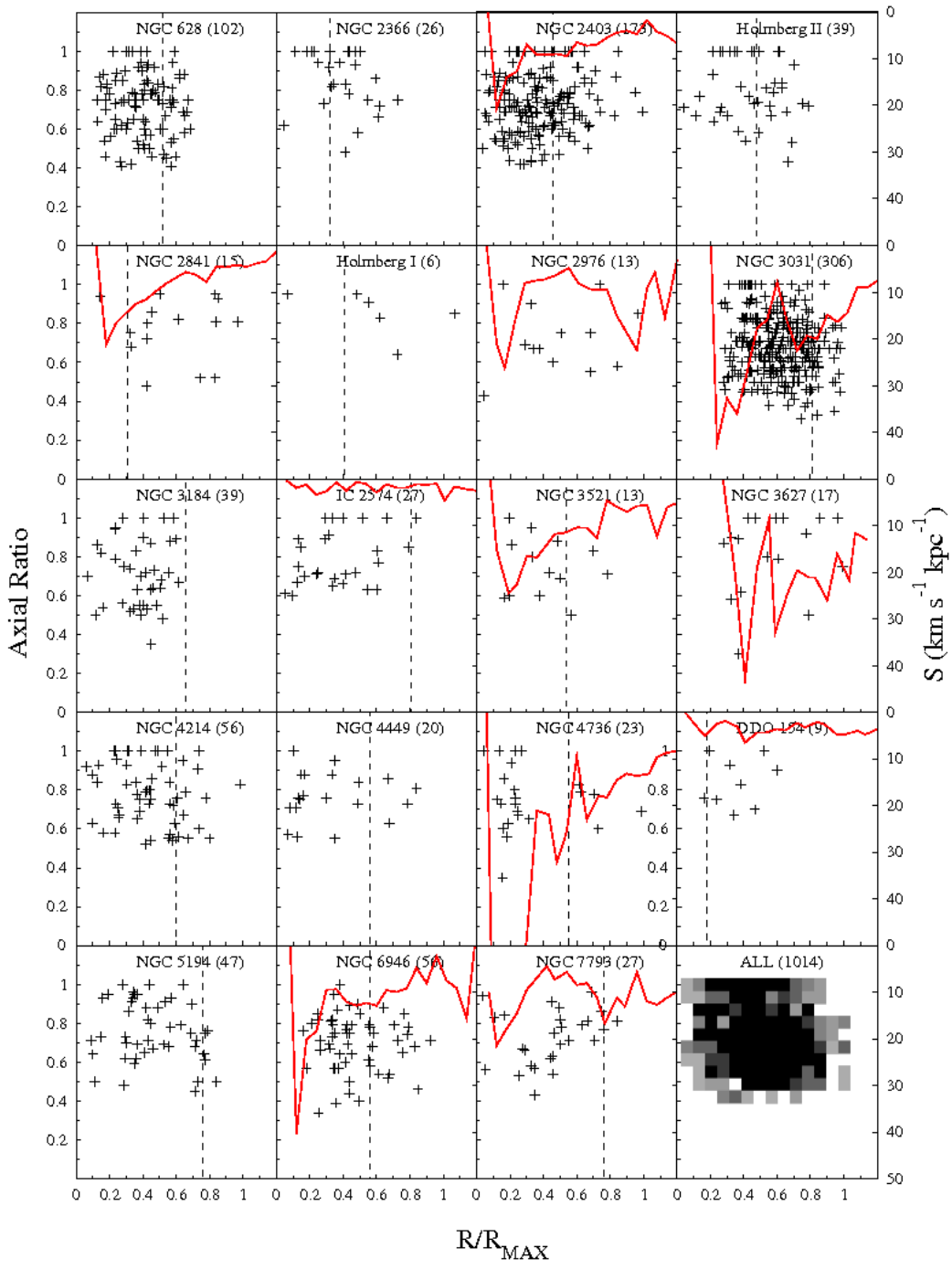

Figure 3.10: Axial ratio vs. radial distribution normalised to $R_{\max}$ with shear over-plotted (red line, axis on the right hand side of the plots and maximum value on the bottom). The dashed vertical line indicates for each galaxy the corresponding location of R_{25}. The bottom right panel shows the accumulated result for all galaxies where, rather than plotting individual values we present the data binned and in the form of a density plot. Each panel lists the galaxy it refers to; the number in parentheses indicates the total number of holes represented by the histogram.

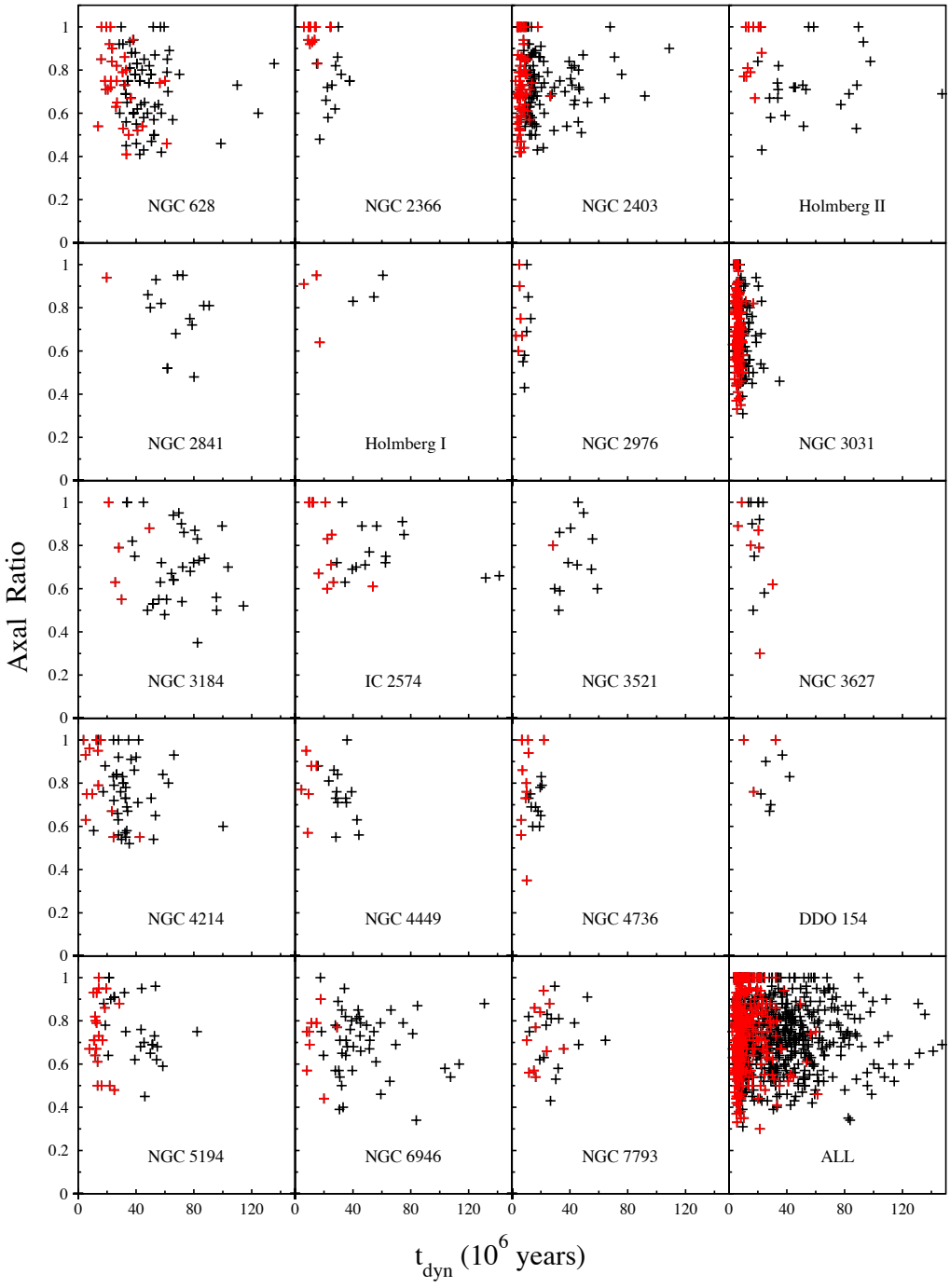

Figure 3.11: Axial ratio vs. kinetic age in units of 10^6 yr of the stalled (black) and expanding (red) H I holes.

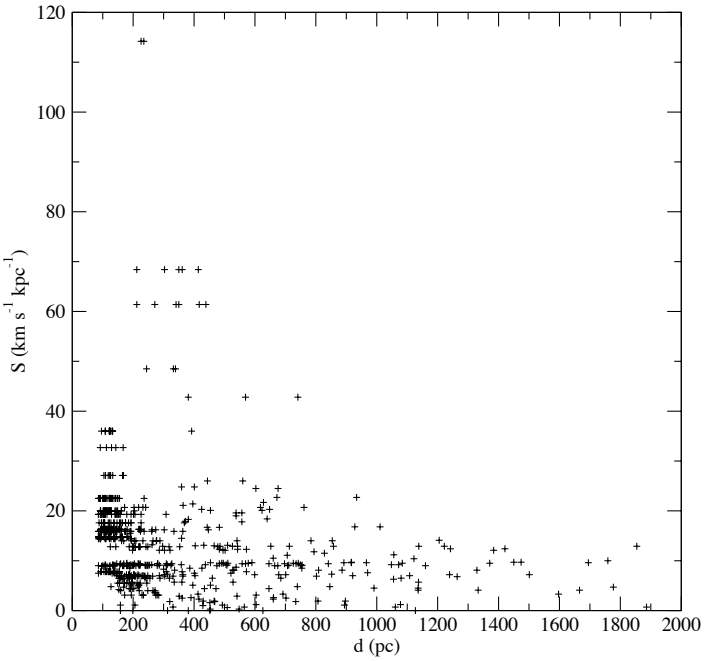

Figure 3.12: Shear vs. diameter of the holes for galaxies for which shear could be measured.

and dwarf galaxies ($\rho < 0.0001$). This can be understood as follows. The kinetic age is driven by the diameter distribution, as the expansion velocities cover a limited range, as mentioned earlier. Discs of earlier type spirals present shear and spiral density waves, both mechanisms actively rearranging the gas within the discs and limiting the time an H I hole may survive. Dwarf irregulars lack both shear and spiral arms. In spiral galaxies where shear is strong (NGC 2976, NGC 3031, NGC 3627, and NGC 4736) the maximum kinetic age is observed to be 40 Myr in contrast to the dwarf galaxies where we find holes of up to 140 Myr. Overall the kinetic age ranges from 10 to 140 Myr, the upper limit reflecting the fact that holes would blend and possibly be destroyed after one full rotation of the disc. A second explanation for the observed trend is the same argument that applies as used when discussing Fig. 3.8, namely that the scaleheights of the discs in early-type spirals are small in comparison with those in dIrrs which means that shells will break out of the disc sooner in the former and the remnant shell will stall, leading to H I holes in spirals having on average smaller diameters, hence leading to systematically lower age estimates.

In order to make this analysis more quantitative we decided to split the sample up in spiral and dwarf galaxies. The sub-samples consist of 12 and 7 members,

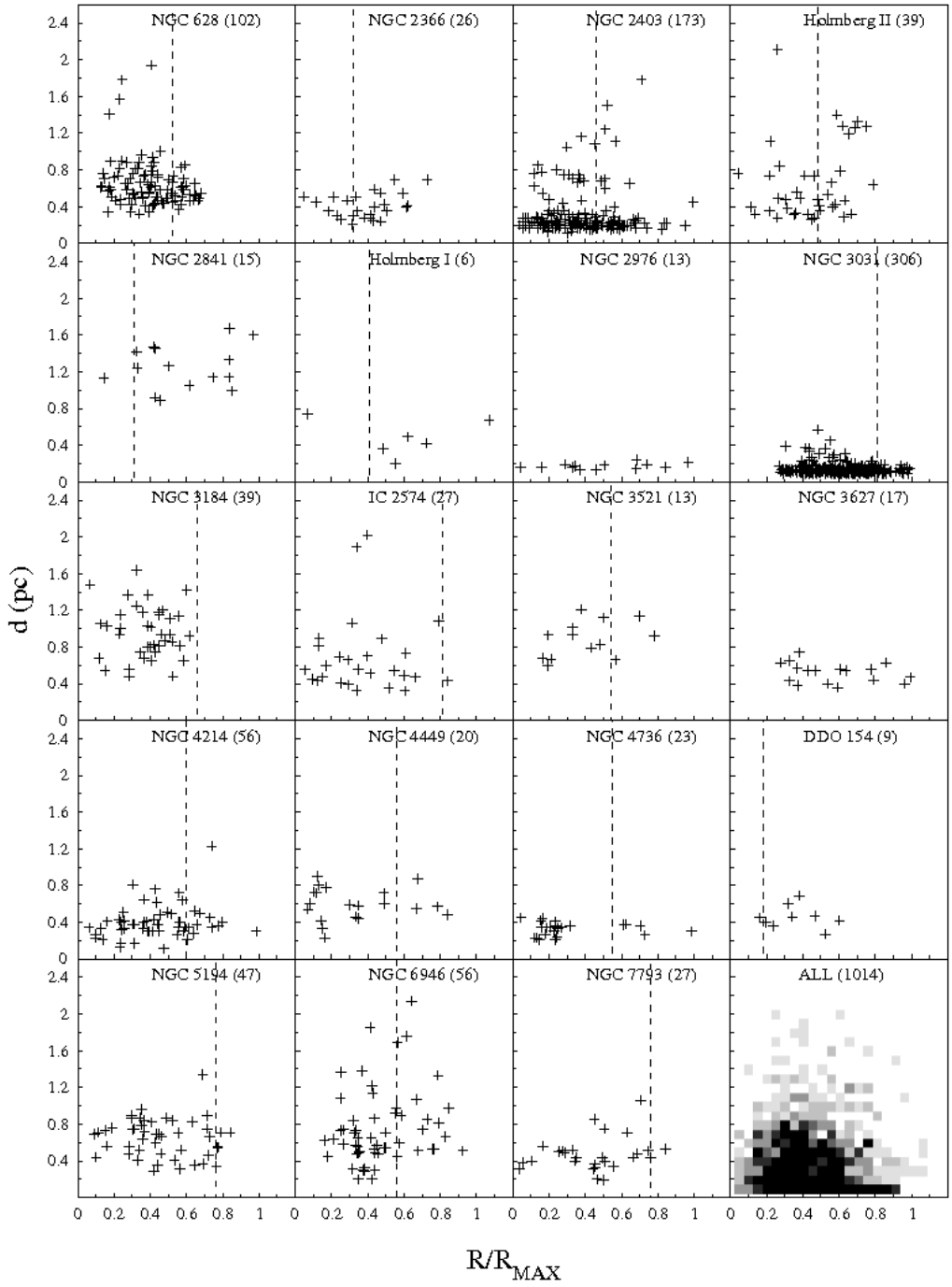

Figure 3.13: As Fig. 3.10 but showing diameter vs. normalised radial distribution. The dashed vertical line indicates for each galaxy the corresponding location of R_{25}. The bottom right panel shows the accumulated result for all galaxies where, rather than plotting individual values we present the data binned and in the form of a density plot.

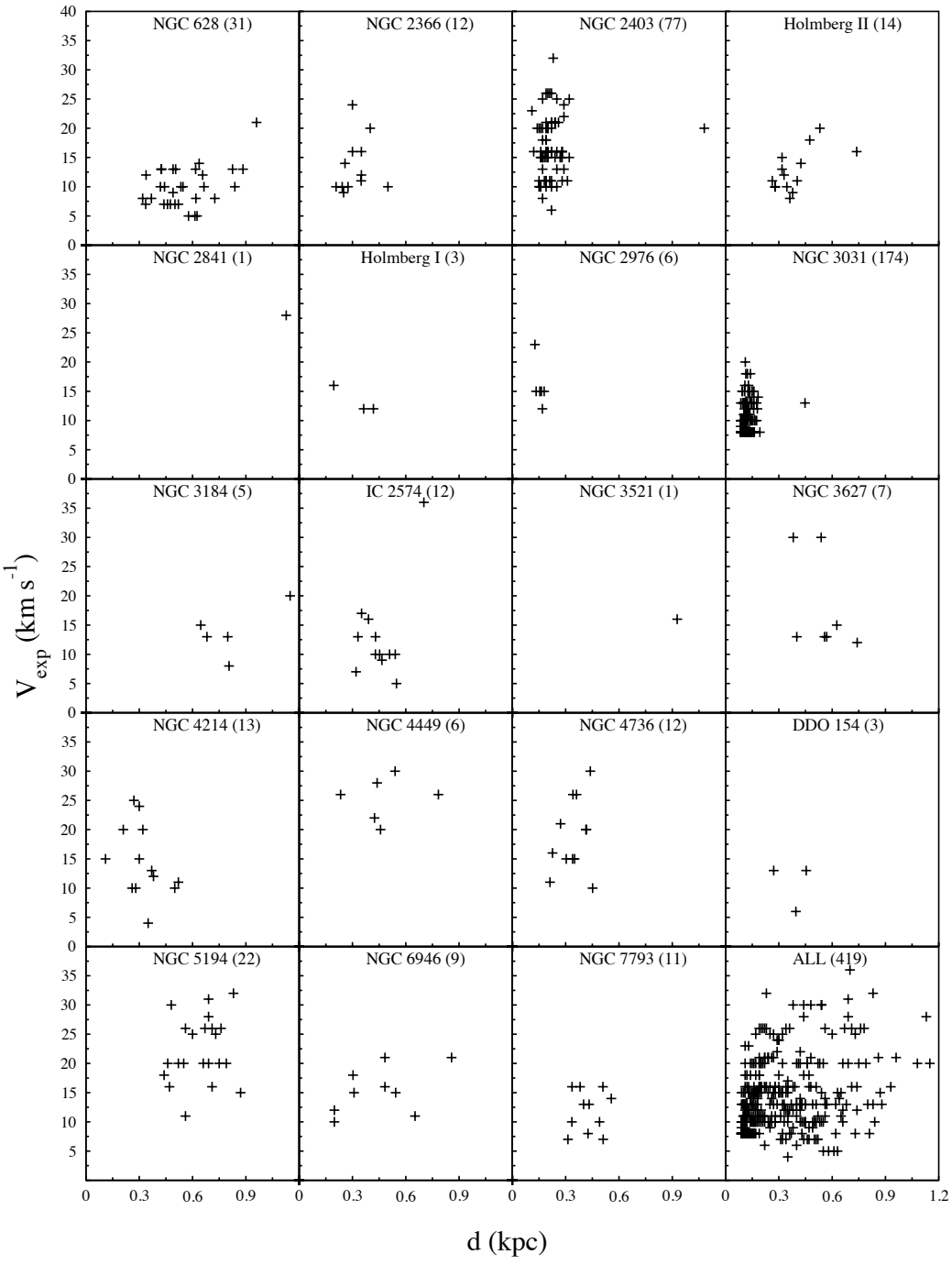

Figure 3.14: Diameter vs. expansion velocity of the expanding H I holes.

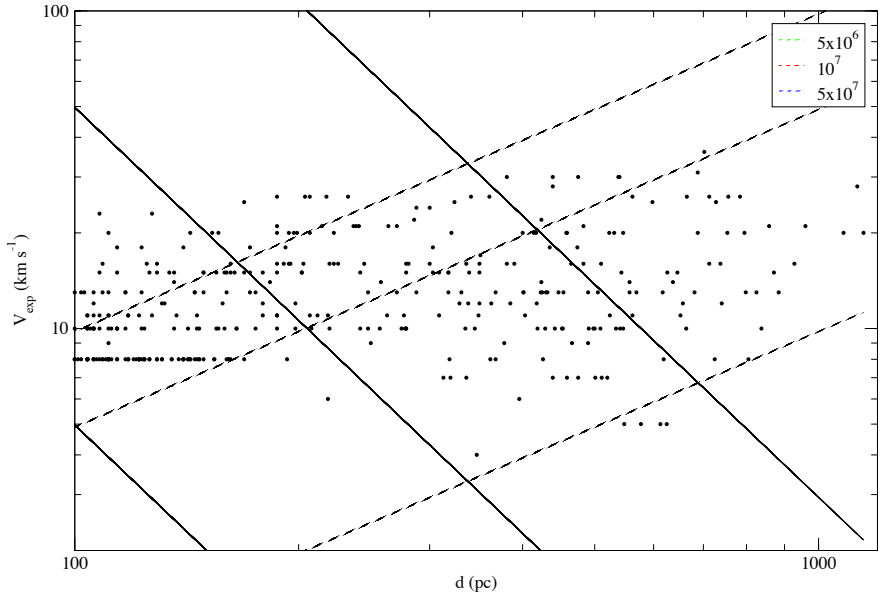

Figure 3.15: Diameter vs. expansion velocity of the expanding H I holes across the entire sample of galaxies. The dotted lines represent kinetic ages of 5, 10 and 50 Myr. The solid line represents energies of 10^{49} (leftmost line), 10^{50} and 10^{51} (outermost line) erg.

respectively, with a total of 831 versus 183 H I holes. The comparison between the sub-samples was carried out via Mann–Whitney (M–W) and Kolmogorov–Smirnov (K–S) tests. Both are non-parametric tests for assessing whether two samples can be drawn from the same parent distribution based on differences in the location of the medians (M–W) and differences in the shape of the two distributions (K–S). In order to accept or reject a hypothesis we took a 3–sigma level as the minimum significance level on both tests. In the following we compare the two sub-samples of spirals and dwarfs in graphical form. The results of the M–W and K–S tests are summarised in Table 3.2.

Figure 3.18a shows the difference in the distribution of diameters of the holes between dwarf and spiral galaxies. It appears that dwarf galaxies have larger holes on average than spiral galaxies. A Mann–Whitney test confirms this as well. This is of course not surprising in the light of the current discussion. What is surprising is that dwarf galaxies appear to have fewer small holes ($d < 200$ pc) even though the spatial resolution is better on average. This can be understood by realising that whereas star formation is a continuous process in spiral galaxies, it tends to occur in bursts in dwarfs. The time between bursts is longer than the duration of the star formation episodes (e.g., Gerola et al. 1980) so it is likely

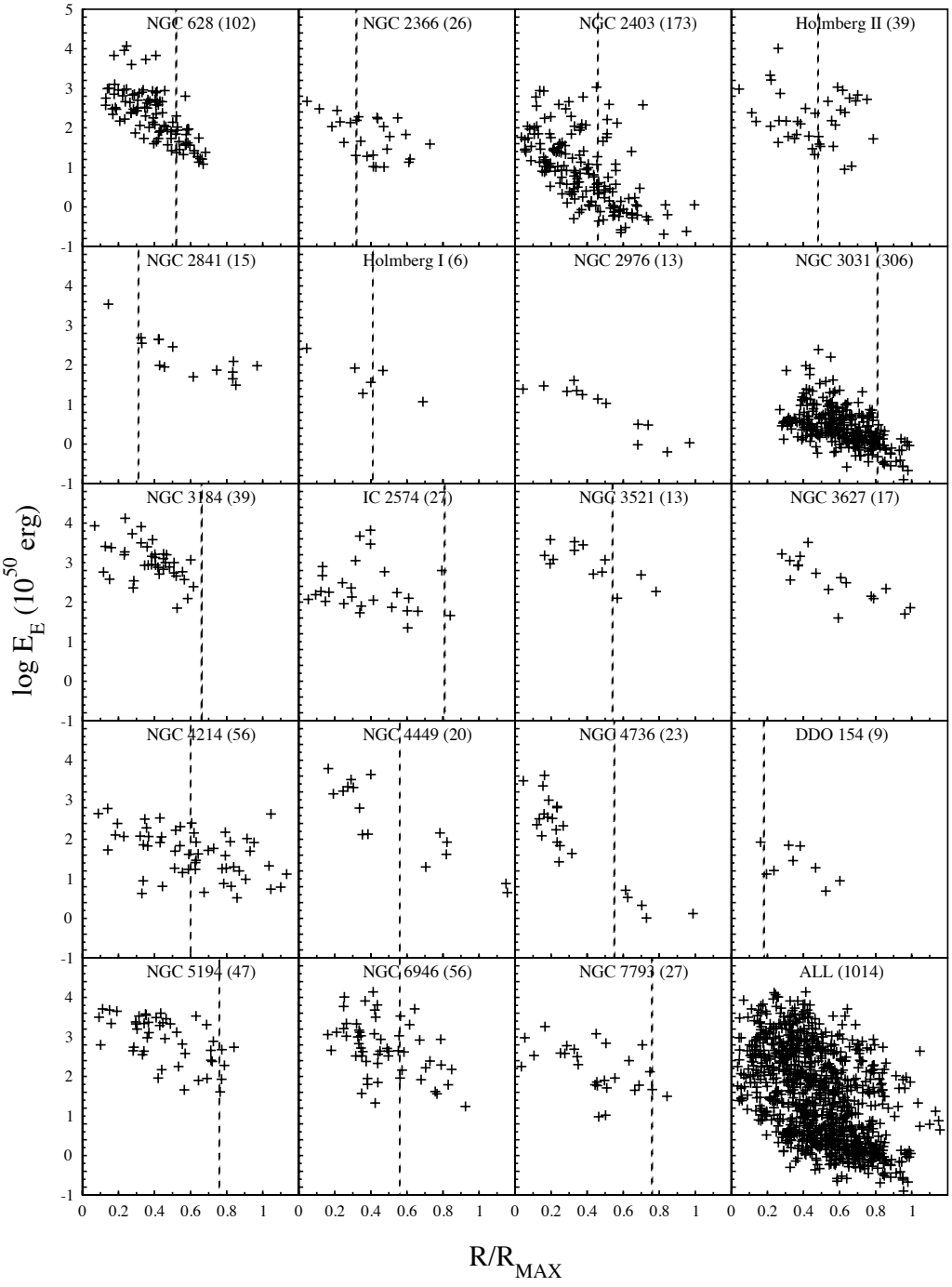

Figure 3.16: Energy requirement, plotted logarithmically, vs. normalised radial distribution of the H I holes. The dashed vertical line indicates for each galaxy the corresponding location of R_{25}. The bottom right panel shows the distribution of all holes combined.

that the dwarf galaxies whose ISM is currently riddled with H I holes are in a post-starburst phase. There will therefore be a relative lack of small holes, most holes having had the time to grow to typically ~ 100 pc and beyond.

In this comparative analysis we included all holes. However, the galaxies are spread over distances which cover a factor of ~ 3 between the closest and most distant one (in addition, the angular resolution varies slightly across the sample). Therefore, small holes in those galaxies that are further away will escape detection. If we exclude NGC 2841 and NGC 3521 from our sample then for the rest of the galaxies there is a minimum common spatial resolution of 280 pc, i.e. we should have a complete sample of holes larger than 280 pc in 17 galaxies.

Figure 3.18b illustrates the distribution of diameters of holes larger than 280 pc between dwarf and spiral galaxies. We now see that spiral galaxies have slightly larger holes than dwarf galaxies. We can understand this as follows: the energy requirement of expanding holes larger than 280 pc, Fig. 3.18c, shows a clear differentiation in the distribution of the two types of galaxies (K–S test). Holes in spiral galaxies appear to be significantly more energetic. Based on the way the energy is derived this difference could be due to the fact that holes in spiral galaxies are intrinsically more energetic, for example because OB associations in spirals are more massive. The effect of spirals having a larger energy input, on average, translates into spiral galaxies having larger H I holes.

The spatial distribution of the holes appears to be dependent on the type of the host galaxy as illustrated in Fig. 3.18e. In spiral galaxies holes appear to be concentrated within a smaller area of the disc, whereas in dwarf galaxies holes are distributed over a larger area. This is confirmed by a Mann–Whitney test. Even though the difference between the two distributions is subtle the result can be understood as being due to the fact that star formation in spiral galaxies mostly happens in the spiral arms which are located within the R_{25} radius. In dwarf galaxies star formation is spread across the entire disc.

To investigate this further we divided our sample of holes based on R_{25}, i.e., holes located inside and outside of this radius. We find that regardless of the type of the galaxy, holes outside R_{25} are larger and older, as illustrated in Fig. 3.19a and b. This is confirmed by the relevant Mann–Whitney test. This is in agreement with holes outside R_{25} being less affected by processes such as shear. When we look at the sample of holes larger than 280 pc no significant differences are found in the diameter and kinetic age distributions within and outside R_{25}.

There is no discernible difference in expansion velocity (Fig. 3.19c) even after

Table 3.2. Significance values of Mann–Whitney and Kolmogorov–Smirnov tests across a number of hole properties. Values less than ~ 0.001 exceed a 3σ significance threshold.

		Dwarf–Spiral		R_{25}	
Property	Sample	M–W	K–S	M–W	K–S
d	All	< 0.0005	< 0.0005	0.015	0.002
d	$d > 280$ pc	< 0.0005	< 0.0005	0.078	0.025
$V_{\rm exp}$	All	< 0.0005	< 0.0005	0.036	0.003
$V_{\rm exp}$	Expanding	0.049	0.006	0.541	0.543
$t_{\rm kin}$	All	< 0.0005	< 0.0005	< 0.0005	0.001
$t_{\rm kin}$	$d > 280$ pc	0.354	0.227	0.408	0.127
$E_{\rm E}$	$d > 280$ pc	< 0.0005	< 0.0005	< 0.0005	< 0.0005
$E_{\rm E}$	$d > 280$ pc, expanding	< 0.0005	< 0.0005	< 0.0005	< 0.0005
Axial Ratio	All	< 0.0005		0.573	0.578
Axial Ratio	$d > 280$ pc	0.001		0.851	0.397
R	All	< 0.0005	< 0.0005	···	···
R	$d > 280$ pc	< 0.0005	< 0.0005	···	···

we remove the stalled holes from our sample (Fig. 3.19d). Looking at the distribution of the energy requirement of holes larger than 280 pc with respect to R_{25} we find that on average holes have higher energies when located inside this radius (Fig. 3.19e). This holds true even when we break down our sample according to galaxy type (dwarf or spiral). Given that the diameter and expansion velocity distributions are similar in these two regions we conclude that this is driven by the difference in volume density.

Regarding the types of the holes we found that in spiral galaxies there are more partially and fully contained holes (type 2 and 3) within R_{25} (Fig. 3.19f). This is in agreement with the fact that holes inside R_{25} are smaller and younger, on average.

Because we are essentially complete (to our detection limit) for holes larger than 280 pc in diameter, we looked for relations of this subset of holes across our galaxy sample (excluding NGC 2841 and NGC 3521). The number per kpc^2 of these holes is presented in Figure 3.20 where this number density is plotted on a log scale against a) optical diameter of the host galaxy and b) against galaxy (Hubble) type. It is clear that despite the scatter there is a clear trend in the sense that the number density of holes decreases with increasing galaxy size (Spearman's $\rho = -0.40$, $p < 0.13$).

In the plot of number density against Hubble Type there is a trend (Spearman's $\rho = 0.53$, $p = 0.03$), the number density remaining more or less constant except for the class of dwarf galaxies (which are dominated by large holes). This trend is also apparent in Figure 3.21 which shows the average porosity of all the holes in

a galaxy, versus the type of the host galaxy. The porosity parameter, Q (Cox & Smith 1974), is the ratio of total volume (or area) occupied by holes to the total volume (or area) of the host galaxy. For the total volume of the galaxy we used $R_{\rm max}$ and the radial scale height as the thickness of the galaxy. The dwarf galaxies stand out as being on average more porous than spirals. Silk (1997) predicted that the porosity should anti-correlate with star formation surface density. As illustrated in Figure 3.21, later Hubble types have higher porosity (Spearman's $\rho = 0.47$, $p = 0.07$), and these same late-type galaxies form stars at a lower rate per unit mass than earlier types (Leroy et al. 2008). Figure 3.22 shows the 2–D porosity as a function of radius. Although similar to the radial H I hole surface density distribution (Fig. 3.7), it is not identical as the 2–D porosity distribution takes into account not just the number of holes, but also their size. What we find is that the porosity generally decreases as a function of radius with, as an exception perhaps, several of the dwarf galaxies such as Ho I and Ho II, where the histograms stay flat. The low porosity in the outskirts is likely a reflection of the generally lower star formation rate (SFR) density in these regions, i.e., well beyond the optical radius of a galaxy.

3.1.4 H I holes and the link with star formation

The ISM of galaxies is dominated by structures which are thought to originate from local energetic events. Even though OB associations, through the effects of stellar winds and supernovae, seem to be the obvious mechanism behind the creation of these structures (Oey & Clarke 1997), a direct correlation between OB associations and H I holes is often lacking (e.g., Kamphuis & Sancisi 1993; van der Hulst 1996; Rhode et al. 1999; Pasquali et al. 2008; Weisz et al. 2009b). Furthermore, there have been cases of holes with energy requirements that surpass the energy input from OB associations, or of holes which are found in regions, such as the Magellanic Bridge (Stanimirović 2007) where star formation is essentially absent. This has often been used as an argument to question the supernova origin leading to the many alternative explanations listed in the introduction. There are cases, notably the LMC/SMC where a clear link is found between massive stars and the location of H I holes (Stanimirović 2007), although even there in some 10% of the cases no such link is evident (Hatzidimitriou et al. 2005).

As Fig. 3.6 illustrates, in all but three galaxies many holes are found beyond the optical disc (R_{25}) of the parent galaxy. If the holes are indeed due to OB associations this picture may be problematic as the SFR density drops steeply beyond

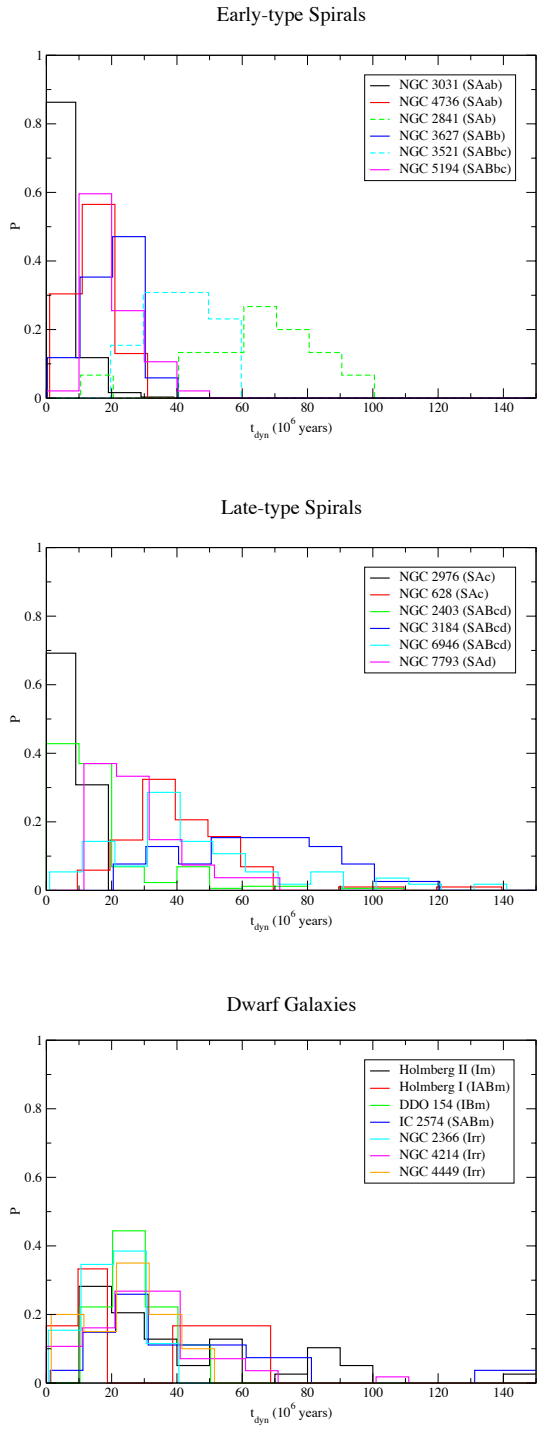

Figure 3.17: The distributions of the kinetic ages of the H I holes divided into 3 different groups of galaxies (from early-type spirals to dwarf galaxies) The dashed lines represent galaxies with the worst resolution hence their distributions are skewed to the right. The $y-$axis shows the relative number distribution, P.

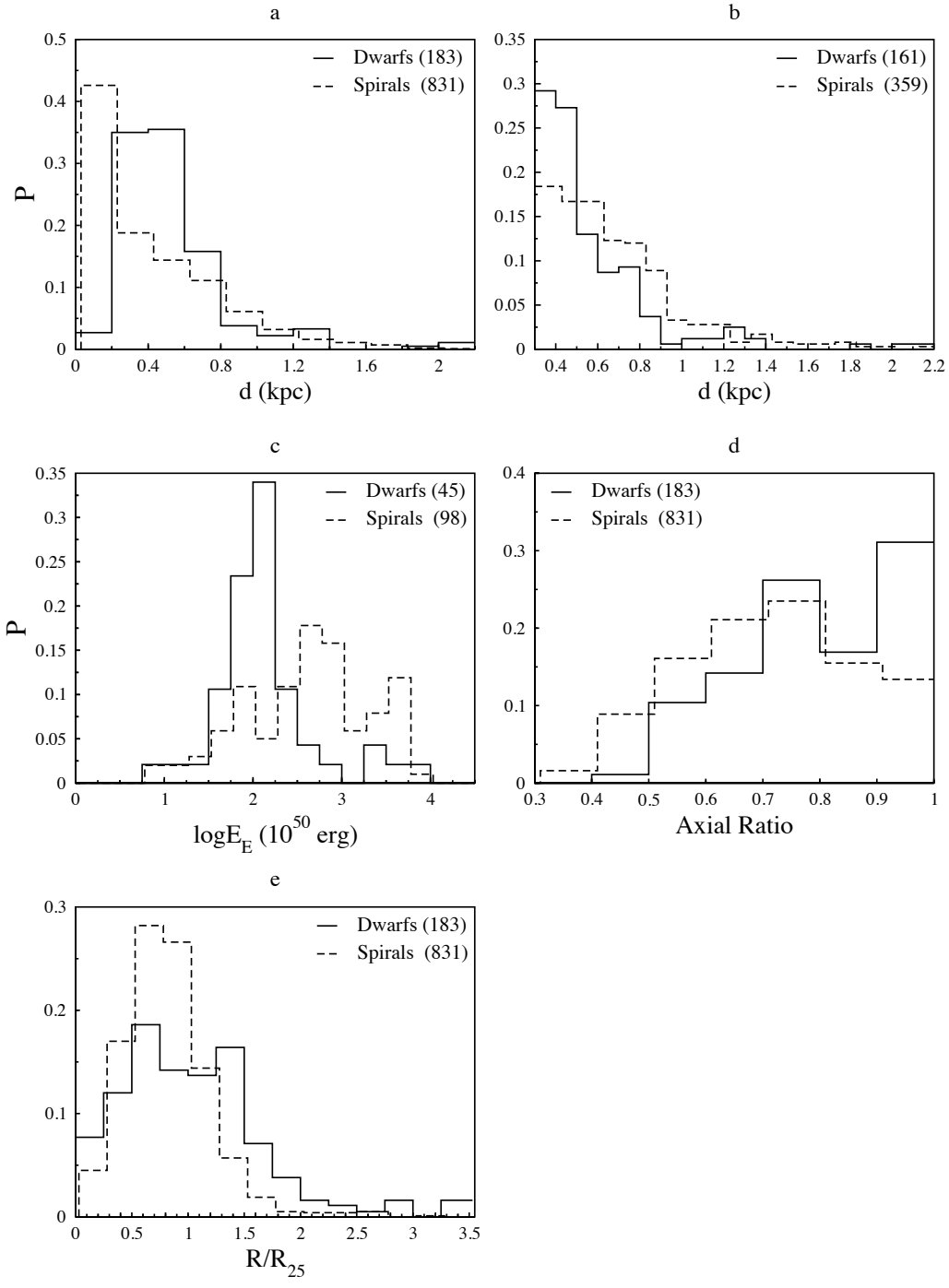

Figure 3.18: Histograms of various observed and derived properties of the H I holes, split over two sub-samples: spiral and dwarf galaxies. The numbers in parentheses indicate the number of holes in each group. Panels a, d and e include all holes, panel b includes holes larger than 280 pc and panel c includes all expanding holes larger than 280 pc. See Section 3.1.3 for details.

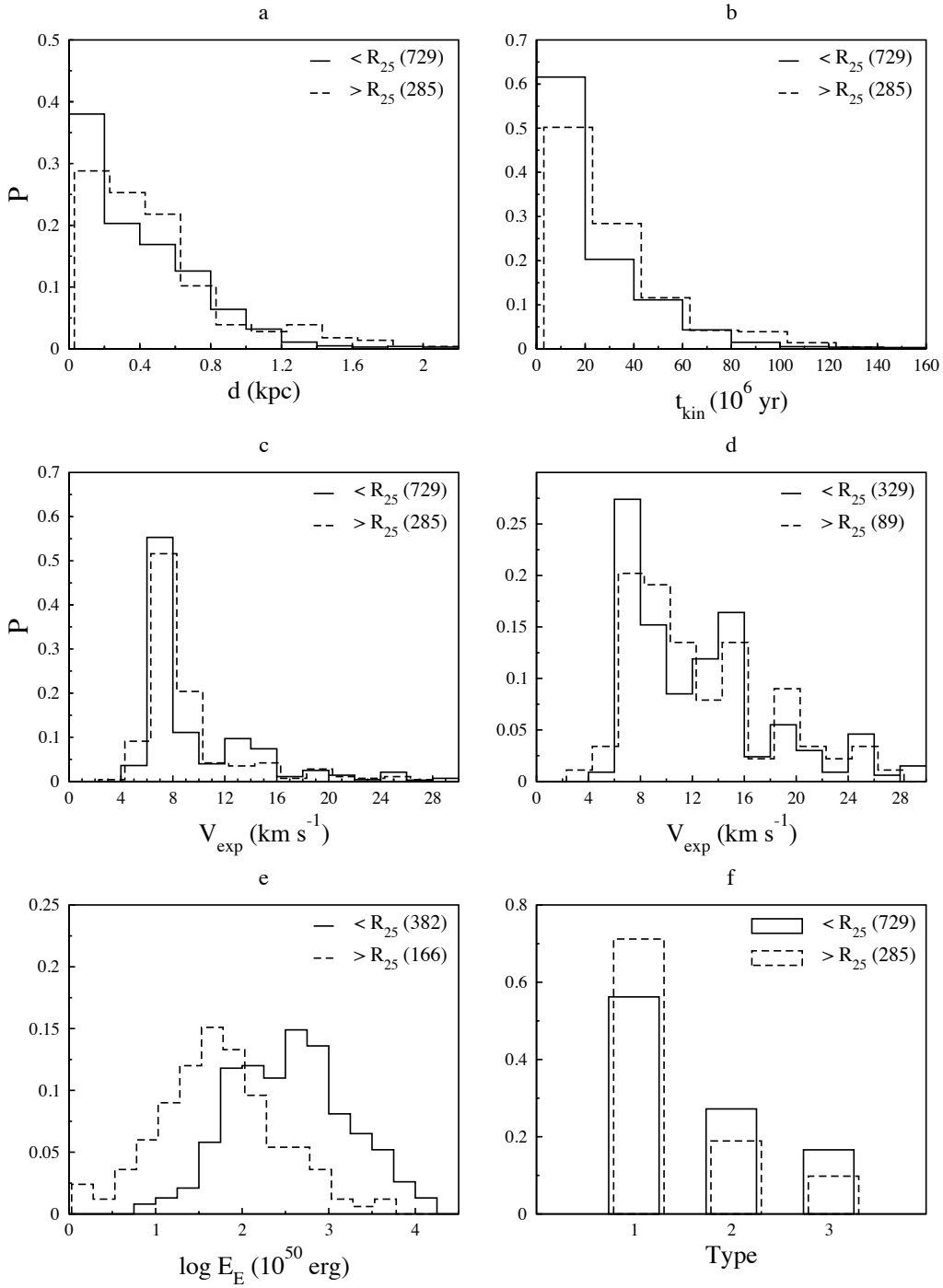

Figure 3.19: Histograms of various observed and derived properties of the H I holes, split over two sub-samples: holes located within or outside R_{25}. See Section 3.1.3, for details.

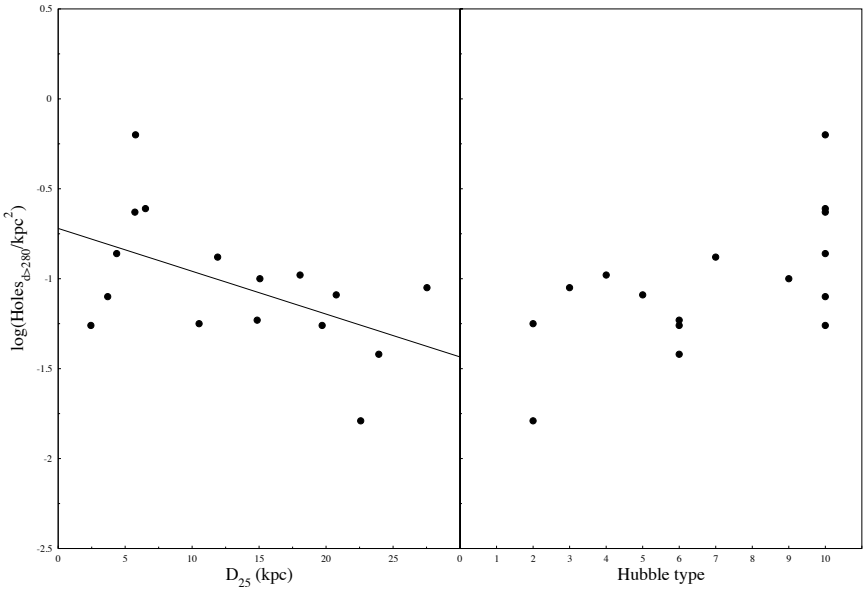

Figure 3.20: Log of the number of holes ($d > 280$ pc) per square kpc versus a) D_{25}, and b) Hubble Type. Each point represents one galaxy and the solid lines represent a least squares linear fit to the data.

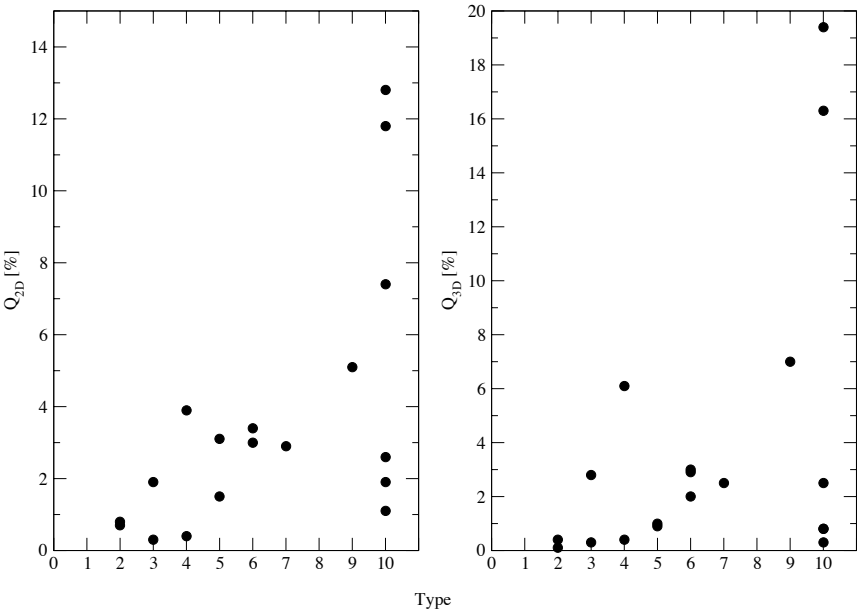

Figure 3.21: Surface (Q_{2D}) and volume (Q_{3D}) porosities of the H I holes versus Hubble Type.

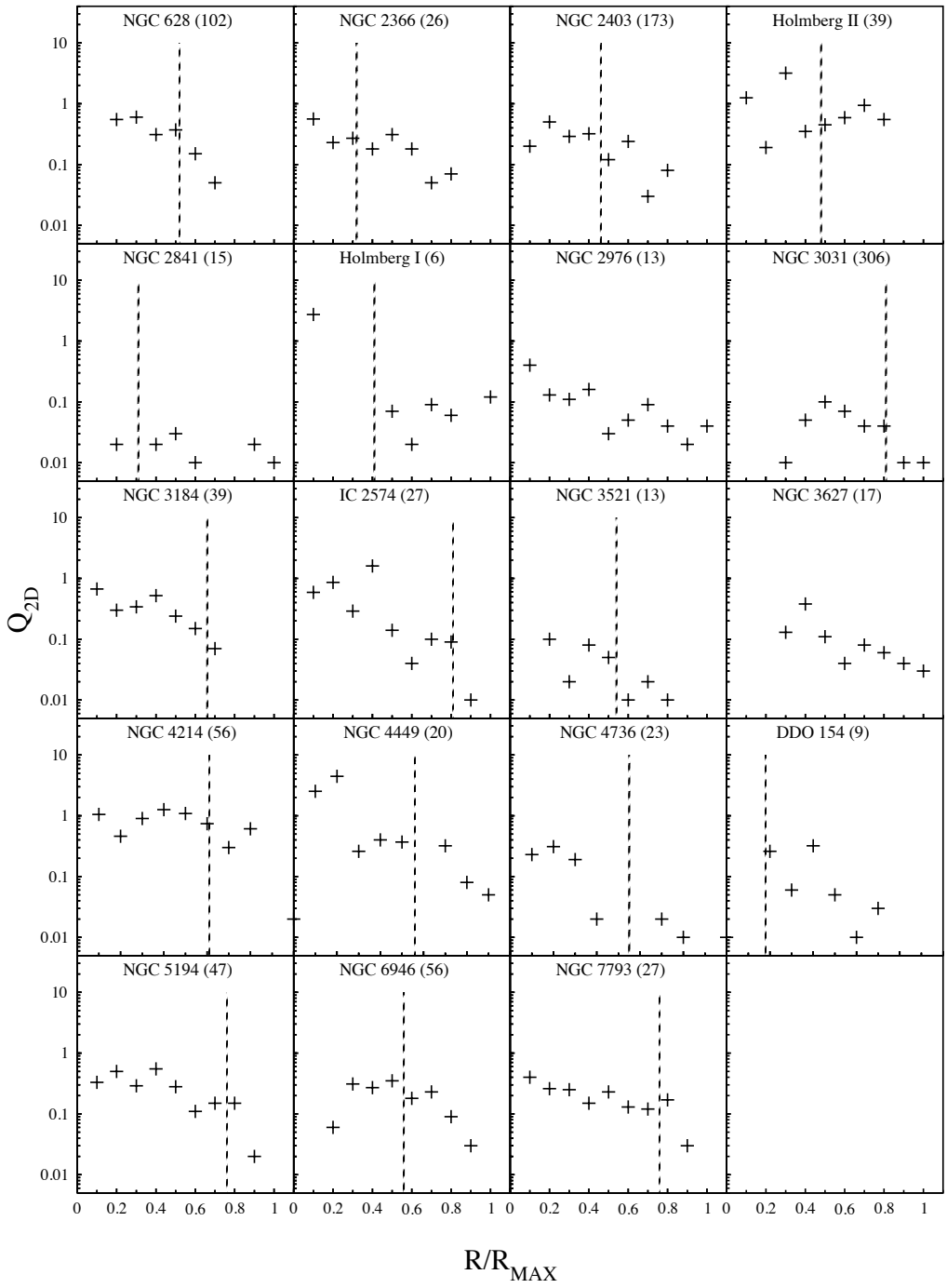

Figure 3.22: The 2–dimensional surface porosity distribution (per annulus) as a function of normalised radius. The vertical, dashed line is drawn at R_{25}.

R_{25}. It has been suggested that a "galactic fountain" (Bregman 1980), i.e., material expelled into the halo of the galaxy by supernova explosions, could be invoked. Hot fountain gas would eventually cool and fall back on to the disc, creating holes away from the original location of the OB association. If this is indeed the case then one would expect to find extraplanar gas in abundance surrounding the H I disc. Evidence of extraplanar gas expelled from galaxy discs, as expected in the "galactic fountain" model has recently been found by Oosterloo et al. (2007) and Boomsma et al. (2008). In addition, models of extraplanar gas by Fraternali & Binney (2006) and deep H I studies by Sancisi et al. (2008) do show a substantial supply of gas within a thick H I disc and halo, but their analysis seems to favour an external origin for this gas.

Recent results from the *GALEX* Nearby Galaxies Survey (Gil de Paz et al. 2007; Thilker et al. 2007) have obviated the need for these alternative explanations. Many galaxies show extended UV (XUV) discs. *HST* ACS observations resolve these XUV–disc sources into loosely clustered complexes, likely evolved OB associations (Thilker et al. 2008) and it thus seems safe to assume for the moment that the majority of H I holes, even those well beyond R_{25} are the result of massive star formation. If this is the case we can derive an independent estimate of the SFR of the host galaxy based on the energy requirements of the holes in a manner similar to how H II regions are related to the SFR based on measurements of their Hα flux; for an instantaneous burst and as long as the SF region is younger than 20 Myr, the Lyman–continuum output is constant and scales linearly with the SFR. An instantaneous burst does not have a SF rate but taking an ensemble average over an entire galaxy, this becomes equivalent to seeing a continuous SFR. The conversion between Ly–cont flux and SFR thus becomes independent of burst age. In the case of H I holes we are looking at individual and instantaneous events which, if averaged over an entire galaxy can similarly be linked to a SFR, under the assumption that every SF event will result in a hole. This assumption is likely to lead to an underestimate of the true SFR, of course.

If we assume that the supernovae that create H I holes are all of Type II and that the kinetic energy released by a Type II supernova is 10^{51} erg (McCray & Kafatos 1987) we can estimate for each hole the number of stars in the parent stellar association with masses above 8 $M_\odot$ (the minimum mass a star must have to go off as a Type II supernova, Biermann & Tinsley 1974).

Figure 3.23 shows the number of SNe per 10 Myr bin i.e the star formation history of each galaxy by plotting a histogram of the number of SNe needed per

hole against age of the hole for all holes in a galaxy. The letters E, L, D in the upper right corner stand for early-type, late-type and dwarf galaxy. For most of the galaxies (and especially all early-types) there is a cut-off at ~ 60 Myr indicating there is large incompleteness due to shear and diffusion. The lack of SNe younger than $\sim$ 10 Myr in some of the galaxies is a reflection of the lower resolution obtained for these galaxies. So, overall, holes trace the supernova history from 10 to 60 Myr, a time frame of 50 Myr. From Fig. 3.23 we learn that for most galaxies the SN history as derived from the H I holes is more or less constant. What this means is that by taking an ensemble average over a galaxy, and assuming a typical lifetime for an H I hole of 60 Myr, we can convert the supernova history into a supernova rate. The values for the calculated SN rates are listed in Table 3.3.

The supernova rate is proportional to SFR(M$>$ 8M$_\odot$), the star formation rate for stars more massive than 8 M$_\odot$. We can derive the total SFR by assuming a Salpeter IMF and integrating this between upper and lower stellar mass limits of 120 and 0.1 M$_\odot$. Given the fairly large uncertainty in the energy requirements of the holes the choice of IMF is not particularly critical. Using a Salpeter IMF we find that SFR $\sim 134 \times$ SFR(M$>$ 8M$_\odot$). The calculated SFR over 50 Myr, hereafter referred to as SFR$_{Holes}$, correlates very well (Spearman's $\rho = 0.78$, $p < 0.0001$) with the current (Hα–based) SFR as illustrated in Fig. 3.24 and Table 2.1 but our values fall short by 2–3 orders of magnitude. The error bars are formal errors using the uncertainties quoted in the observed and derived quantities.

The SFR based on the H I holes is a lower limit and depends critically on the energies we estimated. Various factors conspire to make this a lower limit. Our estimate for the kinetic age is an upper limit therefore the SFR derived here is a lower limit by default. In addition, our limited spatial resolution means that we are missing holes smaller than 100–200 pc in size. Given that these dominate the H I distribution (compare, e.g., the higher linear resolution data on the LMC/SMC) they account for a large fraction of the star formation. From theoretical models (Oey & Clarke 1997) and from studies of the Magellanic Clouds we know that the size distribution of holes follows a power-law. This is also evident from our data for the galaxies with the highest resolution (e.g., NGC 3031, NGC 2403 and Holmberg II). We derived an H I–hole distribution function for each of the galaxies and fitted a power-law to the high end part of each galaxy. On average we find an exponent of $a_\nu = -2.9$, in good agreement with Oey & Clarke (1997) who predict $-4 < a_\nu < -2$. This is illustrated in Fig. 3.25 for the integrated distribution function over all galaxies, for holes with sizes larger than 280 pc. The average

error of a_ν is of order 25% although in cases where the sample of holes is small the error is of order 50%. As Fig. 3.26 illustrates there is a correlation between a_ν and the type of the galaxy. Early-type spirals exhibit a steeper slope than late-type spirals and dwarf galaxies. This is a consequence of what we discussed above, namely that early-type spirals are dominated by a large number of small holes whereas dwarf galaxies have proportionally larger holes. We can extrapolate this power-law to the smallest size hole that has been discovered (Milky Way and SMC). Integrating from 10 pc to the spatial resolution in a particular galaxy we can derive corrected supernova and SF rates, $\nu_{\rm SN}^{corr}$ and SFR$_{corr}$ for all galaxies, assuming that every star forming region will create a hole. These values (tabulated again in Table 3.3) are likely to be representing the current SF since the vast majority of holes will now be small and young. We plot SFR$_{corr}$ in Fig. 3.27 and find that our rather bold extrapolation indeed brings the corrected SFR to within the range found based on other SFR indicators, although the scatter has increased considerably as well (Spearman's $\rho = 0.57$, $p = 0.031$). We do not wish to push this exercise too far but if anything, the hypothesis that holes are a consequence of massive star formation is compatible with our observations. Moreover, future studies at higher linear resolution and increased sensitivity should allow us to probe the size distribution down to H I holes created by a single SN event, leading to a near complete census of such features and a thorough testing of this assertion. Deep optical and UV observations that are able to resolve individual stars will be instrumental in characterising the expected remnant stellar population inside the holes.

3.2 Summary

In Chapter 3 we presented, for the first time, a comparative analysis of 1000 H I holes in 20 nearby galaxies based on the catalogues given in Chapter 2. This analysis was divided into four parts: an overview of the overall properties of the holes, a study of the relations between their properties, a comparison of these properties across all galaxies and the connection of holes with star formation. With respect to the overall properties we found that the diameters of H I holes range from 100 pc (the resolution limit for the closest targets) to ~ 2 kpc and the expansion velocities (where they could be measured) from 4 to 36 km s^{-1}. Their kinetic age varies from 3 to 150 Myr while the energy requirements span five orders of magnitude (10^{49}-10^{54} erg). In two galaxies, NGC 3031 and NGC 2976, we see

Table 3.3. Supernova and star formation rates

Galaxy	$log(SFR_{H\alpha})$ ($M_\odot\,yr^{-1}$)	$log(SFR_{Holes})$ ($M_\odot\,yr^{-1}$)	$log(SFR_{corr})$ ($M_\odot\,yr^{-1}$)	$log(E_E)$ (10^{50} erg)	$log(\nu_{SN})$ ($SN\,yr^{-1}$)	$log(\nu_{SN}^{corr})$ ($SN\,yr^{-1}$)	a_ν	Q_{2D}	Q_{3D}
NGC 628	0.1	−2.0	1.3	4.9	−4.2	−0.8	−3.6	3.1%	4.8%
NGC 2366	−1.0	−3.2	−1.2	3.4	−5.3	−3.3	−2.6	2.6%	0.8%
NGC 2403	−0.1	−2.8	−0.6	4.0	−4.9	−2.7	−2.7	2.7%	2.9%
Holmberg II	−1.1	−2.7	−2.2	4.4	−4.8	−4.3	−0.8	12.8%	16.3%
DDO 53	−2.1	−4.2	...	2.0	−6.1	...	...	...	...
NGC 2841	−0.7	−3.0	...	3.8	−5.1	...	...	0.3%	0.3%
Holmberg I	−2.2	−4.3	...	2.7	−6.4	...	...	1.9%	0.8%
NGC 2976	−1.0	−5.1	...	2.3	−7.2	...	...	1.5%	0.9%
NGC 3031	0.0	−3.5	0.3	3.3	−5.6	−1.8	−3.9	0.8%	0.4%
NGC 3184	0.2	−2.2	−0.4	4.9	−4.3	−2.5	−2.7	3.0%	2.0%
IC 2574	−0.9	−3.1	−1.8	4.3	−5.3	−4.0	−1.8	5.1%	7.0%
NGC 3521	0.5	−2.3	...	4.3	−4.4	...	...	0.4%	0.4%
NGC 3627	0.4	−2.7	0.6	4.1	−4.8	−1.6	−3.5	1.9%	2.8%
NGC 4214	−1.3	−3.1	−0.2	3.7	−5.2	−2.3	−3.1	11.8%	19.4%
NGC 4449	−0.3	−2.4	−0.1	4.3	−4.5	−2.2	−3.1	7.4%	2.5%
NGC 4736	−0.4	−2.7	0.7	4.2	−4.8	−1.4	−3.8	0.7%	0.1%
DDO 154	−2.4	−4.1	...	2.5	−6.2	...	...	1.1%	0.3%
NGC 5194	0.8	−1.7	0.4	4.9	−3.8	−1.7	−3.1	3.9%	6.1%
NGC 6946	0.7	−2.1	0.3	5.0	−4.2	−1.8	−2.8	3.4%	3.0%
NGC 7793	−0.3	−2.6	−1.2	4.0	−4.8	−3.3	−2.4	2.9%	2.5%

Note. — Col 1: Galaxy name; Col 2: SFR based on Hα; Col 3: SFR based on observed holes; Col 4: Corrected SFR derived from hole distribution function; Col 5: Total energy of holes; Col 6: SN rate based on observed holes; Col 7: Corrected SN rate derived from hole distribution function; Col 8: the slope of the hole distribution function; Col 9: surface porosity; Col 10: volume porosity

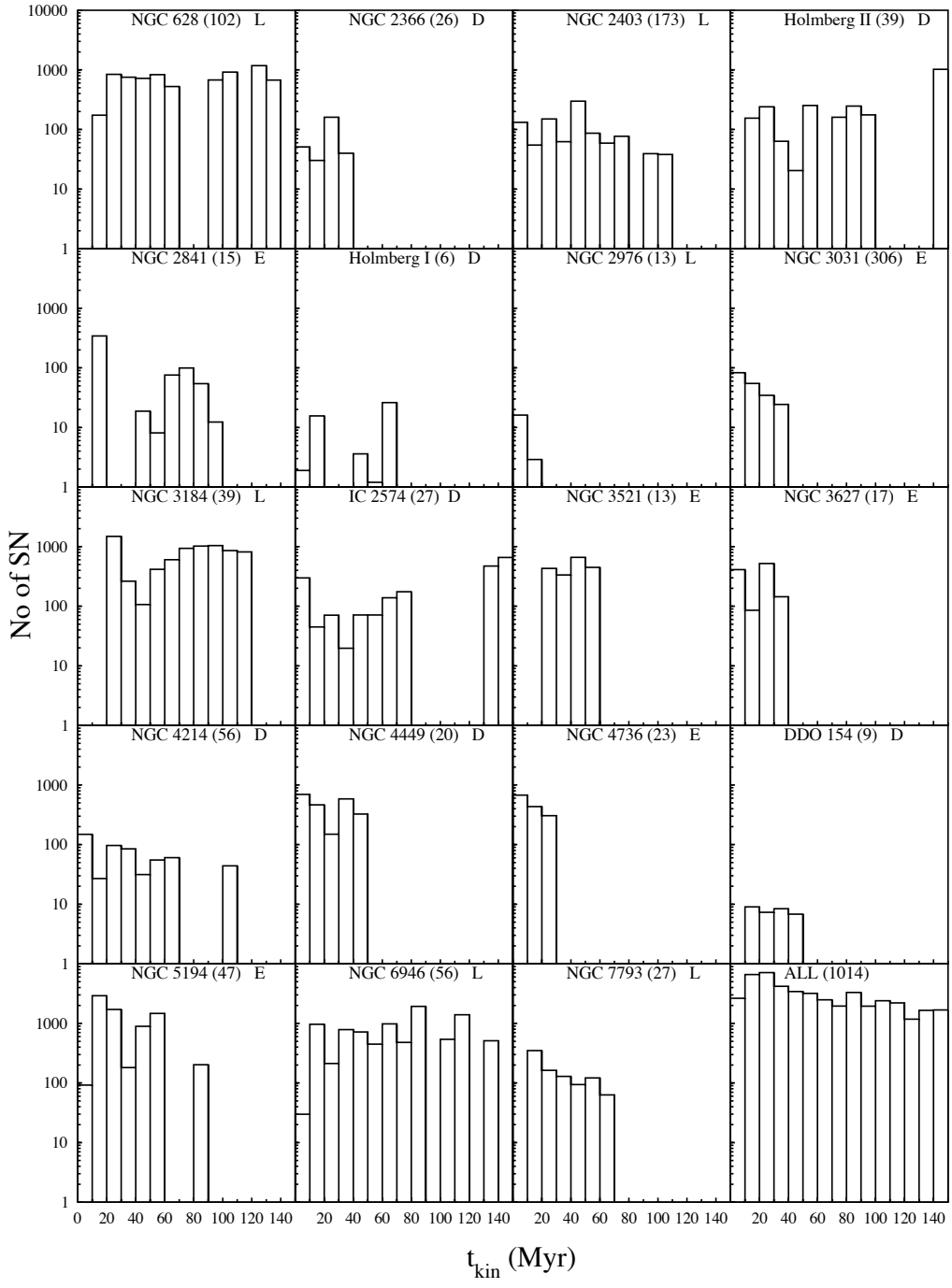

Figure 3.23: The number of SNe needed to create the H I holes as a function of the kinetic age in bins of 10 Myr. Note that the y–axis is on a logarithmic scale.

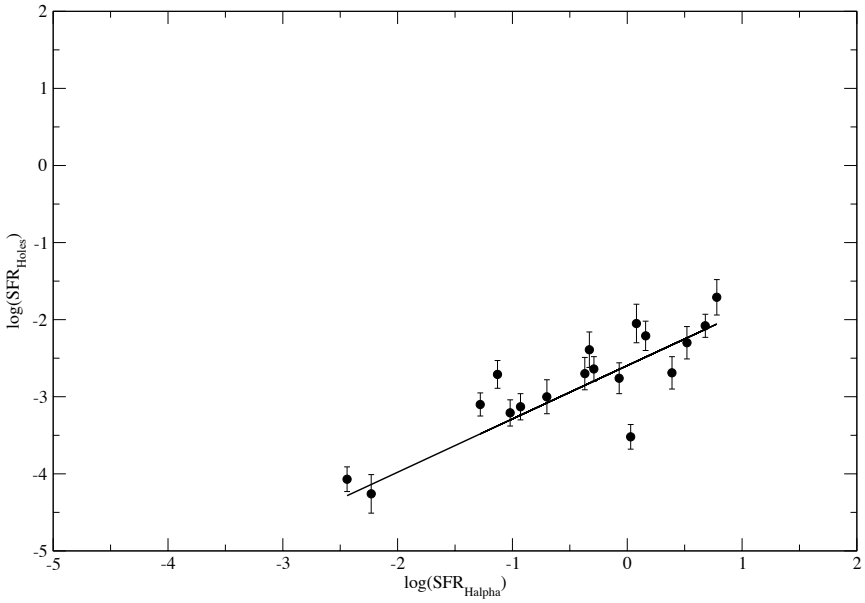

Figure 3.24: SFR derived from the H I holes plotted against the literature SFR based on observations of the Hα flux. The fitted least squares solid line has a correlation coefficient of 0.78 and corresponds to $\log(\mathrm{SFR_{Holes}}) = -2.60(\pm0.15) + 0.69(\pm0.15)\log(\mathrm{SFR_{H\alpha}})$

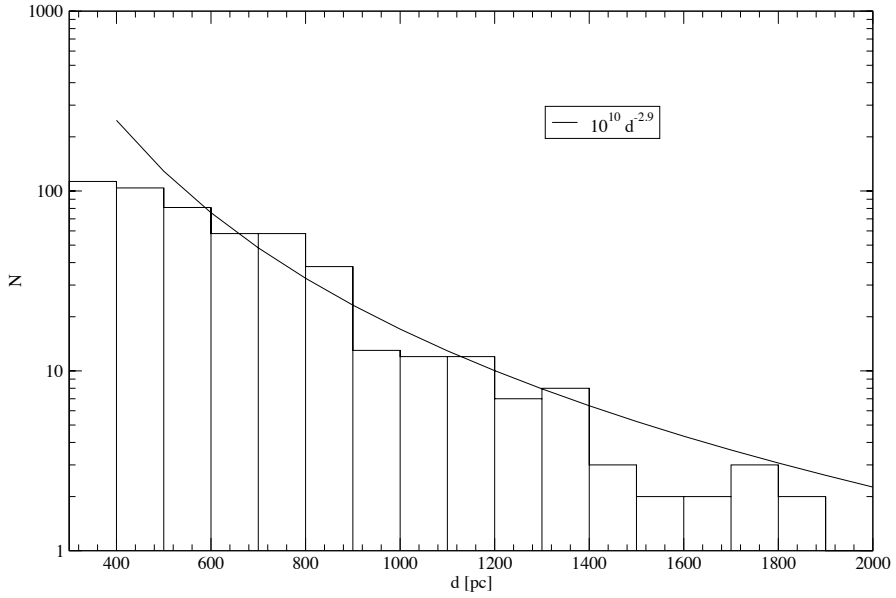

Figure 3.25: The distribution function of the H I holes across the entire sample of galaxies. Only holes larger than 280 pc were used. The least squares solid line represents the best power law fit to the data.

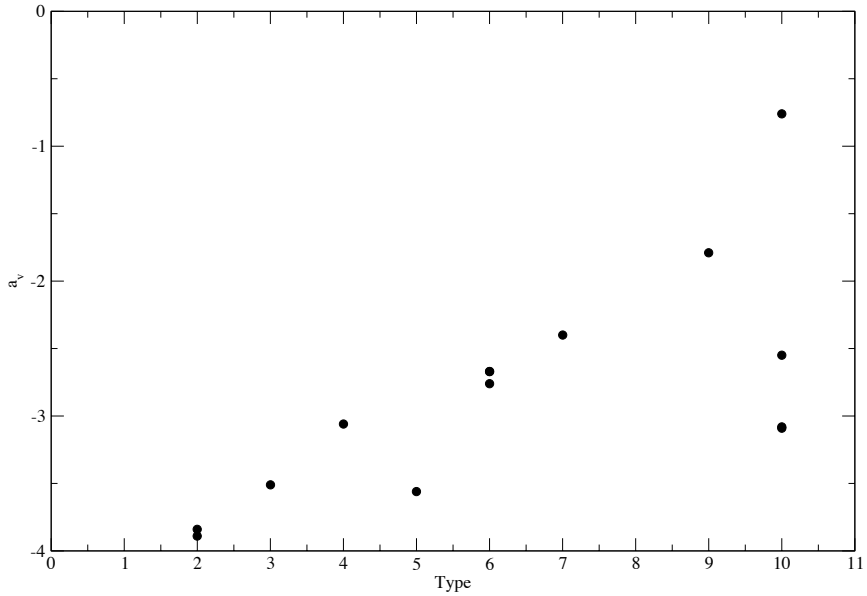

Figure 3.26: The slope of the distribution function of the H I holes vs. the type of the galaxy. Early-type spirals have a steeper slope compared to late-type and dwarf galaxies.

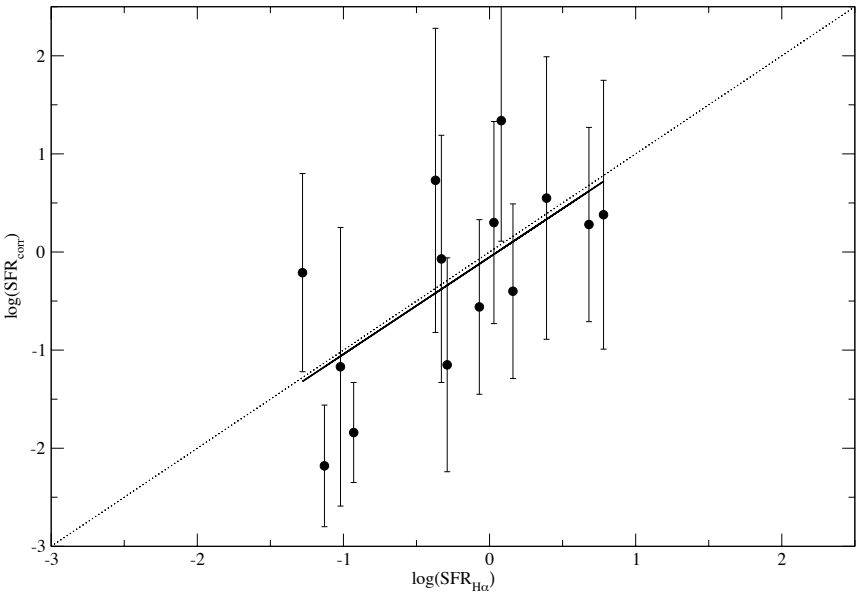

Figure 3.27: Corrected SFR derived from the H I holes plotted against the literature SFR based on observations of the Hα flux. The fitted solid line has a correlation coefficient of 0.78 and corresponds to $\log(\mathrm{SFR_{corr}}) = -0.05(\pm0.23) + 0.99(\pm0.34)\log(\mathrm{SFR_{H\alpha}})$. The dotted line corresponds to a one to one correlation.

a sharp cut-off in the kinetic age of the holes at roughly 40 Myr, which can be attributed to a recent burst of star formation due to interactions in the M81 group of galaxies. Looking at their position, H I holes are found throughout the H I disc of the parent galaxy, all the way to the edge of the disc. Specifically, 77% of the holes fall within R_{25} with a nearly constant number surface density while 23% are found outside this radius where we see a drop in their number surface density.

An investigation of the relation between the properties of the holes revealed that holes in dwarfs are rounder, on average than in spirals. We attribute this difference on the effect of shear in differentially rotating discs; in spirals shear modifies the geometry of holes and sets a limit to their age, which we found to be of order 50 Myr. In contrast, dwarf galaxies rotate as solid bodies and consequently the lack of shear in these systems allows for longer-lived and older structures. We find that the lower limit of the axial ratio of 0.4 is an indication that structures more elongated than this value can not be classified as holes in our method. In addition we find that, blow-out holes in spirals are not circular as, otherwise, the inclination under which the discs are viewed would cause the major axis of holes to be aligned with the major axis of the disc, which is not observed. In contrast to findings from previous studies we did not find a correlation between the diameter and expansion velocity. Such a relation has been previously observed in holes smaller than our resolution limit and is due to small holes not having reached their final size yet. If we look at holes larger than 100 pc then our findings agree with those from previous studies.

A comparison of the H I hole properties between different galaxy types revealed that holes in early-types are considerably younger that those in late-type galaxies. This is a consequence of the stronger shear in early-types which smears out holes faster. Dividing the sample into dwarf and spiral galaxies, we find that dwarf galaxies have, on average, fewer young holes than spirals, even though our spatial resolution is higher in these systems. We attribute this trend to differences in the star formation cycle i.e., starbursts in dwarfs as opposed to continuous star formation in spirals. In terms of expansion velocity, no difference is found between dwarfs and spirals.

An investigation of the spatial distribution of holes was carried out by splitting our sample based on the optical disc of each galaxy as defined by the R_{25} radius. Due to lack of shear in dwarfs we observe that the radial distribution of H I holes is more extended in those systems. Similarly we find that holes outside R_{25} in all systems are larger and older as shear has less of an effect in the outer parts of

galaxies.

We looked at the porosity of the ISM and we found this to be higher in dwarf galaxies, another indication of the lack of destruction mechanisms in dwarfs. Specifically, we established a positive correlation between surface and volume porosity (Q_{2D} and Q_{3D}) with Hubble type as predicted by theory. In addition, the porosity decreases as a function of radius reflecting the lower star formation density in the outer parts of galaxies.

Previous studies have often failed to find a direct correlation between H I holes and star formation, even though feedback from OB associations appears to be the obvious mechanism responsible for the formation of H I holes. We presented our attempt to establish such a trend in a way similar to how star formation is linked to H II regions i.e., as an ensemble average of individual regions. Assuming that the SNe that created holes are all of Type II and that holes trace the supernova history from 10 to 60 Myr we estimated the star formation history for each galaxy and found that it correlates with the star formation rate as traced by Hα. Since our spatial resolution is at best 100 pc we miss a substantial number of smaller holes and thus our star formation history values fall 2-3 magnitudes short of the measured star formation rate. From previous studies we know that the size distribution of holes follows a power law which depends on the type of the galaxy. We consequently determined the size distribution of the holes in every galaxy in our sample and found that the average slope is $a_\nu \sim -2.9$ with individual galaxies having slopes ranging from -2 to -4. Assuming a single O star can create a hole with a minimum size of 10 pc, we extrapolated our observations and predicted the total size distribution of holes. This exercise allowed us to estimate the "corrected" star formation history of each galaxy and we found that it is well-correlated with the current star formation rate. As a result of this H I holes can be understood as being the result of massive star formation.

Chapter 4

A Multi-Wavelength View

4.1 Descriptive Analysis

The characterization of the ISM relies upon examining its various components as seen by different tracers. In order to see how each component relates to others, it is important to analyse each tracer in detail. In this exploratory study we decided to focus on the ISM of a single galaxy, NGC 2403. The selection of this particular galaxy among the 20 other galaxies studied so far was based on a number of criteria. The obvious criterion was the availability of ancillary observations and for NGC 2403 we have access to observations covering a large part of the EM spectrum. These include H I from THINGS (Walter et al. 2008), CO(2–1) from HERACLES (Leroy et al. 2009), 8μm, 24μm, and 70μm from SINGS (Kennicutt et al. 2003), Hα from the SINGS Data Release 4 and FUV from the NGS (Gil de Paz et al. 2007). A second criterion was to aim for the highest resolution in order to be able to go down to the smallest possible linear scale and therefore we were looking for the closest galaxy among our THINGS sample. Finally, since we will be looking at individual structures, we selected NGC 2403 for its large number of H I holes detected (Bagetakos et al. 2011). An area of particular interest is how structures in the ISM as traced at different wavelengths relate to areas of star formation. Following Leroy et al. (2008) we created a star formation surface density map as described in Chapter 4.1.1. The available maps for NGC 2403 are presented in Fig. 4.1.

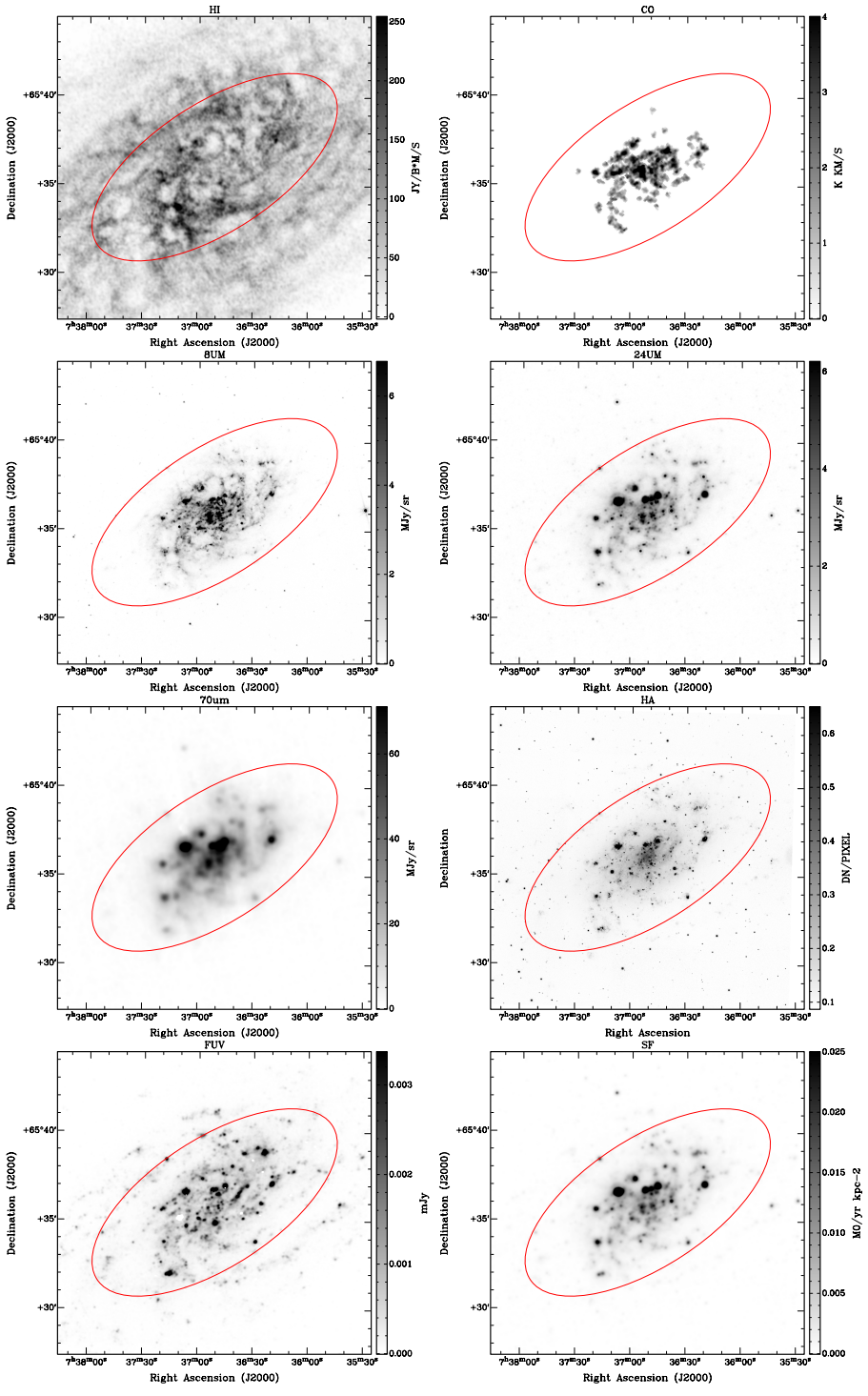

Figure 4.1: The 8 data products of NGC 2403 used in this study. Left column from top to bottom: H I, 8μm, 70μm and FUV. Right column from top to bottom: CO, 24μm, Hα and a composite map tracing current star formation (SF; see text for details). The red ellipse corresponds to R_{25}.

4.1.1 Data

H I map

The H I map comes from observations with the VLA of the 21–cm line obtained as part of THINGS. We use the natural weighted integrated H I map which has a beam size of $8.7'' \times 7.6''$ corresponding to 136×119 pc at the distance of NGC 2403. The data reduction is described in Walter et al. (2008).

CO map

A significant mass fraction of the ISM is in the form of molecular gas, mainly molecular hydrogen (H_2) gas, most commonly found in giant molecular clouds (GMCs). It is widely accepted that all stars form out of molecular clouds and therefore studies of star formation rely heavily on observations of the molecular gas. However, H_2 can not be observed directly as it does not have a dipole moment and the temperature in GMCs is not high enough to excite quadrupole or vibrational transitions. Indirect observations of H_2 are based on the lower CO transition lines, mainly the transitions between the first rotationally excited state and the ground state ($J = 1 \rightarrow 0$) as well as between the second state and the first ($J = 2 \rightarrow 1$). The conversion from CO intensity to H_2 abundance carries some uncertainty and it also shows a metallicity dependence. Typical vales are of order $2.0 \times 10^{20}\,\mathrm{cm^{-2}}\,(\mathrm{K\,km\,s^{-1}})^{-1}$. We use the HERACLES map obtained at the IRAM 30 m telescope of the CO $J = 2 \rightarrow 1$ transition. The angular resolution is $13.4''$ which corresponds to 210 pc. The calibration and data reduction are described in Leroy et al. (2009).

SINGS maps

The 8μm emission traces dust and in particular polycyclic aromatic hydrocarbons (PAHs). These aromatic molecules are typically a few Å in size and consist of a few hundred carbon atoms which absorb ultraviolet and optical photons and re-emit in the mid-infrared band and specifically at 7.7μm. Studies of the PAH distribution in the Galaxy and nearby galaxies revealed a very confined structure, compared to the optical disc, not only because dust is less abundant in the outskirts of galaxies but also because of there being fewer massive stars that are required to heat the grains. In addition, 8μm emission is mainly detected on the rims of star-forming regions implying that it is suppressed within strong star-forming regions (e.g. Smith et al. 2007).

The 24μm emission traces thermal emission by warm ($\sim$ 100 K) dust heated by young stars and it strongly depends on the strength of the radiation field. It usually peaks within star-forming regions coinciding with H II regions and consequently has been used as a star formation indicator (Calzetti et al. 2007). Extended 24μm emission is also common in nearby galaxies and originates from the diffuse interstellar medium.

The 70μm emission traces colder ($\sim$ 20 K) dust which accounts for the majority of the total dust mass. It has also been used as a SFR indicator (Calzetti et al. 2010) in individual galaxies as well as large galaxy samples.

We use IRAC 8μm and MIPS 24μm and 70μm data obtained with the *Spitzer* Space telescope as part of SINGS. The angular resolution is 2″, 6″ and 16″, corresponding to 31, 94 and 250 for the 8μm, 24μm and 70μm respectively. Details of observations are described by Kennicutt et al. (2003) whereas data reduction and processing are given in Gordon et al. (2005).

Hα map

The Hα spectral line traces ionized hydrogen and is most commonly associated with H II regions, the sites of current massive star formation, as well as diffuse ionized interstellar gas. The most massive stars emit UV radiation which heats and ionizes the hydrogen gas causing it to emit the Hα line. For this study we use the NGC 2403 Hα map from SINGS Data Release 4 which we continuum subtract and from which we remove artefacts left by foreground stars.

FUV map

The source of UV radiation is massive young stars. UV is efficiently absorbed by dust and re-emitted at FIR wavelengths so it is heavily affected by internal extinction. It predominantly traces the unobscured recent (10–100 Myr) SF (e.g. Kennicutt 1998). The FUV map comes from the *GALEX* space telescope. *GALEX* is a NASA space observatory which observes simultaneously in two channels; a FUV band covers wavelengths from 1350Å to 1750Å and a NUV band which covers the wavelength range 1750–2800Å. The angular (FWHM) resolution for the FUV is 4″ corresponding to a spatial resolution of 62 pc. Gil de Paz et al. (2007), Martin et al. (2005), and Morrissey et al. (2007) provide full details on the satellite, telescope, instrument and calibration, and data processing pipeline.

SFR map

As was mentioned earlier FUV radiation traces the unobscured recent star formation but suffers from internal extinction. Dust absorbs FUV and re-emits at mid-infrared wavelengths. It is possible therefore to estimate the embedded SFR from 24μm as proposed by Calzetti et al. (2007) and Kennicutt (2008). We created SFR surface density maps by combining the 24μm and FUV maps as described in Leroy et al. (2008). The map was obtained using the formula:

$$\Sigma_{SFR}[\,\mathrm{M_\odot yr^{-1}kpc^{-2}}] = 3.2\times10^{-3} I_{24}[\mathrm{MJy\,ster^{-1}}] + 8.1\times10^{-2} I_{FUV}[\mathrm{MJy\,ster^{-1}}], \tag{4.1}$$

where Σ_{SFR} is the SFR surface density, I_{24} is the 24μm intensity and I_{FUV} is the FUV intensity.

4.1.2 Visual comparison

The 8μm map is illustrated in Fig. 4.2 with 24μm emission contours superimposed. The correlation between these two maps is striking and expected since both the 8μm and 24μm trace the interstellar dust. This correlation is apparent in terms of emission peaks as well as in the general distribution of dust and holds down to a scale of 35″ (550 pc; Fig. 4.3). The distribution of PAHs as traced by 8μm is also similar to the distribution of H I (Fig. 4.4). Large-scale structures appear identical in the two maps. However the biggest difference is that the H I distribution is much more extended. In addition, the agreement breaks down when looking at areas smaller than $\sim 50'' \times 50''$ (780×780 pc) in size (Fig. 4.5). With respect to the H I holes, these match well with "holes" in the 8μm distribution as Fig. 4.6 illustrates. Overall, it appears that PAHs are well mixed with atomic hydrogen. The 8μm map is closely related to the Hα map but loosely related to the FUV map especially on small scales (Fig. 4.7). However, most of the 8μm emission peaks coincide with peaks both in the FUV and Hα maps illustrating the heating of PAH molecules by massive stars in star forming regions.

Looking at the dust component as traced by the 24μm map we see that it strongly correlates with the FUV and Hα maps revealing the connection between warm dust and star forming regions (Fig. 4.8). It is also well linked to the H I map, albeit the emission is much more centrally concentrated. Looking at the H I holes we see that no 24μm emission is detected from the interior of the majority of holes a situation similar to that of the 8μm map. Unlike the 8μm–H I holes

relation however, there are cases where 24μm emission is prominent on the rims of some holes (hole numbers 74, 81, 83, 76, 94, 100 from Bagetakos et al. 2011 and Chapter 2) possibly highlighting areas of propagating star formation.

The distribution of the molecular gas, as traced by the CO line, is closely related to that of the atomic gas as well as the dust component as Fig. 4.9, Fig. 4.10 and Fig. 4.11 illustrate. On these figures the contours represent the molecular gas. The CO emission follows the H I distribution closely, i.e., CO emission is only detected where there is H I emission and the peaks of the H I and CO emission are well correlated which fits a picture in which CO forms out of atomic gas. The opposite is not always true; many H I peaks do not have a CO counterpart an indication that molecular clouds have not formed in these areas. This is possibly due to the intense interstellar radiation field and/or a low metallicity environment which fails to effectively shield the cold atomic clouds from interstellar radiation (Krumholz et al. 2009). With respect to the H I holes, molecular gas is absent from the vast majority of these. This finding reinforces the idea that molecular gas is dissociated and subsequently ionized inside H I holes by the UV radiation of the massive stars, and swept up by SNe.

Nine out of sixteen holes younger than 5.2 Myr and within R_{25} have FUV flux emission in their interiors. In addition, 6 older holes (hole numbers 55, 74, 81, 85, 102, 128 from Bagetakos et al. 2011 and Chapter 2) have FUV offset from their centres which is expected given that, with a stellar velocity dispersion of 10 km s^{-1}, a cluster will disperse over 100 pc in 10 Myr and 1 kpc in 100 Myr (see Dobbs & Pringle (2009) for models). The distribution of FUV emission is illustrated in Fig. 4.12. The most striking characteristic of FUV emission is that it is quite extended and goes out to the outskirts of the H I disc at a radius of $\sim$ 16 kpc, well outside the R_{25} radius (Fig. 4.13). When compared to other maps, the FUV map is most similar to the Hα map and 24μm maps, an observation which shows that all star formation tracers, whether direct or indirect, are well correlated. In contrast, there is almost an anti-correlation of the FUV and Hα maps with both of the gas tracers (H I and CO). This is to be expected; in areas where there is intense FUV and/or Hα emission the gas will become ionized and where there is abundant gas, there is accompanying dust which absorbs especially FUV. However, some FUV peaks coincide with peaks in the CO map (Fig. 4.14). We speculate that these areas are sites of current, ongoing star formation where new stars are still largely embedded in the parent molecular cloud. The ionizing radiation in these sites is still shielded and can not dissociate and ionize the molecular and atomic clouds

which explains why FUV also correlates with H I emission in these areas. Looking at specific areas of interest, we have identified 8 regions (X1–X8) where the FUV emission peaks (Fig. 4.12). Four of these (X1, X2, X3 and X5) coincide with peak areas on the Hα and 24μm maps. Consequently, these correspond to sites of current ($<$ 15 Myr) star formation. The other 4 regions (X4, X6, X7 and X8) have very weak (in terms of flux) counterparts in the 8μm and Hα maps. Since FUV is still emitted by stars of class B9 and later we can assume that these regions correspond to sites of recent (15–30 Myr) star formation activity. By this time the more massive O and B stars will have exploded as SNe creating holes in the H I distribution which is exactly what we observe. Specifically, holes no 50, 74, 90 and 128 (with estimated kinetic ages 4.7, 9.1, 4.1 and 45.8 Myr) are found to be related spatially to X4, X6, X7 and X8 respectively. Holes 74 and 128 are offset from the FUV peaks by 15$''$ and 22$''$ respectively but given their larger estimated kinetic ages the parent cluster might have moved with respect to the gas.

The by-eye comparison of various maps described here is a qualitative one and as such it carries a certain degree of subjectivity and incompleteness. The human brain is an excellent instrument in deciding whether 2–D structures are similar or not, but it might miss out on such information especially on small scales. Another issue is that it is impossible to assign a well defined degree of agreement between structures, which hinders any comparison. For these reasons one would ideally want to invoke a more objective method which can also provide a "hard number" on the similarities and differences between two maps at different scales. In what follows, we describe a first attempt at such a method using 2–D cross-correlations.

4.2 The Cross-Correlation Method

The cross correlation coefficient $r_{i,j}$ is defined as

$$r_{i,j} = \frac{\sum_i \sum_j [F(x_i, y_j) - \overline{F}][G(x_i, y_j) - \overline{G}]}{\sqrt{\sum_i \sum_j [F(x_i, y_j) - \overline{F}]^2 \sum_i \sum_j [G(x_i, y_j) - \overline{G}]^2}} \tag{4.2}$$

where $F(x_i, y_j)$, $G(x_i, y_j)$ are the pixel intensities at point (x_i, y_j) and $\overline{F}$, $\overline{G}$ are the mean values of the intensity matrices F and G, respectively.

The correlation coefficient value ranges from -1 (perfect anti-correlation) to 1 (perfect correlation). We used the IDL function *correl_images* to compute the cross-correlation of two images. This function allows for the shifting of the two

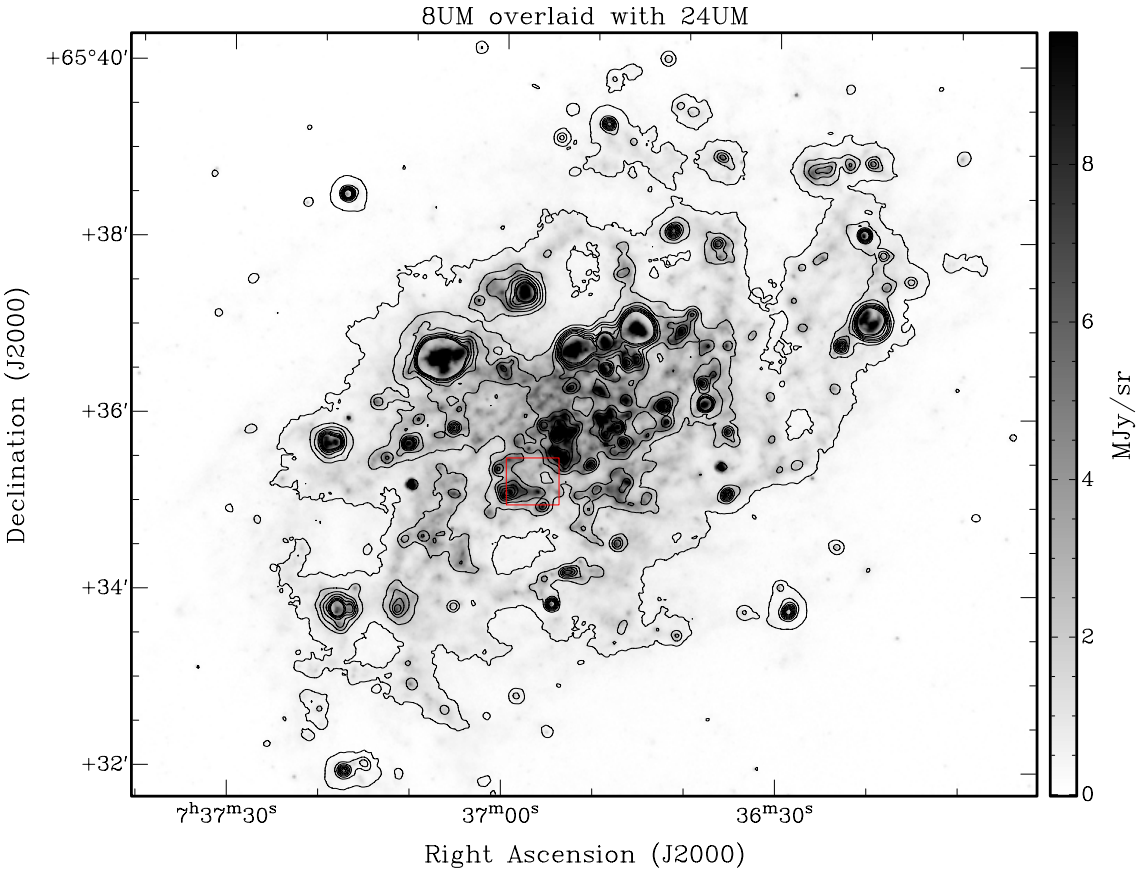

Figure 4.2: The 8μm map with 24μm emission superimposed as contours. Contour levels are from 0.5 to 7.5 MJy sr^{-1} in steps of 1 MJy sr^{-1}. The red box indicates the close-up area in Fig. 4.3.

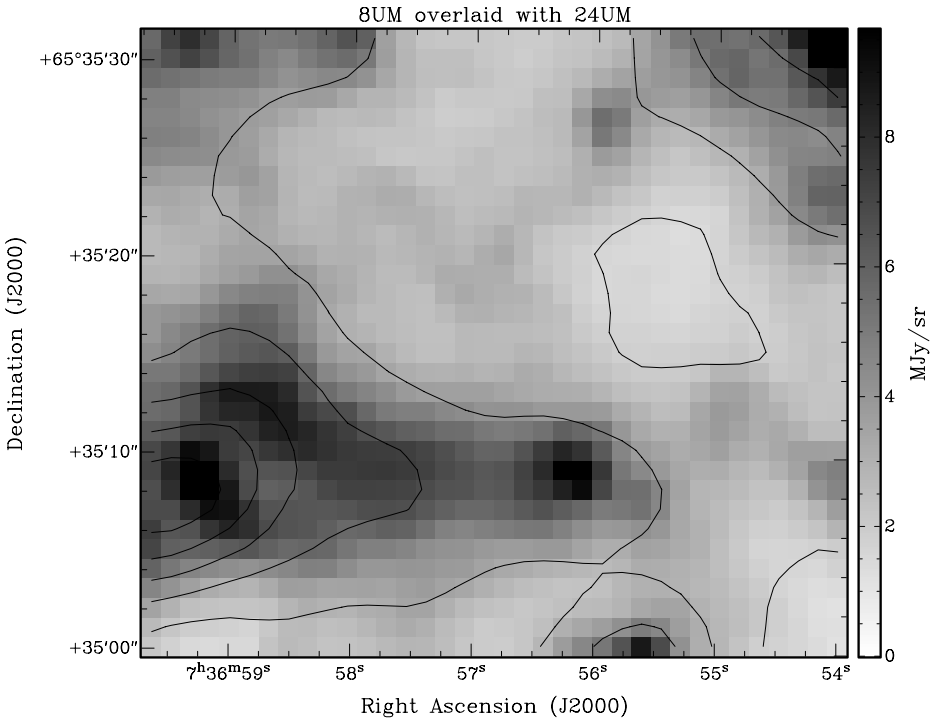

Figure 4.3: A close-up of the 8μm map with 24μm emission superimposed as contours. Contour levels are from 0.5 to 7.5 MJy sr^{-1} in steps of 1 MJy sr^{-1}.

images relative to each other thus computing the correlation coefficient at each new position. The result is a two-dimensional matrix of all the possible correlation coefficients. The IDL procedure *cormat_analyze* was then used to extract certain parameters (namely the peak correlation value from all possible shifting positions and the correlation value at zero shifting) from the correlation matrix.

This method of correlation is dependent on the number of pixels being correlated. Thus it is possible to get a high correlation coefficient if the overlapping area between the two images is very small and the pixels correlate by chance. To avoid this issue we multiply the correlation coefficient with the following weighting factor:

$$(\frac{N(x_i, y_j)}{N_{max}})^{1/4} \tag{4.3}$$

where $N(x_i, y_j)$ is the number of pixels being correlated at position (x_i, y_j) and N_{max} is the maximum number of pixels from the correlation matrix. The slope of 1/4 was preferred over a slope of 1/2 so that in cases of close to maximum overlap the weighting is still near unity, but diminishes more rapidly for progressively smaller overlaps. We will refer to this weighted cross-correlation coefficient as C_{coef}.

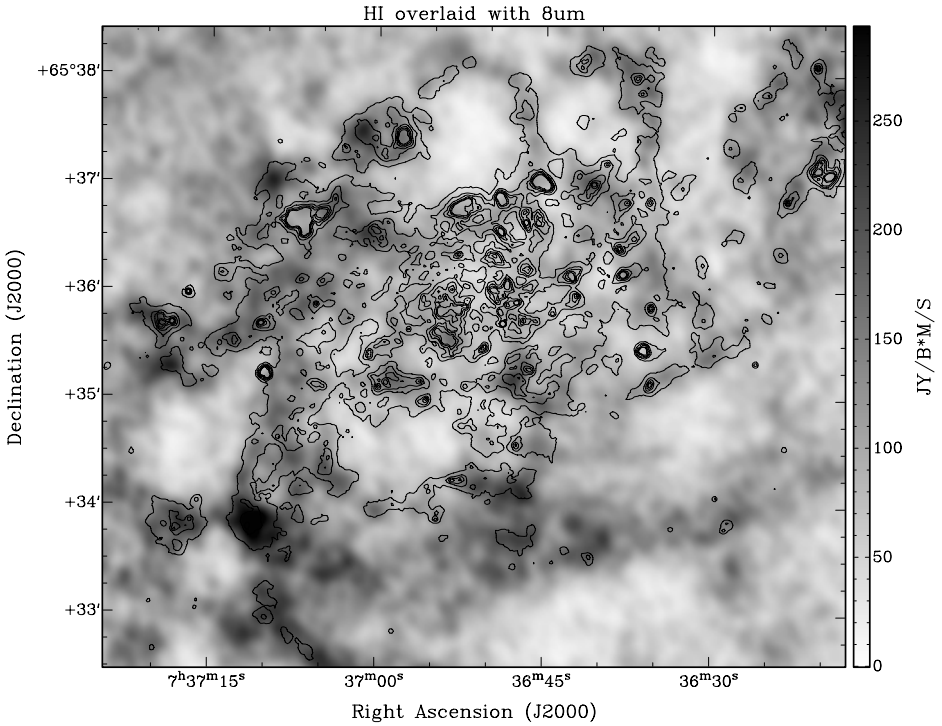

Figure 4.4: The H I map with 8μm emission superimposed as contours. Contour levels are from 1.5 to 12 MJy sr^{-1} in steps of 2 MJy sr^{-1}.

Figure 4.15 shows the cross correlation of an image with itself (auto-correlation). The image (left panel) is $152'' \times 140''$ (2.4×2.2 kpc) and the correlation is done allowing a shift of up to 100 pixels. The resulting correlation matrix can be displayed as a false colour image (right panel). The central pixel corresponds to a shift of zero, i.e. when the two images overlap exactly. In this case we see that the maximum correlation coefficient of 1.0 is at the central pixel which is of course what one would expect. This method of auto-correlation was used to check the method on all maps of different wavelengths and the result was always the same, i.e., C_{coef} was equal to 1 at the central position.

In order to verify that the cross correlation method yields sensible results and to get a feel for what the typical variation in C_{coef} is we compared images of a region in a map wth different regions of the same map so a correlation should not be expected. Figure 4.16 shows a typical example of such an exercise. Panels a and b illustrate the two (unrelated) images of the H I map and panel c presents their correlation matrix. As is expected, the correlation coefficient has low values overall and the peaks are random. This test was performed on various areas on 5 different maps (H I, CO, 8μm, 24μm and FUV) and the average C_{coef} was found

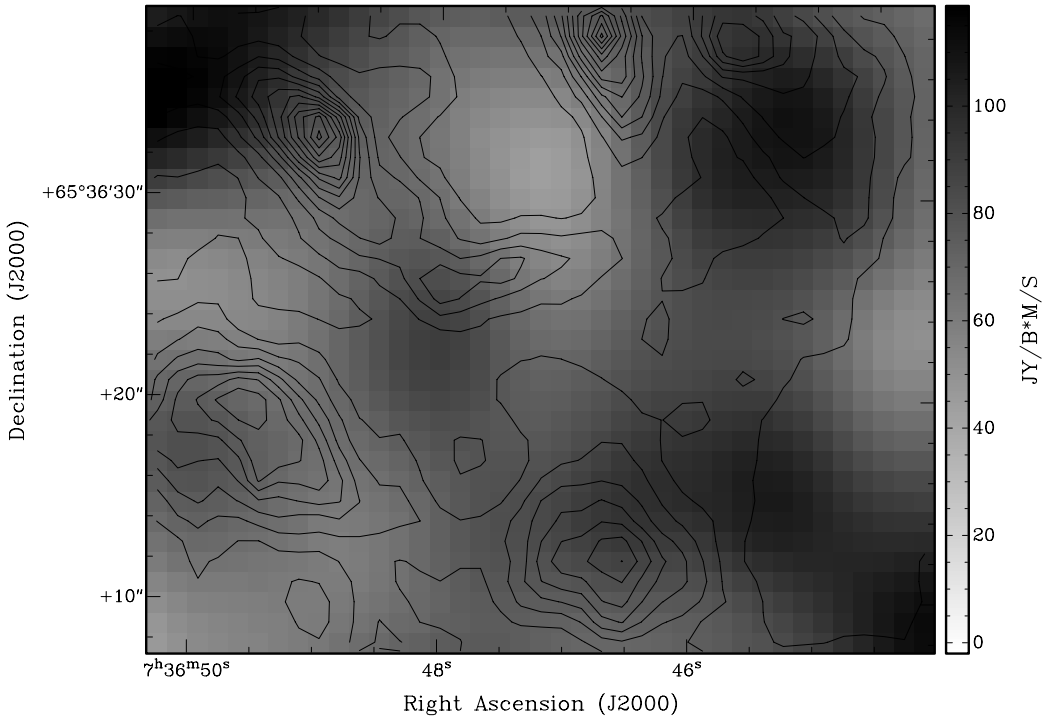

Figure 4.5: A close-up of the H I map with 8μm emission superimposed as contours. Contour levels are from 1.5 to 12 MJy sr^{-1} in steps of 2 MJy sr^{-1}.

to be close to zero in all cases.

The cross-correlation method we use is traditionally employed to align two images, e.g., using stars. We performed a similar test with our data in order to see if we can get the expected results. On the 8μm map two sub-images with dimensions $152'' \times 140''$ were chosen which are offset as illustrated in Fig. 4.17 (left image, rectangular boxes). The bottom left corner of the top sub-image coincides with the centre of the bottom sub-image. Their correlation matrix is shown in Fig. 4.17 (right image) where the maximum correlation ($C_{coef} = 0.96$) is at point (176, 170) which is indeed in agreement with by how much the central box needs to be shifted for it to coincide with the NW box.

Our tests returned sensible results when comparing sub-images of the same map. In a similar fashion we proceeded to compare different maps, such as H I and 8μm. Figure 4.18 illustrates the comparison of the H I map (panel a) with the 8μm map (panel b) on the same region. The size of this region is $152'' \times 140''$ (2.4×2.2 kpc) and the shifting is performed over 100 pixels. Panel c presents the correlation matrix where it is evident that the peak correlation is at the centre, i.e., at a shift of zero. To take this exercise one step further we compared one sub-

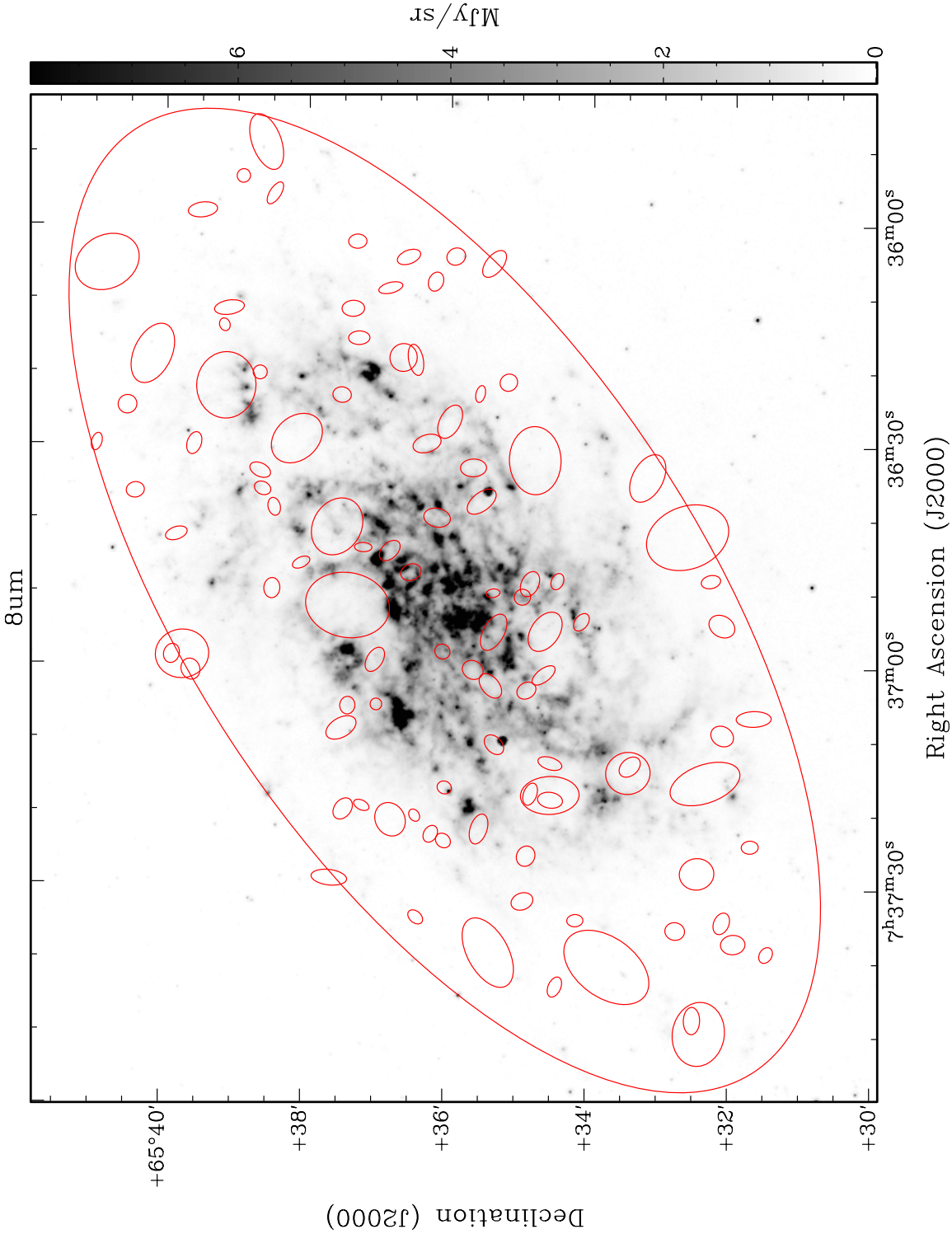

Figure 4.6: The H I holes within R_{25} superimposed on the 8μm map.

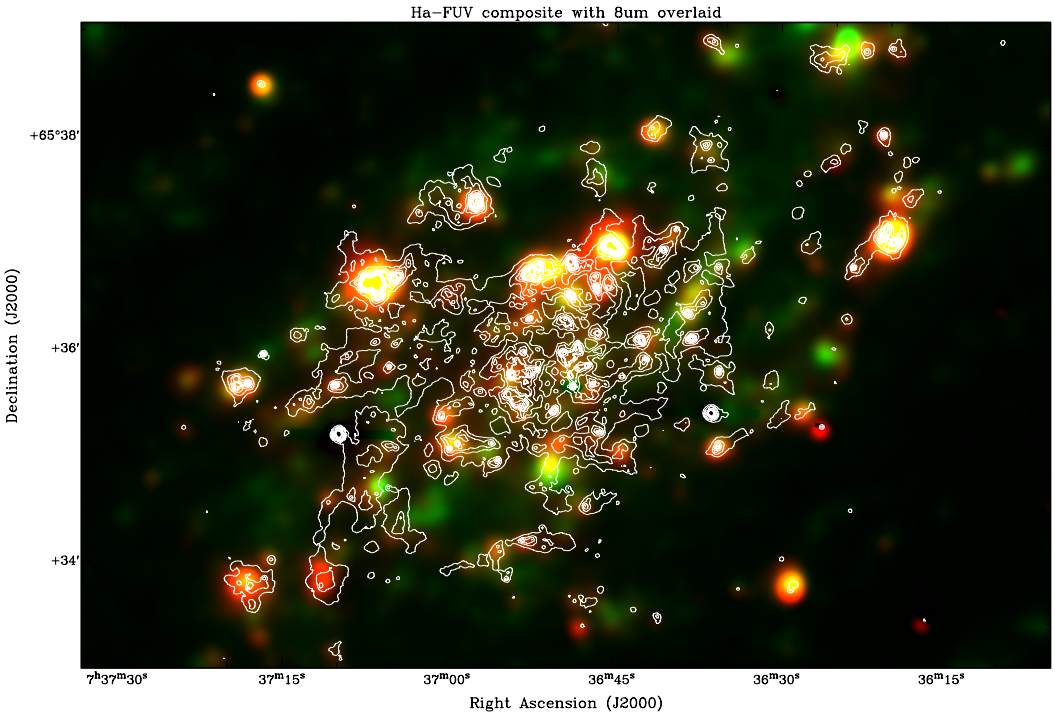

Figure 4.7: A composite Hα (red) - FUV (green) map with 8μm emission superimposed as contours. Contour levels are from 2 to 20 MJy sr^{-1} in steps of 2 MJy sr^{-1}.

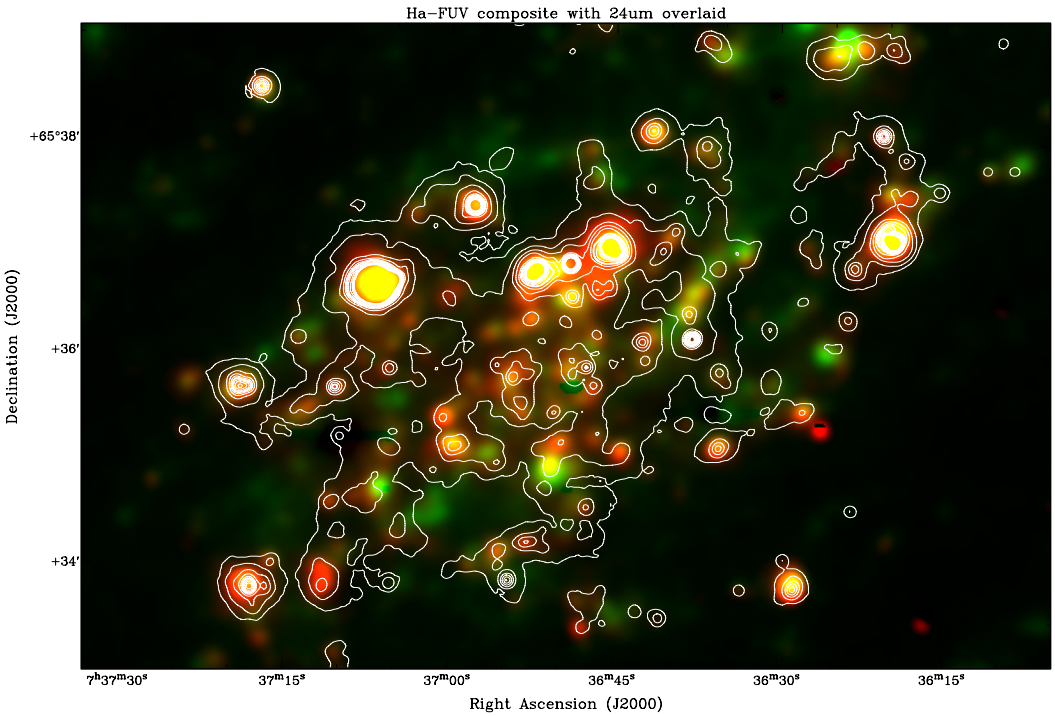

Figure 4.8: A composite Hα (red) - FUV (green) map with 24μm emission superimposed as contours. Contour levels are from 1 to 21 MJy sr^{-1} in steps of 2 MJy sr^{-1}.

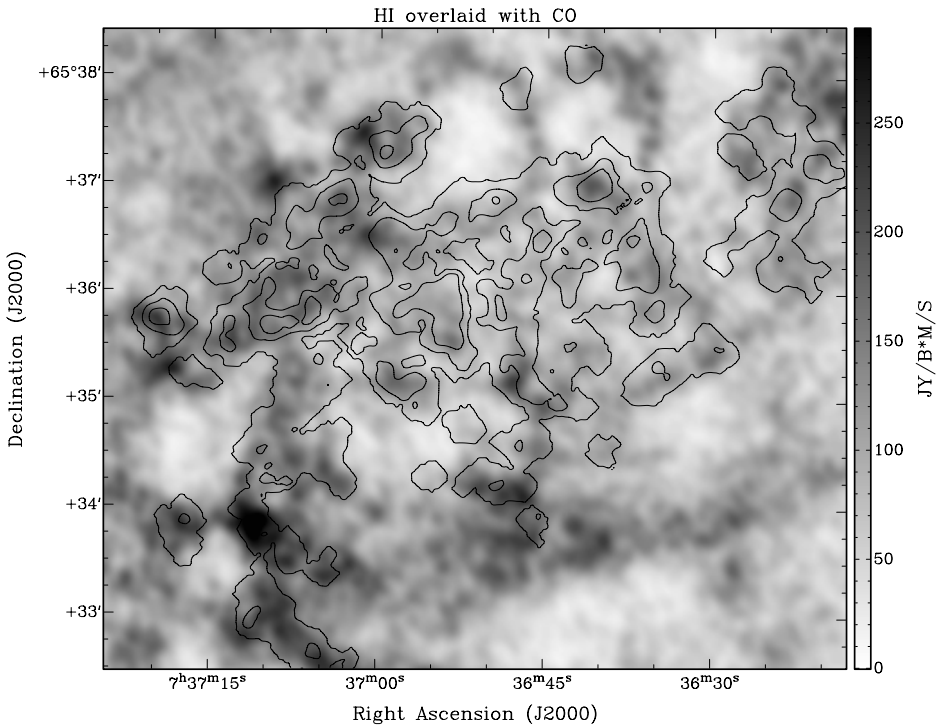

Figure 4.9: The H I map with CO emission superimposed as contours. Contour levels are from 0.5 to 6 K km s^{-1} in steps of 2 K km s^{-1}.

image (the parent image) of the 8μm map with 100 sub-images of the H I map, one of which was at the same position as the parent image. The result of this exercise was that the highest C_{coef} indeed corresponded to the sub-images that were at the same physical location.

All of the aforementioned exercises and tests showed that this method of cross-correlating images returns the expected results. In addition, we found that the agreement depends on the area as well as the scale of the images. This behaviour is evident only when comparing images of different wavelengths and so we decided to investigate this further. We randomly selected five areas of the galaxy and created sets of sub-images out of each map totalling 25 sets. Each set consisted of 32 images of various sizes from $5'' \times 5''$ (80×80 pc) to $\sim 1000'' \times 1000''$ (15×15 kpc). We then proceeded to do all possible cross-correlations, but shifting over 2 pixels only resulting in a 5×5 correlation matrix, in order to find C_{coef} when the images are perfectly aligned. We only shift over 2 pixels as we know that the images are already aligned perfectly (i.e., we do not wish to try to improve on this alignment). All we need from the 2–D correlation matrix is C_{coef} at the central pixel, which then tells us the degree of correlation between two different wavelength bands,

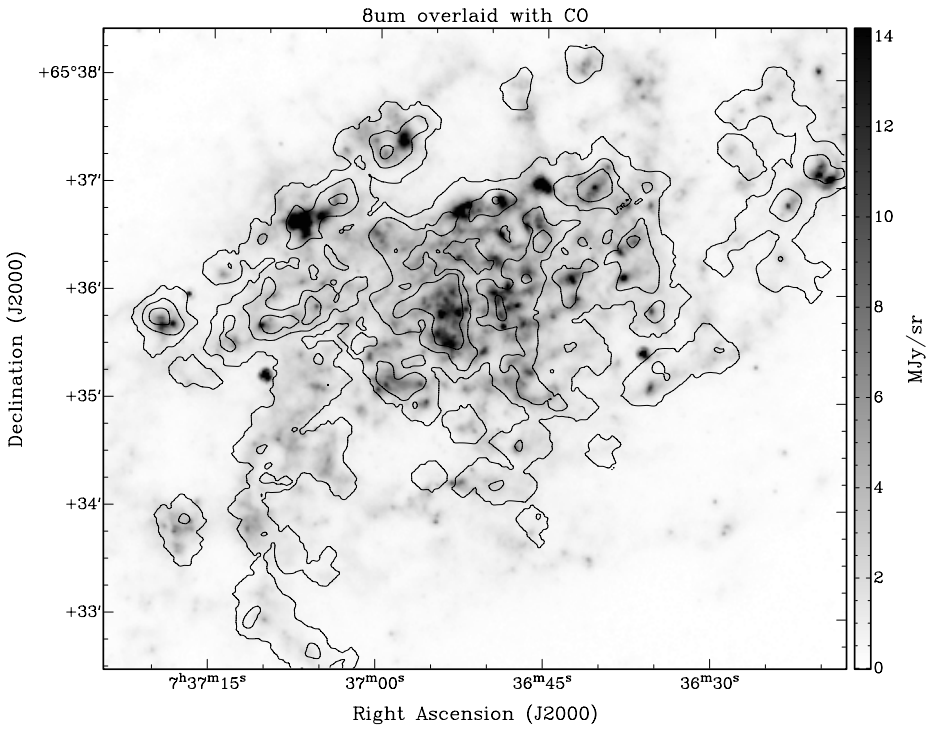

Figure 4.10: The 8μm map with CO emission superimposed as contours. Contour levels are from 0.5 to 6 K km s^{-1} in steps of 2 K km s^{-1}.

such as 8μm and 24μm. An example of our result is shown in Fig. 4.19 where we present the correlation coefficient as a function of image size from the correlation of the 8μm and 24μm maps over the 5 areas. It is evident that C_{coef} varies substantially when the image size is smaller than $\sim 200'' \times 200''$ (3.1×3.1 kpc), is fairly constant above this threshold value and almost the same across the 5 areas. This behaviour of C_{coef} is also apparent on the correlations on all wavelength bands albeit the threshold value ranges from $\sim 50''$ to $\sim 300''$ (0.8 to 4.7 kpc) depending on which wavelength bands are compared (see Fig. A.1–A.10 in Appendix A for the complete set of correlations). Overall, it appears that the value of C_{coef} varies significantly when the size of the images is small but it is not clear whether this is an artefact of the method or a real effect. One would expect that in small sized images (of order a few pixels) C_{coef} can have a large value because by chance, spatial intensity variations follow a similar pattern. On the other end, the value of C_{coef} when comparing large images (of order the size of the galaxy) will reflect the large-scale structure of the galaxy, a piece of information that is already known.

One way to distinguish between the artefact and real effects is to study the correlation of small scale images in detail and to locate the threshold above which

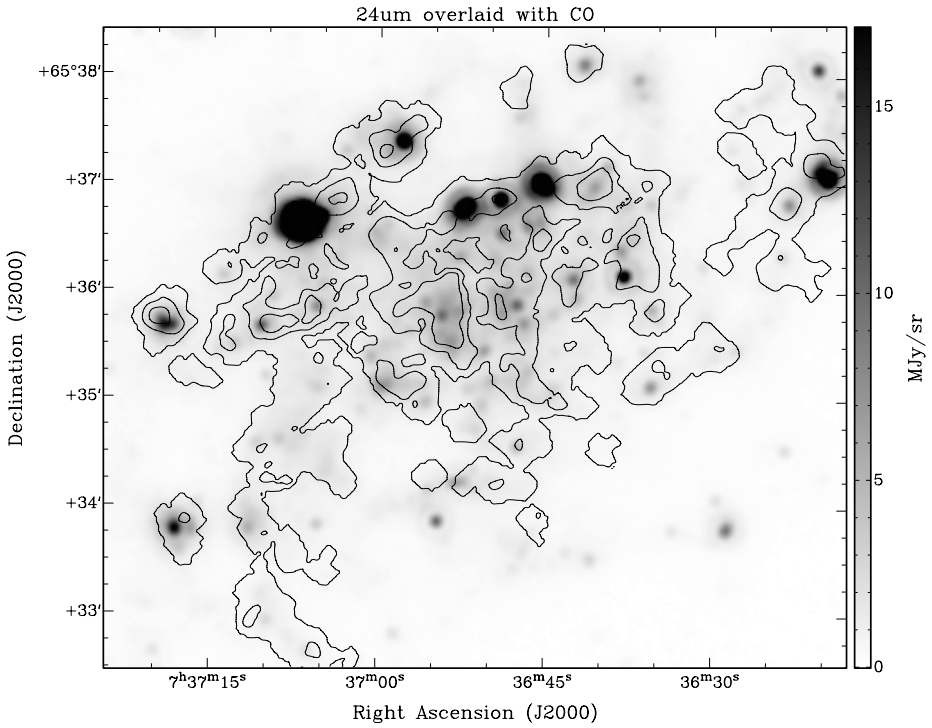

Figure 4.11: The 24μm map with CO emission superimposed as contours. Contour levels are from 0.5 to 6 K km s^{-1} in steps of 2 K km s^{-1}.

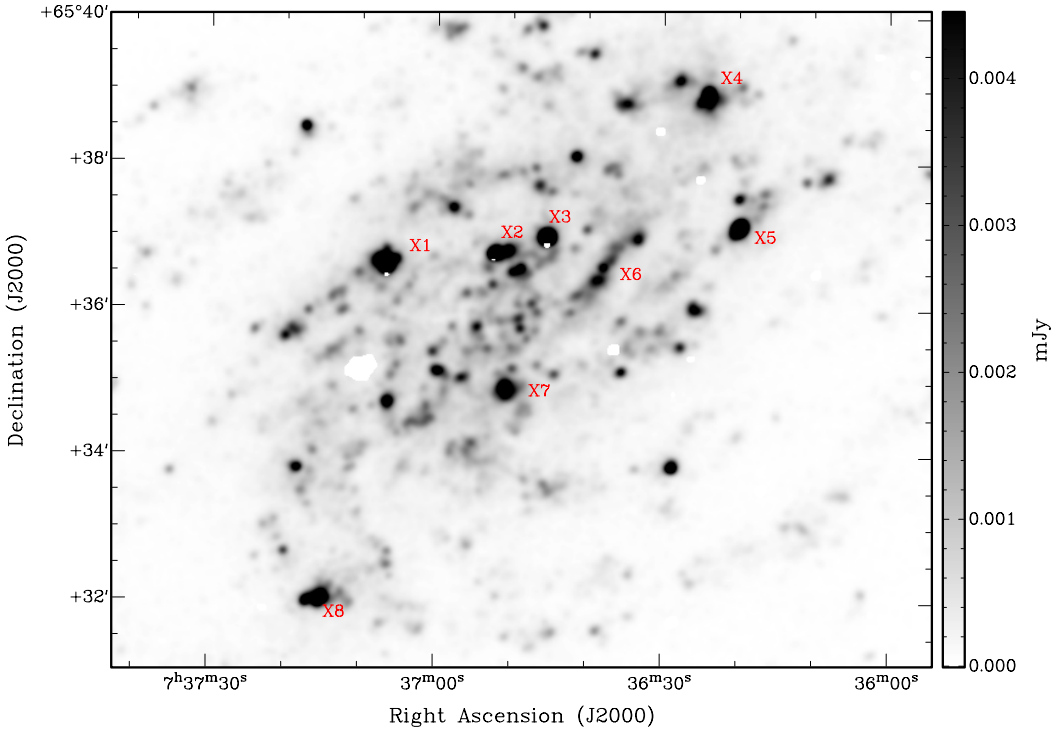

Figure 4.12: The FUV map with regions X1–X8 indicated.

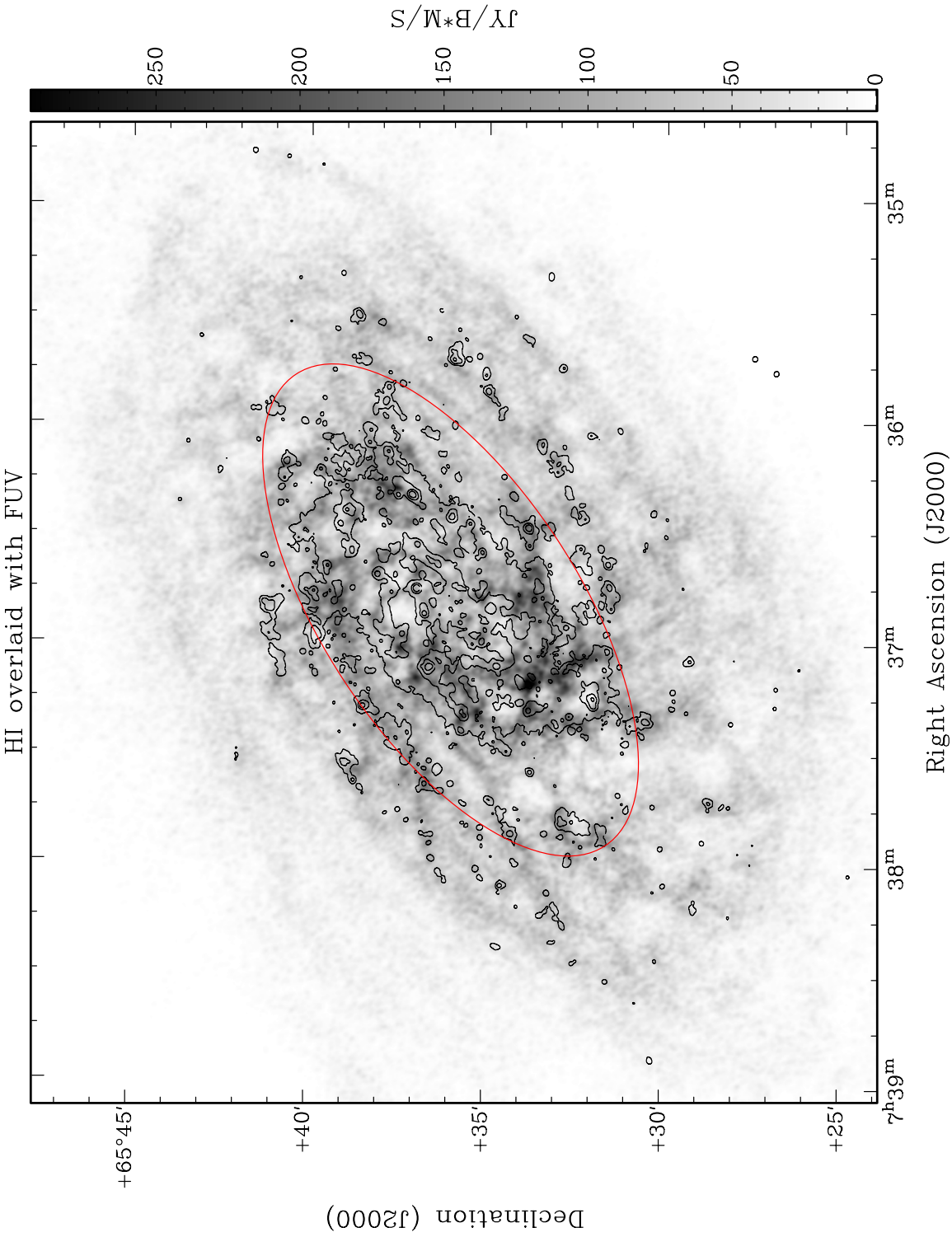

Figure 4.13: The H I map with FUV emission superimposed as contours. The red ellipse corresponds to R_{25} and contour levels are from 2×10^{-4} to 2×10^{2} mJy in levels incremented by a factor of 4.

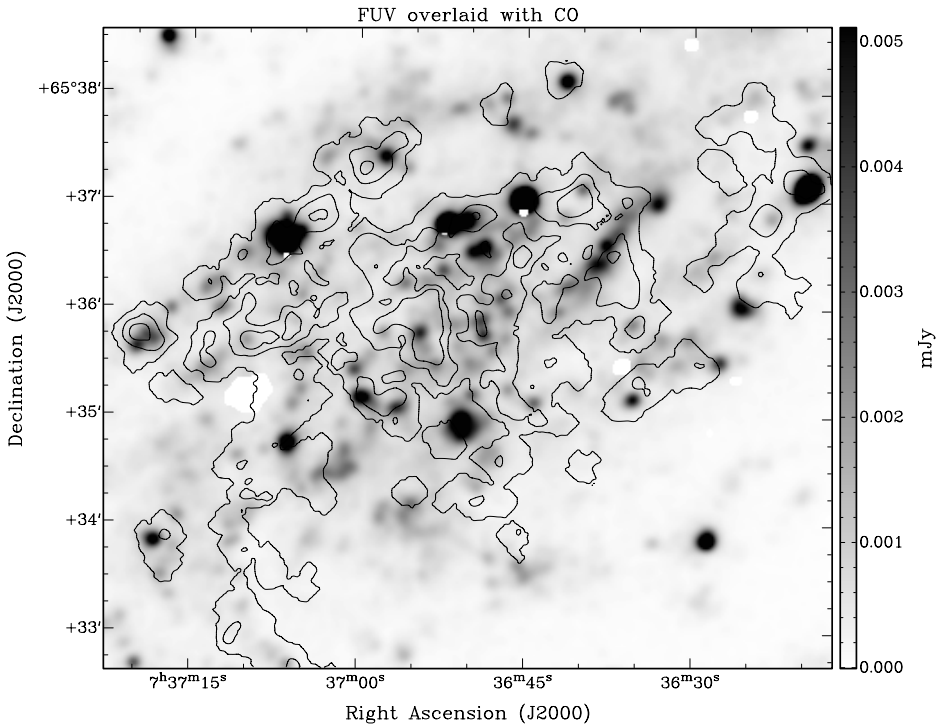

Figure 4.14: The FUV map with CO emission superimposed as contours. Contour levels are from 0.5 to 6 K km s^{-1} in steps of 2 K km s^{-1}.

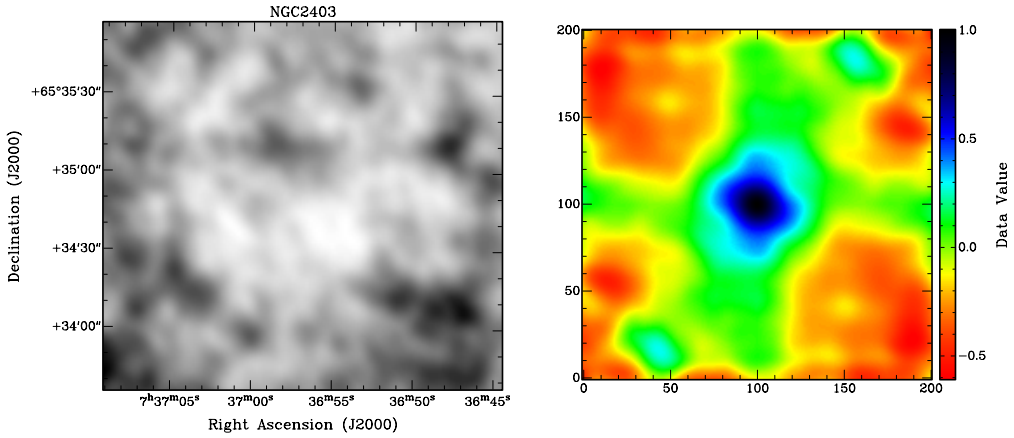

Figure 4.15: A random H I sub-image (left) and the auto-correlation matrix of this image (right).

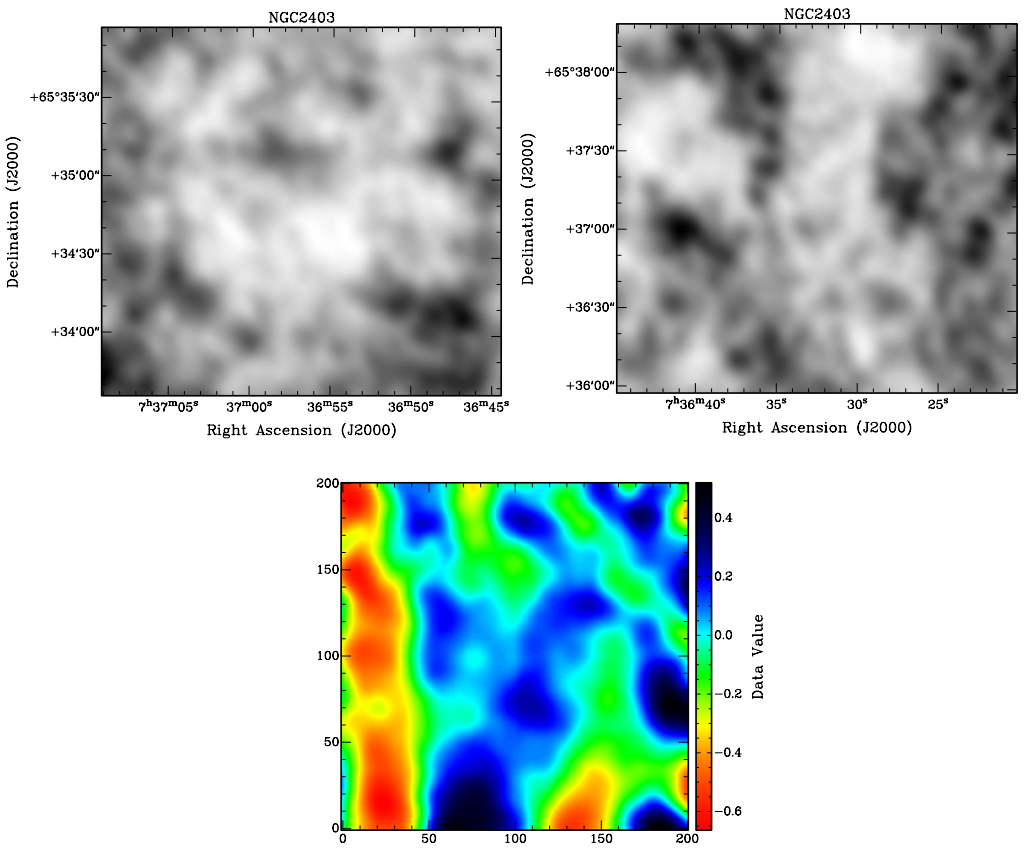

Figure 4.16: Two random and unrelated H I sub-images (top) and their correlation matrix (bottom).

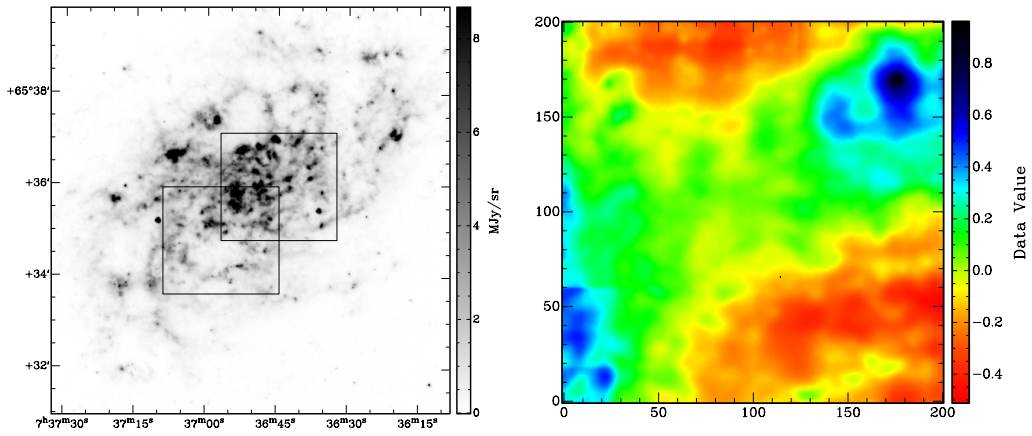

Figure 4.17: Two partially overlapping sub-images on the 8μm map (left, rectangular boxes) and their correlation matrix (right).

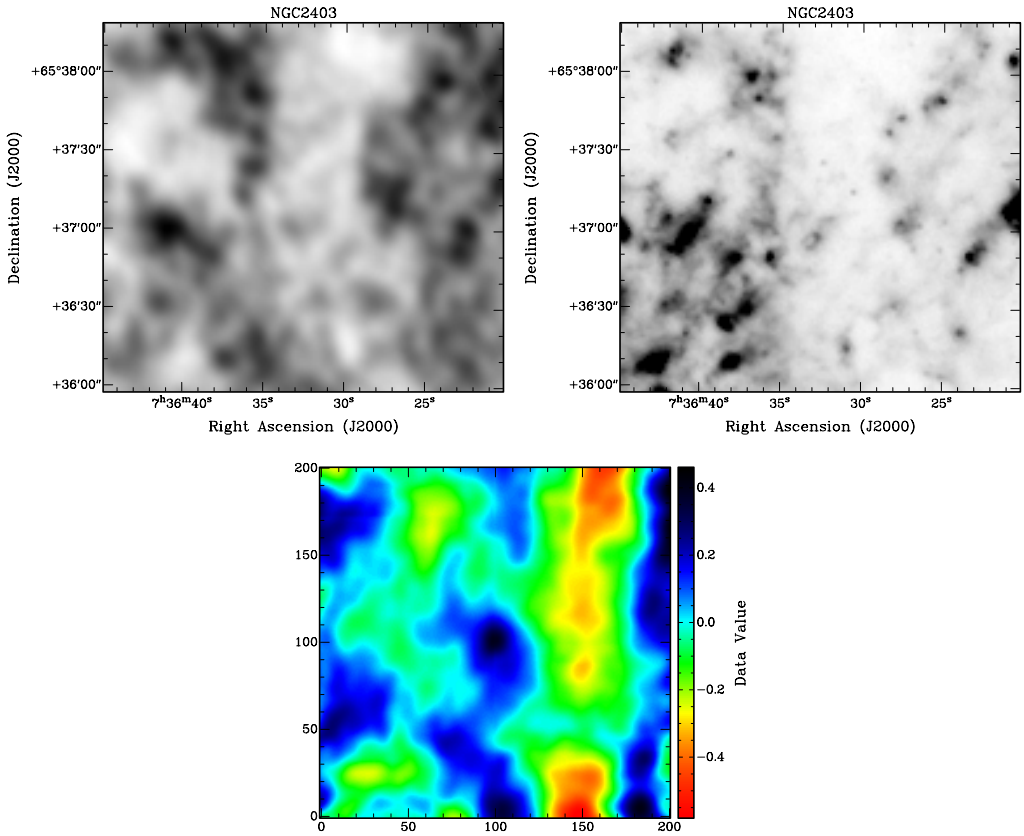

Figure 4.18: A random sub-image in H I (top left) and the same area at 8μm (top right) and their correlation matrix (bottom).

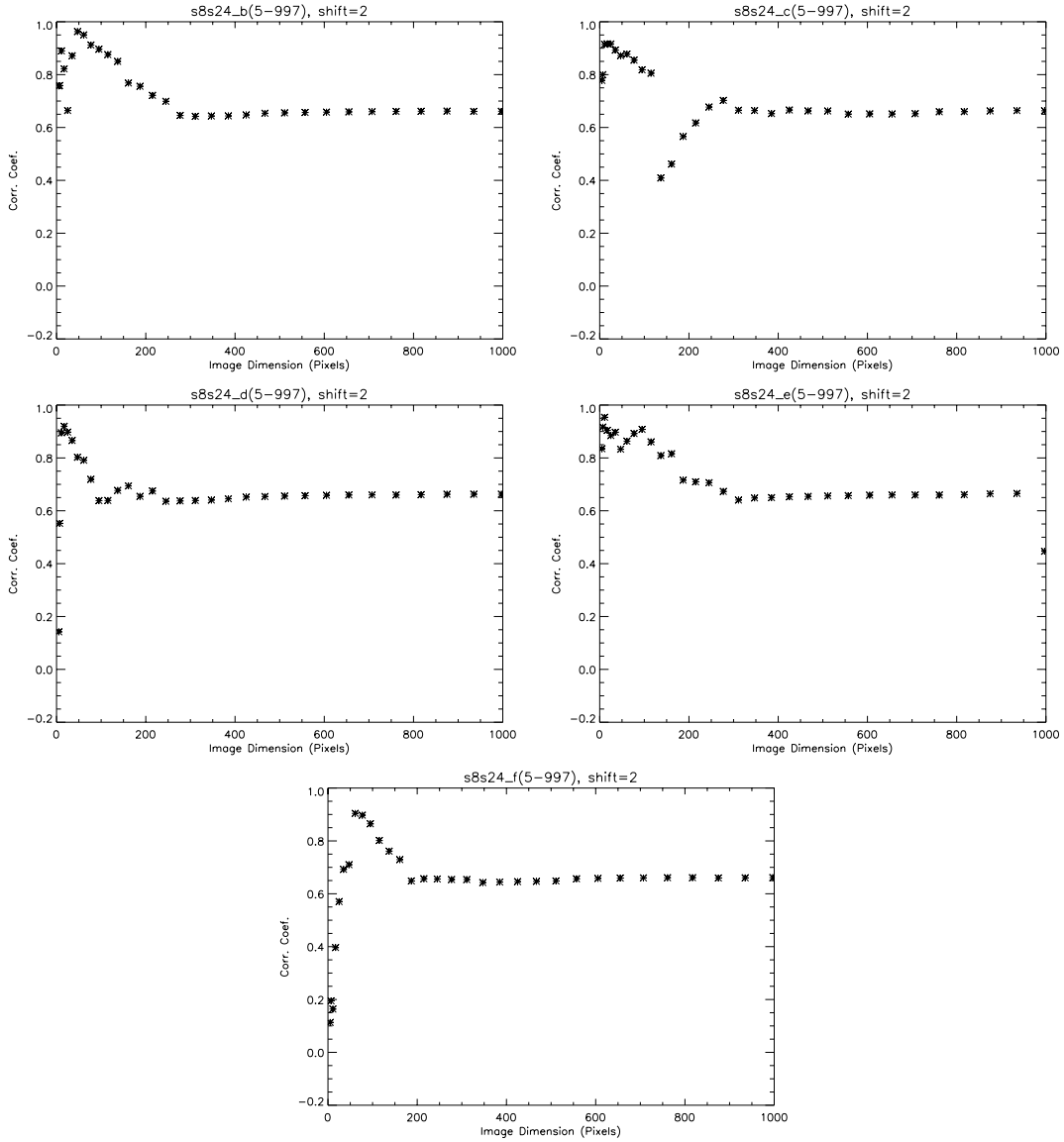

Figure 4.19: The correlation coefficient of the 8μm with 24μm maps over 5 different areas. The x–axis represents the size of the individual images.

C_{coef} reflects the true agreement between two images. To achieve this we focused on images with dimensions of less than 200″ (3.1 kpc). We divided almost the entire galaxy into 100 areas as shown in Fig. 4.20. For each of these areas we created 15 variable-sized sub-images; the smallest being $5'' \times 5''$ (80×80 pc) and the largest being $215'' \times 215''$ (3.4×3.4 kpc). The whole process was repeated for all 5 maps and 7500 images were created in total. We cross correlated the 8μm areas with the respective (and equally sized) 24μm areas (without shift). In order to eliminate the effect that individual areas have on the correlation we averaged C_{coef} over the 100 areas. The same was done for all possible correlations between the different wavelength maps. In Fig. 4.21 we plot the mean C_{coef} as a function of image dimensions. In most cases C_{coef} starts with a low value and reaches a plateau at a certain image dimension. However, the point where each curve turns flat differs; e.g. for the H I–8μm case this happens at $\sim 35''$ (550 pc) and for the H I–FUV at $\sim 95''$ (1.5 kpc). In the case of the 8μm–24μm correlation the value increases steeply up to about 50″ (780 pc) but also continues to rise slightly up to 200″ (3.1 kpc). It appears that both the statistical fluctuations and the real variations in correlation are evident in the behaviour of C_{coef}.

In order to get a feel for the noise in C_{coef} we repeated this experiment with unrelated areas. For all possible combinations we correlated the 100 areas in a mixed fashion, e.g., area 100 of the H I map with area 150 of the 8μm map. The resulting mean C_{coef} is presented as dashed lines in Fig. 4.21. It's evident that the C_{coef} noise is almost constant regardless of image size or wavelength pair and close to 0 (see also Fig. 4.22 for a detailed graph). Moreover the values have a low dispersion for image sizes above $\sim 10''$ reflecting the robustness of the C_{coef} values. From all the above graphs it appears that C_{coef} does not exhibit a specific pattern and only for really small areas drops down to the noise level.

The above results are based on the mean C_{coef} over 100 areas which were defined based on the H I map. However, in a number of areas there is no emission from other tracers resulting in lower values of C_{coef}. In order to see how the correlation is affected by this we focused on areas close to the centre of the galaxy where emission from all tracers is evident. We selected a total of 19 areas (122–124, 132–135, 142–146, 153–156, 164–166) and repeated the calculation of the mean C_{coef}. The results are presented in Fig. 4.23. The main difference compared to the correlations over the 100 areas is that C_{coef} has increased significantly in almost all pairs. Another notable difference is that in some cases (e.g., the H I with all the dust tracers) C_{coef} peaks early and then declines.

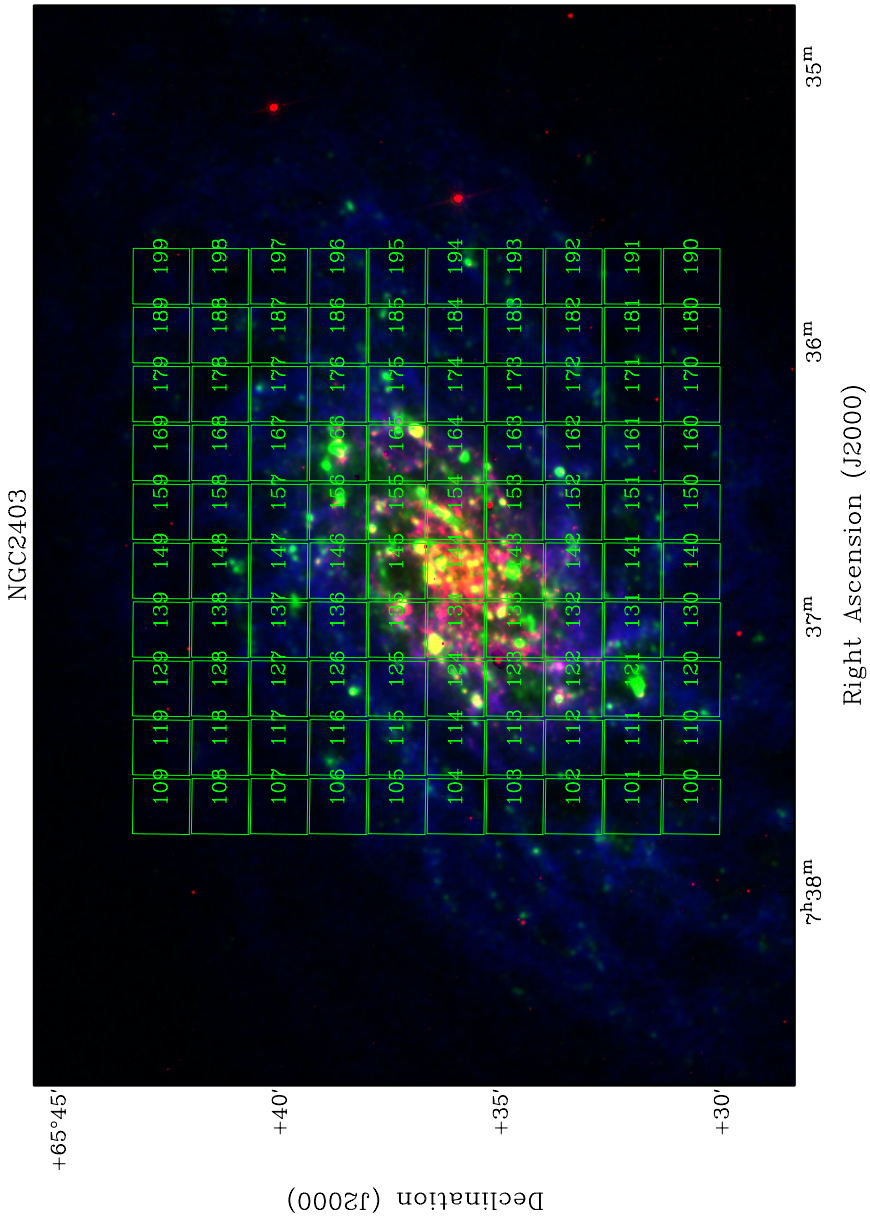

Figure 4.20: The division of NGC 2403 in 100 areas illustrated by the boxes.

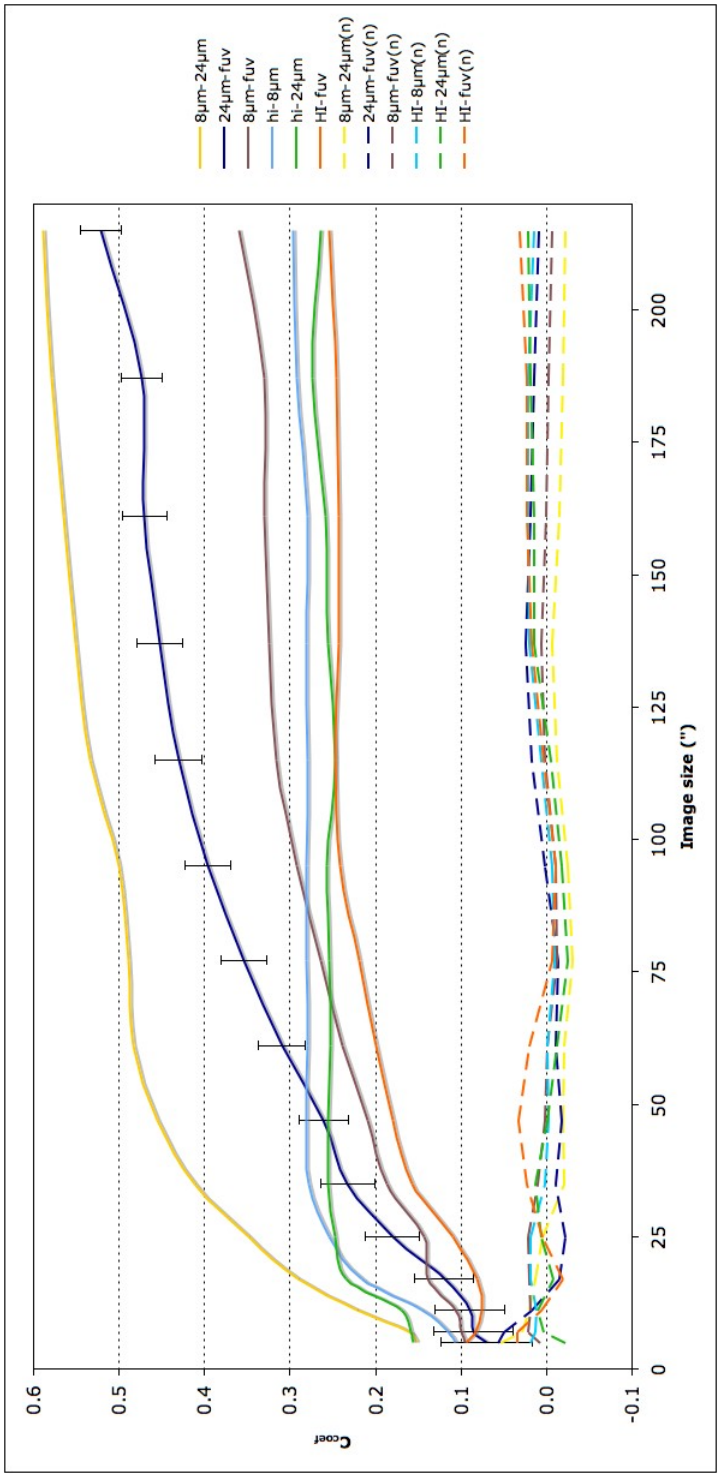

Figure 4.21: The mean C_{coef} over 100 areas as a function of image dimension for all cases. The dashed lines correspond to the C_{coef} noise (see text for a description). The error bars on the 24μm–FUV case represent the typical uncertainty.

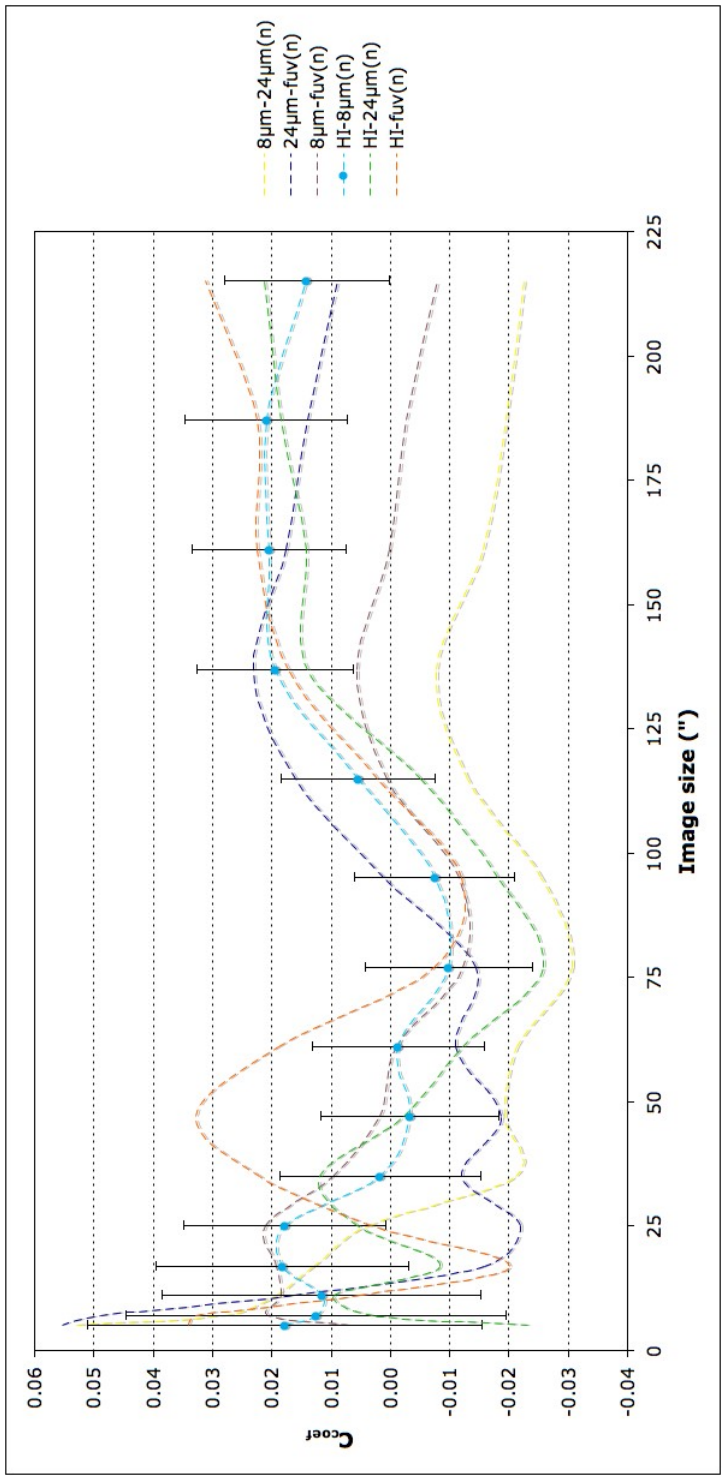

Figure 4.22: The mean C_{coef} over 100 random areas as a function of image dimension for all cases. This is a blow-up of Fig. 4.21 with typical uncertainties shown on the H I–8μm case.

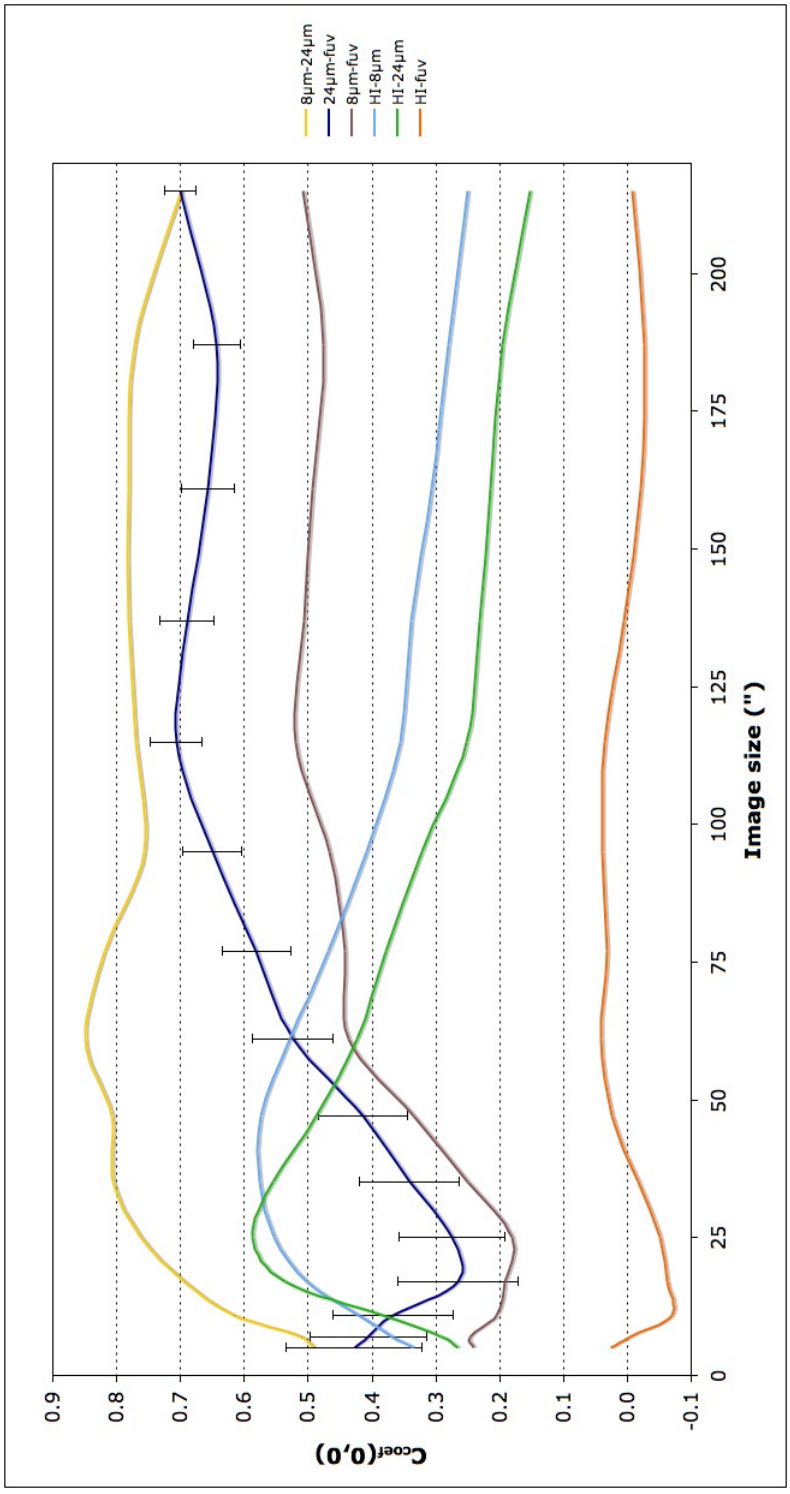

Figure 4.23: The mean C_{coef} over the central areas as a function of image dimension for all cases. The error bars on the 24μm–FUV case represent the typical uncertainty.

So far we have compared maps at their native resolution which varies from one map to another. This could potentially lead to an underestimation of the correlation coefficient especially in cases where the difference in resolution between a pair is considerable. To eliminate any such effect we degraded our images to a common angular resolution. The resolution of the CO map is $\sim 13''$, the lowest between our images. However, reducing the resolution of all the other images to that of the CO, would mean that we would lose substantial information. Therefore, we decided to convolve all our images to the next lower resolution ($8''$) of the H I map. Consequently, and due to its low sensitivity, we excluded the CO map from any further analysis.

As we saw earlier, the correlation is also affected by the presence (or lack) of emission in a specific area of the galaxy. The H I and FUV maps have a more extended emission than for example the *Spitzer* images, thus making any comparison between these two groups meaningless on the outskirts. Consequently, for the following analysis we will focus on areas within R_{25}. We define three image sizes of $15'' \times 15''$ (235×235 pc), $30'' \times 30''$ (470×470 pc) and $60'' \times 60''$ (940×940 pc) as illustrated in Fig. 4.24. The reasoning behind the selection of these patches is to be able to see how different maps correlate at different scales. We selected the smallest sub-images ($15'' \times 15''$) to be twice the size of our beam.

We then proceeded to correlate every map with every other map at the three different scales ($15''$, $30''$ and $60''$) and a sample of the results is given in Tables 4.1 to 4.2. It is evident that C_{coef} has some dispersion over the various areas reflecting structural differences. The average C_{coef} over all sub-images that lie within R_{25} and within $0.5\,R_{25}$ are presented in Table 4.3 and a sample of the correlations within R_{25} is illustrated in Fig. 4.25.

4.3 Discussion

4.3.1 Correlations

As we probe larger scales the probability of structures matching increases as explained above. Table 4.3 also shows that the correlation improves when we average over areas within $0.5\,R_{25}$. This is of course expected in light of our previous discussion; in most maps the emission is either weak or absent outside this radius resulting in a lack of matched structures and therefore a lower value for C_{coef}. For the discussion that follows we will focus on the correlations within $0.5\,R_{25}$ and on

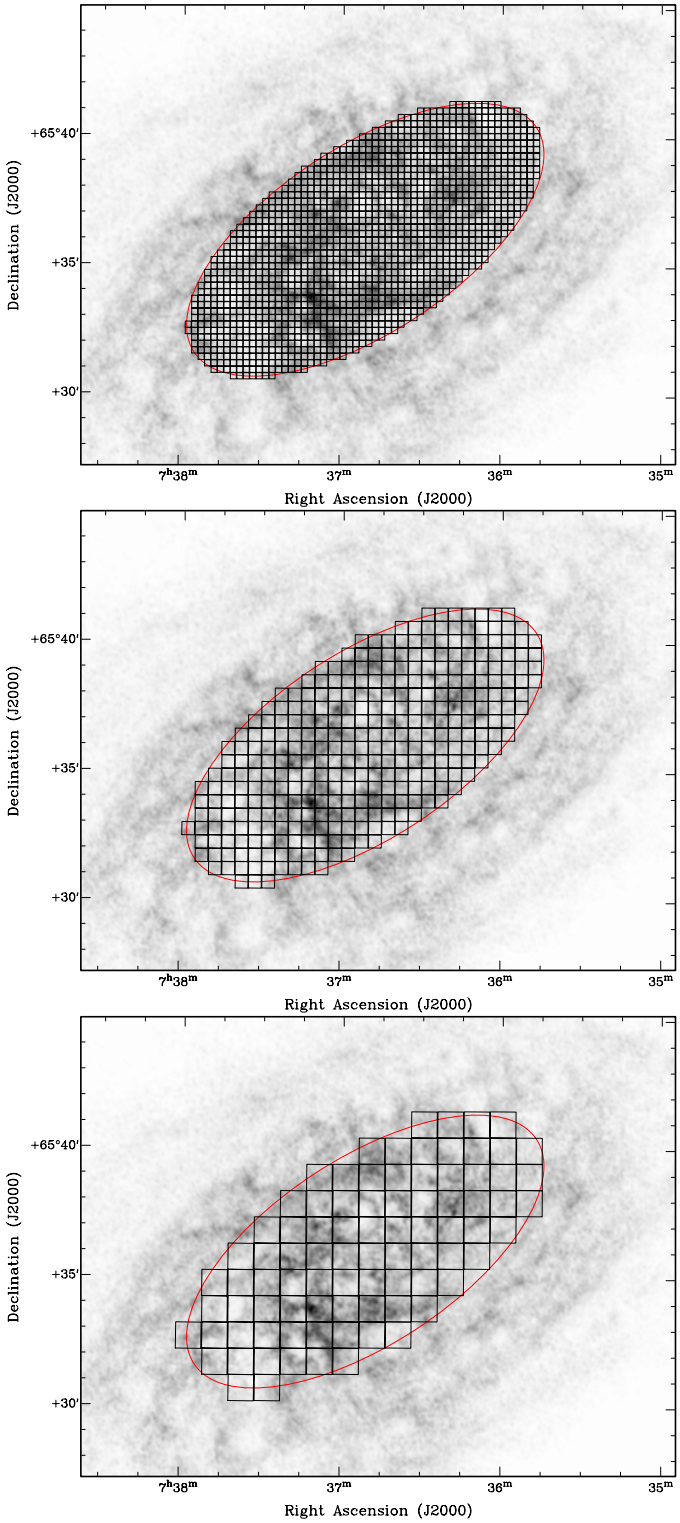

Figure 4.24: The division of the galaxy in sub-images of $15'' \times 15''$ (235×235 pc, top panel), $30'' \times 30''$ (470×470 pc, middle panel) and $60'' \times 60''$ (940×940 pc, bottom panel) overlaid on the H I integrated map. The red ellipse corresponds to R_{25}.

Table 4.1. The C_{coef} values for a sample of $15'' \times 15''$ areas for all possible combinations of images. Table 4.1 continues on to Table 4.2. The full set of tables will be made available in electronic form upon request.

Area	RA	Dec	H I–8μm	H I–24μm	H I–70μm	H I–Hα	H I– FUV	H I– SFR	8μm–24μm	8μm–70μm	8μm–Hα	8μm–FUV	8μm–SFR
0	114.4875	65.5407	0.33	-0.31	-0.52	0.31	0.80	-0.09	0.43	-0.27	0.62	0.50	0.54
1	114.4876	65.5448	-0.05	-0.22	-0.83	0.90	0.79	0.08	0.88	0.04	0.15	0.13	0.91
2	114.4770	65.5282	0.87	0.59	0.53	0.01	0.81	0.71	0.88	0.78	0.24	0.89	0.93
3	114.4771	65.5324	0.74	0.34	0.24	-0.17	0.21	0.33	0.77	0.67	0.29	0.69	0.79
4	114.4773	65.5366	0.83	0.86	-0.43	-0.21	0.24	0.85	0.90	-0.28	-0.26	0.17	0.86
5	114.4774	65.5407	0.18	0.60	-0.08	0.03	-0.06	0.52	0.36	0.28	0.35	0.52	0.54
6	114.4776	65.5449	-0.43	-0.34	-0.56	-0.16	-0.18	-0.35	0.93	0.52	0.37	0.16	0.92
7	114.4777	65.5491	-0.14	-0.54	-0.17	0.51	0.30	-0.52	0.66	-0.15	-0.23	0.17	0.76
8	114.4779	65.5532	-0.21	0.62	0.31	-0.47	0.67	0.69	0.17	0.45	0.47	-0.12	0.18
9	114.4780	65.5574	0.32	0.73	0.65	-0.50	0.11	0.81	-0.27	0.20	0.32	0.66	-0.04
10	114.4782	65.5615	0.74	0.43	-0.06	0.32	-0.54	0.25	0.69	0.11	0.42	-0.50	0.53
11	114.4668	65.5241	0.49	0.51	0.60	0.05	0.86	0.67	0.84	0.09	-0.10	0.30	0.79
12	114.4669	65.5283	0.38	0.53	0.67	0.63	0.50	0.53	0.96	0.69	0.84	0.71	0.92
13	114.4671	65.5324	0.29	0.26	0.01	0.20	0.16	0.25	0.97	0.77	0.88	0.68	0.97
14	114.4672	65.5366	0.75	0.23	0.44	-0.64	-0.50	-0.28	0.68	0.33	-0.32	-0.14	0.19
15	114.4674	65.5408	0.77	0.78	0.03	-0.24	-0.69	0.02	0.90	0.14	-0.20	-0.59	0.26
16	114.4675	65.5449	0.55	0.26	0.05	-0.15	-0.03	0.24	0.82	0.80	0.60	0.48	0.88
17	114.4677	65.5491	0.83	0.62	0.84	0.61	-0.02	0.63	0.86	0.87	0.84	0.17	0.92
18	114.4678	65.5533	0.46	0.40	0.24	0.47	0.29	0.40	0.99	0.28	0.98	0.91	0.99
19	114.4680	65.5574	0.73	0.62	0.59	0.64	0.61	0.66	0.97	0.85	0.97	0.97	0.99
20	114.4681	65.5616	-0.24	0.17	0.24	-0.49	-0.47	0.05	-0.26	-0.59	-0.15	-0.05	-0.19
21	114.4683	65.5658	0.85	0.59	0.53	0.50	0.37	0.62	0.82	0.60	0.79	0.63	0.86
22	114.4684	65.5699	0.44	0.31	0.14	0.36	0.30	0.31	0.97	0.84	0.98	0.94	0.97
23	114.4566	65.5200	-0.12	-0.50	-0.35	0.64	0.25	-0.48	0.49	0.74	-0.37	-0.18	0.49
24	114.4567	65.5242	0.11	-0.19	-0.28	-0.29	0.67	-0.13	0.91	0.49	0.31	0.36	0.94
25	114.4568	65.5283	-0.12	-0.12	0.12	0.14	-0.37	-0.33	0.86	0.22	0.30	0.29	0.92
26	114.4570	65.5325	0.69	0.31	0.35	-0.50	0.04	0.21	0.70	0.61	-0.29	0.47	0.67

Table 4.2. The C_{coef} values for a sample of $15'' \times 15''$ areas for all possible combinations of images. The full set of tables will be made available in electronic form upon request.

Area	RA	Dec	24μm–70μm	24μm–Hα	24μm–FUV	24μm–SFR	70μm–Hα	70μm–FUV	70μm–SFR	Hα–FUV	Hα–SFR	FUV–SFR
0	114.4875	65.5407	-0.18	0.07	0.06	0.96	-0.49	-0.53	-0.29	0.35	0.14	0.31
1	114.4876	65.5448	0.18	-0.06	-0.09	0.91	-0.91	-0.90	-0.18	0.96	0.32	0.32
2	114.4770	65.5282	0.90	0.43	0.83	0.98	0.57	0.90	0.93	0.38	0.43	0.92
3	114.4771	65.5324	0.84	0.70	0.90	0.98	0.42	0.92	0.90	0.67	0.69	0.95
4	114.4773	65.5366	-0.24	-0.20	0.26	0.96	-0.34	-0.65	-0.43	0.80	0.04	0.52
5	114.4774	65.5407	0.40	0.40	0.35	0.93	0.21	0.32	0.43	0.93	0.65	0.65
6	114.4776	65.5449	0.59	0.49	0.27	1.00	0.67	0.17	0.59	0.45	0.52	0.32
7	114.4777	65.5491	0.15	-0.72	-0.30	0.97	-0.56	-0.61	-0.01	0.78	-0.59	-0.10
8	114.4779	65.5532	0.47	-0.23	0.23	0.98	-0.03	0.50	0.55	-0.37	-0.26	0.37
9	114.4780	65.5574	0.45	-0.69	-0.16	0.95	-0.28	0.21	0.53	0.35	-0.60	0.11
10	114.4782	65.5615	0.09	0.54	-0.25	0.95	0.65	0.67	0.17	0.44	0.65	-0.01
11	114.4668	65.5241	0.23	-0.23	0.53	0.97	-0.46	0.61	0.41	-0.20	-0.28	0.70
12	114.4669	65.5283	0.70	0.84	0.81	0.98	0.66	0.56	0.71	0.55	0.76	0.91
13	114.4671	65.5324	0.73	0.87	0.71	0.99	0.56	0.35	0.72	0.79	0.88	0.80
14	114.4672	65.5366	-0.12	-0.13	0.32	0.65	0.02	-0.25	-0.22	0.65	0.48	0.92
15	114.4674	65.5408	0.26	-0.05	-0.50	0.45	0.78	0.38	0.69	0.64	0.64	0.54
16	114.4675	65.5449	0.71	0.58	0.28	0.94	0.83	0.75	0.88	0.71	0.77	0.57
17	114.4677	65.5491	0.88	0.71	-0.02	0.95	0.61	-0.20	0.82	0.38	0.82	0.26
18	114.4678	65.5533	0.21	0.96	0.89	0.99	0.36	0.52	0.27	0.93	0.97	0.92
19	114.4680	65.5574	0.75	0.97	0.96	0.99	0.76	0.87	0.83	0.94	0.97	0.98
20	114.4681	65.5616	0.08	-0.21	0.27	0.96	-0.14	0.29	0.08	-0.06	-0.18	0.48
21	114.4683	65.5658	0.54	0.78	0.67	0.98	0.80	0.76	0.65	0.92	0.88	0.78
22	114.4684	65.5699	0.88	0.99	0.99	1.00	0.89	0.89	0.91	0.98	0.99	0.99
23	114.4566	65.5200	0.89	-0.92	-0.06	1.00	-0.80	-0.14	0.90	0.31	-0.91	-0.04
24	114.4567	65.5242	0.61	0.40	0.07	0.99	0.41	-0.03	0.63	-0.31	0.40	0.15
25	114.4568	65.5283	0.46	0.08	-0.11	0.92	0.09	-0.62	0.22	0.39	0.23	0.26
26	114.4570	65.5325	0.54	0.14	0.79	0.96	-0.50	0.71	0.63	0.09	0.13	0.91

Table 4.3. The average C_{coef} over scales of 15″, 30″ and 60″ within R_{25} and within 0.5 R_{25}

Pair	R_{25}			$0.5\ R_{25}$		
	15″ × 15″	30″ × 30″	60″ × 60″	15″ × 15″	30″ × 30″	60″ × 60″
H I–8μm	0.50 ± 0.01	0.55 ± 0.02	0.57 ± 0.02	0.60 ± 0.02	0.60 ± 0.03	0.57 ± 0.05
H I–24μm	0.36 ± 0.01	0.40 ± 0.02	0.43 ± 0.03	0.49 ± 0.02	0.50 ± 0.03	0.47 ± 0.05
H I–70μm	0.25 ± 0.01	0.33 ± 0.02	0.39 ± 0.03	0.37 ± 0.02	0.40 ± 0.04	0.39 ± 0.06
H I–Hα	0.19 ± 0.01	0.24 ± 0.02	0.27 ± 0.03	0.24 ± 0.02	0.30 ± 0.04	0.24 ± 0.05
H I–FUV	0.05 ± 0.01	0.13 ± 0.02	0.17 ± 0.03	-0.05 ± 0.03	0.01 ± 0.04	-0.01 ± 0.06
H I–SFR	0.32 ± 0.01	0.38 ± 0.02	0.41 ± 0.03	0.42 ± 0.02	0.44 ± 0.04	0.41 ± 0.05
8μm–24μm	0.72 ± 0.01	0.78 ± 0.01	0.83 ± 0.02	0.89 ± 0.01	0.89 ± 0.02	0.88 ± 0.02
8μm–70μm	0.50 ± 0.01	0.60 ± 0.02	0.71 ± 0.02	0.63 ± 0.02	0.70 ± 0.03	0.75 ± 0.03
8μm–Hα	0.50 ± 0.01	0.58 ± 0.02	0.61 ± 0.03	0.61 ± 0.02	0.69 ± 0.03	0.69 ± 0.04
8μm–FUV	0.30 ± 0.01	0.41 ± 0.02	0.49 ± 0.03	0.27 ± 0.03	0.39 ± 0.04	0.44 ± 0.07
8μm–SFR	0.70 ± 0.01	0.77 ± 0.01	0.82 ± 0.02	0.83 ± 0.01	0.85 ± 0.02	0.86 ± 0.02
24μm–70um	0.52 ± 0.01	0.60 ± 0.02	0.69 ± 0.02	0.72 ± 0.02	0.78 ± 0.02	0.77 ± 0.02
24μm–Hα	0.49 ± 0.01	0.57 ± 0.02	0.64 ± 0.03	0.71 ± 0.02	0.82 ± 0.02	0.81 ± 0.03
24μm–FUV	0.32 ± 0.01	0.43 ± 0.02	0.53 ± 0.03	0.37 ± 0.03	0.51 ± 0.04	0.54 ± 0.06
24μm–SFR	0.95 ± 0.00	0.96 ± 0.00	0.97 ± 0.00	0.96 ± 0.00	0.98 ± 0.00	0.98 ± 0.01
70μm–Hα	0.42 ± 0.01	0.46 ± 0.02	0.51 ± 0.03	0.59 ± 0.02	0.65 ± 0.03	0.64 ± 0.04
70μm–FUV	0.31 ± 0.01	0.38 ± 0.02	0.46 ± 0.03	0.31 ± 0.03	0.40 ± 0.04	0.45 ± 0.06
70μm–SFR	0.55 ± 0.01	0.62 ± 0.02	0.71 ± 0.02	0.72 ± 0.02	0.78 ± 0.02	0.78 ± 0.02
Hα–FUV	0.53 ± 0.01	0.61 ± 0.02	0.68 ± 0.03	0.57 ± 0.02	0.67 ± 0.03	0.70 ± 0.04
Hα–SFR	0.56 ± 0.01	0.63 ± 0.02	0.70 ± 0.03	0.75 ± 0.01	0.85 ± 0.01	0.85 ± 0.02
FUV–SFR	0.50 ± 0.01	0.60 ± 0.02	0.69 ± 0.02	0.51 ± 0.02	0.62 ± 0.03	0.65 ± 0.05

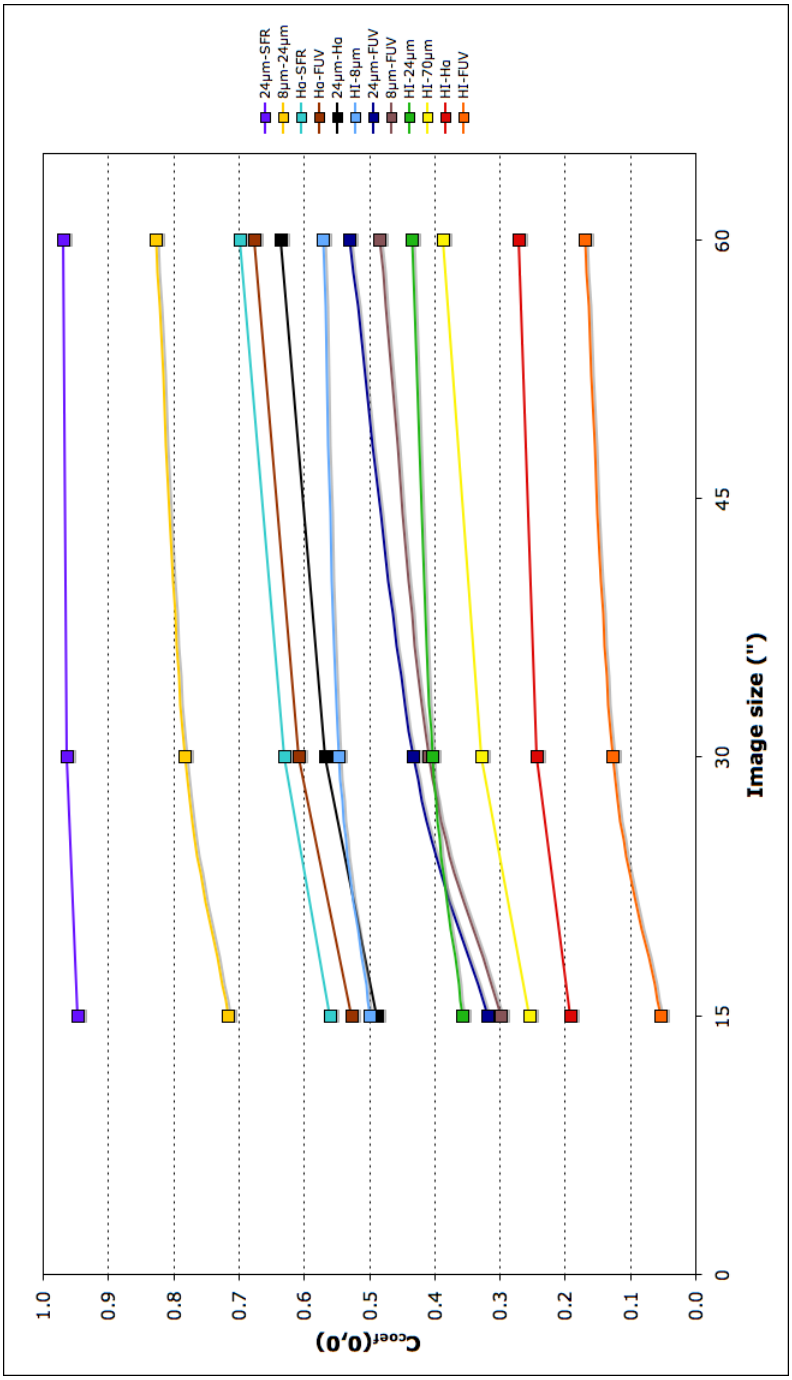

Figure 4.25: The mean C_{coef} within R_{25} as a function of image dimension for a sample of the cases.

maps at a matched resolution of 8″ or 120 pc.

Dust tracers

All the dust tracers (8μm, 24μm and 70μm) appear to be well linked with the strongest correlation being between the 8μm map and the 24μm map ($C_{coef} \sim$ 0.89). The 8μm–24μm relation is almost the same on all 3 scales and illustrates the excellent agreement in the distribution between PAH molecules and warm dust. It thus follows that the 8μm emission can be used as an indirect tracer of star formation (Calzetti et al. 2007), much as the 24μm emission. The 70μm map is well correlated with both the 24μm and 8μm maps with C_{coef} values of 0.77 and 0.75, respectively, at 60″ scale. However, at smaller scales (15″) the correlation 24μm–70μm drops to 0.72 whereas the 8μm–70μm drops to 0.63. In effect, this means that at smaller scales there are more areas where there is poorer correlation between the 8μm and 70μm emission. We speculate that this is a reflection of the 70μm maps tracing a cooler dust component that is not necessarily related to the warmer 8μm and 24μm emission.

SF tracers

The correlation between the FUV and SFR maps is high (0.65) at 60″ but drops considerably to 0.51 at 15″. Since the SFR map is a composite of the FUV and 24μm maps the high correlation is not surprising. The drop of this correlation indicates that the 24μm emission dominates the SFR map at smaller scales and shows that in star forming regions FUV emission is absorbed by dust. Looking at the more direct tracer of star formation, the Hα is well linked to the SFR map illustrating the relationship between current and recent star formation (C_{coef} = 0.85 at 30″ and 60″). Again, there is a drop in C_{coef} at the 15″ scale (C_{coef} = 0.75) which reflects an offset between current and recent star formation probably attributed to a dispersion of the star forming cluster. This is also illustrated by the Hα–FUV correlation which exhibits a very similar behaviour; at 30″ and 60″ scales the C_{coef} has a value of 0.67 and 0.70 respectively, while at 15″ it drops down to 0.57.

Dust–SF tracers

The 24μm–SFR pair has the highest correlation ($\geq$ 0.96) among our sample and this comes as no surprise since the SFR map is created, for the larger part, from the

24μm map. The 8μm map is also highly correlated with the SFR map ($C_{coef} \geq$ 0.83) thus reinforcing the suggestion that 8μm emission can be used as a star formation tracer. The same is true, to a lesser extent, for the 70μm map ($C_{coef} \geq$ 0.72) and it appears that all the dust tracers are associated to varying degrees with sites of star formation. The Hα map is well correlated with the 24μm, 8μm and 70μm with C_{coef} values of 0.81, 0.69 and 0.64 at 60″ respectively. At 15″ all three correlations drop (0.71, 0.61, 0.59) which again shows an offset between Hα and FUV sources. In contrast, the FUV map appears to be poorly correlated to any of the dust tracers especially at the smallest scale. The 24μm–FUV, 70μm–FUV and 8μm–FUV correlations have values of $\leq$ 0.37 at the scale of 15″. This is, of course, a direct consequence of the fact that dust absorbs FUV.

Gas–Dust tracers

The gas distribution as traced by the H I is better associated ($C_{coef} \sim 0.60$) with the 8μm map than with any other map examined here. It appears therefore that PAHs are well mixed with the gas in the disc. The H I map is moderately correlated with the 24μm and 70μm maps with average C_{coef} values of 0.47 and 0.39 respectively. No significant change of the C_{coef} value is observed at different scales.

Gas–SF tracers

As expected, the lowest correlations in our sample are those of the H I with the Hα ($C_{coef} \leq 0.30$) and the FUV ($C_{coef} \sim 0$) maps. The H I distribution appears to be completely unrelated to that of the FUV on all three scales. However, looking at the C_{coef} values of individual areas in Tables 4.1 and 4.2 we see that these range from 0.94 to -0.96. Therefore, the correlation of two maps on a specific area must depend on the location of this area in the galaxy. It is also interesting to note that the H I map is correlated with the SFR map ($C_{coef} \sim 0.42$) on all scales examined here, even though H I "per se" is not where SF occurs, but rather the H_2 dominated part of the ISM as traced by CO (Bigiel et al. 2008; Leroy et al. 2008).

Radial dependence

To investigate any possible trends of the correlation as a function of galactocentric radius we averaged the C_{coef} values over areas within concentric rings in steps of

0.5 kpc. The results are presented in Fig. 4.26 and 4.27. Almost all correlation pairs show an almost flat value of C_{coef} up to ~ 4 kpc which is roughly $0.5\,R_{25}$. Beyond this radius most correlations decline and this behaviour can be attributed to the fact that emission is weak on most of the maps as was discussed previously. One interesting aspect is that in many cases C_{coef} exhibits a wave-like pattern in the inner part of the galaxy. Since in these central regions the structure of the galaxy is more complex (e.g., due to active star forming sites) the relation between different components will vary to a large degree. This variation is illustrated in Fig. 4.28 where we plot C_{coef} as a function of position in the galaxy for the H I–8μm case. The complete set of comparisons can be found in Appendix A (Fig. A.11 to A.22). A detailed analysis of these images is beyond the scope of this work and these figures are included here as an illustration of the capabilities of the cross-correlation method.

4.3.2 Concluding remarks

In Section 4.1.2 we gave a descriptive comparison between maps of certain wavelengths. This visual comparison gave us an insight in the similarities and differences of different maps on a qualitative basis and thus a subjective view. The cross-correlation method described in Section 4.2 is a first attempt to compare maps in an objective way by eliminating any subjective bias. The results of this method with respect to 8 different images were presented in Section 4.3.1. The obvious question is then how does the cross-correlation method compare to the visual method.

As a reminder, please note that in the visual method we excluded the 70μm and SFR images from any comparison. In addition, we excluded the CO image from the cross-correlation method. Judging by the rest of the images the results obtained by the two methods are in good agreement at least to first order. The 8μm–24μm pair was correctly identified as the strongest correlation in both methods. The same is true for the other extreme, i.e., in both methods the H I–FUV and H I–Hα pairs were identified as being the least similar images. For most of the remaining cases both methods agree to a good extent with the only exception being that of the 8μm–Hα pair, which the cross-correlation method ranks as a higher correlation than the visual method.

A general conclusion is that the eye tends to focus on emission peaks and depressions thus missing out on information on the general distribution of an image. This is obviously not a problem when using the cross-correlation method

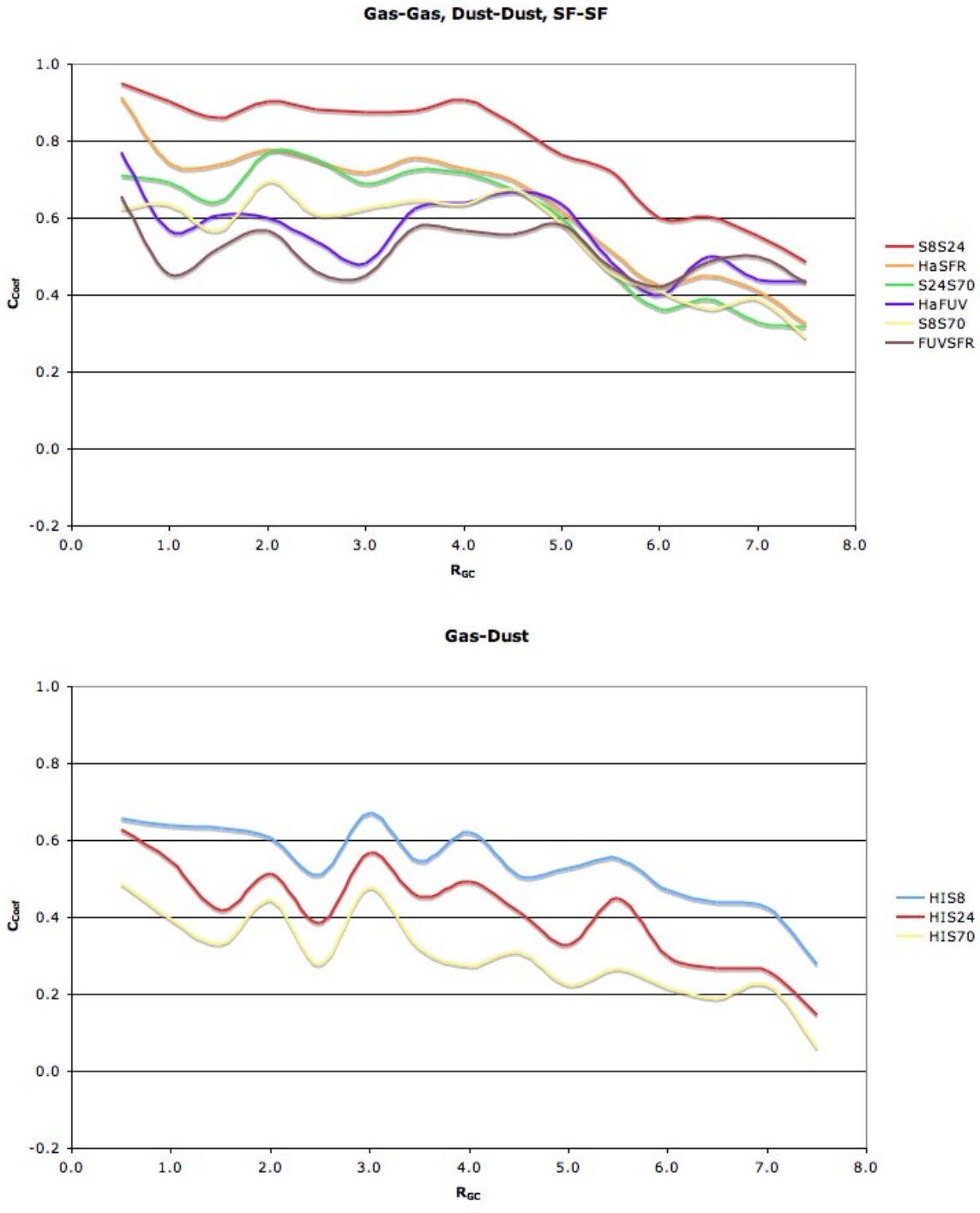

Figure 4.26: The average cross-correlation coefficient over concentric rings versus galactocentric radius, in kpc.

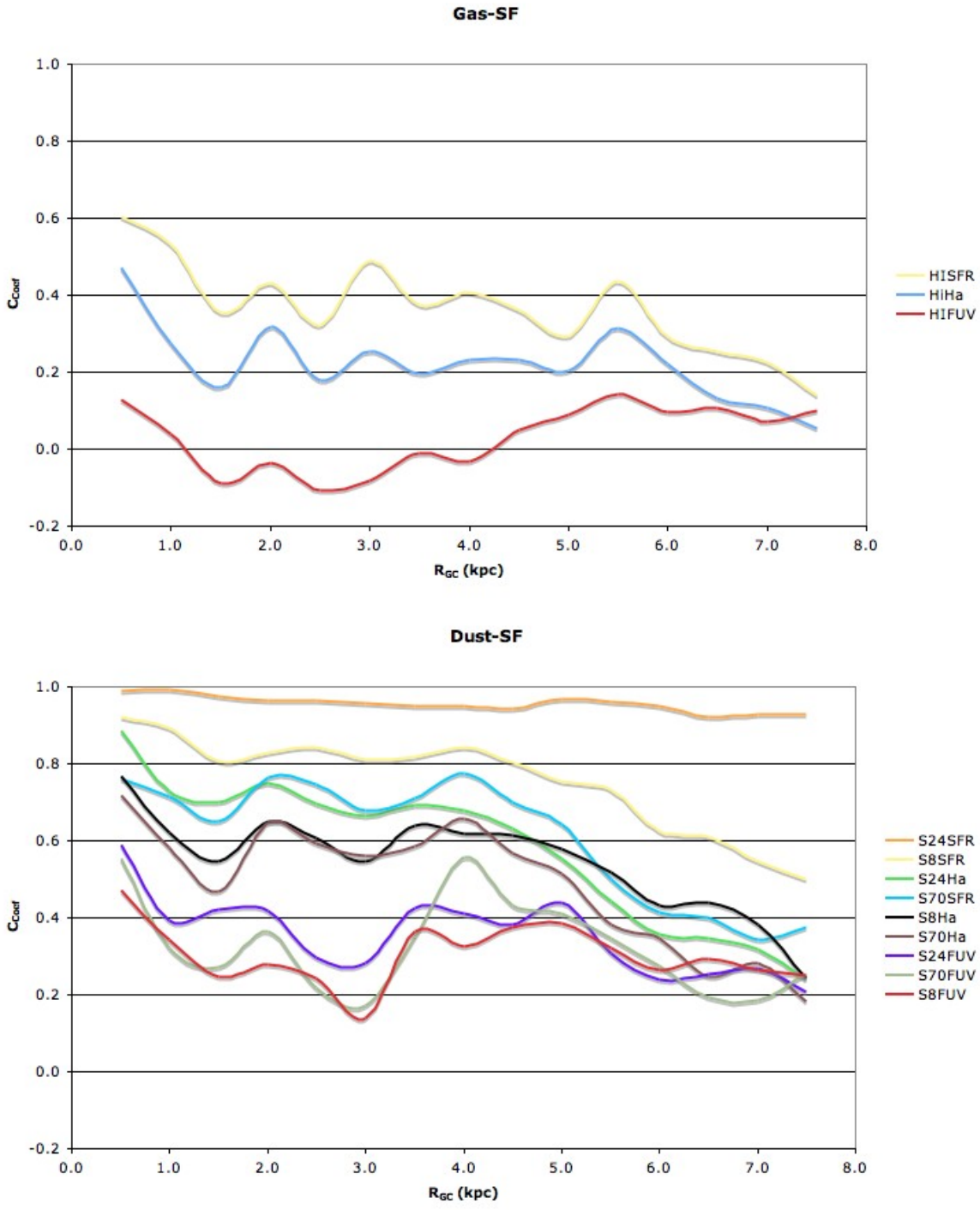

Figure 4.27: The average cross-correlation coefficient over concentric rings versus galactocentric radius, in kpc.

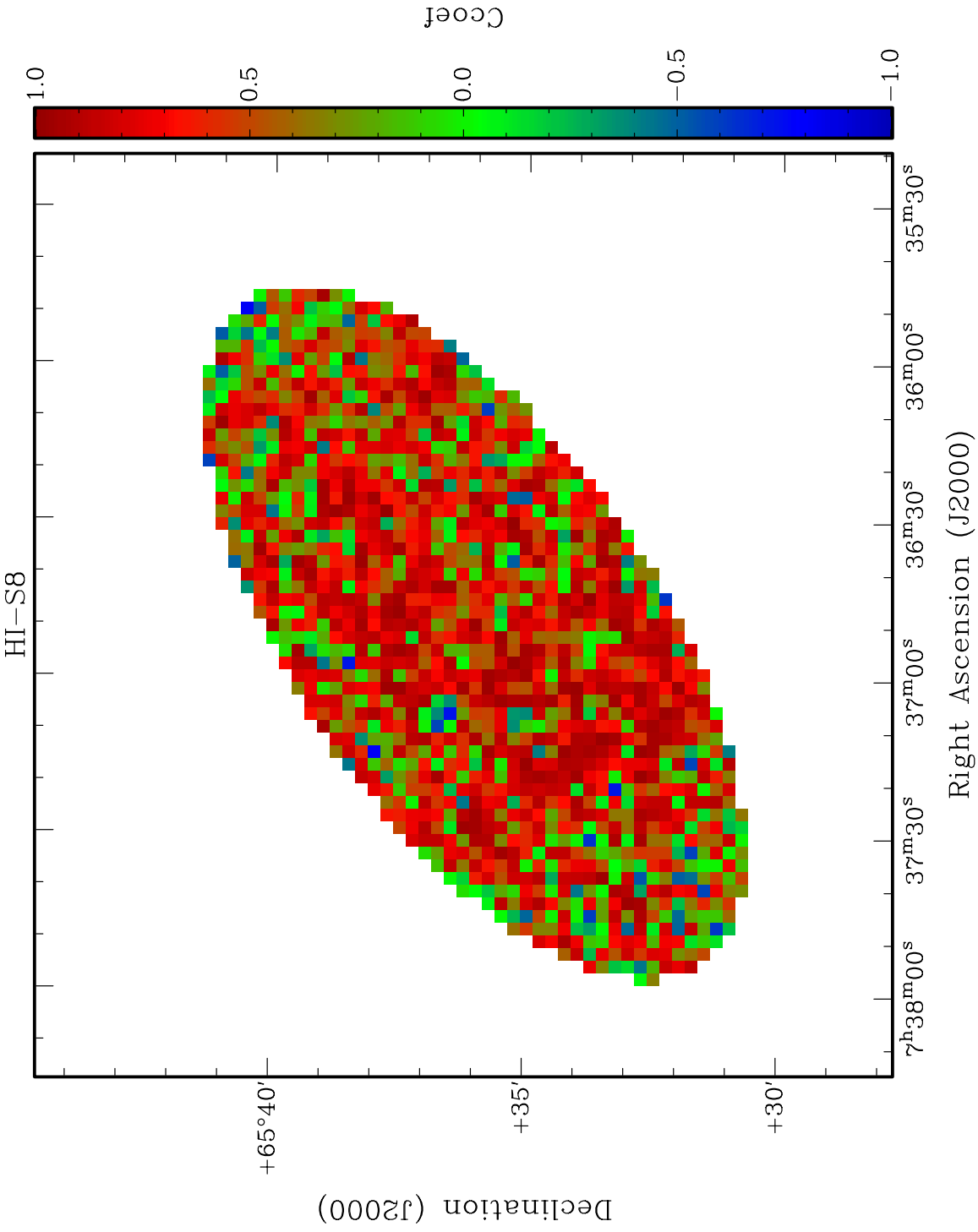

Figure 4.28: The C_{coef} as a function of position in the galaxy for the H I–8μm case. The size of each box is $15'' \times 15''$.

as it treats every point on an equal basis. The biggest advantage of the method described here is that each comparison is assigned a certain value (C_{coef}) and thus it is possible to establish a ranking among the various image pairs. This value can also be used to compare two maps on different scales and hence provide information on the physical processes at different scales. Using the cross-correlation method one can also get an insight on how the relation between two maps varies from area to area a result which is extremely time-consuming, if not impossible, to get by a visual inspection of two maps. In addition, a first attempt of the application of our method to other THINGS galaxies revealed that this can be done with virtually no "recalibration". The behaviour of C_{coef} appears to be the same in other galaxies as in NGC 2403. This preliminary result makes us confident that our method can now be applied to a large number of galaxies over a wide range of maps.

From the application of the cross-correlation method we found that that C_{coef} is nearly constant at scales larger than $\sim 200''$ (3.1 kpc) while it varies below this value due to structural differences in the various maps. Subsequently, we focused on smaller scales ($15''$, $30''$ and $60''$) in order to discover any structural relations. We find that all the dust tracers are well correlated ($C_{coef} > 0.7$) at all scales illustrating the agreement in the distribution between PAH molecules, warm and cold dust. At the $15''$ scale we note a decline in the 8μm–70μm correlation ($C_{coef} = 0.5$); the cooler dust component is not necessarily related to the warmer 8μm and 24μm dust components. Current and recent star formation sites appear to be offset at the $15''$ scale attributed to the dispersion of the star forming cluster and consequently an offset between Hα and FUV emission. However this offset is not evident at larger scales ($30''$ and $60''$) as expected ($C_{coef} > 0.6$).

The strongest correlation we find is that of the 24μm with the SFR map ($C_{coef} > 0.9$) as expected. In general, all star formation tracers are well linked with the dust tracers especially at the $30''$ and $60''$ scales. However, at $15''$ we see evidence of FUV absorption by dust grains as the correlation between FUV and all dust tracers is poor $C_{coef} \sim 0.3$. Looking at the H I component we find that it is well mixed with PAH's on all scales ($C_{coef} \sim 0.6$) while moderately related to the cold ($C_{coef} \sim 0.4$) and warm dust components ($C_{coef} \sim 0.5$). We observe a relation between the gas and the SF map ($C_{coef} \sim 0.4$) which is surprising given that FUV and H I emissions were found to be completely unrelated ($C_{coef} \sim 0$).

Chapter 5

Summary and Future Work

5.1 Summary

The present study is the first attempt to identify and compare in a systematic and consistent way H I holes across a range of nearby galaxies. Our sample consists of 20 spiral and dwarf galaxies which have been observed as part of the THINGS project. A detailed examination of the neutral ISM reveals a wealth of structures, the dominant one being formed by H I holes; out of more than 4000 candidate holes we catalogued the 1000 highest quality ones for which we determined a set of observed and derived properties. The number of these structures varies from galaxy to galaxy, partly because of the different linear resolution of our observations at the distance of the targets, and partly due to intrinsic differences between the galaxies, such as viewing angle. The target selection, and the wide range of observed characteristics, preclude us from performing any type of statistical analysis on a "complete" sample. Instead, we base our study on a comparative analysis, identifying broad trends.

Diameters of H I holes range from 100 pc (the resolution limit for the closest targets) to $\sim 2\,\mathrm{kpc}$ with the majority being smaller than 200 pc. Holes for which we could measure an expansion velocity (types 2 & 3, typically making up 10% to 50% of the holes) list values in the range of $4 - 36\,\mathrm{km\,s^{-1}}$. Their kinetic age varies from 3 to 150 Myr. H I holes are found throughout the H I disc of the parent galaxy, all the way to the edge of the observed atomic gas distribution. Across the sample, 77% of the holes fall within R_{25}, the main optical body of a galaxy, the remainder populate the outskirts. Their number surface density is fairly constant within R_{25} but drops at larger radii. A comparative analysis shows that:

1. H I holes in dwarfs are rounder, on average than in spirals;

2. blow-out holes in spirals are not circular as, otherwise, the inclination under which the discs are viewed would cause the major axis of holes to be aligned with the major axis of the disc;

3. there is a lower limit to the axial ratio at 0.4.

The above results lead us to propose that in spiral galaxies, shear is an important mechanism that not only modifies the shape of the holes but also limits the time they are observable, i.e., their kinetic age. This age limit is of order 50 Myr. Dwarf galaxies predominantly rotate more like solid bodies, hence shear does not play a major role there and consequently holes in dwarf galaxies are rounder, larger and older than in spirals. Here we note that diameter and kinetic age are closely linked as the expansion velocity covers a modest range (typically a factor of a few) whereas the diameter of the holes covers an order of magnitude in range.

Dividing the sample into dwarf and spiral galaxies, we were able to draw the following broad conclusions.

1. we find no difference in expansion velocity between dwarfs and spirals;

2. the radial distribution of H I holes is more extended in dwarf galaxies;

3. holes outside R_{25} are larger and older;

The fact that holes outside R_{25} are larger and older is likely again a consequence of shear which is most effective within R_{25}. We did not find a correlation between the diameter and expansion velocity as found in the LMC/SMC (Stanimirović 2007). We note that their correlation is strongest for small holes and speculate that this relation is due to small holes not having reached their final size yet, but that they are still being powered by ongoing SN explosions.

The porosity of the ISM was found to be higher in later Hubble types. We speculate that the lack of destruction mechanisms in dwarf galaxies contributes to this trend. In addition, higher porosity values translate to a more dynamic ISM where star formation becomes inefficient. The surface and volume porosity ($Q_{\rm 2D}$ and $Q_{\rm 3D}$) correlate with the type of the host galaxy as predicted by Silk (1997): later Hubble types tend to be more porous which reflects their current lower star formation rate per unit mass.

The size distribution of the holes in our sample follows a power law with a slope of $a_\nu \sim -2.9$ in broad agreement with Oey & Clarke (1997). Individual

galaxies have slopes ranging from −2 to −4. Since our spatial resolution is at best 100 pc, we are missing a substantial number of small holes. Assuming a power law shape for the size distribution, and a minimum hole size of 10 pc, expected to be the size of a shell created by a single O star, we can extrapolate our observations and predict the total size distribution of holes.

Assuming that the holes are the result of massive star formation, we derive values for the SFR over a time-frame of 50 Myr that correlate with the SFR derived based on other tracers but at the same time underestimating the true SFR if we restrict ourselves to the observed holes. When we apply an extrapolation to holes created by a single supernova, we find a surprisingly close agreement. This agreement does not mean that one would able to estimate the SFR of a galaxy based on the holes, but it does show that H I holes can be understood as being the result of star formation.

In Chapter 4 we described the development of a method to compare multi-wavelength maps and gave some first results from the application of this method to the nearby galaxy NGC 2403. Specifically, in Section 4.1.2 we attempted to visually examine the similarities and differences in the distribution of certain ISM components of this galaxy. Based on the study of H I holes as presented in Chapter 3 we focused our analysis on three constituents of the ISM, gas, dust and massive stars. For the gas component in its neutral atomic, neutral molecular and ionized phases we used maps of H I from THINGS, CO(2–1) from HERACLES and Hα from the SINGS Data Release 4. For the dust component we used 8μm, 24μm, and 70μm maps from SINGS which trace dust at different temperatures. A FUV map from the NGS was used to trace the distribution of massive young stars. Finally, following Leroy et al. (2008) we created a map of star forming regions based on the 24μm and FUV maps. The visual inspection of the aforementioned images revealed the following relations:

1. the 8μm map is similar to the 24μm map. This can be understood as both maps trace dust. The 8μm map is also similar to that of the H I indicating that PAH molecules are well mixed with atomic hydrogen;

2. the 24μm map correlates well with the FUV and Hα maps illustrating the heating of dust in star formation regions;

3. all the gas tracers are well correlated with all the dust tracers;

4. the FUV map has an extended distribution much like the H I and is closely linked to the Hα map, as expected, since both trace star formation;

5. there is an almost anti-correlation between both the FUV and Hα maps and the gas tracers (CO and H I) in line with the fact that the gas gets ionized due to intense radiation near sites of star formation;

6. CO emission is only detected where there is H I emission, but the opposite is not always true. This fits a picture in which CO forms out of atomic gas.

A visual inspection of the various images with respect to individual H I holes revealed certain interesting connections:

1. the vast majority of H I holes are also prominent in the 8μm map and to some extent in the 24μm map. The 24μm emission peaks on the rims of some of the holes, an indicator of propagating star formation;

2. there is a lack of molecular gas from the interior of nearly all the holes, which is consistent with the idea that the latter are rather filled with hot gas;

3. almost 57% of young holes have FUV emission detected in their interiors highlighting the presence of the parent OB association. Furthermore, FUV was detected on the rims of 37% of the older H I holes, presumably due to the dispersion of the OB association with respect to the gas. Only 1 hole (6%) was found to be unrelated to any FUV emission.

In order to quantify the above relations we proceeded to develop a method of comparing multi-wavelength images based on 2–D pixel-by-pixel cross-correlations. This method was then applied to all the aforementioned images, excluding CO, after convolving every image to the same spatial resolution. The result of the cross-correlation is quantified by the cross-correlation coefficient C_{coef} which takes values from 1 (perfect correlation) to -1 (perfect anti-correlation). In order to verify the robustness of this method we performed several tests, all of which yielded the expected results. From these tests we found that C_{coef} varies significantly at scales less than $\sim 200''$ (3.1 kpc) reflecting structural differences in the various maps. The C_{coef} value was also found to drop significantly when comparing sub-images centred at areas outside the R_{25} radius due to low signal -to-noise ratios in most of the maps. Consequently, we decided to compare sub-images at three different scales ($15''$, $30''$ and $60''$) located within R_{25}. Here "scale" means the area over which the cross-correlation is evaluated. Comparing every image with every other image we established the following key results:

1. all the dust tracers are well correlated ($C_{coef} > 0.7$) at all scales with the exception of 8μm–70μm at 15″ ($C_{coef} = 0.5$);

2. all the star formation tracers are well linked at 30″ and 60″ as expected ($C_{coef} > 0.6$). However the correlations drop at the 15″ scale where there is an offset between current and recent star formation;

3. with respect to the relations between star formation and dust tracers we found that most are well matched ($C_{coef} > 0.7$) as dust grains are heated by radiation in star forming regions. At the 15″ scale FUV correlates poorly ($C_{coef} \sim 0.3$) with all the dust tracers, a direct consequence of the absorption of FUV photons by dust;

4. the gas component is reasonably related to the 8μm emission ($C_{coef} \sim 0.6$) illustrating the fact that H I is mixed with PAH's;

5. the H I map shows some correlation with the SF map ($C_{coef} \sim 0.4$) even though FUV and H I emissions were found to be completely unrelated ($C_{coef} \sim 0$).

The two methods (visual and cross-correlation) employed in this study gave us similar results. However, the advantage of using the latter is that the results are quantified and free from any subjectivity. Moreover, maps can be compared at different scales thus revealing information on the physical processes in the ISM. Finally, we showed some first results on how the correlation of images varies with respect to the location in the galaxy.

5.2 Future Work

The analysis presented in Chapter 3 was of a comparative nature rather than a statistical one due to the relatively small galaxy sample. A statistical analysis could shed more light into the similarities and differences of the population of H I holes in spiral and dwarf galaxies. For instance, it would be interesting to see whether dwarf galaxies have indeed a higher porosity and consequently how feedback affects their morphology, chemistry and dynamics. This would require a further increase in the galaxy sample with the need to survey more dwarf galaxies in particular. Such an opportunity now arises with LITTLE THINGS (Local Irregulars That Trace Luminosity Extremes; Hunter et al. 2007), a VLA survey of

42 dwarf galaxies. This sample along with the THINGS sample of galaxies can also be used to calculate the scale height, as described in Section 2.2 and elaborated in Banerjee et al. (2011), and study its variation with respect to Hubble type, star formation history and dark matter content.

With respect to the scale height in large spirals the author is currently working on deriving data of 20 THINGS galaxies including gas and star disk properties, which will be used to derive the gas scale height of these galaxies in collaboration with Banerjee. We expect to have the calculated scale heights within the next three months and proceed on a statistical study of our sample. The aim is to have this work published by the end of 2012.

The work presented in Chapter 2 dictates the need for an automated method to detect and characterize H I holes in external galaxies. It would allow for an unbiased and practical way of surveying large samples of galaxies for holes and thus provide the opportunity to do a robust statistical analysis on the population of H I holes. Given that the number of holes follows a power law, as we saw in Section 3.1.4, the vast majority of holes in any given galaxy is less than 100 pc in diameter. Therefore, with higher resolution observations of nearby galaxies in the near future, the number of holes per galaxy can only be detected using an automated method. One would then be able to study hole properties and distribution as a function of galactic properties and reveal the connection with star formation in greater detail. In addition to considering getting involved in such an automated shell identification code, I will strive to become involved, during my time as PDRA, in ASKAP and MEERKAT collaborations such as MHONGOOSE, that will eventually give me access to a large number of objects.

The cross-correlation method described in Chapter 4 can now be applied extensively on a single galaxy and study the relation of the various ISM components on a wider range of spatial scales. High resolution maps now exist across the whole of the EM spectrum which would allow for a clearer picture on how all ISM components relate to each other. Such a study could also investigate how the similarities or differences of these components depend on the location within the galaxy and how these vary with certain physical processes such as star formation sites, PDR's, outflows, etc. The work presented on Chapter 4 is being finalised by the author and will be published within the next three months. The next step will then be to apply this method to a large sample of galaxies such as based on THINGS and help establish trends with Hubble type, metallicity and star formation history. This is a substantial project with a large number of unknowns

however, the aim is to reach the publication state within the course of my next PDRA appointment.

I expect that such a study would be transformational. To date no practical method has been deployed, to my knowledge, to compare maps across the electromagnetic spectrum of galaxies while preserving spatial information. Some methods that have been used, such as wavelet analysis, although useful to a certain extent, lead to a loss of this important information. I look forward to applying this method to the wealth of data that have that have and will become available based on observations with the new generation of telescopes such as the EVLA (now JVLA), ALMA and satellites such as GALEX, SPITZER and recently Herschel.

Bibliography

Bagetakos, I., Brinks, E., Walter, F., de Blok, W. J. G., Usero, A., Leroy, A. K., Rich, J. W., & Kennicutt, R. C. 2011, The Astronomical Journal, 141, 23

Banerjee, A., Jog, C. J., Brinks, E., & Bagetakos, I. 2011, Monthly Notices RAS, 415, 687

Biermann, P., & Tinsley, B. M. 1974, Astronomical Society of the Pacific, 86, 791

Bigiel, F., Leroy, A., Walter, F., Brinks, E., de Blok, W. J. G., Madore, B., & Thornley, M. D. 2008, The Astronomical Journal, 136, 2846

Boomsma, R. 2007, PhD thesis, AA(Kapteyn Astronomical Institute, University of Groningen)

Boomsma, R., Oosterloo, T. A., Fraternali, F., van der Hulst, J. M., & Sancisi, R. 2008, Astronomy and Astrophysics, 490, 555

Boomsma, R., van der Hulst, T., Oosterloo, T., Fraternali, F., & Sancisi, R. 2004, International Astronomical Union Symposium no. 217, 217, 142

Brand, P. W. J. L., & Zealey, W. J. 1975, Astronomy and Astrophysics, 38, 363

Bregman, J. N. 1980, Astrophysical Journal, 236, 577

Brinks, E. 1981, Astronomy and Astrophysics, 95, L1

Brinks, E., & Bajaja, E. 1986, Astronomy and Astrophysics, 169, 14

Brinks, E., & Burton, W. B. 1984, Astronomy and Astrophysics, 141, 195

Brinks, E., Walter, F., & Ott, J. 2002, Disks of Galaxies: Kinematics, 275, 57

Bronkalla, W., Notni, P., & Mutter, A. A.-R. 1992, Astronomische Nachrichten, 313, 1

Bureau, M., & Carignan, C. 2002, The Astronomical Journal, 123, 1316

Burstein, P. H. 1976, PhD thesis, University of Wisconsin

Calzetti, D., et al. 2007, The Astrophysical Journal, 666, 870

—. 2010, The Astrophysical Journal, 714, 1256

Cannon, J. M., et al. 2005, The Astrophysical Journal, 630, L37

Castor, J., McCray, R., & Weaver, R. 1975, Astrophysical Journal, 200, L107

Charbonneau, D., et al. 2005, The Astrophysical Journal, 626, 523

Chevalier, R. A. 1974, Astrophysical Journal, 188, 501

Chu, Y.-H., Guerrero, M. A., & Gruendl, R. A. 2004, How Does the Galaxy Work? A Galactic Tertulia with Don Cox and Ron Reynolds. Edited by Emilio J. Alfaro, 315, 165

Cox, D. P., & Smith, B. W. 1974, Astrophysical Journal, 189, L105

Daigle, A., Joncas, G., Parizeau, M., & Miville-Deschênes, M.-A. 2003, The Publications of the Astronomical Society of the Pacific, 115, 662

de Blok, W. J. G., & Walter, F. 2006, The Astronomical Journal, 131, 343

Deharveng, L., Zavagno, A., Schuller, F., Caplan, J., Pomarès, M., & Breuck, C. D. 2009, Astronomy and Astrophysics, 496, 177

Deming, D., Seager, S., Richardson, L. J., & Harrington, J. 2005, Nature, 434, 740

Deul, E. R., & den Hartog, R. H. 1990, Astronomy and Astrophysics, 229, 362

Dib, S., Bell, E., & Burkert, A. 2006, The Astrophysical Journal, 638, 797

Dib, S., & Burkert, A. 2005, The Astrophysical Journal, 630, 238

Dobbs, C. L., & Pringle, J. E. 2009, Monthly Notices RAS, 396, 1579

Dopita, M. A., & Ryder, S. D. 1994, The Astrophysical Journal, 430, 163

Draine, B. T. 2003, Annual Review of Astronomy &Astrophysics, 41, 241

—. 2011, Physics of the Interstellar and Intergalactic Medium by Bruce T. Draine. Princeton University Press

Dumas, G., Schinnerer, E., Tabatabaei, F. S., Beck, R., Velusamy, T., & Murphy, E. 2011, The Astronomical Journal, 141, 41

Dyson, J. E. 1977, Astronomy and Astrophysics, 59, 161, a&AA ID. AAA019.064.053

Dyson, J. E., & Williams, D. A. 1980, New York

Efremov, Y. N., Ehlerová, S., & Palouš, J. 1999, A&A, 350, 457

Ehlerová, S., & Palouš, J. 2005, Astronomy and Astrophysics, 437, 101

Elmegreen, B. G., Palouš, J., & Ehlerová, S. 2002, Monthly Notices RAS, 334, 693

Field, G. B., Goldsmith, D. W., & Habing, H. J. 1969, Astrophysical Journal, 155, L149

Fraternali, F., & Binney, J. J. 2006, Monthly Notices RAS, 366, 449

Frick, P., Beck, R., Berkhuijsen, E. M., & Patrickeyev, I. 2001, Monthly Notices RAS, 327, 1145

Gerola, H., Seiden, P. E., & Schulman, L. S. 1980, Astrophysical Journal, 242, 517

Gil de Paz, A., et al. 2007, The Astrophysical Journal Supplement Series, 173, 185

Goldsmith, P. F., et al. 2011, The Astrophysical Journal, 737, 96

Gordon, K. D., et al. 2005, The Publications of the Astronomical Society of the Pacific, 117, 503

Gorenstein, P., Harnden, F. R., & Tucker, W. H. 1974, Astrophysical Journal, 192, 661

Hatzidimitriou, D., Stanimirović, S., Maragoudaki, F., Staveley-Smith, L., Dapergolas, A., & Bratsolis, E. 2005, Monthly Notices RAS, 360, 1171

Heiles, C. 1979, Astrophysical Journal, 229, 533

—. 1984, Astrophysical Journal Supplement Series, 55, 585

Hindman, J. V. 1967, Australian Journal of Physics, 20, 147

Hoffman, G. L., Salpeter, E. E., & Carle, N. J. 2001, The Astronomical Journal, 122, 2428

Hughes, A., Wong, T., Ekers, R., Staveley-Smith, L., Filipovic, M., Maddison, S., Fukui, Y., & Mizuno, N. 2006, Monthly Notices RAS, 370, 363

Hunter, D. A., Brinks, E., Elmegreen, B., Rupen, M., Simpson, C., Walter, F., Westpfahl, D., & Young, L. 2007, in Bulletin of the American Astronomical Society, Vol. 38, American Astronomical Society Meeting Abstracts, 895

Hunter, D. A., & Elmegreen, B. G. 2004, The Astronomical Journal, 128, 2170

Hunter, D. A., Elmegreen, B. G., & van Woerden, H. 2001, The Astrophysical Journal, 556, 773

Hunter, D. A., van Woerden, H., & Gallagher, J. S. 1999, The Astronomical Journal, 118, 2184

Hunter, D. A., Wilcots, E. M., van Woerden, H., Gallagher, J. S., & Kohle, S. 1998, Astrophysical Journal Letters v.495, 495, L47

Kalberla, P. M. W., & Kerp, J. 2009, Annual Review of Astronomy & Astrophysics, 47, 27

Kamphuis, J., & Sancisi, R. 1993, Astronomy and Astrophysics V.273, 273, L31

Kamphuis, J., Sancisi, R., & van der Hulst, T. 1991, Astronomy and Astrophysics, 244, L29

Kennicutt, R. C. 1989, Astrophysical Journal, 344, 685

—. 1998, Annual Review of Astronomy and Astrophysics, 36, 189

—. 2008, The Second Annual Spitzer Science Center Conference: Infrared Diagnostics of Galaxy Evolution. ASP Conference Series, 381, 103

Kennicutt, R. C., Bresolin, F., Bomans, D. J., Bothun, G. D., & Thompson, I. B. 1995, Astronomical Journal, 109, 594

Kennicutt, R. C., et al. 2003, The Publications of the Astronomical Society of the Pacific, 115, 928

Kim, S., Dopita, M. A., Staveley-Smith, L., & Bessell, M. S. 1999, The Astronomical Journal, 118, 2797

Kregel, M., van der Kruit, P. C., & de Grijs, R. 2002, Monthly Notices RAS, 334, 646

Krumholz, M. R., McKee, C. F., & Tumlinson, J. 2009, The Astrophysical Journal, 693, 216

Kulkarni, S. R., & Heiles, C. 1988, IN: Galactic and extragalactic radio astronomy (2nd edition). Berlin and New York, 95

Kwok, S. 2007, Physics and Chemistry of the Interstellar Medium by Sun Kwok. University Science Books

Leroy, A., Bolatto, A., Walter, F., & Blitz, L. 2006, The Astrophysical Journal, 643, 825

Leroy, A. K., Walter, F., Brinks, E., Bigiel, F., de Blok, W. J. G., Madore, B., & Thornley, M. D. 2008, The Astronomical Journal, 136, 2782

Leroy, A. K., et al. 2009, The Astronomical Journal, 137, 4670

Lockman, F. J. 1984, Astrophysical Journal, 283, 90

Loeb, A., & Perna, R. 1998, Astrophysical Journal Letters v.503, 503, L35

Low, M.-M. M., & Ferrara, A. 1999, The Astrophysical Journal, 513, 142

Martin, C. L. 1998, The Astrophysical Journal, 506, 222

Martin, C. L., & Kennicutt, R. C. 2001, The Astrophysical Journal, 555, 301

Martin, D. C., et al. 2005, The Astrophysical Journal, 619, L1

Mashchenko, S., & St-Louis, N. 2002, Interacting Winds from Massive Stars. ASP Conference Proceedings, 260, 65

Mashchenko, S. Y., Thilker, D. A., & Braun, R. 1999, Astronomy and Astrophysics, 343, 352

Mathis, J. S. 1990, IN: Annual review of astronomy and astrophysics. Vol. 28. Palo Alto, 28, 37

McCray, R., & Kafatos, M. 1987, Astrophysical Journal, 317, 190

McCray, R., & Snow, T. P. 1979, In: Annual review of astronomy and astrophysics. Volume 17. Palo Alto, 17, 213

McKee, C. F., & Ostriker, J. P. 1977, Astrophysical Journal, 218, 148

Morrissey, P., et al. 2007, The Astrophysical Journal Supplement Series, 173, 682

Mühle, S., Klein, U., Wilcots, E. M., & Hüttemeister, S. 2006, The Astronomical Journal, 132, 443

Murray, S. D., & Lin, D. N. C. 2004, The Astrophysical Journal, 615, 586

Narayan, C. A., & Jog, C. J. 2002, Astronomy and Astrophysics, 394, 89

Oey, M. S. 2007, Triggered Star Formation in a Turbulent ISM, 237, 106

Oey, M. S., & Clarke, C. J. 1997, Mon. Not. R. Astron. Soc., 289, 570

Oosterloo, T., Fraternali, F., & Sancisi, R. 2007, The Astronomical Journal, 134, 1019

Ott, J., Walter, F., Brinks, E., Dyk, S. D. V., Dirsch, B., & Klein, U. 2001, The Astronomical Journal, 122, 3070

Pasquali, A., et al. 2008, The Astrophysical Journal, 687, 1004

Perna, R., & Raymond, J. 2000, The Astrophysical Journal, 539, 706

Pidopryhora, Y., Lockman, F. J., & Shields, J. C. 2007, The Astrophysical Journal, 656, 928

Pikel'Ner, S. B. 1968, Astrophysical Letters, 2, 97

Puche, D., Westpfahl, D., Brinks, E., & Roy, J.-R. 1992, Astronomical Journal, 103, 1841

Rand, R. J., & Stone, J. M. 1996, Astronomical Journal v.111, 111, 190

Relaño, M., Beckman, J. E., Daigle, O., & Carignan, C. 2007, A&A, 467, 1117

Reynolds, R. J. 1993, Back to the Galaxy. AIP Conference Proceedings, 278, 156

Rhode, K., Salzer, J., Westpfahl, D., & Radice, L. 1999, The Astronomical Journal, 118, 323

Rich, J. W., de Blok, W. J. G., Cornwell, T. J., Brinks, E., Walter, F., Bagetakos, I., & Kennicutt, R. C. 2008, The Astronomical Journal, 136, 2897

Sancisi, R., Fraternali, F., Oosterloo, T., & van der Hulst, T. 2008, Astron Astrophys Rev, 15, 189

Santillán, A., Franco, J., Martos, M., & Kim, J. 1999, The Astrophysical Journal, 515, 657

Schaye, J. 2004, The Astrophysical Journal, 609, 667

Shapiro, P. R., & Field, G. B. 1976, Astrophysical Journal, 205, 762

Silich, S., Elias, F., & Franco, J. 2008, The Astrophysical Journal, 681, 1327

Silich, S., Lozinskaya, T., Moiseev, A., Podorvanuk, N., Rosado, M., Borissova, J., & Valdez-Gutierrez, M. 2006, Astronomy and Astrophysics, 448, 123

Silich, S., & Tenorio-Tagle, G. 2001, The Astrophysical Journal, 552, 91

Silich, S. A., & Mashchenko, S. Y. 1996, Astronomical and Astrophysical Transactions, 10, 225

Silk, J. 1997, Astrophysical Journal v.481, 481, 703

Simpson, C. E., Hunter, D. A., & Knezek, P. M. 2005a, The Astronomical Journal, 129, 160

Simpson, C. E., Hunter, D. A., & Nordgren, T. E. 2005b, The Astronomical Journal, 130, 1049

Smith, J. D. T., et al. 2007, The Astrophysical Journal, 656, 770

Spitzer, L. 1956, Astrophysical Journal, 124, 20

Stanimirović, S. 2007, Triggered Star Formation in a Turbulent ISM, 237, 84

Stanimirović, S., Staveley-Smith, L., Dickey, J. M., Sault, R. J., & Snowden, S. L. 1999, Monthly Notices RAS, 302, 417

Stanke, T., et al. 2010, Astronomy and Astrophysics, 518, L94

Stewart, S. G., & Walter, F. 2000, The Astronomical Journal, 120, 1794

Struve, O. 1928, Astrophys. J., 67, 353

Tabatabaei, F. S., et al. 2007, Astronomy and Astrophysics, 466, 509

Tamburro, D., Rix, H.-W., Leroy, A. K., Low, M.-M. M., Walter, F., Kennicutt, R. C., Brinks, E., & de Blok, W. J. G. 2009, The Astronomical Journal, 137, 4424

Tenorio-Tagle, G. 2000, New Astronomy Reviews, 44, 365

Tenorio-Tagle, G., & Bodenheimer, P. 1988, IN: Annual review of astronomy and astrophysics. Volume 26. Palo Alto, 26, 145

Tenorio-Tagle, G., Silich, S., Rodríguez-González, A., & Muñoz-Tuñón, C. 2005, The Astrophysical Journal, 628, L13

Thilker, D. A., Braun, R., & Walterbos, R. M. 1998, Astronomy and Astrophysics, 332, 429

Thilker, D. A., et al. 2007, The Astrophysical Journal Supplement Series, 173, 538

—. 2008, Formation and Evolution of Galaxy Disks ASP Conference Series, 396, 223

Thornley, M., Braine, J., & Gardan, E. 2006, The Astrophysical Journal Letters, 651, L101

Tielens, A. G. G. M. 2005, The Physics and Chemistry of the Interstellar Medium, iSBN: 0521826349

Trumpler, R. J. 1930, Lick Observatory bulletin ; no. 420; Lick Observatory bulletins ; no. 420., 14, 154

van der Hulst, J. M. 1996, The Minnesota lectures on extragalactic neutral hydrogen. Astronomical Society of the Pacific Conference Series, 106, 47

van der Kruit, P. C. 1988, Astronomy and Astrophysics, 192, 117

Wada, K., Spaans, M., & Kim, S. 2000, The Astrophysical Journal, 540, 797

Walter, F., & Brinks, E. 1999, The Astronomical Journal, 118, 273

—. 2001, The Astronomical Journal, 121, 3026

Walter, F., Brinks, E., de Blok, W. J. G., Bigiel, F., Kennicutt, R. C., Thornley, M. D., & Leroy, A. 2008, The Astronomical Journal, 136, 2563

Walter, F., Weiss, A., Martin, C., & Scoville, N. 2002, The Astronomical Journal, 123, 225

Weaver, R., McCray, R., Castor, J., Shapiro, P., & Moore, R. 1977, Astrophysical Journal, 218, 377

Weisz, D. R., Skillman, E. D., Cannon, J. M., Dolphin, A. E., Kennicutt, R. C., Lee, J., & Walter, F. 2009a, The Astrophysical Journal, 704, 1538

Weisz, D. R., Skillman, E. D., Cannon, J. M., Walter, F., Brinks, E., Ott, J., & Dolphin, A. E. 2009b, The Astrophysical Journal Letters, 691, L59

Westerlund, B. E., & Mathewson, D. S. 1966, Monthly Notices RAS, 131, 371

Wilcots, E. M., & Miller, B. W. 1998, The Astronomical Journal, 116, 2363

Wills, K. A., Pedlar, A., & Muxlow, T. W. B. 2002, Monthly Notices RAS, 331, 313

Yamaguchi, R., Mizuno, N., Onishi, T., Mizuno, A., & Fukui, Y. 2001, The Astrophysical Journal, 553, L185

Yun, M. S. 1999, Galaxy Interactions at Low and High Redshift, 186, 81

Appendices

Appendix A

Supplemental Figures

A.1 The C_{coef} over 5 areas

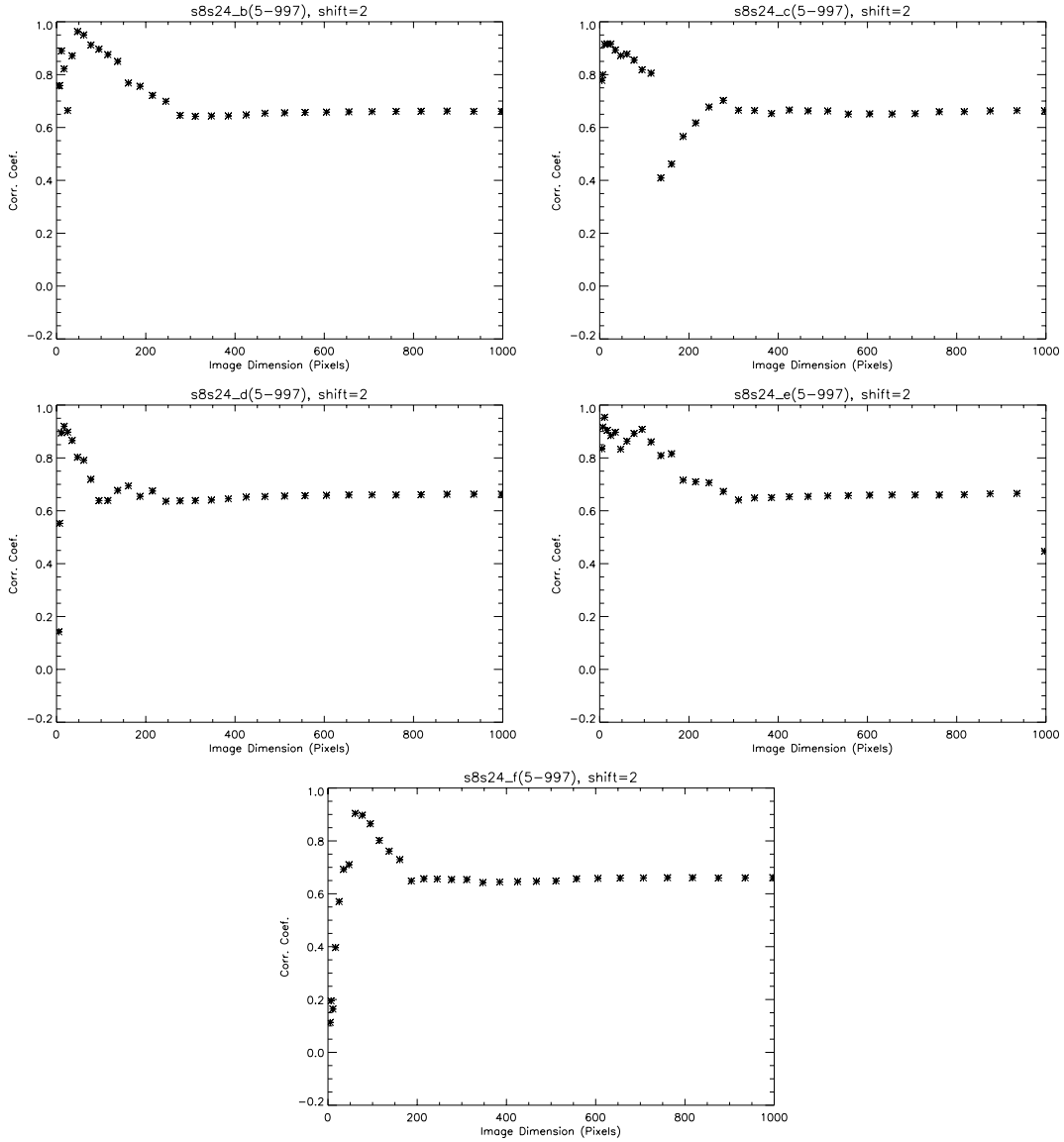

Figure A.1: The correlation coefficient of the 8μm and 24μm maps over 5 different areas. The x–axis represents the size of the individual images.

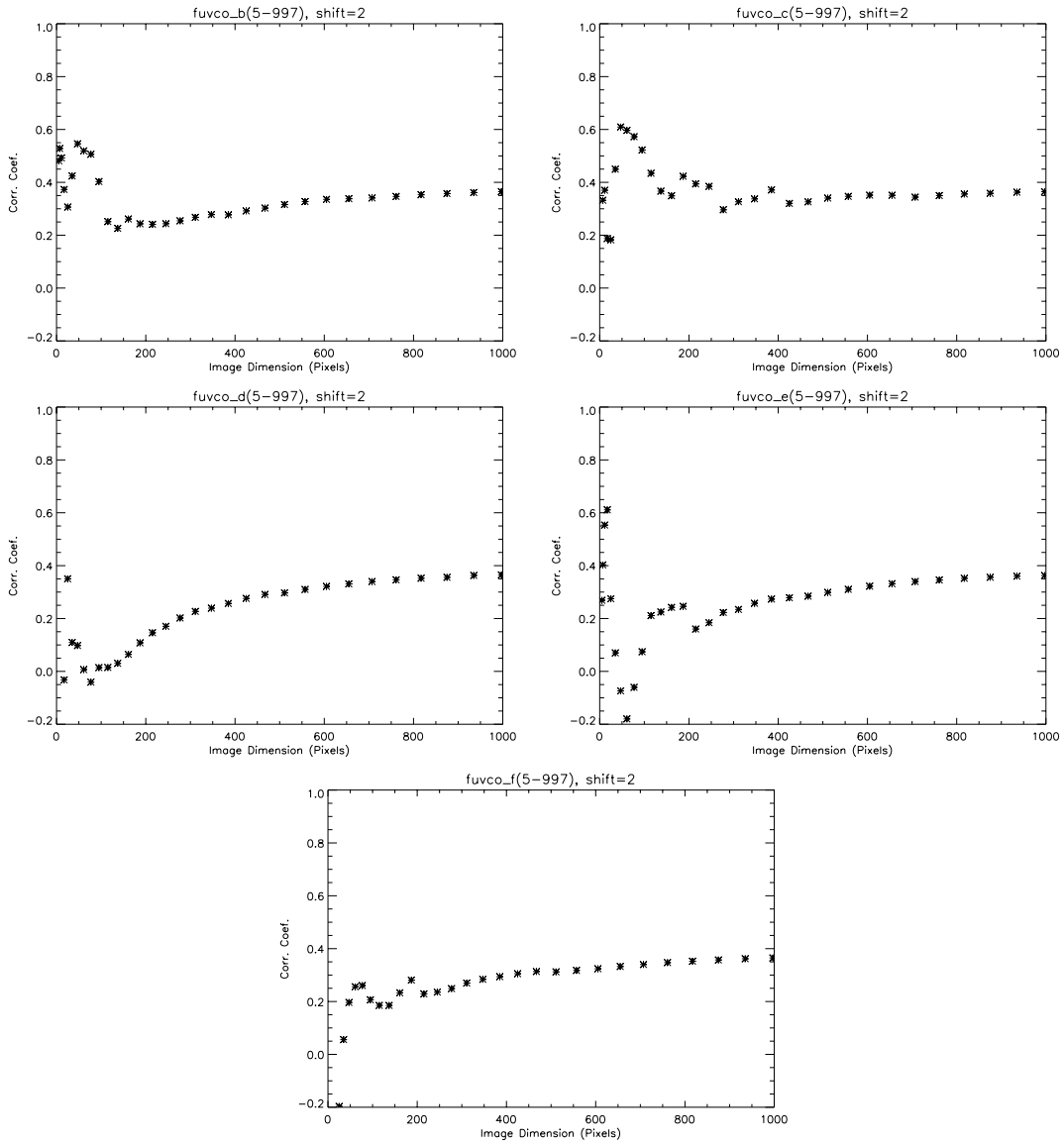

Figure A.2: The correlation coefficient of the FUV and CO maps over 5 different areas. The x–axis represents the size of the individual images.

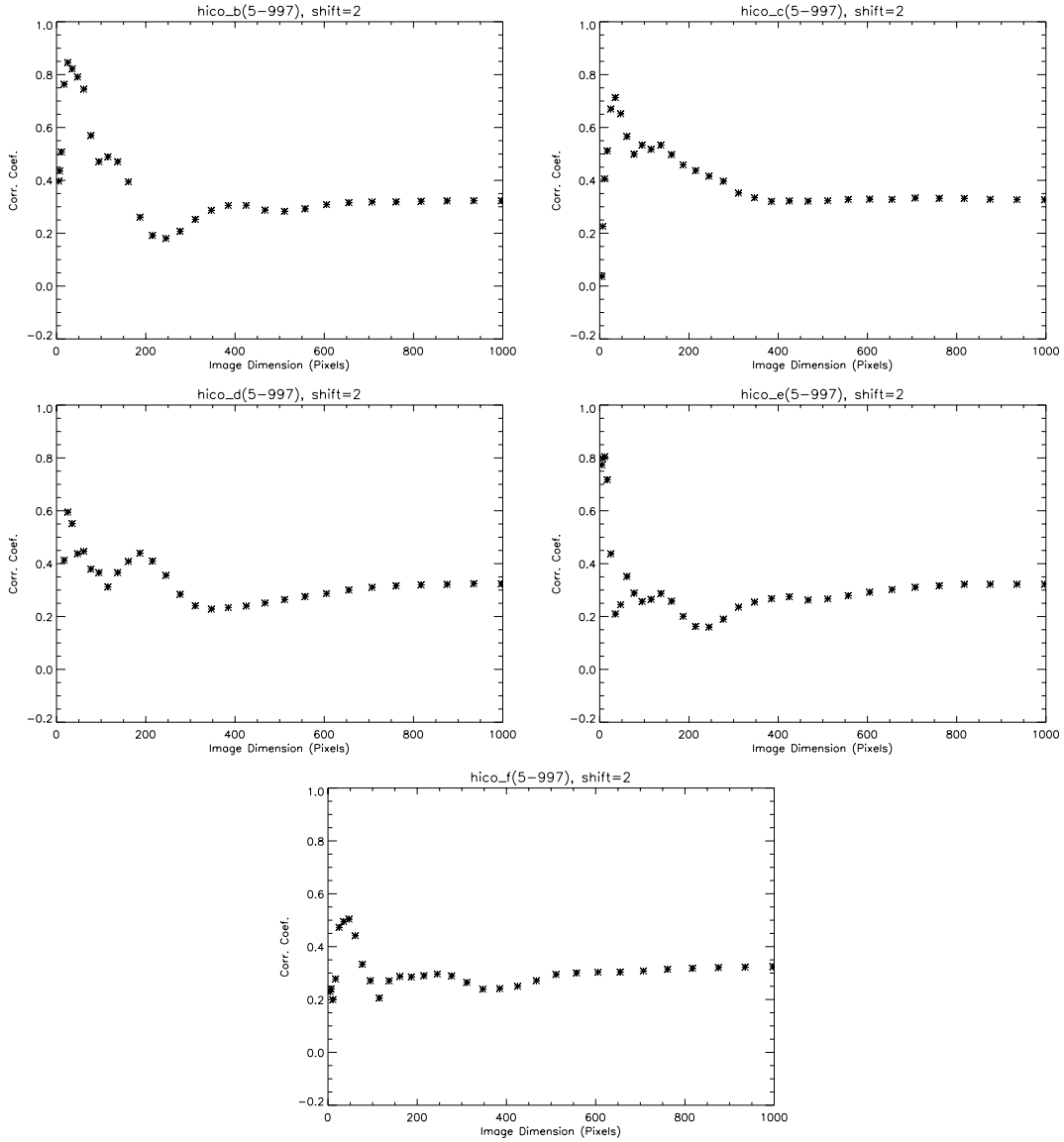

Figure A.3: The correlation coefficient of the HI and CO maps over 5 different areas. The x–axis represents the size of the individual images.

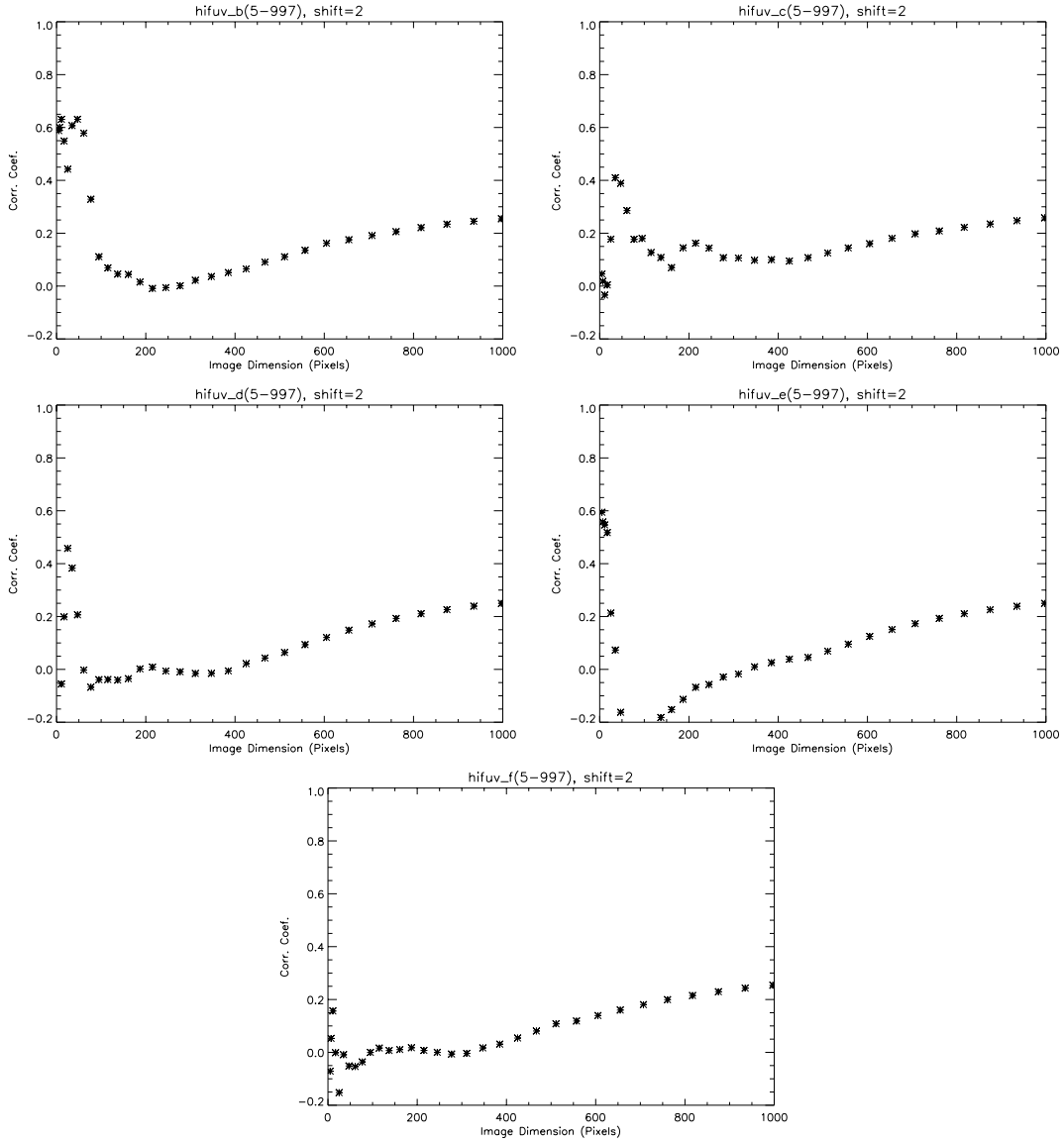

Figure A.4: The correlation coefficient of the H I and FUV maps over 5 different areas. The x–axis represents the size of the individual images.

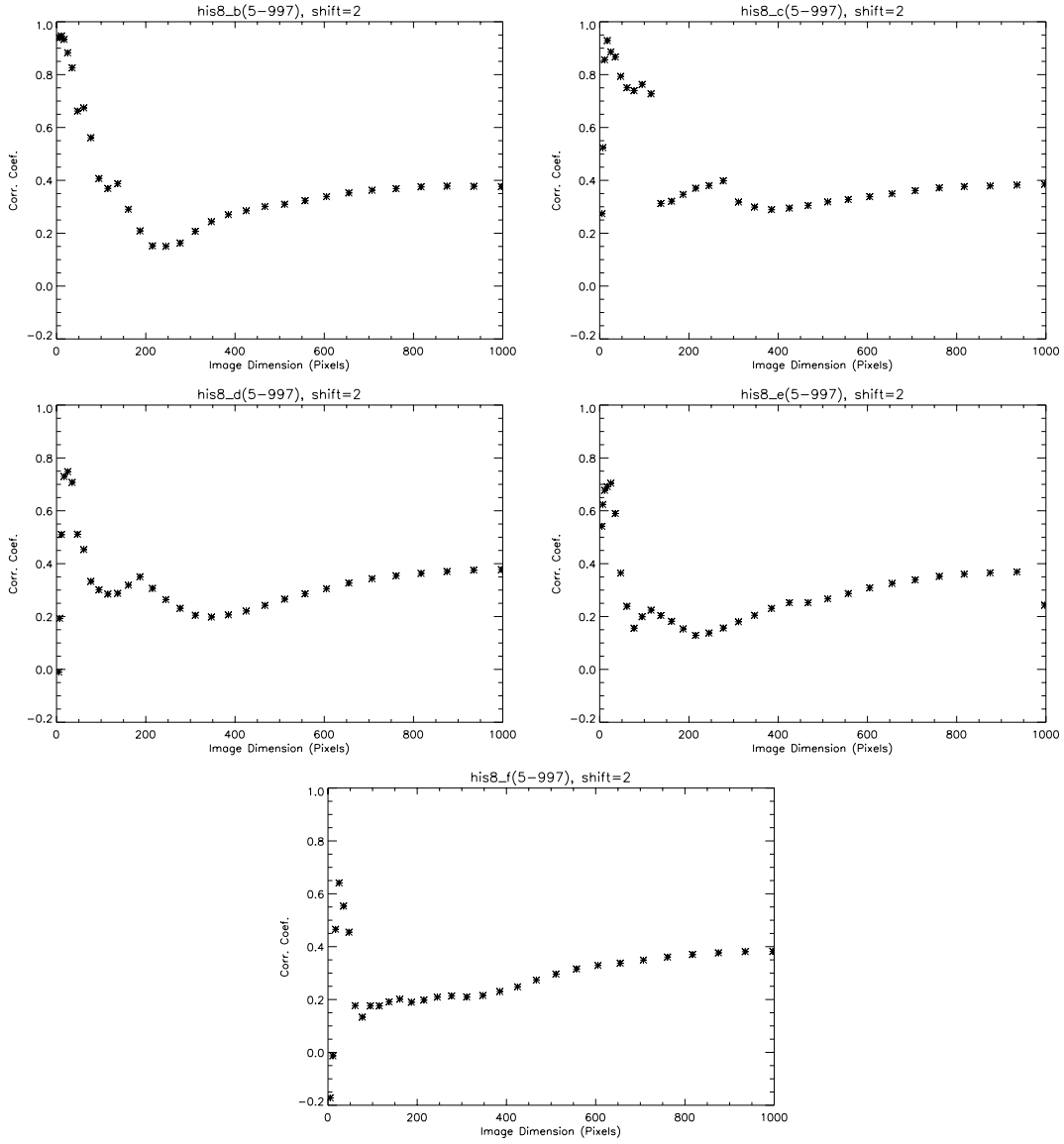

Figure A.5: The correlation coefficient of the H I and 8μm maps over 5 different areas. The x–axis represents the size of the individual images.

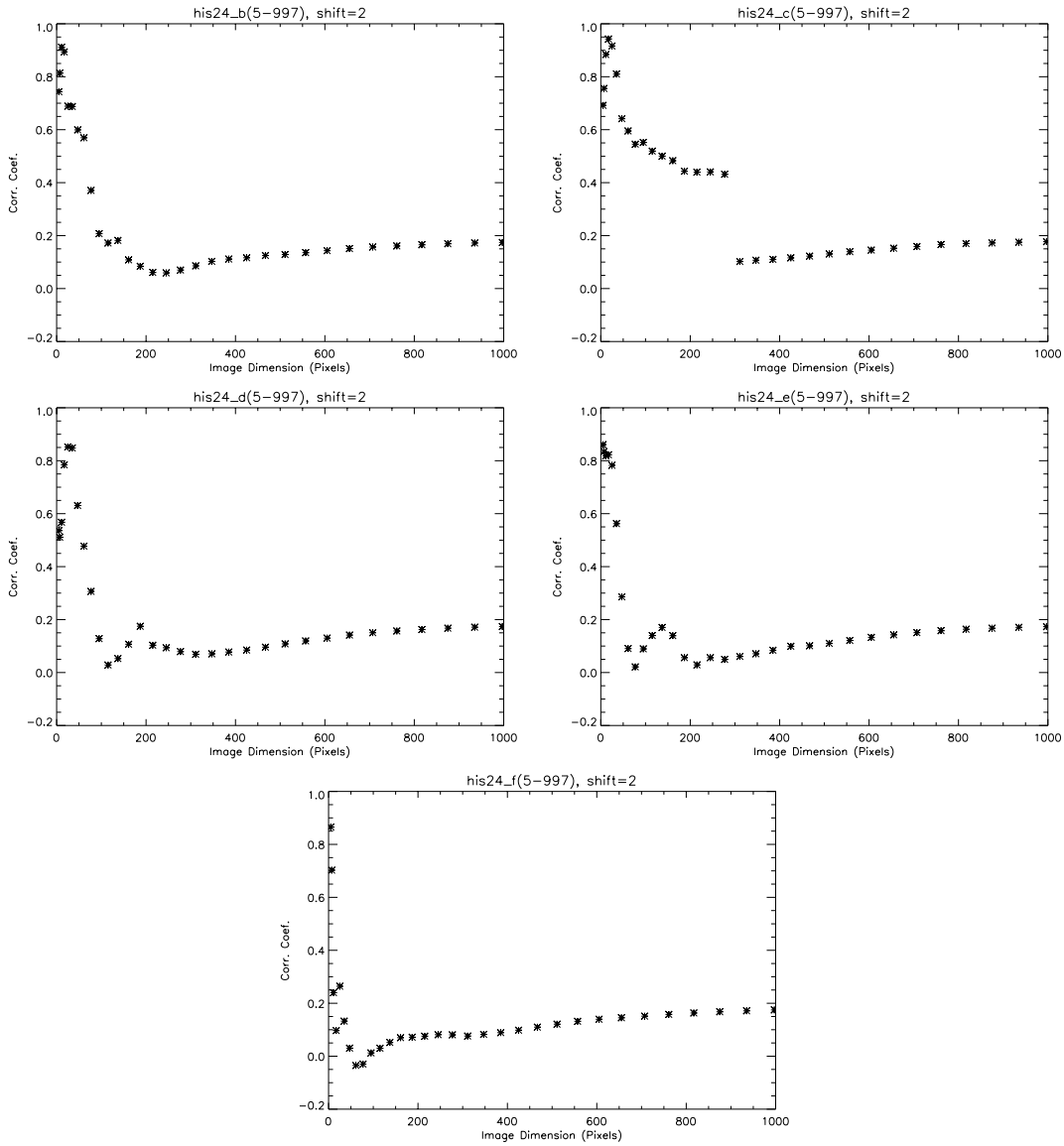

Figure A.6: The correlation coefficient of the H I and 24μm maps over 5 different areas. The x–axis represents the size of the individual images.

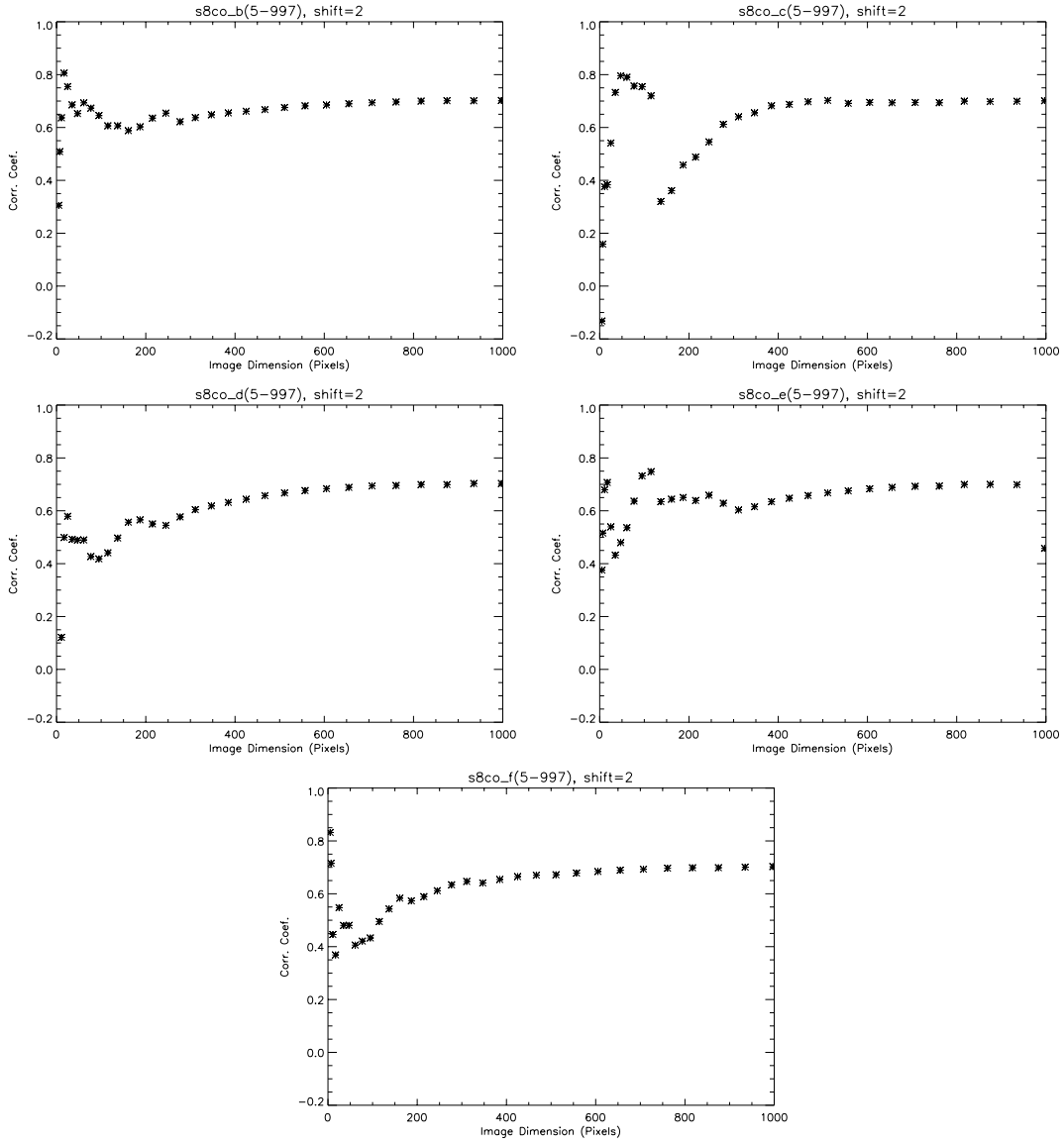

Figure A.7: The correlation coefficient of the 8μm and CO maps over 5 different areas. The x–axis represents the size of the individual images.

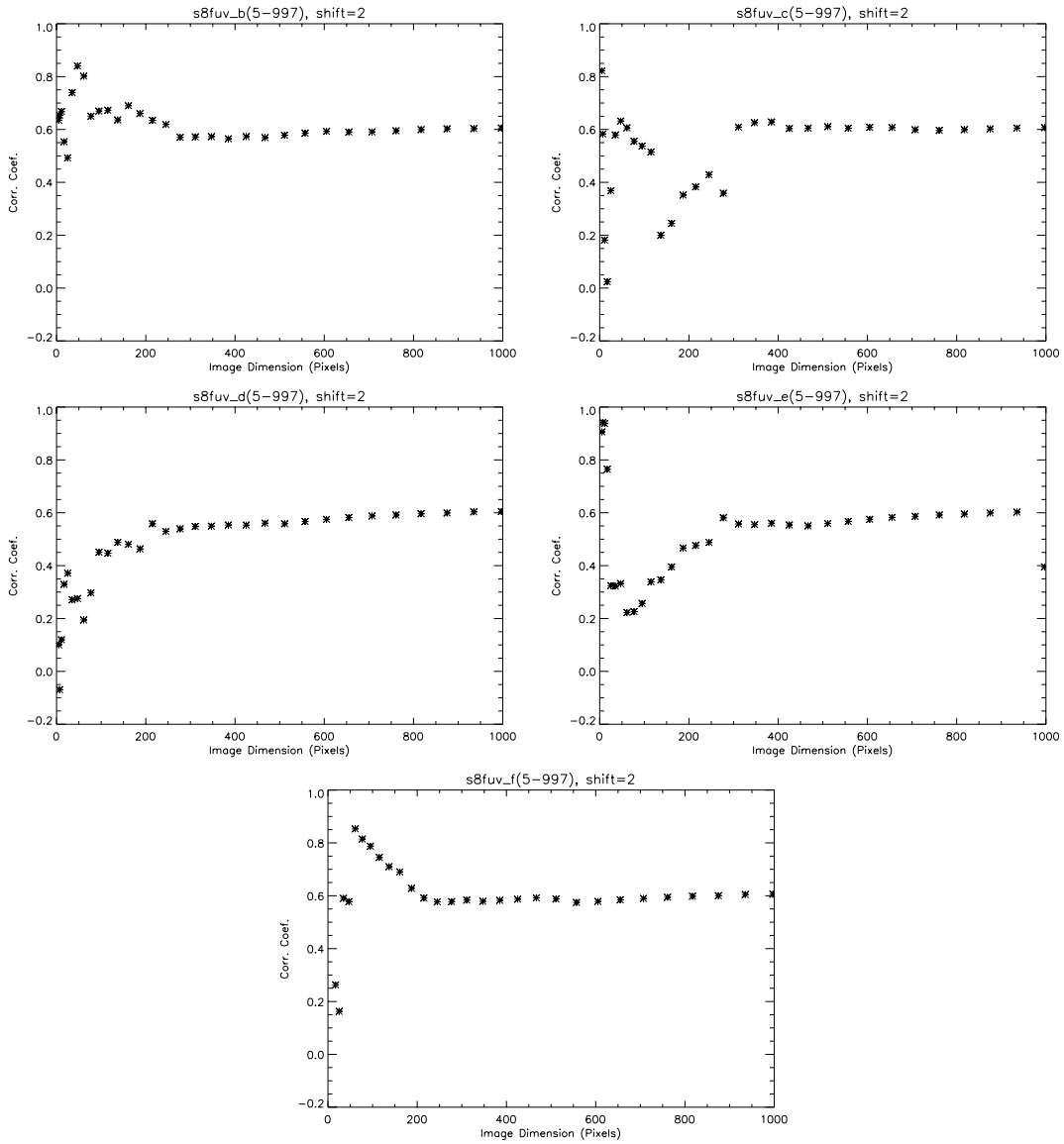

Figure A.8: The correlation coefficient of the 8μm and FUV maps over 5 different areas. The x–axis represents the size of the individual images.

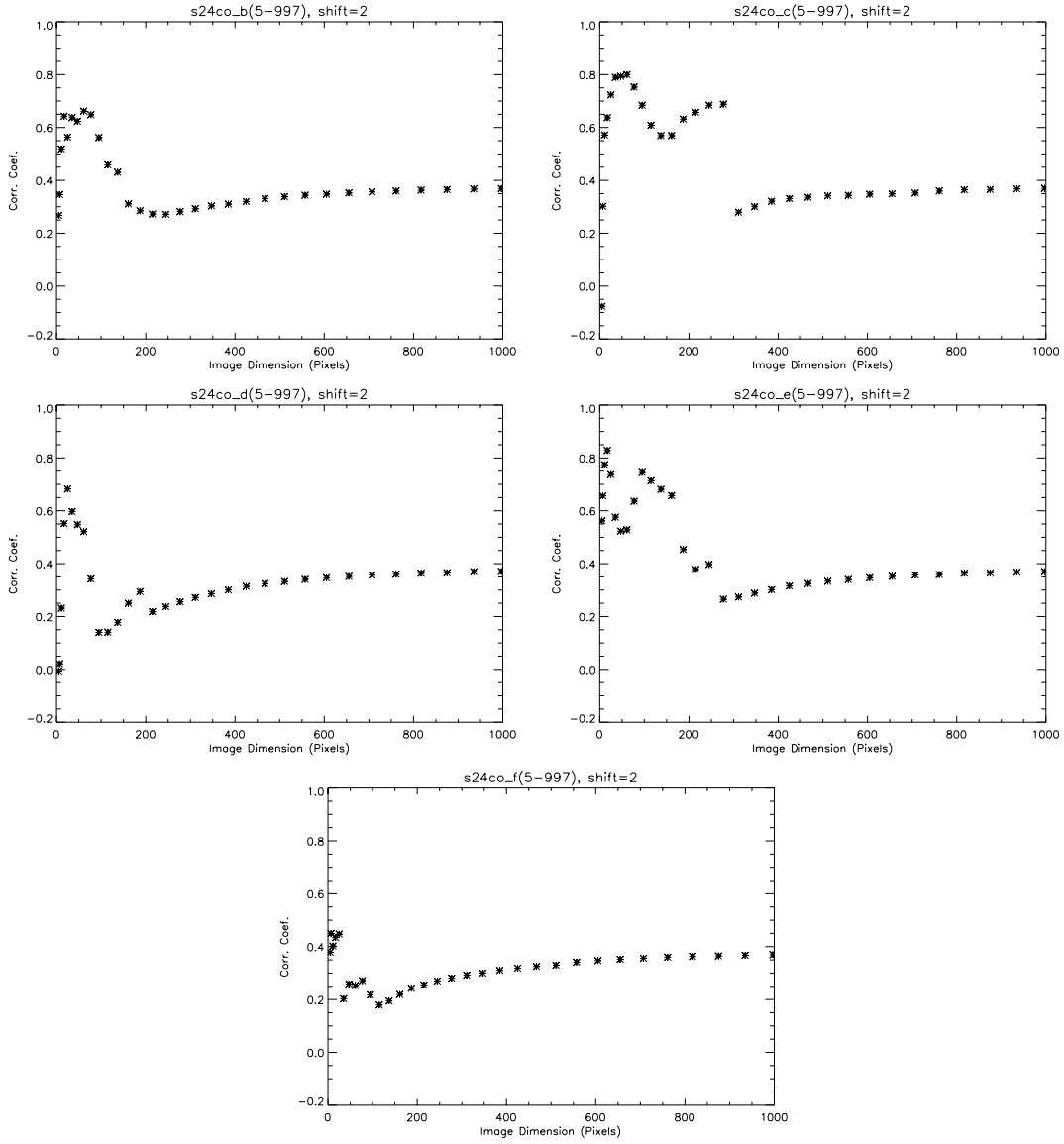

Figure A.9: The correlation coefficient of the 24μm and CO maps over 5 different areas. The x–axis represents the size of the individual images.

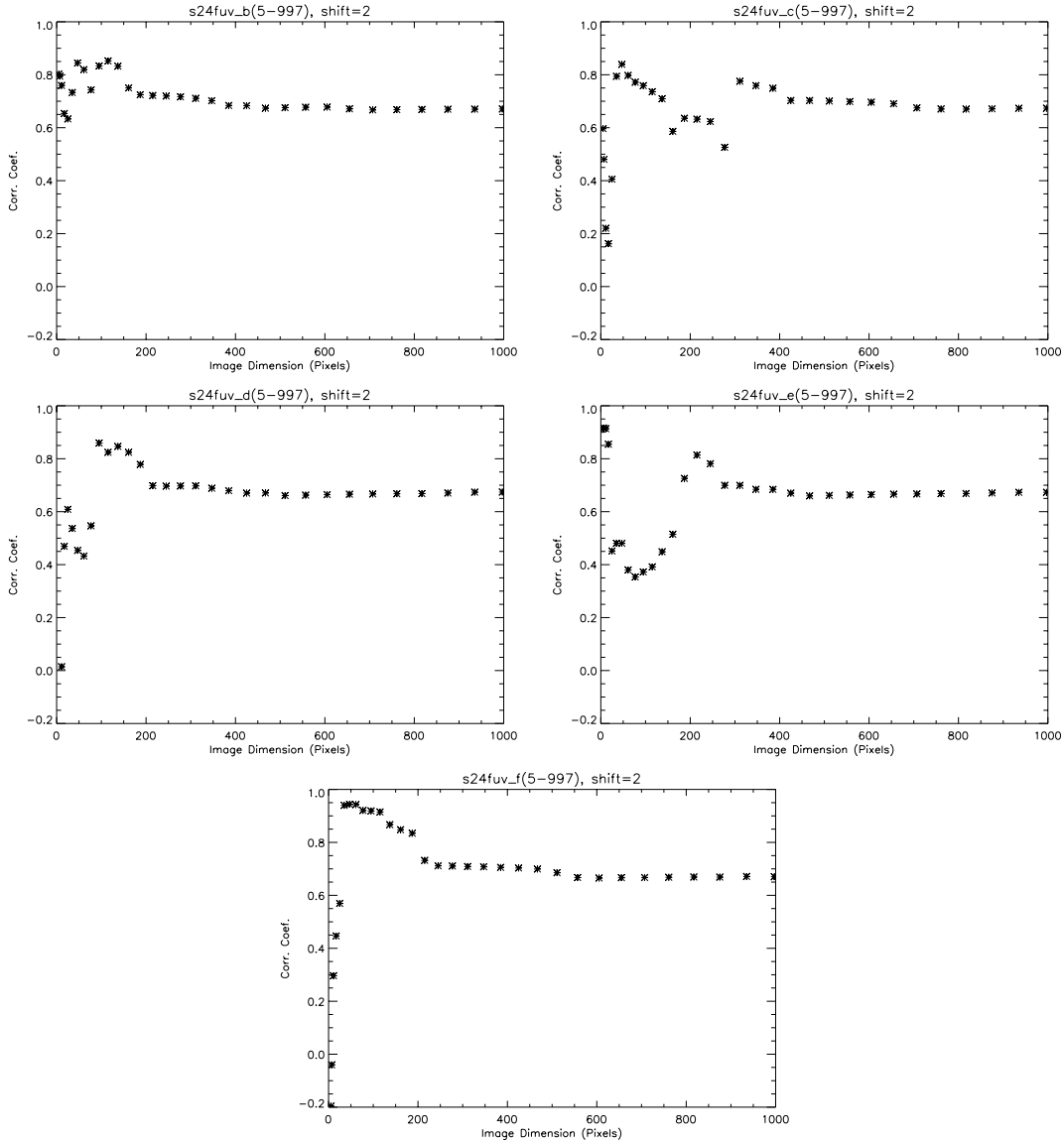

Figure A.10: The correlation coefficient of the 24μm and FUV maps over 5 different areas. The x–axis represents the size of the individual images.

A.2 The spatial distribution of C_{coef}

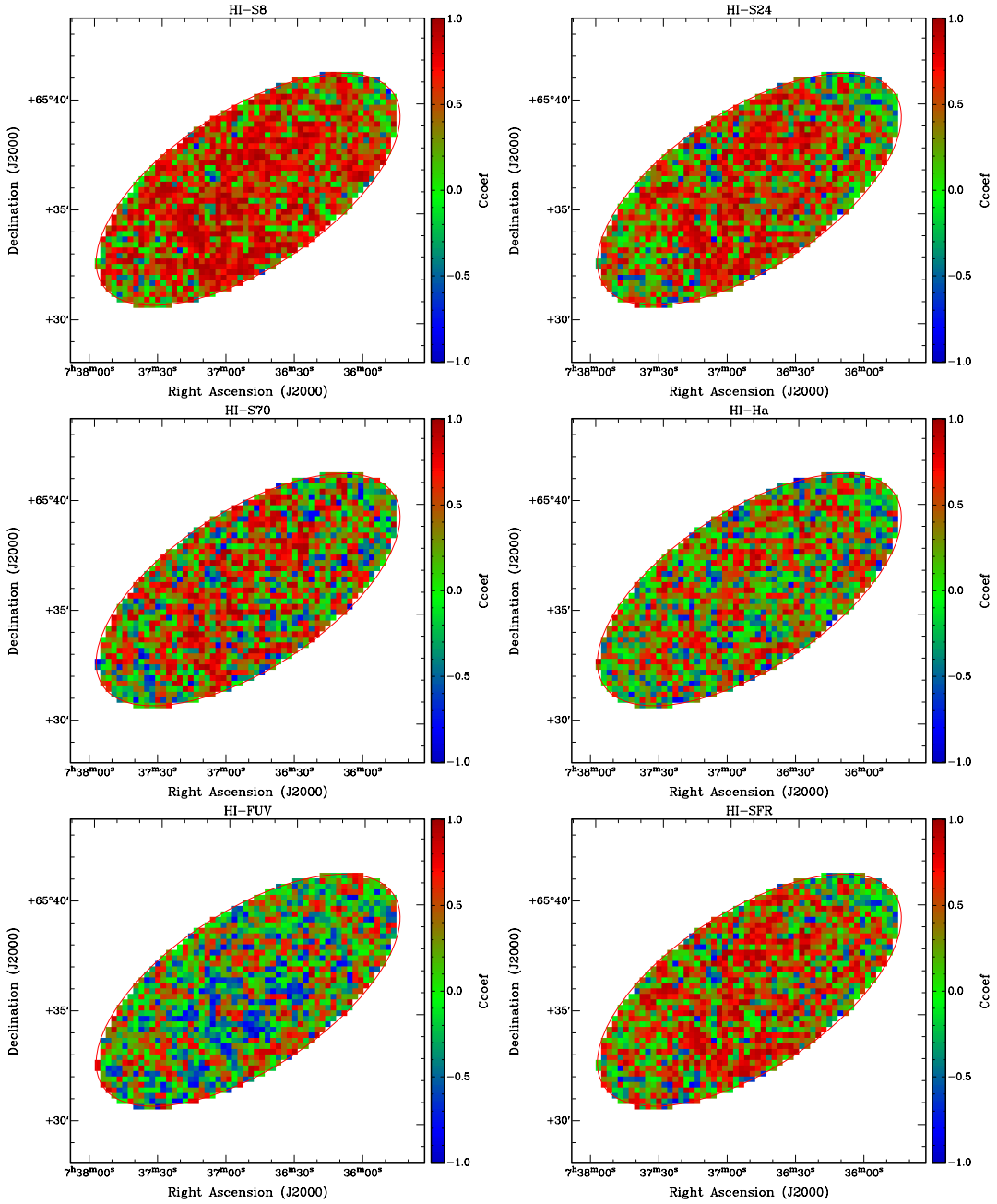

Figure A.11: The distribution of the correlation coefficient across the galaxy within R_{25}. Each box is $15'' \times 15''$ in size.

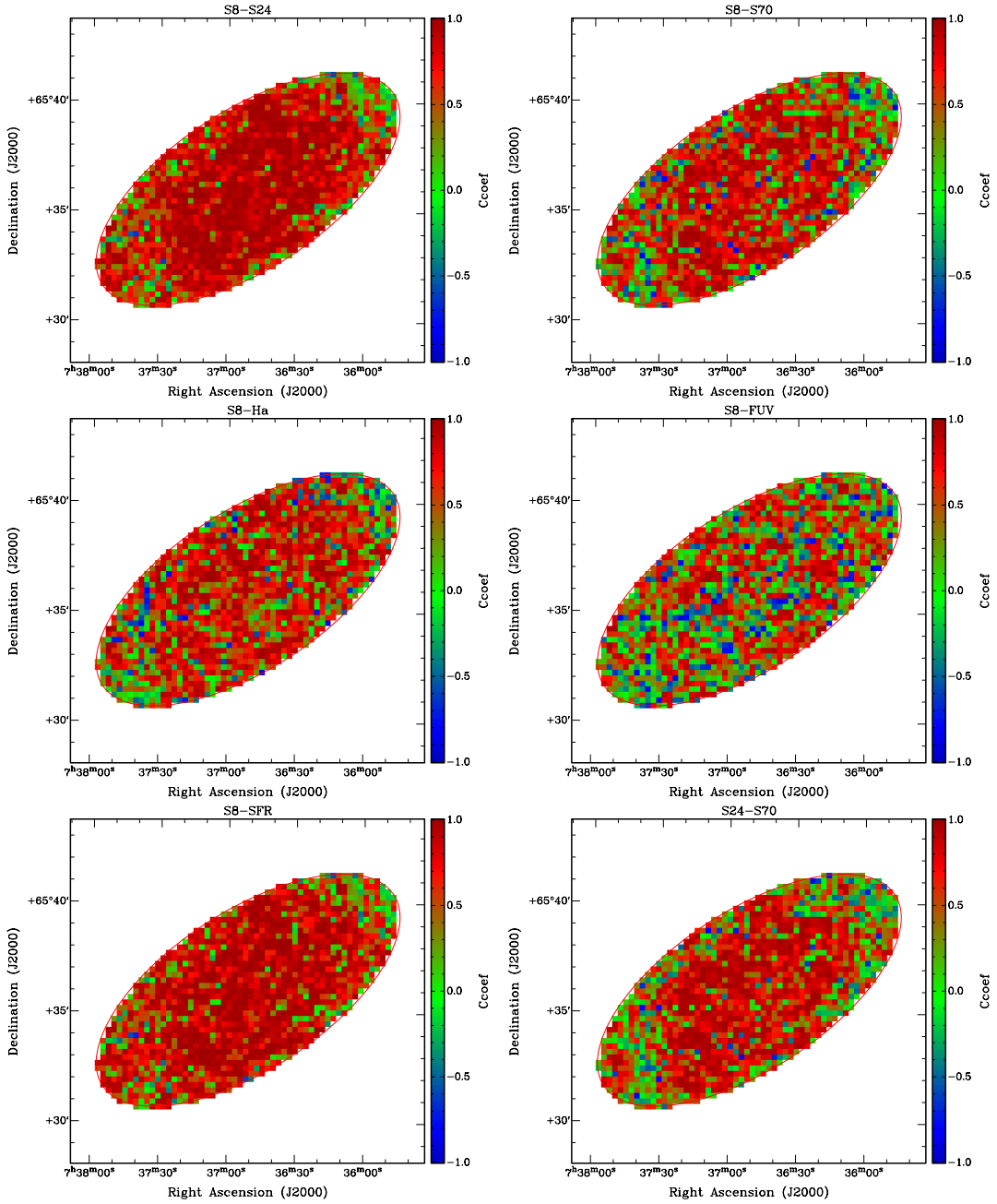

Figure A.12: The distribution of the correlation coefficient across the galaxy within R_{25}. Each box is $15'' \times 15''$ in size.

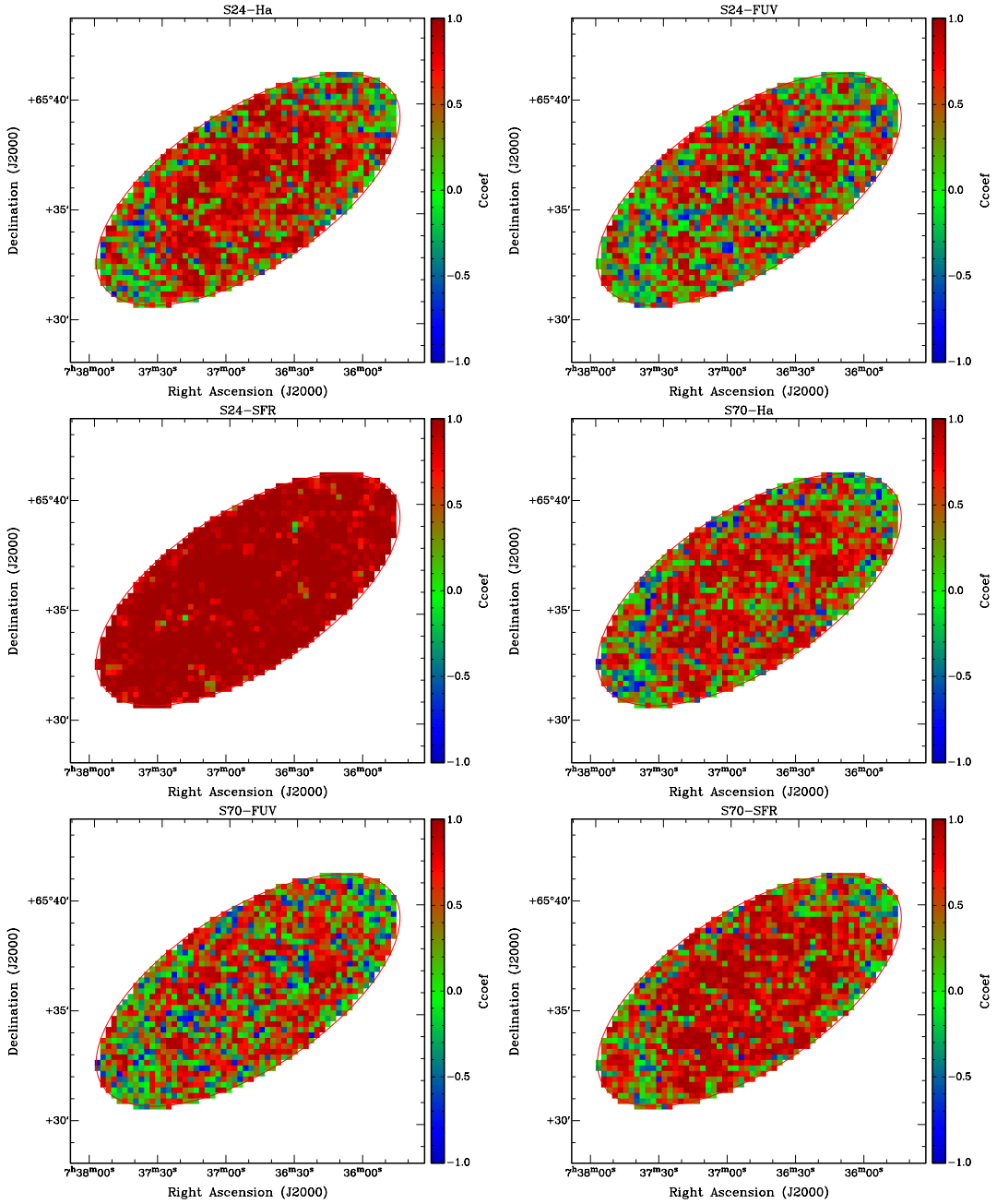

Figure A.13: The distribution of the correlation coefficient across the galaxy within R_{25}. Each box is $15'' \times 15''$ in size.

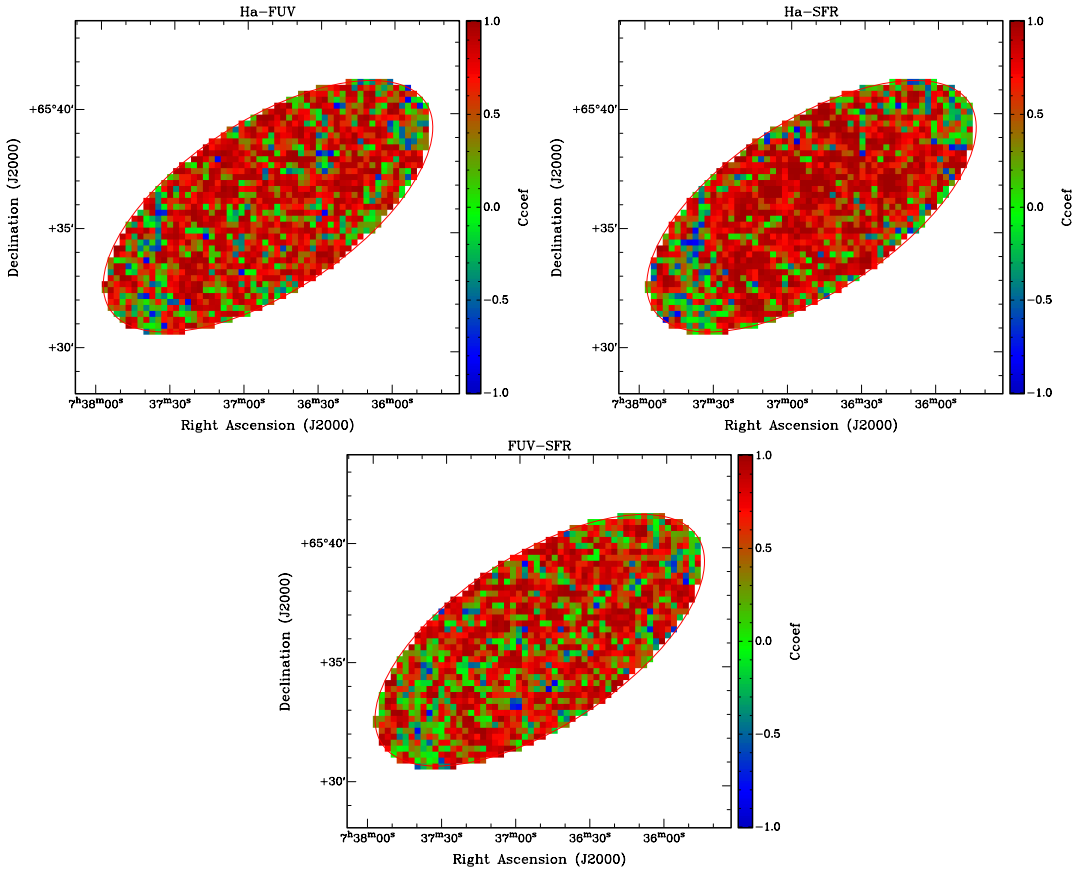

Figure A.14: The distribution of the correlation coefficient across the galaxy within R_{25}. Each box is $15'' \times 15''$ in size.

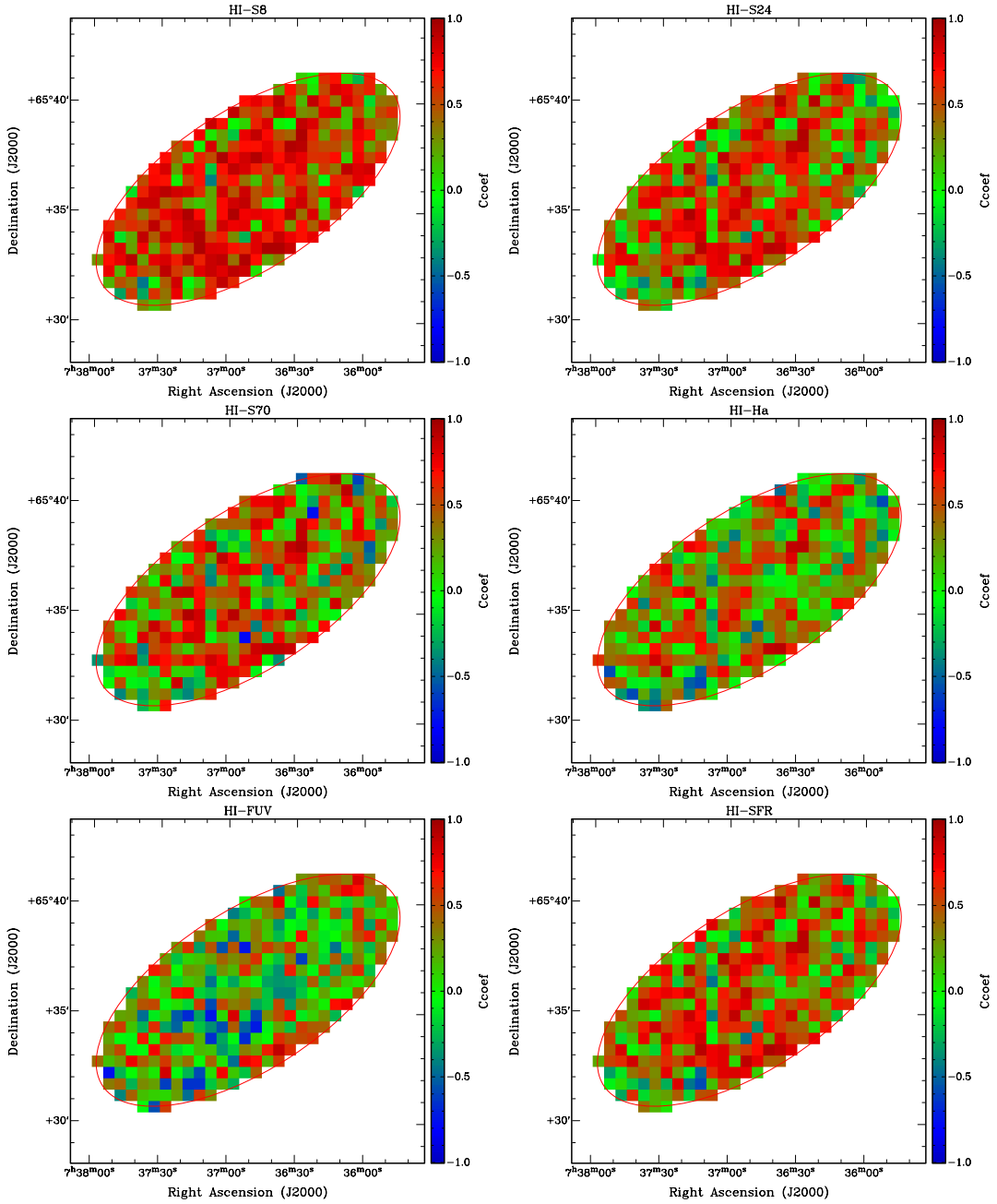

Figure A.15: The distribution of the correlation coefficient across the galaxy within R_{25}. Each box is $30'' \times 30''$ in size.

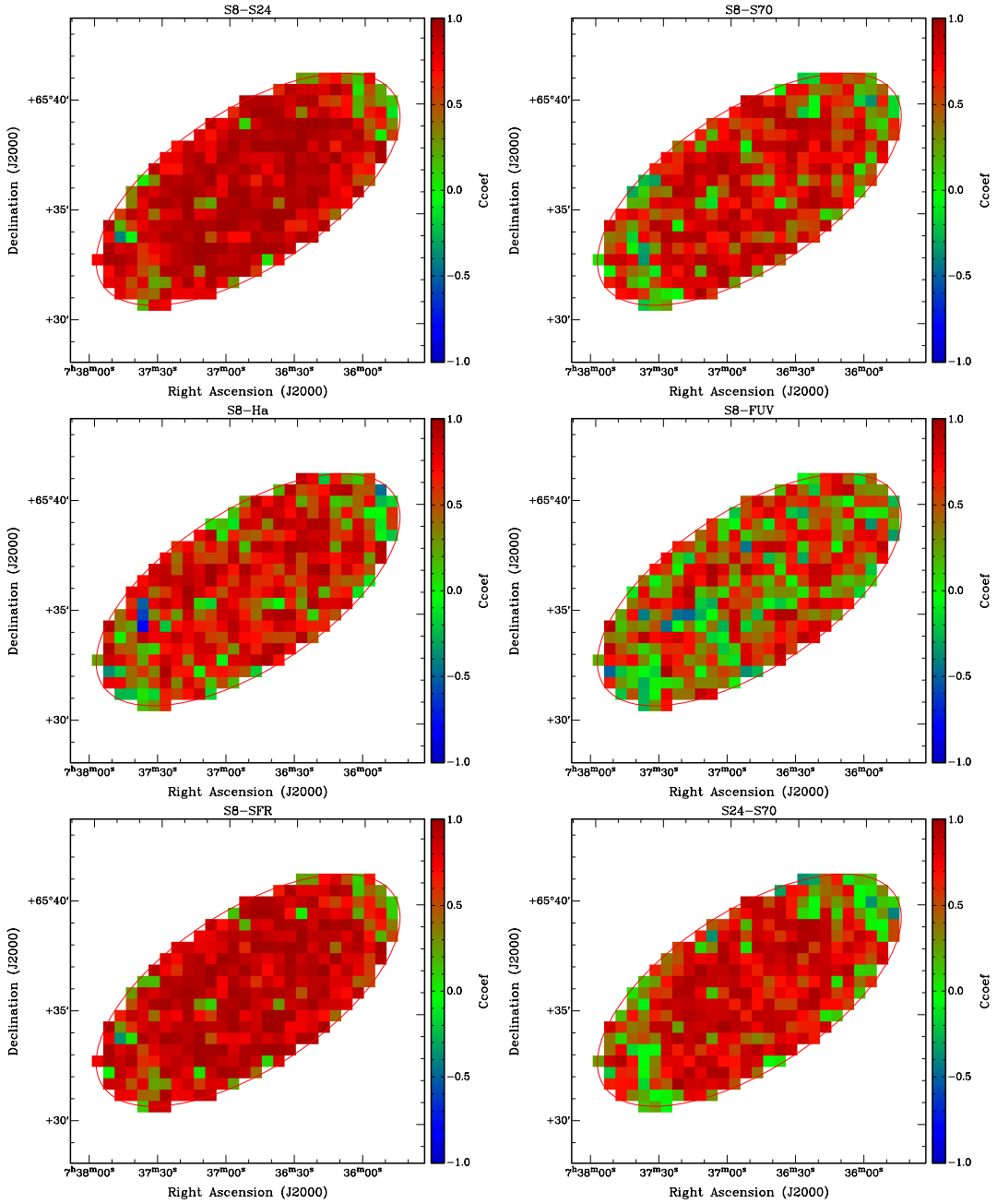

Figure A.16: The distribution of the correlation coefficient across the galaxy within R_{25}. Each box is $30'' \times 30''$ in size.

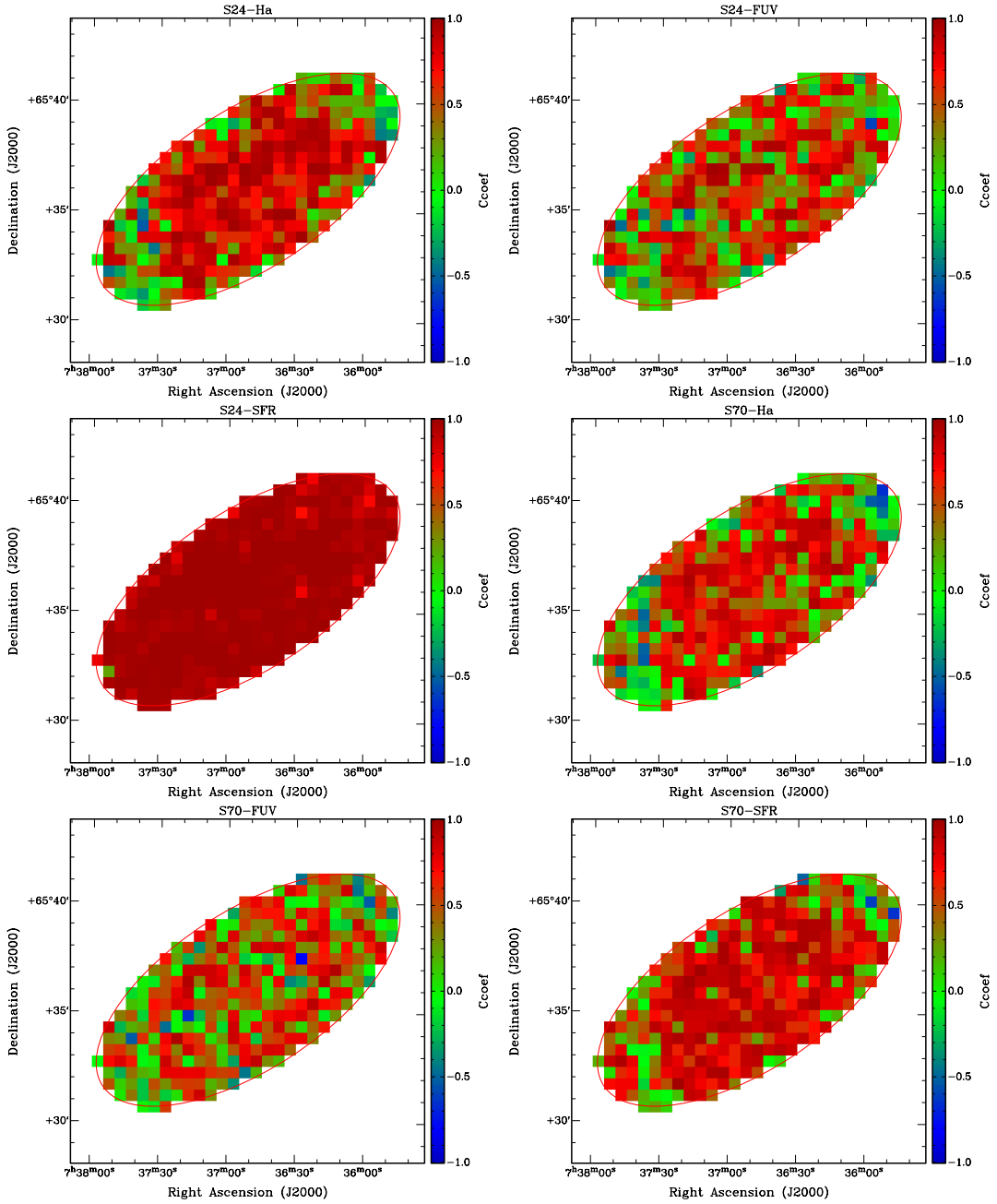

Figure A.17: The distribution of the correlation coefficient across the galaxy within R_{25}. Each box is $30'' \times 30''$ in size.

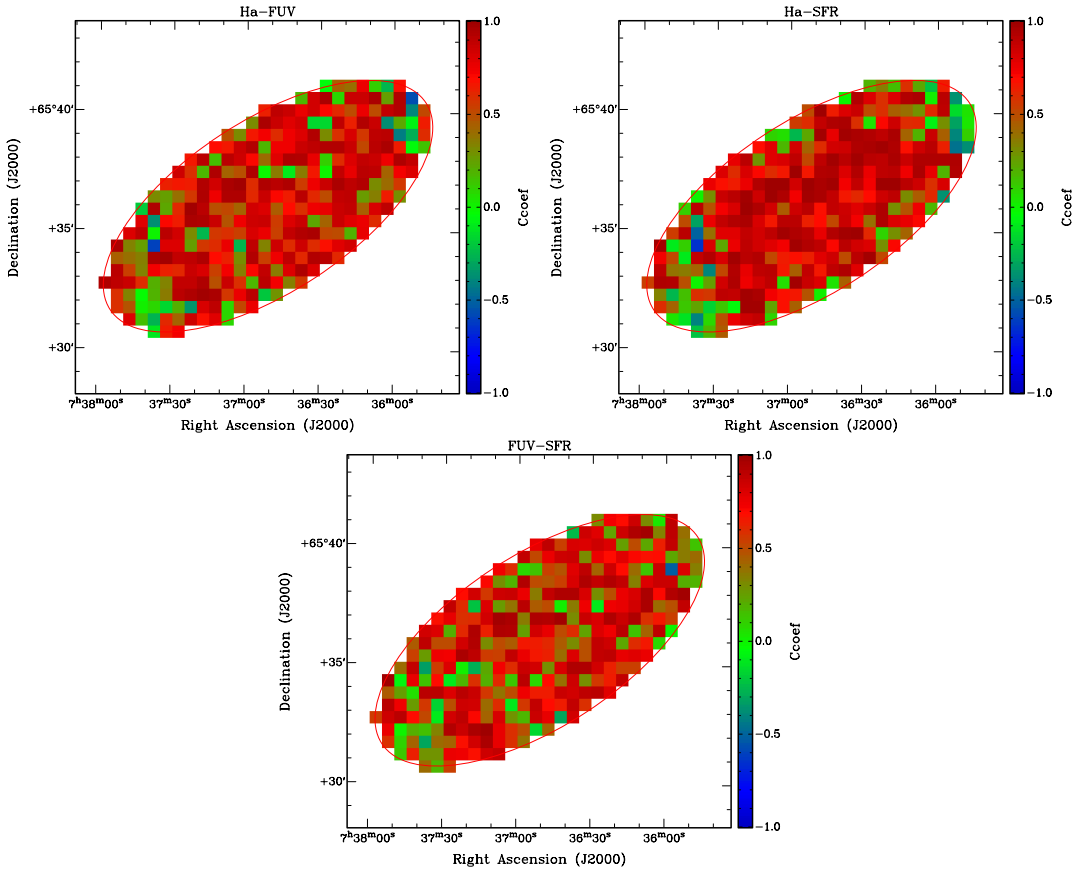

Figure A.18: The distribution of the correlation coefficient across the galaxy within R_{25}. Each box is $30'' \times 30''$ in size.

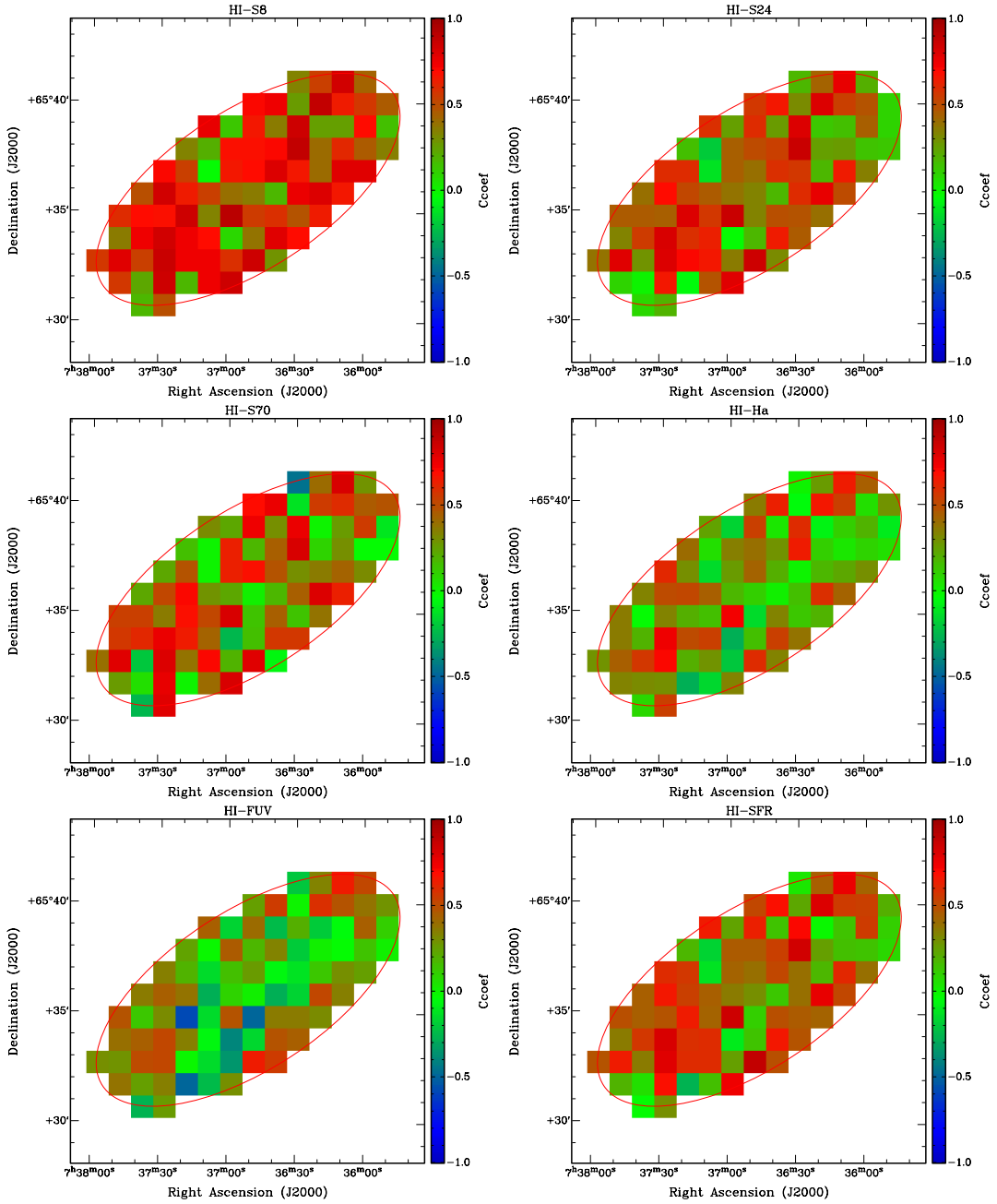

Figure A.19: The distribution of the correlation coefficient across the galaxy within R_{25}. Each box is $60'' \times 60''$ in size.

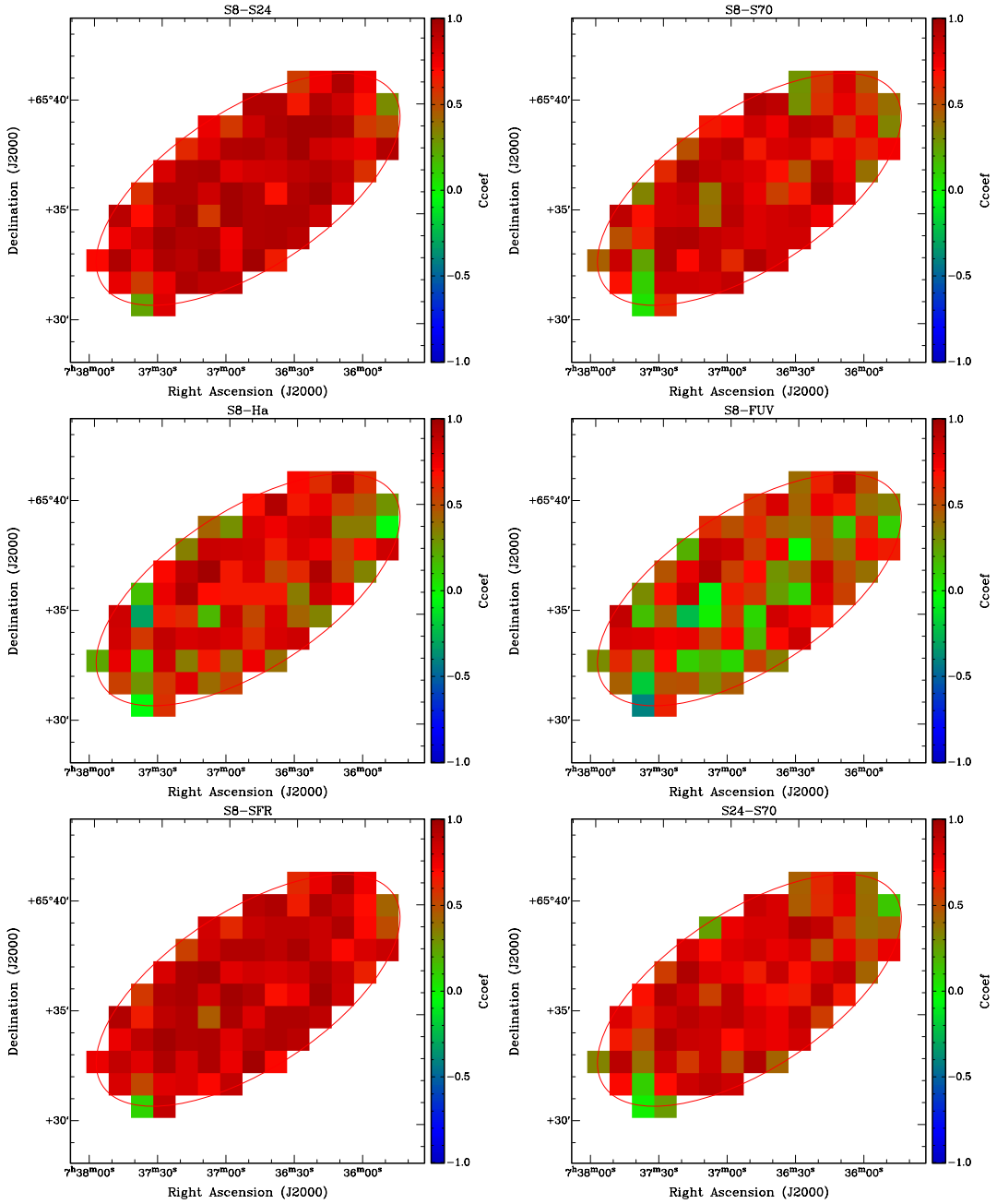

Figure A.20: The distribution of the correlation coefficient across the galaxy within R_{25}. Each box is $60'' \times 60''$ in size.

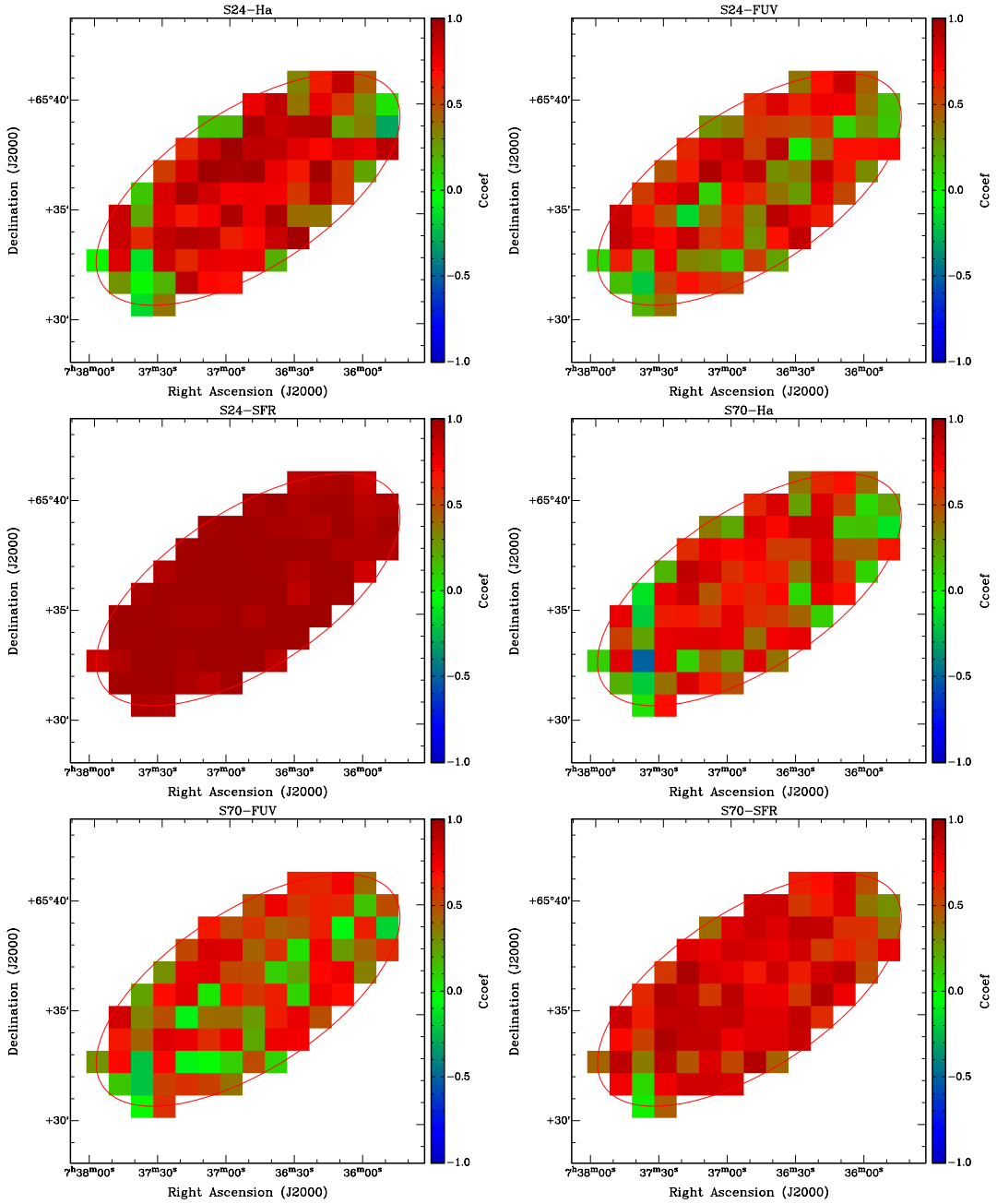

Figure A.21: The distribution of the correlation coefficient across the galaxy within R_{25}. Each box is $60'' \times 60''$ in size.

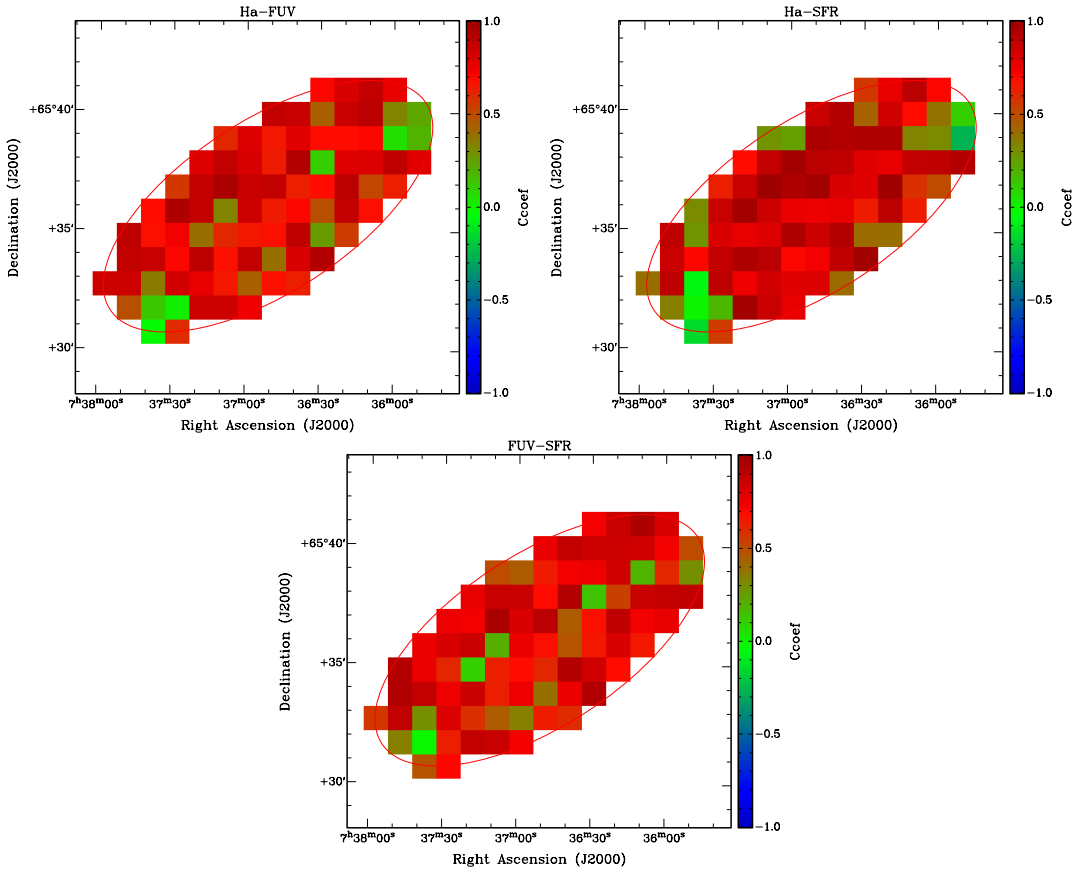

Figure A.22: The distribution of the correlation coefficient across the galaxy within R_{25}. Each box is $60'' \times 60''$ in size.

Appendix B

Publication List

Refereed Publications

1. Bagetakos I., Brinks E., Walter F., de Blok W. J. G., Usero A., Leroy A. K., Rich J. W., Kennicutt R. C., Jr., 2011, AJ, 141, 23

ABSTRACT: We present an analysis of the properties of H I holes detected in 20 galaxies that are part of "The H I Nearby Galaxy Survey." We detected more than 1000 holes in total in the sampled galaxies. Where they can be measured, their sizes range from about 100 pc (our resolution limit) to about 2 kpc, their expansion velocities range from 4 to 36 $\mathrm{km\,s^{-1}}$, and their ages are estimated to range between 3 and 150 Myr. The holes are found throughout the discs of the galaxies, out to the edge of the H I disc; 23% of the holes fall outside R_{25}. We find that shear limits the age of holes in spirals (shear is less important in dwarf galaxies) which explains why H I holes in dwarfs are rounder, on average than in spirals. Shear, which is particularly strong in the inner part of spiral galaxies, also explains why we find that holes outside R_{25} are larger and older. We derive the scale height of the H I disc as a function of galactocentric radius and find that the disc flares up in all galaxies. We proceed to derive the surface and volume porosity (Q_{2D} and Q_{3D}) and find that this correlates with the type of the host galaxy: later Hubble types tend to be more porous. The size distribution of the holes in our sample follows a power law with a slope of a $a_\nu \sim -2.9$. Assuming that the holes are the result of massive star formation (SF), we derive values for the supernova rate and star formation rate (SFR) which scales with the SFR derived based on other tracers. If we extrapolate the observed number of holes to include those that fall below our resolution limit, down to holes created by a single supernova, we find that our results are compatible with the hypothesis that H I holes result from SF.

2. Banerjee A., Jog C. J., Brinks E., Bagetakos I., 2011, MNRAS, 415, 687

ABSTRACT: In this paper, we model dwarf galaxies as a two-component system of gravitationally coupled stars and atomic hydrogen gas in the external force field of a pseudo-isothermal dark matter halo, and numerically obtain the radial distribution of H I vertical scale heights. This is done for a group of four dwarf galaxies (DDO 154, Ho II, IC 2574 and NGC 2366) for which most necessary input parameters are available from observations. The formulation of the equations takes into account the rising rotation curves generally observed in dwarf galaxies. The inclusion of self-gravity of the gas into the model at par with that of the stars results in scale heights that are smaller than what was obtained by previous authors. This is important as the gas scale height is often used for deriving other physical quantities. The inclusion of gas self-gravity is particularly relevant in the case of dwarf galaxies where the gas cannot be considered a minor perturbation to the mass distribution of the stars. We find that three out of four galaxies studied show a flaring of their H I discs with increasing radius, by a factor of a few within several disc scale lengths. The fourth galaxy has a thick H I disc throughout. This flaring arises as a result of the gas velocity dispersion remaining constant or decreasing only slightly while the disc mass distribution declines exponentially as a function of radius.

3. Rich J. W., de Blok W. J. G., Cornwell T. J., Brinks E., Walter F., Bagetakos I., Kennicutt R. C., Jr., 2008, AJ, 136, 2897

ABSTRACT: A practical evaluation of the multi-scale CLEAN algorithm is presented. The data used in the comparisons are taken from The H I Nearby Galaxy Survey. The implementation of multi-scale CLEAN in the CASA software package is used, although comparisons are made against the very similar multi-resolution CLEAN algorithm implemented in AIPS. Both are compared against the classical CLEAN algorithm (as implemented in AIPS). The results of this comparison show that several of the well-known characteristics and issues of using classical CLEAN are significantly lessened (or eliminated completely) when using the multi-scale CLEAN algorithm. Importantly, multi-scale CLEAN significantly reduces the effects of the clean "bowl" that is caused by missing short-spacings, and the "pedestal" of low-level un-cleaned flux (which affects flux scales and resolution). Multi-scale CLEAN can clean down to the noise level without the divergence suffered by classical CLEAN. We discuss practical applications of the added contrast provided by multi-scale CLEAN using two selected astronomical examples: H I holes in the interstellar medium and anomalous gas structures outside the main galactic disc.

Other Publications

1. Bagetakos I., Brinks E., Walter F., de Blok W. J. G., Rich J. W., Usero A., Kennicutt R. C., Jr., 2009, eimw.conf

2. Bagetakos I., Brinks E., Walter F., de Blok E., 2007, IAUS, 237, 394

3. Bagetakos I., Brinks E., Walter F., de Blok E., 2007, IAUS, 237, 393

4. Brinks E., Bagetakos I., Walter F., de Blok E., 2007, IAUS, 237, 76

5. Brinks E., Bigiel F., Leroy A., Walter F., de Blok W. J. G., Bagetakos I., Usero A., Kennicutt R. C., 2009, IAUS, 254, 301

6. Brinks E., et al., 2008, IAUS, 255, 265

7. de Blok E., et al., 2007, atnf.prop, 730

8. de Blok W. J. G., et al., 2009, ASPC, 407, 88

9. Thornley M. D., Leroy A. K., Schruba A., Bagetakos I., Portas A., Usero A., Bigiel F., Foyle K., 2010, ASPC, 438, 3